SYNTHESIS OF RUTHENIUM(II) AND OSMIUM(II) COMPLEXES [Ru/Os(η^6-ARENE)L, L = BIS(PYRAZOL-1-YL)METHANE; L = (3-CHLORO-6-(1H-PYRAZOL-1-YL)PYRIDAZINE]: ASSESSMENT OF THEIR DNA BINDING AND CYTOTOXICITY ACTIVITY

KANYORA AMOS KIMEMIA

A Thesis Submitted to the Graduate School in Partial Fulfilment for the Requirements of the Degree of Doctor of Philosophy in Chemistry of Egerton University

EGERTON UNIVERSITY

JUNE 2025

DECLARATION AND RECOMMENDATION

Declaration

This thesis is my original work and has not been presented for the award of a degree in any other institution, except where the work of others has been acknowledged within the text.

Signature  Date 23/06 /2025

Kanyora Amos Kimemia

SD11/12277/16

Recommendation

The research work presented in this thesis was conducted by the candidate and is submitted for examination with our approval as University supervisors.

Signature:  Date 24/06/2025

Dr. P. O Ongoma

Egerton University

Signature:  Date 27/06/2025

Prof. J. O Omolo

Egerton University

Signature:  Date 24/06/2025

Prof. J. M Gichumbi

Chuka University

COPYRIGHT

DEDICATION

This thesis is dedicated to the cherished memory of my dear wife, *Peris Wangari*, whose love, strength, and unwavering support continue to inspire me each day. To our daughter, *Leanne Wambui*, you are the light of my life and a constant reminder of hope and purpose. I am deeply grateful to my parents and siblings for their steadfast encouragement, love, and support throughout this journey. To my father, thank you for your guidance and for the many sacrifices that laid the foundation for my success.

ACKNOWLEDGEMENTS

This thesis would not have been accomplished without the providence, grace, and strength of God, whose guidance and sustenance have been a constant source of support throughout this academic journey. I am profoundly thankful to my supervisors—Dr. P. O. Ongoma, Prof. J. O. Omolo, and Prof. M. Gichumbi—for their exceptional mentorship, invaluable guidance, and continuous encouragement throughout my doctoral journey. I also appreciate the support of the technical staff in the Department of Chemistry and extend special thanks to my colleague, Divinah, for her unwavering assistance.

Special appreciation goes to Dr. A. Mambanda and Dr. R. Ochola for their invaluable mentorship and support. I am thankful to Leigh A. Hunter for his assistance with DFT calculations and X-ray diffraction data; to C. G. Grimmer for support with NMR analysis; to C. J. Van Rensburg for mass spectrometry assistance; and to Athi Welsh for his insights during cytotoxicity studies. I also acknowledge Prof. Gregory S. Smith and Prof. Sharon Prince for their generous support in funding the DNA and cytotoxicity investigations.

I am sincerely thankful to Egerton University for the opportunity to pursue my doctoral studies, and to the Department of Chemistry for providing an academic environment conducive to research. I also acknowledge the University of KwaZulu-Natal (School of Chemistry and Physics, PMB Campus, RSA) for facilitating key aspects of the project including characterisation, single-crystal X-ray diffraction, and DFT studies. Additionally, I thank the University of Cape Town, Departments of Chemistry and Human Biology, for supporting the DNA interaction and cytotoxicity components of this work.

Finally, my heartfelt appreciation goes to my late wife, Peris, whose memory continues to inspire and strengthen me each day. To our daughter, Leanne, thank you for being a constant source of light, joy, and hope. I am also deeply grateful to my parents and siblings—Beth, Irene, the late Ruth, and Andrew—for their unwavering love and support. Special thanks to Hellen, Beth, and Dr. Kariukis for their kindness, sacrifices, and continued encouragement throughout this academic journey.

ABSTRACT

Cancer, a non-communicable disease, continues to rank among the top causes of mortality globally, with a substantial number of new diagnoses reported annually. Although platinum-based drugs are involved in nearly 50% of cancer treatment regimens and are highly effective against various types of cancer, they suffer from drawbacks that limit their broader application and efficacy. As alternatives, (η^6-arene)ruthenium(II)/osmium(II) complexes have shown better antiproliferative properties and more favourable toxicity profiles, making them promising candidates for further exploration. This work reports the synthesis of fifteen mononuclear Ru(II) and Os(II) complexes bearing η^6-arene ligands in combination with either bis(pyrazol-1-yl)methane or pyrazolyl-pyridazine donor systems. Comprehensive characterization was carried out using a suite of techniques, including CHN elemental analysis, FTIR, UV–Vis spectroscopy, ^{1}H and ^{13}C NMR, mass spectrometry, and single-crystal X-ray diffraction. The electronic structures of the complexes were further examined through density functional theory (DFT) calculations. A subset of five Ru(II) pyrazolyl–pyridazine complexes was selected to probe their binding interactions with calf thymus DNA (CT-DNA) and glutathione (GSH) *via* UV–Vis absorption and fluorescence titration assays. The findings revealed that the Ru(II) compounds demonstrated moderate to strong affinities for CT-DNA, with binding occurring predominantly through minor groove interactions. Molecular docking studies further supported these findings, indicating stable binding conformations. The relative binding affinities were determined as follows: -5.8 kcal/mol (**9**) > -5.7 (**4a**) > -5.6 (**3a**) > -5.4 (**3c**) > -5.3 (**4c**) > -3.6 (cisplatin), suggesting stronger DNA binding than the standard drug cisplatin. Moderate anticancer activity was observed against the MCF-7 breast cancer cell line, with complex **9** being the most potent (IC_{50} = 41.94 ± 2.05 μM), though none of the compounds showed efficacy against MDA-MB-231. Ru(II) complexes with bis(pyrazol-1-yl)methane ligands showed low cytotoxicity across all cell lines tested. DFT results indicated that electron density on the metal centre and surrounding ligands significantly influenced reactivity. GSH studies revealed that chloro analogues were more readily deactivated than iodo analogues. Collectively, the results indicate that these complexes hold promise as foundational structures for designing more effective anticancer therapeutics.

TABLE OF CONTENTS

LIST OF FIGURES

LIST OF TABLES

LIST OF SCHEMES

LIST OF ABBREVIATIONS AND ACRONYMS

δ	Chemical shift
ΔG	Gibbs energy
Å	Angstrom
B3LYP	Hybrid Becke, 3-parameter, Lee-yang-Parr
CT	Calf Thymus
CV	Cyclic Voltammetry
DACH	Diaminocyclohexane
DFT	Density functional theory
DMSO	Dimethyl sulfoxide
DNA	Deoxyribonucleic Acid
DNA	Deoxyribonucleic acid
eV	Electronvolt
FTIR	Fourier Transform Infrared
HIV	Human Immunodeficiency Virus
HOMO	highest occupied molecular orbital
HPV	Human Papilloma Virus
IC_{50}	Concentration of a compound that induces 50% of growth inhibition of cells compared to untreated cells
J	Coupling constant
Kcal	Kilocalorie
kJ	Kilojoules
KP1019	Indazolium *trans*-[tetrachloridobis(*1H*-indazole)ruthenate(III)]
KP1339	Sodium *trans*-[tetrachloridobis(1H-indazole)ruthenate(III)]

LANL2DZ Los Alamos National Laboratory 2 double

LMCT Ligand-to-metal charge transfer

LUMO Lowest occupied molecular orbital

MCF-7 Breast carcinoma

MLCT Metal-to-charge transfer

MTT 3-(4, 5-dimethyl-2-thiazolyl)-2, 5-diphenyl-2Htetrazolium bromide

NAMI-A Imidazolium*trans*-[tetrachlorido(dimethylsulfoxide)(*1H*-imidazole)ruthenate(III)]

NBO Natural bond orbital

NCDs Non-communicable Diseases

ORTEP Oak Ridge Thermal Ellipsoid Plot

PBS Phosphate Buffered Saline

PHEHAT 1, 10-phenanthrolino[5, 6-b]-1, 4, 5, 8, 9, 12-hexaazatriphenylene

RAPTA-C [Ru(η^6-*p*-cymene)(PTA)Cl_2] PTA = 1, 3, 5-triaza-7-phosphaadamantane

RM175 [Ru(η^6-biphenyl)Ru(en)Cl]$^+$, *en* = ethylenediamine)

S, d, t, m (NMR) Singlet, doublet, triplet, multiplet

$TBABF_4$ Tetrabutylammoniumtetrafluoroborate

CHAPTER ONE

INTRODUCTION

1.1 Background Information

The investigation of metal-based therapeutics is largely driven by mechanistic insights into the biochemical functions and coordination behaviour of metal ions within living systems. Transition metal coordination compounds, in particular, are essential to various physiological functions, including enzymatic activity, maintenance of homeostasis, and molecular transport. A notable example is the heme complex, which contains iron(II) ions and facilitates oxygen transport within the bloodstream. Moreover, inorganic compounds have long been employed in medicine to address specific health conditions. For instance, iron(III) and gold(I) compounds have therapeutic applications in the treatment of arthritis and cardiovascular disorders, respectively, while platinum(II) complexes are commonly used in cancer chemotherapy (Sodhi & Paul, 2019).

In 2020, cancer claimed nearly 10 million lives globally, representing approximately one in six fatalities, and continues to rank high among non-communicable disease-related deaths. The most frequently occurring cancers include breast (2.26 million cases), lung (2.21 million), colorectal (1.93 million), prostate (1.41 million), skin (1.02 million), and stomach (1.09 million) cancers. The World Health Organization (WHO) has noted that the global incidence of cancer is projected to continue increasing over the next two decades (Ferlay *et al.*, 2021).

Cancer treatment typically involves a combination of surgery, radiation therapy, and chemotherapy. Surgical intervention is commonly employed when the tumour is localised and accessible, often followed by chemotherapy and/or radiation to target residual malignant cells that may not have been eliminated during surgery. Additionally, chemotherapy can also be employed in a neoadjuvant setting to shrink tumour prior to surgical intervention (Huang *et al.*, 2023; Peacock & Sadler, 2008). Therefore, it is imperative to develop additional chemotherapeutic agents to complement existing treatments in the ongoing effort to combat cancer.

Several clinically approved Platinum(II) derivatives have been widely utilised in cancer chemotherapy and continue to form a critical component of treatment strategies for diverse

tumour types (Lopez-Valbuena *et al.*, 2010; Ongoma & Jaganyi, 2012; Wheate *et al.*, 2007; Zhou *et al.*, 2023). Despite their efficacy, platinum-based treatments are hindered by the onset of resistance and substantial toxicities (nervous system damage, hearing loss, and kidney damage) have strongly restricted their therapeutic importance in clinical use and thus led researchers to explore non-platinum metal complexes for anticancer drug discovery (Boulikas *et al.*, 2007; Wong & Ang, 2012). An alternative approach in anticancer drug development focuses both on generating structurally diverse platinum analogues and investigating other metal centres with unique properties and therapeutic mechanisms, aimed at overcoming the drawbacks linked to platinum-based treatments (Govender *et al.*, 2009). Compounds of ruthenium(II) (Nongpiur *et al.*, 2023), Iron(II) (Wani *et al.*, 2016), Palladium(II) (Omondi *et al.*, 2022), Gold(I) (Sze *et al.*, 2020), Osmium(II) (Nabiyeva *et al.*, 2020; Ywaya *et al.*, 2024), and Titanium(IV) (Nahari & Tshuva, 2021) compounds have demonstrated notable anticancer activity.

Ruthenium-based compounds have gained increasing attention for their design and potential use as anticancer agents. These metal complexes are characterised by advantageous features, including minimal systemic toxicity, biological behaviour that parallels iron, and exceptional stability across various oxidation states—particularly +2 to +4—under physiological environments (Matveevskaya *et al.*, 2021). In contrast to the planar configuration typical of cisplatin, octahedral architectures provide enhanced three-dimensional flexibility and allow coordination with additional ligands, facilitating the integration of functional or bioactive groups into the molecular framework (Eswaran *et al.*, 2022; Wu *et al.*, 2014). This feature makes Ru(II) advantageous over Pt(II).

Ruthenium compounds are characterised by slower ligand-exchange kinetics compared to platinum and palladium, which helps them remain intact as they approach DNA (Omondi *et al.*, 2022). Ruthenium(II) complexes demonstrate robust stability in both solid and solution phases, providing a versatile platform for fine-tuning ligand binding strength, kinetic substitution behaviour, and redox properties. This ability to influence kinetic stability is essential for drug development (Bruijnincx & Sadler, 2009). Ruthenium complexes thus emerge as promising alternatives, offering therapeutic benefits that address several shortcomings associated with platinum-based agents (Maximiano *et al.*, 2024).

Certain investigational Ru(III)-based drug candidates—among them well-known agents (NAMI-A and KP1339) evaluated for activity against metastatic tumour—have progressed into

clinical trials targeting cancers like those of the lung and colon (Hartinger *et al.*, 2008; Maikoo *et al.*, 2021). However, these trials were terminated due to limited therapeutic efficacy and poor aqueous solubility of the compounds (Khater *et al.*, 2023). Mechanistic investigations have demonstrated that Ru(III) complexes act as prodrugs, undergoing *in vivo* reduction within cancer cells to generate more labile and cytotoxic Ru(II) species (Brindell *et al.*, 2008; Eswaran *et al.*, 2022). Due to their enhanced kinetic inertness and thermodynamic robustness compared to Ru(III) counterparts, Ru(II) compounds have attracted growing interest, with recent studies emphasizing their direct preparation and therapeutic potential.

Ru(II)-based therapeutic agents incorporating an η^6-arene moiety, a stabilising donor ligand, and a labile chloride ion have garnered considerable interest as promising candidates for novel chemotherapeutics with reduced toxicity, improved biocompatibility, and enhanced tumour selectivity (Kokkosi *et al.*, 2024). Notable examples include RAPTA-C (Zeng *et al.*, 2017) and RM175 (Anthony *et al.*, 2020; Tomaz *et al.*, 2012). These η^6-arene Ru(II) compounds demonstrate comparable, and in certain instances superior, antitumour efficacy, while demonstrating lower systemic toxicity, minimal cross-resistance in cell lines exhibiting resistance to cisplatin (CisRPt), and improved aqueous solubility.

Analogous to treatments based on platinum(II), the primary cytotoxic target of Ru(II) complexes is DNA; however, they are also capable of binding to a diverse array of biomolecules. Their high specificity is largely attributed to their ability to mimic the transport mechanisms, cellular uptake pathways, and biodistribution patterns of the essential micronutrient iron(III) ions within the bloodstream (Zeng *et al.*, 2017). This iron(III) ions are required to meet the high metabolic demand of anoxic cancer cells. The η^6–arene Ru(II) complexes have high specificity and less toxicity due to their slow deactivation rates by non-target compounds such as proteins, enzymes, and healthy cells, which make them the main targets for research.

Osmium complexes, structurally and mechanistically analogous to ruthenium complexes, have also attracted growing interest in anticancer research. Compared to their ruthenium counterparts, osmium complexes exhibit slower ligand-exchange rates and reduced reactivity. This decreased reactivity enables osmium complexes to remain intact until reaching their cellular targets, potentially enhancing their anticancer efficacy (Ywaya *et al.*, 2024). Despite these advantageous properties, osmium(II) complexes have been comparatively underexplored as chemotherapeutic agents relative to platinum(II) and ruthenium(II) complexes (Hernández-

García *et al.*, 2023). Nonetheless, several η⁶-arene Os(II) complexes have demonstrated significant cytotoxicity, with activity levels comparable to cisplatin, including effectiveness against cisplatin-resistant (CisRPt) cancer cell lines (Ywaya *et al.*, 2024; Zhang & Huang, 2018).

Most metallodrugs' ability to treat cancer is correlated with how reactive they are to specific biological nucleophiles (receptors of proteins and other functional macromolecules). One of the key factors influencing metallodrugs' optimal biological activity and, ultimately, anticancer therapeutic efficacy is the rate of ligand exchange with the co-ligand (Morris *et al.*, 2001). The most effective strategy to control the activation site, specifically the lability of the co-ligand enabling subsequent covalent binding of η⁶ arene Ru(II) or Os(II) complexes to target bio-nucleophilic sites, is through precise structural variation within the η⁶-arene coordination sphere or the bidentate-κ^2-N, N-/O-/S- inert ligands that remain bound. The chemical nature of the ligands—specifically the donor atoms, conformational flexibility or rigidity, the π extended surface of the ancillary bidentate ligands, and their substituents such as electron donating or electron withdrawing groups—plays a critical role in modulating the behaviour of these complexes. The bidentate ligand provides diversity strategies to control the reactivity of the complex towards the formation of cytotoxic crosslinks and adducts with various biomolecules such as DNA, proteins, and enzymes. It can also harness pre-associative non-covalent interactions such as the formation of hydrogen bonding, grooves, electrostatic binding, or partial intercalation with the biohosts before the substitution process (Biancalana *et al.*, 2021). The rate at which the leaving group (X)—commonly a halide or an aqua ligand (H_2O)—is displaced serves as a kinetic indicator of the lability of η⁶-arene Ru(II) complexes. This displacement by biological molecules, particularly nuclear DNA, facilitates the formation of DNA-bound species such as cross-links or adducts, some of which are capable of initiating apoptosis in cancer cells (Mendoza-Ferri *et al.*, 2009). Substituting Os(II) with Ru(II) at the metal centre significantly influences the complex's reactivity (Zeng *et al.*, 2017). These observations suggest that modifying any component of the pharmacophore including the arene moiety, metal centre, coordinating ligand, or leaving group can impact both the biological activity and the underlying mechanism of action of these complexes (Khater *et al.*, 2023).

In this study, η⁶-arene ruthenium(II) and osmium(II) complexes exhibiting a distorted octahedral geometry often described as a half-sandwich configuration were synthesised with the general formulae: [(η^6-*p*-cymene/tolyl)(3-chloro-6-(3,5-dimethyl/1*H*-pyrazol-1-

yl)pyridazine)Ru/Os(X)]BF_4, where X = Cl, Br or I; and [Ru/Os(II)(dpzm(η^6-*p*-cymene/tolyl)Cl]BF_4, where tolyl represents toluene, dpzm denotes di(1*H*-pyrazol-1-yl)methane, and η^6-*p*-cymene refers to *para*-cymene. The molecular structures of the synthesised complexes are illustrated in Figure 1.1. To explore ligand variation within the η^6-arene-coordinated ruthenium(II) and osmium(II) series, bidentate *N,N′*-donor ligands such as dipyrazolylmethane and pyrazolyl-pyridazine were chosen due to their biocompatibility and presence in pharmacologically active organic molecules (Elguero, 1996). Notably, the pyrazolyl group is a key structural motif in several therapeutic agents, including the non-steroidal anti-inflammatory drug celecoxib (Dogné *et al.*, 2005) and the phosphodiesterase inhibitor sildenafil citrate (Padma-Nathan, 2006). Other pyrazole-based compounds have demonstrated cytotoxic and antiretroviral properties (Mizuhara *et al.*, 2013). For example, Crizotinib—a pyridine-pyrazole derivative is an effective treatment for non-small cell lung cancer, and several novel pyrazole derivatives have shown significant antitumour potential (Pal *et al.*, 2012). This study explores how systematic changes in the metal centre and the π-interactions of the N-donor bidentate ligands influence DNA-binding characteristics and cytotoxic activity.

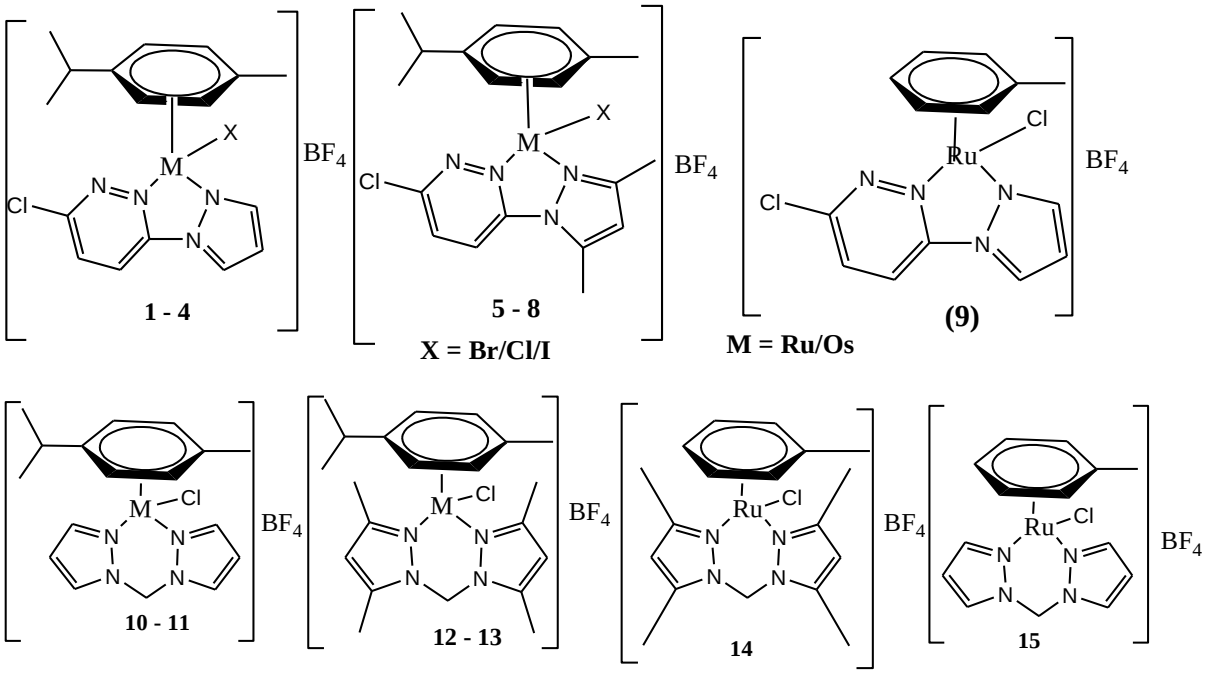

Figure 1.1: Representative molecular structures of the synthesised Ru(II) and Os(II) complexes. X represents halide ligands (Br, Cl, or I); M denotes the metal centre (Ru or Os).

1.2 Statement of the Problem

Platinum complexes have significantly shaped the landscape of chemotherapy for decades; however, the development of novel derivatives with enhanced pharmacological profiles remains a priority. This ongoing pursuit is motivated by critical limitations among the well-known Pt-based therapeutics are acquired resistance, systemic toxicity, and severe side effects including nausea, neurotoxicity, and chronic fatigue. To overcome these challenges, Ru^{II} and Os^{II} complexes have emerged as promising non-platinum alternatives in anticancer therapy. While their anticancer efficacy and DNA-binding capabilities have been widely investigated, most studies treat these aspects separately. Few have combined experimental data with theoretical analyses to comprehensively understand how these complexes interact with DNA within cancer cells and mediate their therapeutic effects at the molecular level. This gap highlights the need for a comprehensive approach that combines experimental and computational insights to better understand the anticancer potential of ruthenium and osmium complexes, especially regarding their DNA interactions within cancer cells.

1.3 General Objective

Developing and investigating organometallic Ru(II)/Os(II) species bearing η^6-arene moieties incorporating bidentate bis(pyrazolyl)/pyrazoyl–pyridazine-based ligands, with a focus on their structural features, computational modelling, DNA-binding affinity, and cytotoxic potential for prospective use as anticancer agents.

1.3.1 Specific Objectives

i. To synthesise and characterise Ru(II) and Os(II) arene complexes using UV-visible, FTIR, $^{13}C/^{1}H$ NMR spectroscopies, elemental analysis (carbon, hydrogen, and nitrogen), mass spectrometry, and X-ray crystallography.
ii. To compute the electronic properties and quantify the DNA-binding affinity of metal complexes using Density Functional Theory (DFT) and molecular docking studies.
iii. To determine the stability of Ru(II) pyrazoyl–pyridazine complexes in DMSO and PBS buffer solutions using spectroscopic and electrochemical techniques.
iv. To examine the interaction between calf thymus DNA (CT-DNA) and Ru(II) pyrazoyl–pyridazine complexes using UV–visible absorption and fluorescence titration techniques.

v. To determine *in vitro* cytotoxicity of the Ru(II) pyrazoyl-pyridazine and dipyrazoyl methane complexes against selected cancer cell lines

1.4 Hypotheses

i. There is no statistically significant difference in the spectroscopic, elemental, or structural characteristics of the synthesised Ru(II) and Os(II) arene complexes.
ii. There is no statistically significant correlation between DFT/molecular docking predictions and the experimental data of the synthesised complexes.
iii. Ru(II) pyrazoyl–pyridazine complexes exhibit no significant changes in electrochemical, spectroscopic, or conductivity properties over time in DMSO and PBS buffer solutions.
iv. There is no significant interaction between Ru(II) pyrazoyl–pyridazine complexes and CT-DNA, as indicated by no measurable changes in UV–visible and fluorescence spectra.
v. Ru(II) pyrazoyl–pyridazine and dipyrazoyl methane complexes exhibit no statistically significant cytotoxic effects on human cancer cell lines (breast, cervical, pancreatic, and rhabdomyosarcoma) *in vitro*.

1.5 Justification

Cancer constitutes a major global health challenge, with an estimated 10 million deaths recorded in 2020. In Kenya, it is the third leading cause of mortality, following infectious diseases and cardiovascular disorders. Projections indicate that by 2040, the global cancer incidence will rise to approximately 28.4 million cases—a 47% increase from 2020—driven by factors such as globalization, urbanization, and economic growth, which contribute to lifestyle-related risk factors. The five most commonly diagnosed cancers worldwide include breast, cervical, prostate, esophageal, and colorectal cancers. An estimated 42,100 individuals were diagnosed with cancer in Kenya in 2020, with about 27,100 succumbing to cancer-related complications, within a population of 53.8 million. The five-year cancer prevalence was estimated at 82,700 cases, with 54,200 in men and 28,500 in women. Current treatment modalities include surgery, chemotherapy, and radiotherapy, often used in combination to eliminate or reduce malignant cell populations. However, the high cancer mortality rates and the known limitations of existing platinum-based chemotherapeutics underscore the urgent need for

novel, more effective anticancer agents. The development of such therapies holds promise for improving treatment efficacy, increasing survival rates, and enhancing well-being for cancer patients.

Advancements in anticancer drug discovery have underscored the therapeutic potential of η^6-arene–coordinated Ru^{II} and Os^{II} chloride complexes. Among these, Ru(II)-based compounds have exhibited marked cytotoxic activity against HCT116 colorectal and MDA-MB-231 breast cancer cell models. Their effectiveness was closely linked to lipophilicity, with more lipophilic compounds showing greater activity in HCT116 cells. In contrast, osmium(II) η^6-arene complexes exhibited comparatively lower potency than their ruthenium(II) counterparts. For example, the compounds $[(\eta^6\text{-arene})Os(Azpy\text{-}NMe_2)Cl]PF_6$ displayed poor solubility in water and exhibited minimal cytotoxic effects on A549 lung cancer cells. Furthermore, the presence of an η^6-arene-Ru(II)/Os(II) unit allows further modification or functionalization of the structure that could alter its anti-tumour activity. The hydrophobic arene moiety and the structural diversity of organometallic half-sandwich compounds make them excellent candidates for chemotherapy drug development. Therefore, a series of Ru(II)/Os(II)(η^6-arene) halide complexes incorporating different ligand systems were investigated to understand how the steric and electronic characteristics of substituents on multidentate ligands influence their chemical reactivity, and to evaluate their interaction with DNA and potential anticancer properties. These efforts align with the Sustainable Development Goals to ensure healthy lives and promote well-being for all.

CHAPTER TWO

LITERATURE REVIEW

2.1 Cancer

Cancer involves the accelerated proliferation of typical cells that extend beyond their normal limits and infiltrate neighbouring tissues, a phenomenon known as metastasis. This ultimately leads to mortality (Hu *et al.*, 2023; Stewart & Wild, 2017). Most causes of cancers are mutations in specific genes or other genetic abnormalities. These genetic changes may be inherited or triggered by environmental factors such as ultraviolet radiation and exposure to chemicals like aflatoxin, asbestos, tobacco, and arsenic. Biological contributors to cancer include various infections such as HIV/AIDS (associated with Kaposi's sarcoma and lymphomas), human papillomavirus (HPV), Hepatitis B and C (linked to liver cancer), bacterial infections like *Helicobacter pylori* (associated with gastric cancer), and parasitic infections such as schistosomiasis (connected to bladder cancer). These agents can directly damage DNA and promote carcinogenesis (Kimani *et al.*, 2016; Parkin, 2011). Genetic predispositions account for approximately 5–10% of cancer cases, while the vast majority—90–95%—are attributed to environmental exposures and lifestyle choices (Anand *et al.*, 2008). Epidemiological data indicate that men are more commonly affected by lung, stomach, prostate, colorectal, liver, and esophageal cancers, whereas women show higher incidence rates of breast, stomach, lung, cervical, and colorectal cancers (Ferlay *et al.*, 2020).

Cancer treatment strategies are determined by the cancer type, extent of spread, the patient's age, overall health, and other individual characteristics (Kinunda, 2013). Common therapeutic approaches encompass surgery, radiation therapy, chemotherapy, and biological treatments such as gene therapy and immunotherapy (Lei *et al.*, 2023; Sharma *et al.*, 2024). For localised solid tumour, surgical excision of the tumour along with surrounding affected tissues is a standard method. Contemporary clinical practices often employ a multimodal approach, integrating methods like chemotherapy and surgery to enhance therapeutic outcomes. The complexity of treatment planning is heightened by the fact that each cancer type possesses distinct biological features, making a universal treatment approach unfeasible. Instead, treatment protocols are customised based on the specific biological profile of each cancer. Although radiation and chemotherapy can cause adverse effects such as hair loss, anaemia, nausea, and

vomiting, they have demonstrated higher efficacy against smaller tumour and hematologic malignancies such as leukaemia (Lu *et al.*, 2022; Reedijk, 1996).

As efforts to develop improved treatments advance, coordination complexes, used directly or as prodrugs, show promise as anticancer agents by modulating processes like cell division and gene expression (Frezza *et al.*, 2010; Huang *et al.*, 2023). Metals like gold, platinum, and ruthenium have been employed in cancer therapy for decades, with the d^8 Pt(II) ion being the most widely utilised, as illustrated in Figure 2.1 (Gichumbi & Friedrich, 2018). A notable example is cis-diamminedichloroplatinum(II), commonly referred to as cisplatin, whose anticancer potential was first recognised in 1969 through the pioneering work of Barnett Rosenberg and his research team (Rosenberg & Vancamp, 1969) and approved in 1978.

2.2 Platinum Cancer Chemotherapy

Chemotherapeutic agents function by inhibiting or halting the proliferation of cancer cells, primarily targeting those that divide rapidly. Various classes of compounds, including antibiotics, hormones, alkylating agents, and plant-derived alkaloids, serve as antitumour agents. Alkylating agents such as cisplatin exert their cytotoxic effects by inducing DNA strand breaks and cross-linking, thereby obstructing DNA replication and triggering cell death (Catalano *et al.*, 2024). Hormone-mimicking compounds like estradiol impede tumour progression by blocking the binding of endogenous ligands to their receptors, which otherwise promotes tumour development. Additionally, doxorubicin, an antitumour antibiotic, inhibits cellular proliferation by interfering with the synthesis of both DNA and RNA, ultimately causing cellular damage (Ongoma, 2012).

Cisplatin (**1**) remains among the most commonly prescribed chemotherapeutic agents in managing a wide spectrum of cancers, including genitourinary, gynaecological, thoracic, and head and neck tumour (Catalano *et al.*, 2024; Lippert, 1999; Oliver *et al.*, 2010). However, its clinical effectiveness is limited by both intrinsic and acquired resistance, and metastatic tumour often exhibit poor responsiveness to the drug (Cohen *et al.*, 2006). Experimental findings suggest that resistance mechanisms can occur at various stages: through detoxification by sulphur-containing reductants like glutathione and metallothioneins, evasion of apoptosis allowing for the removal of platinum–DNA adducts, enhanced DNA repair activity, or decreased intracellular accumulation. The latter may result from either diminished cellular uptake or increased efflux at

the plasma membrane, leading to lower intracellular drug concentrations and, ultimately, insufficient interaction with DNA, contributing to innate resistance (Ongoma, 2012).

While cisplatin remains a cornerstone in chemotherapy, continued efforts focus on designing improved derivatives that can lower its toxic side effects, bypass resistance, and target a wider range of cancers (Amptoulach & Tsavaris, 2011; Fu *et al.*, 2023).

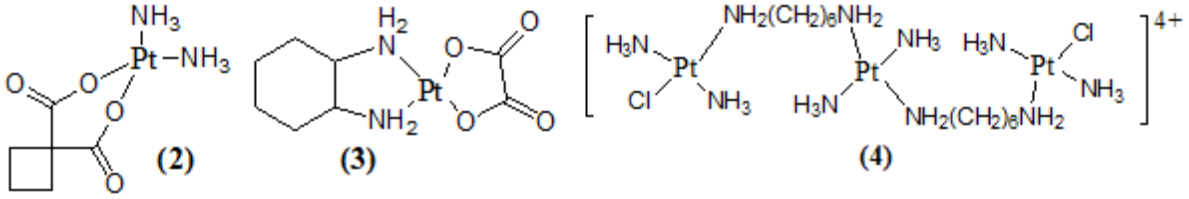

Figure 2.1: Structural representations of the selected platinum compounds

Mechanism of Action of Cisplatin

Cisplatin primarily exerts its anticancer effects through interactions with DNA, and its therapeutic efficacy is closely linked to the degree of DNA binding, or platination. As the compound has poor solubility in water and undergoes rapid hydrolysis in acidic environments such as the stomach, it is administered intravenously in saline-based solutions. The high chloride ion concentration in blood plasma (approximately 100 mM) helps stabilise cisplatin in its original dichloride form, minimising premature hydrolysis. Once in the vicinity of tumour tissue, cisplatin is believed to enter cancer cells through multiple pathways, including passive diffusion and active transport *via* copper transporters like CTR1 or organic cation transport proteins, as shown in Figure 2.2 (Gandin *et al.*, 2023; Puckett *et al.*, 2010).

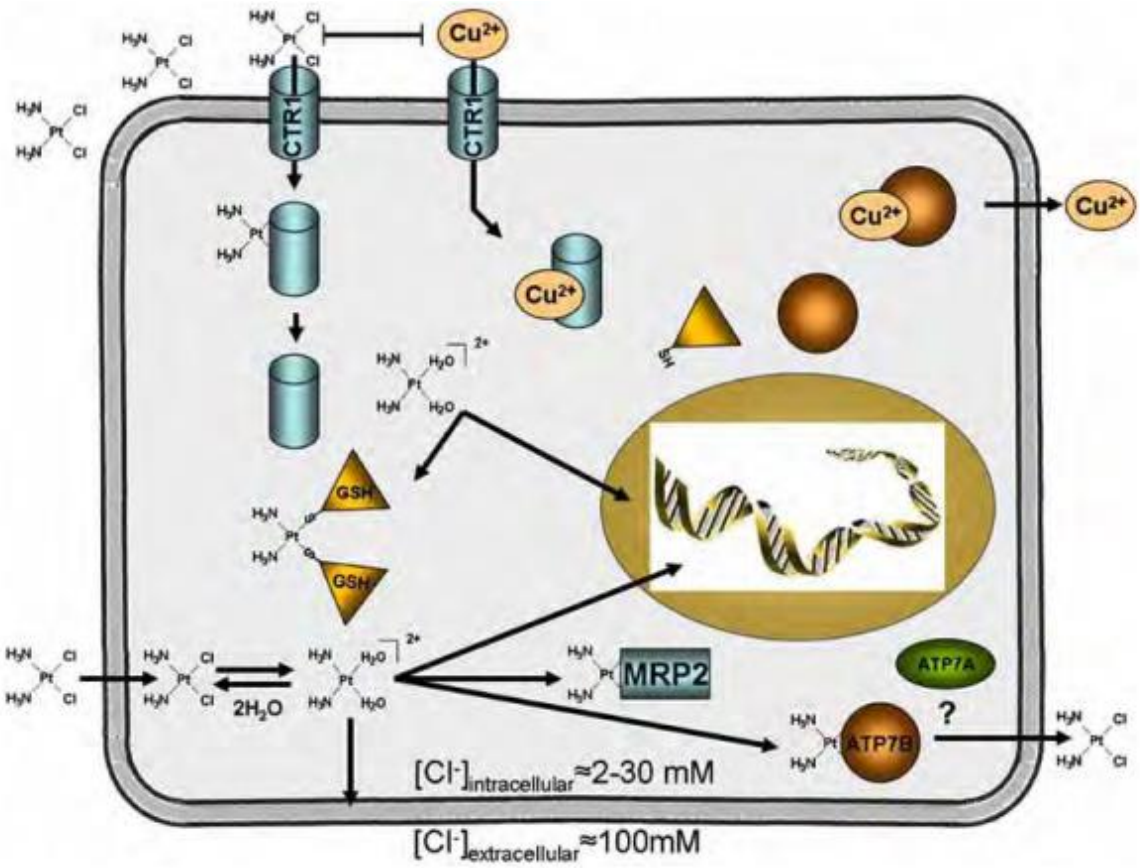

Figure 2.2: Mechanistic representation of cisplatin cellular uptake and DNA binding (Cepeda *et al.*, 2007)

Inside the cell, where chloride ion concentrations are significantly lower than in the extracellular environment, cisplatin undergoes partial hydrolysis. This process leads to the displacement of one or both chloride ligands by water molecules, generating highly reactive aquated species such as $[Pt(NH_3)_2(OH_2)Cl]^+$ and $[Pt(NH_3)_2(OH_2)_2]^{2+}$. These cationic complexes readily interact with nucleophilic sites, particularly the nitrogen atoms in nucleobases, forming stable coordinative bonds and initiating the drug's cytotoxic activity (Lippert, 1999). Hydrolytic activation of cisplatin leads to the formation of *cis*-$[Pt(NH_3)_2Cl(H_2O)]^+$ in approximately 40% of the species, with the aqua ligand contributing to increased kinetic lability owing to its superior leaving group properties compared to chloride. Consequently, these aquated species are widely recognised as the pharmacologically active forms of cisplatin (Cvitkovic, 1998). The hydrolysis of cisplatin leads to DNA platination, predominantly resulting in a 60-65% formation of 1,2-intrastrand cross-links (Figure 2.3), typically involving the N7 positions of sequential guanine

nucleotides (Kostova, 2006). This distorts the structure of the DNA duplex and alters its interactions with proteins, thereby affecting the replication and transcription of DNA and the mechanisms of DNA repair.

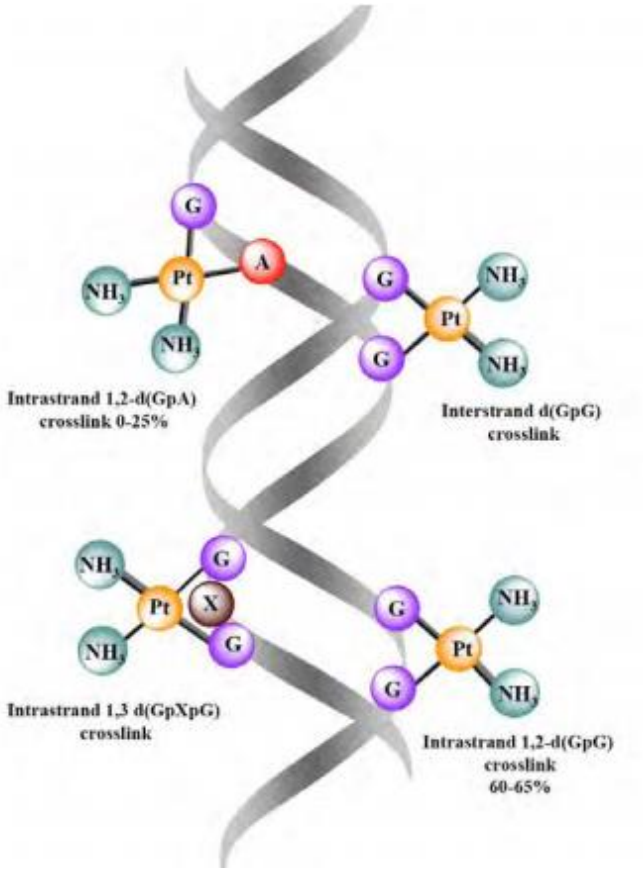

Figure 2.3: Formation of a DNA adduct with cisplatin (Boulikas *et al.*, 2007)

Cisplatin Resistance

Resistance can be classified into two types: acquired, which occurs when tumour become resistant to a drug they were previously responsive to, and intrinsic, where tumour naturally do not respond to the drug (Komeda *et al.*, 2003). According to experimental data, resistance can arise at any of the biochemical pathways listed below (Versantvoort *et al.*, 1995): (a) decreased platinum compound accumulation as a result of either increased efflux or decreased influx at the plasma membrane. Due to modifications in membrane characteristics, decreased drug intake lowers the amount that reaches the intracellular target, DNA, and may cause intrinsic resistance. (b) platinated DNA lesions can be repaired enzymatically using techniques like excision repair, and (c) S-donor reductants like glutathione and metallothioneins can detoxify platinum compounds.

Ongoing research into platinum-based chemotherapeutics has facilitated the development of numerous second- and third-generation complexes, designed through strategic modifications of the carrier ligands and leaving groups (Bloemink & Reedijk, 1996; Coffetti *et al.*, 2023). Despite the extensive evaluation of various cisplatin analogues in clinical settings, the majority failed to progress due to challenges such as poor aqueous solubility, dose-limiting toxicity, and formulation instability. In response to these limitations, new platinum compounds with improved pharmacological profiles were synthesised. A notable success from this effort is carboplatin (**2**), a clinically approved agent. The underlying rationale for its design involved modifying the leaving group to decrease cisplatin-induced systemic toxicity. The incorporation of a cyclobutane-1,1-dicarboxylate (CBDCA) ligand, which is approximately 17 times more water-soluble and hydrolyses at a slower rate (10^{-8} s^{-1}) compared to cisplatin (10^{-5} s^{-1}), significantly enhances the compound's plasma stability and circulation time (Ongoma, 2012). This reduced reactivity minimises off-target interactions with deactivating biomolecules such as plasma proteins and glutathione, thereby decreasing toxicity and permitting higher therapeutic dosing.

Oxaliplatin (oxalato-1, 2-diaminocyclohexaplatinum(II) (**3**) is the most effective treatment for colon cancer resistant to cisplatin and carboplatin. The oxalate-leaving group promotes aqueous solubility while slowing the complex's hydrolysis. The lipophilic chelate amine (dach), a non-hydrolysable and sterically demanding ligand, reduces the polarity of the complex, resulting in improved cellular uptake. Furthermore, by pointing into the major DNA groove, the dach ligand inhibits DNA repair protein binding. These adducts prevent DNA replication inhibition, which results in apoptosis and cell death (Frey *et al.*, 1993). The steric hindrance also makes the complex more resistant to deactivation by S-containing proteins. Other treatments included BBR3664 (**4**), nedaplatin, and lobaplatin (Alberto *et al.*, 2011).

The ongoing challenges linked to platinum-containing chemotherapy agents—including toxicity, the emergence of resistance, and adverse patient responses—have catalysed research into alternative metal-based therapeutics (Coffetti *et al.*, 2023). Increasing attention has turned toward transition metals such as ruthenium, osmium, and iron (Group 8), as well as other candidates like cobalt, palladium, and gold, due to their versatile coordination chemistry and promising biological profiles (Omondi *et al.*, 2020). Although several complexes derived from these metals have exhibited anticancer potential in experimental studies, none have yet matched the clinical efficacy or therapeutic reliability of cisplatin and its structural analogues, which

continue to dominate as the most successful metal-based chemotherapeutic agents to date (Ott & Gust, 2007).

2.3 Medicinal Applications of Ruthenium-Based Compounds

Ruthenium (atomic number 44, atomic mass ~101.07 $g \cdot mol^{-1}$) is increasingly recognised in medicinal inorganic chemistry due to its rich coordination chemistry and biological compatibility. It is a dense metal (12.45 $g \cdot cm^{-3}$) with impressive thermal stability, evidenced by its high melting (~2310 °C) and boiling (~3900 °C) points, which contribute to the robustness of its complexes (Bhattacharya *et al.*, 2025). In nature, it exists as a mixture of seven stable isotopes, with ^{102}Ru and ^{104}Ru being the most prevalent. Its broad redox chemistry allows for oxidation states ranging from –2 to +8, although +2, +3, and +4 dominate in biologically active complexes. Progress in the development of metal-containing therapeutics has brought attention to ruthenium-based compounds due to their diverse pharmacological profiles, such as tumour suppression, antimicrobial efficacy, anti-inflammatory action, and their role in modulating nitric oxide levels (Allardyce *et al.*, 2001; Yan *et al.*, 2005). Several of these complexes have progressed into clinical trials, underscoring their therapeutic relevance and potential as alternatives to traditional platinum-based chemotherapeutics (Kanaoujiya *et al.*, 2023).

In biomedical research, ruthenium complexes have emerged as promising candidates owing to their adaptable coordination geometries and robust chemical stability, especially within physiological environments. Their ability to adopt multiple oxidation states—especially +2, +3, and +4—allows for redox adaptability within biological systems, making them attractive scaffolds for therapeutic design (Han Ang & Dyson, 2006). One of the distinguishing features of ruthenium is its chemical similarity to iron, which allows it to interact with iron-transport proteins like transferrin and human serum albumin. This interaction may support preferential uptake by proliferating cells, particularly cancer cells that overexpress transferrin receptors to satisfy their elevated iron requirements. Such a mechanism offers a potential route for tumour-selective delivery of ruthenium-based therapeutics and may help explain their generally lower systemic toxicity compared to conventional platinum agents (Jakupec *et al.*, 2008; Lu *et al.*, 2022). Furthermore, the structural tunability of ruthenium compounds, particularly through ligand modification, allows fine control over their kinetic and thermodynamic behaviour—an essential consideration in drug development (Bruijnincx & Sadler, 2009). Some of these

compounds have shown cytotoxic effects in tumour cells that are resistant to platinum agents, highlighting their potential as alternatives or complements in resistant cancer cases (Antonarakis & Emadi, 2010). Owing to their unique chemical and biological characteristics, ruthenium complexes are increasingly being explored as potential alternatives in the advancement of metal-based pharmaceutical agents.

2.3.1 Ruthenium(III) Metallodrugs: Prospects for Cancer Therapy

Initial exploration into ruthenium-based anticancer compounds began in the 1980s with the work of Clarke and collaborators, who focused on ruthenium(III) chloroammine complexes. Among the early compounds synthesised were *fac*-[$RuCl_3(NH_3)_3$], (**5)** and *cis*-[$RuCl_2(NH_3)_4$]Cl, which were structurally inspired by cisplatin and designed to replicate or improve upon its therapeutic effects. These compounds demonstrated ruthenium complexes' anticancer activity against sarcoma lines. However, their pharmacological use was hampered by poor aqueous solubility (Clarke, 1980). Later, several Ru complexes with anticancer activity were developed, the majority of which contained Ru(III) Figure 2.4. Keppler and Rupp reported on the antitumour activity of imidazolium *trans*-bis-imidazoletetrachlororuthenate(III), KP418 (**6**), a water-soluble anionic Ru(III) complex, against murine leukaemia and melanoma cancer cells (Keppler & Rupp, 1986). Further investigation into analogues of the ruthenium-based compound KP418 led to the development of KP1019, **(8)**, which showed strong anticancer potential during preclinical evaluation. In experiments involving a rat model of colon cancer, KP1019 achieved tumour reduction of up to 95%, accompanied by low systemic toxicity, as evidenced by maintained body weight and minimal mortality throughout treatment (Kanaoujiya *et al.*, 2023). However, the compound's clinical potential was significantly limited by its poor aqueous solubility. To address this issue, researchers turned to NKP-1339, a sodium salt variant of the same core structure (sodium trans-[tetrachlorobis(indazole)ruthenate(III)]), which offered markedly improved solubility. This modification allowed for higher systemic doses to be safely administered in human trials, thereby overcoming one of the major formulation barriers observed with KP1019 (Garzon *et al.*, 1987; Kokkosi *et al.*, 2024).

A significant milestone in the advancement of ruthenium-based anticancer agents was the development of Ru(III) complexes formulated with DMSO, such as NAMI-A (compound **7**), which exhibit good aqueous solubility and can readily cross cellular membranes. Although

NAMI-A showed activity against lung metastases (Hartinger *et al.*, 2006), its limited therapeutic success, disease progression in phase I trials, and only partial responses in subsequent phases ultimately hindered its clinical progression (Zeng *et al.*, 2017). While these complexes exhibit only modest anticancer activity, their structural and mechanistic insights have been instrumental in guiding the development of more effective ruthenium-based therapeutics.

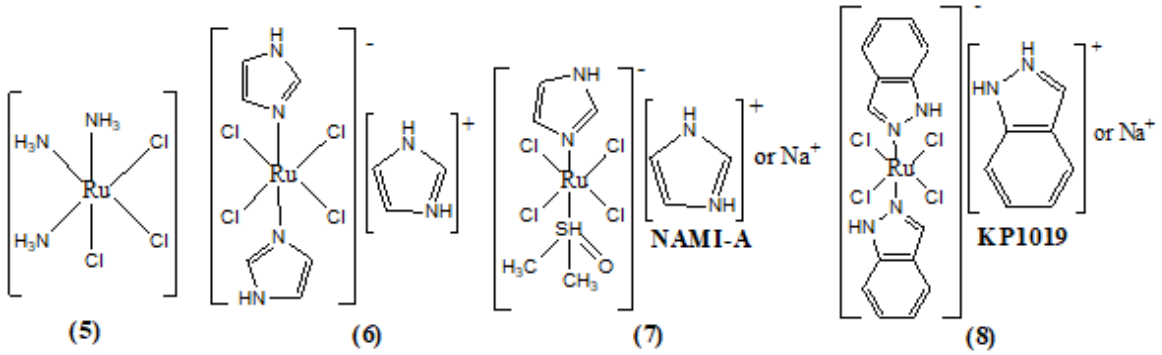

Figure 2.4: Structures of tumour-inhibiting ruthenium(III) complexes

Studies suggest that the pharmacological effectiveness of Ru(III) complexes is closely linked to their *in vivo* reduction to the more reactive Ru(II) form. This redox conversion enhances the complex's biological activity, as ruthenium(II)-chloride bonds exhibit greater substitutional flexibility compared to those in ruthenium(III), allowing more efficient interaction with cellular targets (Clarke *et al.*, 1996). The tumour microenvironment, characterised by hypoxia and acidic conditions, favours this redox transition from Ru(III) to Ru(II). Additionally, cellular reducing agents, including glutathione and various redox-active proteins both inside and outside cells, play a crucial role in facilitating this process (Sava *et al.*, 2002). The identification of Ru(II) as the biologically active form has spurred significant efforts toward the development of organometallic ruthenium(II) compounds tailored for enhanced anticancer performance (Huang *et al.*, 2023; Kokkosi *et al.*, 2024).

2.3.2 Ru(II) η^6-Arene Complexes: Structural Features and Biological Applications

Ruthenium(II) organometallic complexes are commonly investigated in the form [(η^6-arene)Ru(YZ)X], where YZ may comprise a bidentate chelating ligand or two distinct monodentate donors, and X usually corresponds to a halide ion—such as Cl^-, Br^-, or I^-—serving as a labile coordination site (Gupta *et al.*, 2009). These molecules typically adopt a characteristic

"piano-stool" geometry, with the arene ligand coordinating to ruthenium *via* π-interactions across three coordination sites, creating a stable pseudo-octahedral arrangement. The arene moiety not only stabilises the Ru(II) centre but also imparts hydrophobicity, which may improve interaction with biomolecules and promote cellular uptake of the complex (Kokkosi *et al.*, 2024). Common arene ligands employed include benzene, *p-cymene*, toluene, biphenyl, and dihydroanthracene. The YZ ligands often consist of nitrogen, phosphorus, or oxygen donor atoms arranged in various binding motifs such as N,N-, P,*P*-, O,O-, or N,O-chelates; examples include ethylenediamine (*en*), 2,2'-bipyridine (*bpy*), picolinate, acetylacetonate, and malonate (Li *et al.*, 2018; Muley *et al.*, 2021). The halide ligand X serves as a reactive site that can undergo substitution; in aqueous media, the Ru–X bond typically undergoes hydrolysis forming an aqua species (Ru–OH_2), which depending on the pKa, can further lose a proton to yield a hydroxo complex (Dougan & Sadler, 2007). These aqua or hydroxo adducts show a strong affinity for guanine bases in DNA, coordinating specifically at the N7 position, which is believed to be crucial for their biological activity (see Figure 2.5).

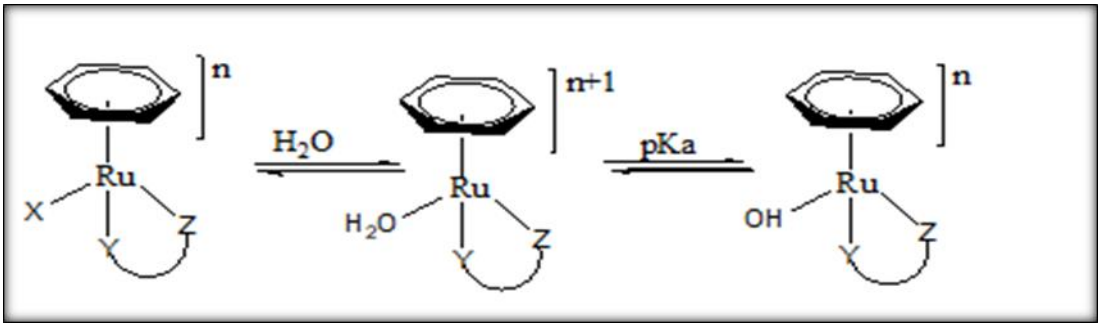

Figure 2.5: Hydrolysis of Ru(II) η^6-arene complexes in aqueous solution

Due to their convenient synthetic route under mild conditions, high product yields, and notable stability in aqueous environments, half-sandwich ruthenium complexes (illustrated in Figure 2.6) have become prominent in the field of organometallic chemistry. Their structural versatility offers ample opportunity for fine-tuning both therapeutic efficacy and toxicity profiles by modifying the arene ligand and other coordinated groups (Yan *et al.*, 2005). The coordinated arene ligand contributes significantly to the stabilization of ruthenium in its +2 oxidation state, effectively hindering its oxidation to the +3 state (Habtemariam *et al.*, 2006). Ruthenium(II) arene complexes have demonstrated potent cytotoxic effects, even against cancer cells that exhibit resistance to cisplatin treatment (Barry & Sadler, 2013; Hartinger & Dyson, 2009).

Among the most studied ruthenium(II)-arene compounds are RAPTA-C ([Ru(η⁶-*p*-cymene)(PTA)Cl_2], **10**), RAPTA-T (**9**), both of which feature the water-soluble phosphine ligand PTA (1,3,5-triaza-7-phosphatricyclo[3.3.1.1]decane), RM175 (**11**) and DW1/2 (**12**). These complexes have garnered considerable attention owing to their distinctive chemical structures and promising anticancer potential (Kokkosi *et al.*, 2024**).** While RAPTA complexes have shown the ability to suppress metastasis in animal models despite lacking *in vitro* cytotoxicity (Lee *et al.*, 2017), RM175 exhibited comparable anticancer activity to cisplatin *in vitro* and demonstrated enhanced efficacy in cisplatin-resistant *in vivo* models.

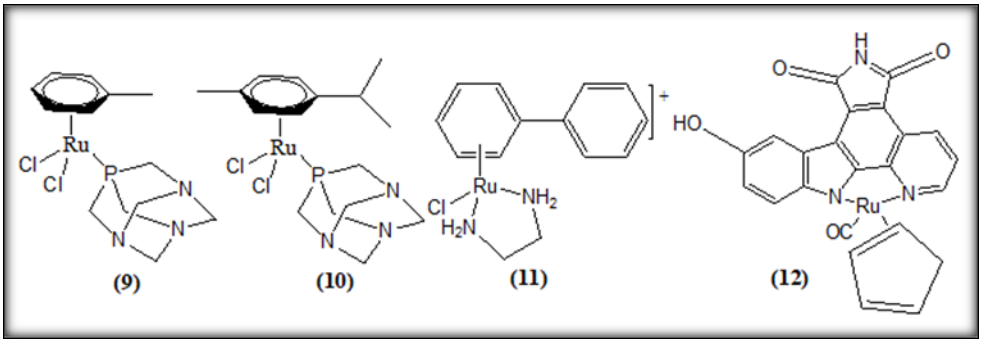

Figure 2.6: Key η^6-arene ruthenium(II) complexes investigated in preclinical cancer studies

Modifying either the arene fragment or the chelating ligands provides a versatile approach to tailoring the cytotoxic efficacy of these ruthenium complexes (Cseh *et al.*, 2022; Khan *et al.*, 2020; Schäfer *et al.*, 2007). In contrast, modifications to the leaving group do not influence cytotoxicity, as the complexes undergo activation through aquation (Mendoza-Ferri *et al.*, 2009). Furthermore, linking multiple metal centres can also affect cytotoxic activity (Hartinger *et al.*, 2011). As a result, some patterns can be identified, and these structure-activity relationships (SARs) have predictive value for future drug development. The justification of these connections by linking biological activity to chemical reactivity is a crucial step. Accordingly, significant attention has been devoted to understanding how ruthenium–arene compounds interact with various biological molecules, both during systemic transport and upon reaching their intended therapeutic targets.

The nature of the halide bound to half-sandwich ruthenium complexes plays a critical role in shaping both their chemical behaviour and anticancer activity, as each halogen—chloride, bromide, or iodide—contributes distinct properties to the complex. A study by (Fu *et al.*, 2017) explored how varying halide ligands influence the reactivity and biological behaviour of

ruthenium and osmium half-sandwich complexes. In one such study, researchers synthesised a range of [M(*p*-cymene)(azo- or imino-pyridine)X]$^{+}$ compounds (M = Ru^{2+} or Os^{2+}; X = Cl^{-} or I^{-}) to assess the effect of halide substitution on both chemical stability and cytotoxic performance. The iodide-containing complexes exhibited enhanced antiproliferative activity and displayed greater selectivity for cancerous cells, likely due to improved membrane permeability (Romero-Canelon *et al.*, 2013). Similarly, (Gichumbi *et al.*, 2017b) prepared a family of [(η^6-arene)Ru(C_5H_4N-2-CH=N-Ar)X]$^{+}$ complexes using either *p*-cymene or phenoxyethylbenzene as the η^6-arene moiety, with halide ligands (I^{-}, Br^{-}, or Cl^{-}) serving as the labile groups. These variations in halide identity were found to significantly modulate the biological responses and DNA interaction profiles of the compounds. The results indicated that complexes bearing bromide or iodide ligands demonstrated moderate cytotoxicity against HepG2 and Caco-2 cancer cell lines, while those with chloride ligands exhibited minimal or no activity. These observations can be attributed to the differing electronic properties of halides, which influence ligand lability through σ-donation and π-backbonding interactions. Such effects modulate the electrophilicity of the ruthenium centre and thereby alter its substitution kinetics.

O'Riley and co-workers (2017) further examined the kinetic and biological implications of halide substitution in [RuX_2([9]aneS_3)(S-dmso)] complexes, where X was either Cl^{-} or Br^{-}. Contrary to expectations, the dichloride complex hydrolysed more rapidly ($(4.5 \pm 0.2) \times 10^{-4}$ s^{-1}) than the dibromide analogue ($(2.6 \pm 0.2) \times 10^{-4}$ s^{-1}), despite the general assumption that bromide, being less basic, should dissociate more readily (O'Riley *et al.*, 2017). This reactivity trend was mirrored in cytotoxicity data, where the chloride complex exhibited greater potency against triple-negative human breast carcinoma (MDA-MB-231) cells (IC_{50} = 5.3 μM) than the bromide complex (IC_{50} = 6.0 μM), supporting the hypothesis that higher ligand lability correlates with enhanced anticancer activity (Casini *et al.*, 2010). Also, studies on dinuclear Ru(II) arene complexes incorporating different halides (Cl^{-}, Br^{-}, I^{-}) and observed only minor differences in cytotoxicity against human colorectal (SW480) and ovarian (A2780) carcinoma models. This suggests that rapid aquation could result in the generation of similar reactive intermediates, thereby reducing the extent to which the original halide ligand affects the compound's biological function (Peacock *et al.*, 2006).

The nature of the arene ligand significantly contributes to the pharmacological behaviour and therapeutic potential of Ru(II)-based complexes. Investigations into compounds of the type

[Ru(η⁶-arene)(en)Cl]⁺, incorporating either biphenyl or *p*-cymene, revealed comparable antiproliferative activity against SW480 colorectal and A2780 ovarian cancer cell lines. These findings imply that variations in arene lipophilicity alone cannot account for the observed biological effects (Peacock *et al.*, 2006). Further exploration into structure–activity relationships by Habtemariam *et al.* (2006) focused on a series of mononuclear Ru(II) complexes formulated as [(η⁶-arene)Ru(chelate)Cl]⁺. These compounds featured diverse arene units ranging from simple benzene moieties to more extended aromatic systems. The ancillary ligands employed included a variety of donor types such as diamines (N,N′-donors), β-diketonates (O,O-donors), and ligands derived from amino acids (N,O-donors), allowing for the systematic evaluation of electronic and steric influences on biological activity. The study found that complexes combining ethylenediamine with bulky polycyclic arenes demonstrated the strongest anticancer effects against A2780 ovarian carcinoma cells. In contrast, introducing polar functional groups on the arene ring or employing chelates based on bipyridine derivatives tended to diminish cytotoxicity, suggesting that the biological activity of metal complexes is strongly modulated by the electronic characteristics and spatial configuration of their ligands (Habtemariam *et al.*, 2006). Ru(II)–arene compounds with the general formula [(η⁶-arene)Ru(X)(Y)(Z)] have been the focus of continued research to investigate how different ligand environments affect their activity, incorporating benzene-based ligands and a diverse set of ancillary groups, including halides, nitriles, isonicotinamide, and diamines like ethylenediamine and its N-ethyl derivative. Among the complexes evaluated, several—including [(η⁶-*p*-cymene)RuCl(en)]PF_6, [(η⁶-*p*-cymene)RuI(en)]PF_6, [(η⁶-biphenyl)RuCl(en)]PF_6, and [(η⁶-biphenyl)RuCl(en-Et)]PF_6—exhibited cytotoxic activity on par with carboplatin, each showing IC_{50} values around 6 μM. The results underscore the value of strategically modifying both the arene moiety and coordinating ligands to enhance the anticancer effectiveness of these metal-based compounds (Morris *et al.*, 2001).

In efforts to understand how metal centre substitution affects biological performance, (Dyson, 2007) investigated osmium analogues of the RAPTA-C framework and observed that exchanging ruthenium for osmium resulted in only slight variations in cytotoxic potency in cell-based assays. Separately, (Peacock *et al.*, 2006) synthesised a range of Ru(II) arene-based complexes incorporating either ethylenediamine or acetylacetonate as co-ligands, combined with different arene groups such as biphenyl, benzene, or *p*-cymene. These compounds demonstrated

notable cytotoxic responses when evaluated against human ovarian (A2780) and lung (A549) cancer cell lines. However, analogous Os(II) complexes generally lacked comparable activity. (Schmid *et al.*, 2007) conducted a similar comparative analysis of Ru and Os ethylenediamine derivatives, confirming that ruthenium species tended to be more potent overall, though certain osmium variants matched or surpassed their Ru counterparts in select cases. This variability may stem from the enhanced lipophilic nature and greater kinetic stability of Os(II), attributes typical of heavier transition metals. More recent investigations by (Hildebrandt *et al.*, 2022) into arene–metal complexes incorporating O,S-chelating ligands demonstrated that several Os(II) complexes exhibited pronounced cytotoxicity, outperforming both their ruthenium analogues and cisplatin across multiple cancer cell lines. Complementary work by (Ywaya *et al.*, 2024) investigated Ru and Os half-sandwich complexes coordinated with imidazole-2-thione ligands featuring either pyridine-2,6-diyl or alkyl chains linkers as bridging groups. The synthesised compounds were evaluated for their effects on HeLa cervical carcinoma cells and HEK293 normal kidney cells. Notably, some osmium-centred complexes exhibited enhanced cytotoxic potency and selectivity, demonstrating approximately twice the tumour-targeting efficacy compared to 5-fluorouracil. These observations emphasise the fundamental influence of the central metal ion in modulating biological performance and further support the growing potential of osmium in therapeutic inorganic drug development.

Polynuclear ruthenium compounds have emerged as a promising class of metal-based therapeutics, especially in the fight against drug-resistant cancers (Hartinger *et al.*, 2011). These systems incorporate multiple ruthenium centres—commonly arranged in di-, tri-, tetra-, or hexanuclear frameworks—linked *via* various bridging ligands. In a study by (Mendoza-Ferri *et al.*, 2009), a series of Ru(II)(η^6-arene)X complexes (X = Cl^-, Br^-, or I^-) were synthesised, incorporating pyridinone-derived linkers to form multinuclear architectures. Their structure–activity relationship (SAR) analysis revealed that biological performance was primarily influenced by the electronic and steric nature of the arene ligand, the spatial separation between ruthenium centres, and the coordination environment surrounding each metal site. Interestingly, the type of halide ligand played a minimal role in modulating cytotoxicity, likely due to rapid aquation processes in physiological media that yield similar reactive intermediates. Substitution of the *p*-cymene moiety with a biphenyl ligand did not significantly alter anticancer potency. Among the series, dinuclear complexes demonstrated the most pronounced cytotoxic effects,

outperforming both mononuclear and trinuclear variants. This was reflected in IC_{50} values against SW480 and A2780 cell lines, where the dinuclear species demonstrated the highest potency (26 ± 8 μM and 30 ± 6 μM, respectively), while mono- and trinuclear complexes were significantly less active (42 ± 1 and 88 ± 12 μM for mononuclear; 59 ± 18 and 80 ± 7 μM for trinuclear). These observations were attributed to enhanced lipophilicity and cellular uptake associated with increased spacer length (Romerosa *et al.*, 2006).

2.3.4 Cellular Uptake Pathways and Molecular Targets of Ruthenium(II)-Based Complexes

The cellular uptake of ruthenium (Ru) complexes plays a pivotal role in their effectiveness as targeted cancer therapeutics. For these compounds to exert their biological activity, they must first traverse the cell membrane—a dynamic structure composed primarily of lipids and proteins that regulates the entry and exit of molecules. Ru(II) complexes can enter cells through various pathways, including passive diffusion, active transport, and endocytosis (Zeng *et al.*, 2017). Once inside, many Ru-based anticancer agents primarily target DNA (Hosoya & Miyagawa, 2014), which contributes to their selectivity and therapeutic potential. Ruthenium(II) complexes, such as RAPTA-C and RM175, are known to engage with cellular components through diverse mechanisms that contribute to their anticancer activity. These compounds can associate with DNA through both covalent and non-covalent modes. In covalent interactions, they typically form persistent adducts with the DNA backbone, which disrupt essential processes like DNA replication and transcription, leading to cellular damage and apoptosis. In contrast, non-covalent interactions occur through mechanisms such as groove binding, intercalation, or electrostatic interactions, where the Ru(II) complexes modify the DNA structure without permanently attaching to it (Chen *et al.*, 2003). In addition to their interaction with DNA, several Ru(II) complexes, including DW1/2, demonstrate a strong preference for binding to specific proteins, particularly protein kinases. This preference is attributed to the unique structural and physicochemical properties of the complexes. By mimicking the natural kinase inhibitor staurosporine, these ruthenium-based compounds effectively inhibit kinase activity, interfering with vital cellular signalling pathways and potentially reducing cancer cell viability (Meggers *et al.*, 2009).

Investigating how ruthenium(II) arene compounds associate with DNA has become a central focus in elucidating their viability as drug candidates. DNA binding plays a crucial role in drug action, aiding in the design of targeted therapies with fewer side effects (Sirajuddin *et al.*,

2013). Various analytical methods, including electronic absorption, emission-based assays, and redox profiling, are frequently employed to examine how these metal complexes engage with DNA. Ruthenium(II) arene compounds are particularly notable for their capacity to influence both the rate and energetics of key biomolecular processes, positioning them as strong contenders for therapeutic advancement.

2.3.5 Proposed Mechanistic Pathways of Ruthenium-Based Therapeutics

Anticancer drugs containing ruthenium are commonly introduced in the form of Ru(III) complexes, which remain relatively stable in systemic circulation until they are activated within the tumour environment. These compounds exhibit iron-mimicking properties that enable them to associate with key plasma transport proteins, including transferrin and albumin (Čanović *et al.*, 2017), both of which play crucial roles in iron metabolism and systemic distribution. Cancer cells often overexpress transferrin receptors compared to normal cells, enabling them to preferentially capture metal-loaded transferrin from circulation (Figure 2.7, inset). This selective uptake enhances drug specificity, allowing the ruthenium complex to preferentially accumulate in cancerous tissue, thereby minimising toxicity to healthy cells (Omondi *et al.*, 2018). In the tumour microenvironment, which typically exhibits acidic conditions, hypoxia, and increased levels of cellular reductants such as glutathione (GSH), ruthenium in the +3 oxidation state is transformed into its more reactive +2 form with faster ligand exchange kinetics (Omondi *et al.*, 2018) (see Figure 2.7). This redox transformation activates the drug, enabling the Ru(II) species to form bifunctional intrastrand adducts with double-stranded DNA, ultimately disrupting RNA synthesis and inhibiting cancer cell proliferation (Kopel *et al.*, 2015).

Once the complex leaves the hypoxic tumour environment, biological oxidants convert Ru(II) back to Ru(III), returning it to its inactive form (Ojwach *et al.*, 2007). Nuclear magnetic resonance (NMR) investigations on the Ru(III) compound KP1019 have revealed that glutathione facilitates its reduction to the Ru(II) state, lending support to the hypothesised mechanism of biological activation (Ojwach *et al.*, 2007). Notably, the Ru(III) drug NAMI-A displays distinct behaviour. Following rapid dissociation of its initial ligands, the complex interacts with biomolecules through coordination to donor groups such as the thiol and carboxyl moieties of glutathione or the nitrogen atoms of histidine's imidazole ring (Fuentes *et al.*, 2020)

(Figure 2.7). This unique mechanism underlies NAMI-A's potent antimetastatic activity and its characteristically low cytotoxicity.

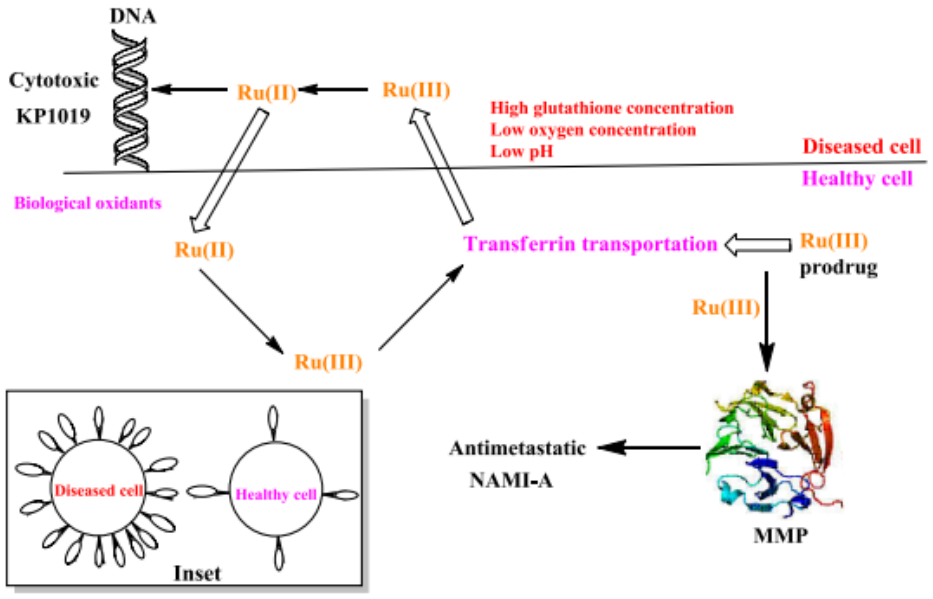

Figure 2.7: Mechanism of ruthenium complexes' action with inset illustrating transferrin receptor distribution on normal and cancer cells (MMP = matrix metalloproteinases)

2.4 Osmium Complexes

Owing to their placement in the same group of the periodic table, ruthenium and osmium display comparable chemical behaviours and coordination preferences. This chemical resemblance has spurred increasing interest in the development of osmium-containing compounds, especially in the wake of promising results obtained from ruthenium-based anticancer agents. Several osmium analogues of well-established ruthenium complexes—such as RAPTA-C, NAMI, RM175, and KP1019—have been synthesised and subjected to biological evaluation (Büchel *et al.*, 2011; Cebrián-Losantos *et al.*, 2007). Osmium complexes are often favoured for their enhanced kinetic inertness and greater resistance to hydrolysis in physiological environments, traits that support their potential as viable alternatives in therapeutic applications (Liu *et al.*, 2012). They also exhibit distinct features, such as a tendency to adopt higher oxidation states and enhanced π-backdonation capabilities in lower oxidation states (Hanif *et al.*, 2014). Notably, replacing ruthenium with osmium has led to varying effects on cytotoxicity: in some cases, such as with NAMI-A analogues, cytotoxicity increased significantly, while in

others, the ruthenium variants remained more active or the metal substitution had little impact on biological properties (Peacock *et al.*, 2007).

Numerous investigations have explored the comparative anticancer potential of Ru(II) η^6-arene complexes versus their osmium analogues. In particular, ruthenium-based complexes incorporating 3-hydroxy-2-pyridone ligands demonstrated measurable cytotoxicity. However, their osmium analogues showed enhanced anticancer activity, which may be attributed to the greater kinetic inertness and improved stability of osmium in biological settings (Ting-WaiáCheung & Wai-YináSun, 2011). Conversely, Os(II)-arene complexes bearing phosphorus-based ligands showed reduced cytotoxicity compared to their ruthenium counterparts, a difference attributed to the osmium species' diminished DNA-binding affinity—a critical interaction for anticancer action (Lee *et al.*, 2014). The concept of multinuclear metal-based drugs gained traction following the introduction of BBR3464, a trinuclear platinum agent capable of bridging DNA duplexes and DNA-protein assemblies (Nováková *et al.*, 2009).

In conclusion, structural modifications—such as variations in the arene ligand, halide leaving group, central metal atom, and chelating ligands—can profoundly influence the cytotoxic properties of η^6-arene ruthenium(II) and osmium(II) complexes. Ruthenium(II) compounds, in particular, have demonstrated notable anticancer activity, including efficacy against cisplatin-resistant cell lines, while osmium(II) analogues also exhibit promising therapeutic potential. This study examines how variations in arene type and halide ligands influence their biological performance, aiming to improve target selectivity and therapeutic potential.

2.5 Interaction between DNA and Drug/Metal Complexes

Contemporary cancer therapies often involve agents that interfere directly with DNA, aiming to disrupt critical cellular processes such as transcription and replication—key functions required for cell division and survival. By targeting the genetic blueprint, these therapeutic agents halt the proliferation of rapidly dividing cancerous cells. Small molecules that can associate with DNA structurally or functionally are thus valuable tools in oncology (Kennard, 1993).

2.5.1 Mechanisms of Drug–DNA Binding

Anticancer agents can interact with DNA through two primary mechanisms: permanent covalent bonding or reversible non-covalent associations. These distinct modes of interaction play a crucial role in determining the drug's biological activity and therapeutic effectiveness.

Covalent Binding

Many widely used chemotherapeutic agents rely on covalent bonding with DNA to exert their effects. These interactions typically involve the irreversible modification of DNA through the formation of chemical bonds—such as alkylation or strand cross-linking (Silvestri & Brodbelt, 2013). This irreversible binding leads to major distortions in DNA structure, impeding normal cellular functions and often initiating programmed cell death. Such binding is especially effective due to its strength and long-lasting nature.(Liu & Sadler, 2011).

Cisplatin serves as a hallmark example, forming both intra- and inter-strand DNA crosslinks by replacing chloride ions with DNA nucleobases. Some advanced systems, such as metal-linked intercalators, employ a dual strategy: they insert aromatic moieties between DNA base pairs while their metal centres simultaneously coordinate with nucleophilic DNA sites (Hadjiliadis & Sletten, 2009). These dual-action agents combine non-covalent stacking with covalent modification, enhancing their therapeutic efficacy.

Alkylating agents, in particular, function by transferring alkyl groups (CnH2n+1) to nucleophilic sites on DNA. This modification can result in three main outcomes: (1) Base alkylation, which induces structural changes and often misleads DNA repair enzymes, causing fragmentation; (2) Formation of covalent crosslinks between or within DNA strands, preventing strand separation required for replication and transcription; and (3) Mispairing of bases or base excision due to chemical modification, which disrupts replication fidelity and can activate apoptotic pathways (Sirajuddin *et al.*, 2013). Many such alkylators demonstrate significant antitumour activity under physiological conditions.

Non-Covalent Binding Modes

Drugs may also bind DNA reversibly, employing mechanisms such as intercalation, groove binding, or surface association. These modes of interaction affect DNA integrity by altering its structure, affecting supercoiling, or hindering regulatory enzymes and mitochondrial

DNA function (Ni *et al.*, 2006). Though these effects are reversible, they can substantially impair gene regulation, and are often favored in drug design for their lower toxicity and reversible nature.

(Lerman, 1961) introduced the idea of intercalation, where planar aromatic ligands insert themselves between DNA base pairs, disrupting the helical structure. These molecules, such as acridine derivatives, stabilize the DNA–drug complex through π–π interactions, hydrophobic effects, and charge transfer mechanisms without disrupting hydrogen bonding (Martinez & Chacon-Garcia, 2005). This mode of binding can cause localized unwinding of the DNA helix—up to 26% in the case of ethidium bromide—interfering with replication and transcription (Keck & Lippard, 1992). Although generally non-specific, intercalators can sometimes show a preference for GC-rich sequences and are commonly composed of extended polyaromatic systems such as PHEHAT or DPPZ (Haq *et al.*, 1995; Moucheron & Kirsch-De Mesmaeker, 1998).

Another key mode of DNA interaction is groove binding, particularly within the minor groove. Compounds that bind here typically have crescent-shaped, aromatic-rich frameworks that can adapt to the DNA groove geometry. These compounds, which frequently incorporate pyrrole or imidazole moieties, interact with DNA through stabilizing hydrogen bonds and van der Waals interactions. Artificial groove-binding agents—such as polyamide derivatives and lexitropsins—can be tailored to recognize and attach to particular DNA sequences, thereby improving their binding specificity (Sirajuddin *et al.*, 2013).

Finally, electrostatic or external binding refers to the interaction driven by the attraction between cationic ligands and the anionic phosphate groups along the DNA backbone. In some instances, these ligands may stack on the DNA surface or assemble into larger aggregates that engage with the helix in a non-specific fashion. A well-known example is the increased fluorescence of $[Ru(bpy)_3]^{2+}$ upon binding to DNA, with this enhancement being sensitive to ionic strength—highlighting a charge-dependent binding mechanism (Kelly *et al.*, 1985). Due to their dicationic nature, Ruthenium(II) complexes frequently utilize this mode of association.

2.5.2 Techniques for Investigating Drug–DNA Interactions

Understanding how metal-based drugs interact with DNA is vital for designing effective anticancer agents (Mondal & Paira, 2020). Numerous analytical techniques have been developed

to investigate these interactions, including spectroscopic, electrochemical, and fluorescence-based methods. These tools help elucidate binding mechanisms and assess structural or conformational changes in DNA upon drug association.

UV–Visible Absorption Spectroscopy

Ultraviolet–visible (UV–Vis) absorption spectroscopy serves as a common analytical technique for studying the interactions between small molecules and DNA. It tracks changes in the absorbance of either the DNA or ligand, reflecting conformational alterations or complex formation (Khan *et al.*, 2020). Ligands usually show characteristic absorbance bands in the visible range, and shifts in these bands upon interaction with DNA often signify binding events (Jaumot & Gargallo, 2012). DNA itself exhibits strong absorbance in the UV region (200–350 nm), particularly around 260 nm, due to π–π* electronic transitions in its purine (adenine, guanine) and pyrimidine (cytosine, thymine) bases (González-Ruiz *et al.*, 2011). Spectral shifts or intensity changes in this band may arise from variations in pH or ionic strength and are used to monitor structural changes in DNA.

Intercalative binding is typically indicated by a decrease in absorbance (hypochromism) along with a red shift in the absorption maximum (bathochromic shift). These spectral modifications arise from pronounced π–π stacking interactions between the aromatic regions of the ligand and the DNA base pairs. This interaction brings the chromophores into closer spatial alignment, thereby enhancing electronic delocalization and coupling (Liu *et al.*, 2002).

In contrast, hyperchromism (increased absorbance) is typically associated with electrostatic interactions or partial denaturation of the DNA double helix. This effect exposes more nucleobase regions, enhancing absorption—often by ~40% in single-stranded DNA compared to double-stranded (Khan *et al.*, 2020). Disruption of hydrogen bonding and base stacking by metal ions or denaturing agents promotes a more relaxed or random coil DNA structure. Cationic ligands may further enhance hyperchromism by interacting with the phosphate backbone, inducing conformational strain and exposing more bases (Arjmand & Jamsheera, 2011). Weak or non-specific interactions tend to yield minimal absorbance changes, typically without significant shifts in wavelength (González-Ruiz *et al.*, 2011).

Fluorescence-Based Analysis of Small Molecule–DNA Interactions

Fluorescence spectroscopy is a highly sensitive and selective technique for investigating small molecule–DNA interactions. It is especially useful when studying compounds with

aromatic or conjugated systems, which often exhibit efficient fluorescence due to low-energy π–π* transitions (Jaumot & Gargallo, 2012). Fluorescence methods, including fluorescence anisotropy and Förster resonance energy transfer (FRET)**,** are valuable tools for probing the spatial orientation and binding environment of ligands within the DNA helix. Fluorescence quenching experiments provide insights into the location and accessibility of binding sites (González-Ruiz *et al.*, 2011).

The fluorescence behaviour of a compound can change significantly upon DNA binding. In intercalative binding**,** fluorescence is usually enhanced due to the restricted rotation and reduced non-radiative decay pathways caused by insertion between DNA base pairs. Conversely, groove-binding ligands—which interact *via* hydrogen bonding or electrostatic forces—often exhibit quenching upon binding, likely due to increased solvent exposure or altered local environments (Li *et al.*, 1997). Halide-induced fluorescence quenching can distinguish between intercalation and groove binding. Groove-binding ligands are more easily quenched, as their binding sites are more accessible to quenchers. In contrast, intercalated ligands are shielded by the DNA helix, limiting quencher access. Electrostatic repulsion between negatively charged DNA and anionic quenchers further reduces quenching efficiency in these tightly bound complexes.

Cyclic Voltammetry (CV)

Cyclic voltammetry is a valuable electrochemical method for probing the binding interactions between metal-based drugs and DNA. Binding events typically cause measurable changes in peak current and potential, which offer insights into binding strength and mode (Feng *et al.*, 1997). A shift in the half-wave potential ($E_{1/2}$) toward negative values often indicates electrostatic interaction, whereas positive shifts are characteristic of intercalative binding (Carter & Bard, 1987).

To determine the binding constant (K), changes in the electrochemical current are recorded as the concentration of DNA is gradually increased. This method relies on monitoring how the interaction between the metal complex and DNA affects the electrochemical signal. The relationship between current variation and DNA concentration is described using the following commonly applied equation (Equation 2.1) (Sirajuddin *et al.*, 2013).

$$\text{Log}(I/[DNA]) = \log K + \log(I/(I_0 - I)) \quad (2.1).$$

Where I_o is the peak current in the absence of DNA, and I is the current in its presence. Plotting log(1/[DNA]) versus log($I/(I_o - I)$) gives a straight line from which K (intercept) can be calculated. An alternative method involves Equation 2.2:

$$1/[DNA] = (K(1 - A)/(1- I/I_0)) - K \quad (2.2).$$

Where A is a proportionality constant. By plotting 1/[DNA] against $1/(1 - I/I_o)$ yields a straight line from which K can be derived. For modelling drug-DNA binding behaviour, a site-binding model is applied, as expressed in Equation 2.3:

$$C_b/C_f = K([\text{free base pairs}]/s) \quad (2.3).$$

Where s refers to the number of base pairs per binding site, C_b and C_f are the concentration of bound and free drug, respectively. When DNA is quantified in nucleotide phosphate concentration, base pairs are represented as [DNA]/2, leading to a modified Equation 2.4:

$$C_b/C_f = K([\text{free base pairs}]/2s) \quad (2.4),$$

In experimental terms, the ratio C_b/C_f can be calculated as $C_b/C_f = (I_o - I)/I$, allowing for graphical determination of binding parameters through plots of $(I_o - I)/I$ versus total DNA concentration at a constant drug level.

CHAPTER THREE

MATERIALS AND METHODS

This chapter outlines the materials employed, synthesis strategies followed, and characterisation techniques applied in the development of arene-based ruthenium(II) and osmium(II) complexes. It further details the use of computational approaches—such as density functional theory (DFT) and molecular docking—to explore the electronic configuration and interaction profiles of the synthesized compounds. Moreover, the chapter covers assessments of structural integrity, DNA-binding affinity, and *in vitro* cytotoxic effects of the Ru(II) complexes, each of which is labelled with an identifying number for reference.

3.1 Materials

The bidentate ligands—bis(pyrazol-1-yl)methane (dpzm), bis(3,5-dimethylpyrazol-1-yl)methane (bdmpzm), 3-chloro-6-(1H-pyrazol-1-yl)pyridazine, and 5-chloro-2-(3,5-dimethyl-1H-pyrazol-1-yl)pyridine—were synthesised as per (Thompson *et al.*, 1985) Dinuclear η^6-arene ruthenium and osmium precursors with the general formula $[(\eta^6\text{-arene})M(\mu\text{-}X)X]_2$ (M = Ru or Os; arene = cymene or toluene; X = Cl^-, Br^-, or I^-), ammonium tetrafluoroborate, and solvents (acetonitrile, methanol, ethanol, diethyl ether, and tissue-culture grade DMSO) were purchased from Sigma-Aldrich and Merck, and used without further purification.

Other reagents included phosphate-buffered saline (PBS) tablets, glutathione (GSH), calf thymus DNA, Hoechst 33258, MTT, [3-(4,5-dimethylthiazol-2-yl)-2,5-diphenyltetrazolium bromide], and tetrabutylammonium tetrafluoroborate ($TBABF_4$), all obtained from commercial suppliers. Cell culture experiments utilized RPMI 1640 or Dulbecco's Modified Eagle Medium (DMEM), depending on the cell line. Cell lines included breast cancer (MCF-7, T-47D, MDA-MB-231), cervical carcinoma (Caski, HeLa), pancreatic cancer (CFPAC-1, PANC-1), and rhabdomyosarcoma (RH-30, RD), with media and reagents from Sigma-Aldrich (USA).

DNA-binding studies used Hoechst 33258 as a competitive groove-binding probe. Ru(II) complex stability was assessed in the presence of GSH. Additional assessments were performed in DMSO and PBS, including electrochemical behaviour analysis. *In vitro* cytotoxicity of selected Ru(II) complexes containing dpzm and 3-chloro-6-(1H-pyrazol-1-yl)pyridazine ligands was conducted, with cisplatin as the reference drug.

3.2. Instrumentation

NMR spectra (^{1}H and ^{13}C) were recorded on a Bruker Avance DPX 500 MHz spectrometer at 30 °C using a 5 mm probe in DMSO-d_6. Chemical shifts (δ, ppm) were referenced to tetramethylsilane (TMS). Molecular weights were confirmed by electrospray ionization mass spectrometry (ESI-MS) on an LC Premier Micro mass spectrometer. Elemental analyses (C, H, and N) were performed using a Thermo Scientific elemental analyser, with combustion at 1150 °C in oxygen. Helium was used as the carrier gas, and gases were quantified with a thermal conductivity detector, calibrated using sulphanilic acid. FTIR spectra (3800–600 cm^{-1}) were recorded using an Agilent Cary 630 FTIR spectrometer. Samples were analysed as KBr pellets prepared from a mixture of 2 mg sample and 100 mg KBr.

X-ray data were recorded on a Bruker Apex Duo diffractometer equipped with an Oxford instrument. Single crystal X-ray crystallographic data of complexes were collected on a Bruker APEX Duo (CrysAlis, 2008; Dolomanov *et al.*, 2009) CCD area detector diffractometer with an Incoatec microsource operating at 30 W of power. The crystal was kept at 100.15 K during data collection using an Oxford Instruments Cryojet accessory. The diffraction was conducted using graphite-monochromated Cu(K_α), (λ = 1.54178), at a crystal-to-detector distance of 50 mm. Data collection was performed under the following set conditions: ω-/φ-scans with exposures taken at 30 W X-ray power and 0.50 frame widths using SAINTS' APEX2 (Bruker, 2009). The crystal structure was solved with Olex2, while the SHELXS (Sheldrick, 2015) and SHELX (Sheldrick, 2008) programs were used for structural refinement *via* direct methods. The non-hydrogen atoms were refined anisotropically by full-matrix least-squares minimization/refinement of F^2. Hydrogen atoms were included but not refined. Visualization of the crystallographic data were visualised in WinGX (Farrugia, 2012) and Mercury *v.4.*3 (Macrae *et al.*, 2008).

Electronic absorption spectra were recorded in the 200–800 nm range using a Cary 100 Bio UV–Visible spectrophotometer equipped with a temperature controller (±0.05 °C), with methanol employed as the solvent. Fluorescence emission studies were conducted on a PerkinElmer LS 45 spectrofluorometer. The molar conductivity of 1.0×10^{-3} M solutions in DMSO was determined using a Jenway 4010 conductivity meter. Electrochemical behaviour was analysed *via* cyclic voltammetry (CV) on an Epsilon Eclipse electrochemical workstation.

3.3. Synthesis of Dimeric Ruthenium(II) Precursors and Ligands

The dimeric ruthenium precursors, $[Ru(\eta^6\text{-}p\text{-cymene/toluene})Cl_2]_2$, were synthesised following the method reported by (Hartinger & Dyson, 2009) (Mendoza-Ferri *et al.*, 2009). To obtain bis[bromido(η^6-*p*-cymene)ruthenium(II)]$_2$, an aqueous solution of potassium bromide (3.00 g, 25 mmol dissolved in 20 mL distilled water) was added to a chloroform solution (20 mL) containing bis[chlorido(η^6-*p*-cymene)ruthenium(II)]$_2$ (0.50 g, 0.82 mmol). The biphasic mixture was vigorously stirred at room temperature for 48 hours. Upon completion, the organic (chloroform) layer was carefully separated, and the solvent was removed under reduced pressure to afford a red solid product. Similarly, bis[iodido(η^6-*p*-cymene)ruthenium(II)]$_2$ was synthesised by reacting bis[chlorido(η^6-*p*-cymene)ruthenium(II)]$_2$ (0.60 g, 0.98 mmol) dissolved in 20 mL of chloroform with an aqueous potassium iodide solution (3.25 g, 19.6 mmol in 20 mL water). The resulting mixture was stirred continuously for 48 hours at ambient temperature. After phase separation, the organic layer was evaporated under vacuum, yielding a dark violet solid.

The synthesis of bis(pyrazol-1-yl)methane was carried out using a modified procedure based on (Potapov & Khlebnikov, 2006). A solution of 1H-pyrazole (10.00 g, 147.0 mmol) in 30 mL of dimethyl sulfoxide (DMSO) was treated with finely powdered potassium hydroxide (32.92 g, 588.0 mmol). The resulting mixture was stirred at 60 °C for 1 hour to generate the reactive pyrazolide intermediate. Subsequently, a solution of dibromomethane (12.80 g, 5.2 mL, 73.6 mmol) in 40 mL of DMSO was introduced dropwise over 30 minutes. Stirring was continued at 60 °C for an additional 4 hours to complete the reaction. The reaction mixture was then poured into 300 mL of water, and the product was extracted using chloroform. The organic phase was successively washed with water, dried using anhydrous calcium chloride, and then concentrated under vacuum to yield the crude product. The synthesis of bis(3,5-dimethylpyrazol-1-yl)methane followed a comparable approach, utilising 3,5-dimethylpyrazole as the starting material in place of 1H-pyrazole.

To prepare 3-chloro-6-(1H-pyrazol-1-yl)pyridazine, a solution of pyrazole (9.88 g, 0.144 mol) in tetrahydrofuran (THF, 100 mL) was treated with metallic lithium (1.00 g, 0.144 mol) at 70 °C and stirred for 3 hours to form the pyrazolyl lithium species. Afterward, a solution of 3,6-dichloropyridazine (21.4 g, 0.144 mol) in 100 mL of THF was added slowly to the mixture, which was then stirred at room temperature for 24 hours. Following reaction completion, the

solvent was evaporated under reduced pressure. The residue was dissolved in dichloromethane, washed with water, dried over magnesium sulphate, and recrystallized to obtain the final product as fine microcrystals.

3.4. Synthesis of η⁶-Arene Osmium(II) Complexes

Compounds **10, 20, 30,** and **40** were synthesised under a nitrogen atmosphere using modified Schlenk techniques (Gichumbi *et al.,* 2017c). A solution of [(η⁶-*p-cymene*)Os(μ-Cl)(Cl)]$_2$ (870 mg, 1.1 mmol in 10 mL methanol) was mixed with bis(pyrazol-1-yl)methane or 3-chloro-6-(1H-pyrazol-1-yl)pyridazine (2.2 mmol in 5 mL acetonitrile) for 30 min. Unreacted solids were filtered off, and the filtrate was reduced to 2 mL. Approximately 5 mL of saturated ethanolic NH_4BF_4 was added slowly, and the mixture stirred under ice in the dark for 1 hour. A yellow precipitate formed, which was filtered, washed with cold diethyl ether, and vacuum-dried. Crystals for X-ray analysis of compound **10** were obtained by slow evaporation of methanol. The mixture was stirred for 4 hours at 40 °C. Complex **20**: [(η⁶-*p*-cymene)(bis(3,5-dimethylpyrazol-1-yl)methane)Os(Cl)]BF_4 was prepared using 870 mg of [(η⁶-*p*-cymene)Os(μ-Cl)(Cl)]$_2$, 449.4 mg of ligand, and 2.5 mmol NH_4BF_4. Complex **30**: [(η⁶-*p*-cymene)(3-chloro-6-(1H-pyrazol-1-yl)pyridazine)Os(Cl)]BF_4 was prepared using 870 mg of [(η⁶-*p*-cymene)Os(μ-Cl)(Cl)]$_2$, 399.4 mg of ligand, and 2.5 mmol NH_4BF_4. Complex **40**: [(η⁶-*p*-cymene)(3-chloro-6-(3,5-dimethyl-1H-pyrazol-1-yl)pyridazine)Os(Cl)]BF_4 was synthesised using 870 mg of [(η⁶-*p*-cymene)Os(μ-Cl)(Cl)]$_2$, 457 mg of ligand, and 2.5 mmol NH_4BF_4.

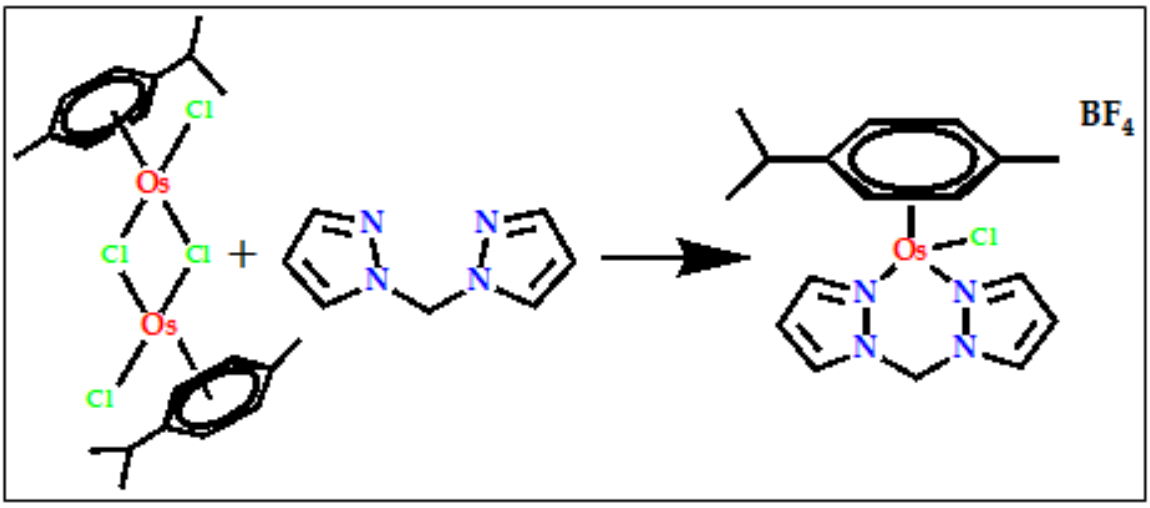

Scheme 3.1: Preparation of complex **10** in methanol/ethanol at 40 °C for 4 h under N_2 flow and subsequent precipitation with NH_4BF_4

3.5. Synthetic Procedure for η^6 -Arene Ruthenium(II) Complexes

A series of arene ruthenium(II) complexes were synthesised, differing in the nature of the η^6-arene ligand (either *p*-cymene or toluene), the halide leaving group (X = Cl, Br, or I), and the type of N,N'-bidentate ligand coordinated to the metal centre. The bidentate ligands employed were either bis(pyrazol-1-yl)methane or 3-chloro-6-(1H-pyrazol-1-yl)pyridazine. For clarity and comparative purposes, the resulting complexes were categorised into groups based on the specific N,N'-donor ligand utilised in their synthesis.

3.5.1 Synthesis of Complexes with Bis(pyrazol-1-yl)methane or Bis(3,5-dimethylpyrazol-1-yl)methane

Complexes **1, 2, 6,** and **7** were synthesised following a modified procedure reported by (Gichumbi *et al.*, 2016b), with slight alterations in the purification steps. Each synthesis involved reacting 1 mmol of the dimeric precursor $[(\eta^6\text{-arene})RuCl(\mu\text{-}Cl)]_2$ (where arene = *p*-cymene or toluene) with 2.2 mmol of either bis(pyrazol-1-yl)methane (326 mg) or bis(3,5-dimethylpyrazol-1-yl)methane (449.4 mg) in acetonitrile at room temperature (Scheme 3.2). The reaction mixture was stirred for 4 hours under a nitrogen atmosphere using Schlenk line techniques to exclude air. The solution was concentrated under reduced pressure, and approximately 5 mL of an ethanolic NH_4BF_4 solution (2.5 mmol) was added dropwise to precipitate the complexes. After standing in

an ice bath for one hour, orange or yellow crystalline products formed. These were stable in air and light. The solids were collected by filtration, washed with cold diethyl ether, and dried under vacuum (Mambanda *et al.*, 2022b).

Complex **1**: [(η⁶-cymene)(bis(pyrazol-1-yl)methane)Ru(Cl)]BF_4 was prepared from 674 mg of [(η⁶-cymene)Ru(μ-Cl)(Cl)]$_2$, 326 mg of bis(pyrazol-1-yl)methane, and 2.5 mmol NH_4BF_4. Complex **2**: [(η⁶-cymene)(bis(3,5-dimethylpyrazol-1-yl)methane)Ru(Cl)]BF_4 was prepared from 674 mg of [(η⁶-cymene)Ru(μ-Cl)(Cl)]$_2$, 449.4 mg of bis(3,5-dimethylpyrazol-1-yl)methane, and 2.5 mmol NH_4BF_4. Complex **6**: [(η⁶-toluene)(bis(3,5-dimethylpyrazol-1-yl)methane)Ru(Cl)]BF_4 was prepared using 581 mg of [(η⁶-toluene)Ru(μ-Cl)(Cl)]$_2$, 449.4 mg of bis(3,5-dimethylpyrazol-1-yl)methane, and 2.5 mmol NH_4BF_4. Complex **7**: [(η⁶-toluene)(bis(pyrazol-1-yl)methane)Ru(Cl)]BF_4 was synthesised from 581 mg of [(η⁶-toluene)Ru(μ-Cl)(Cl)]$_2$, 326 mg of bis(pyrazol-1-yl)methane, and 2.5 mmol NH_4BF_4.

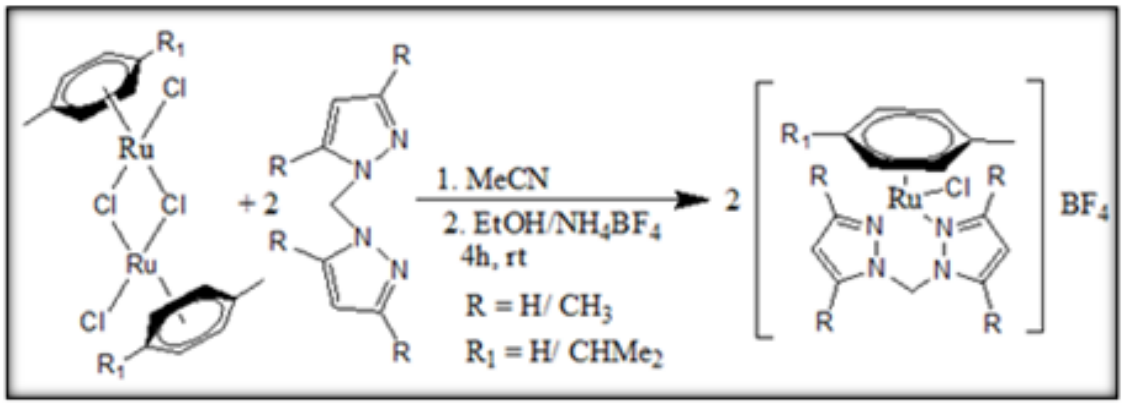

Scheme 3.2: Synthesis of [(η⁶-*p-cymene*/toluene)(bis(pyrazol-1-yl)methane or bis(3,5-dimethylpyrazol-1-yl)methane)Ru(Cl)]BF_4 complexes
1 (R = H, R_1 = $CHMe_2$), **2** (R = CH_3, R_1 = $CHMe_2$); **6** (R = H, R_1 = $CHMe_2$), and **7** (R = CH_3, R_1 = H) complexes.

3.5.2. Synthesis of Complexes with 3-chloro-6-(1H-pyrazol-1-yl)pyridazine or 5-chloro-2-(3,5-dimethyl-1H-pyrazol-1-yl)pyridine

Complexes **3a – c, 4a – c,** and **9** were synthesised based on the method described by (Gichumbi *et al.*, 2016b; Gichumbi *et al.*, 2020) with purification modifications. Precursor dimers [(η⁶-arene)Ru(μ-X)(X)]$_2$ (1.1 mmol; X = Cl, Br, or I) were dissolved in 10 mL acetonitrile: 674 mg for Cl (**3a/4a**), 718.4 mg for Br (**3b/4b**), 1076 mg for I (**3c/4c**), and 581 mg

of toluene-based precursor for complex **9**. These solutions were combined with 10 mL acetonitrile solutions of either 3-chloro-6-(1H-pyrazol-1-yl)pyridazine (399.4 mg, 2.2 mmol) or 5-chloro-2-(3,5-dimethyl-1H-pyrazol-1-yl)pyridine (457 mg, 2.2 mmol). Each mixture was stirred under N_2 at room temperature for 4 hours, then concentrated under vacuum. A solution of NH_4BF_4 (2.5 mmol in ethanol) was added gradually to precipitate the products, which were cooled in an ice bath for 1 h. The resulting orange crystalline solids were filtered, washed with cold diethyl ether, and dried under vacuum (Mambanda, 2022b). These reactions are illustrated in Scheme 3.3.

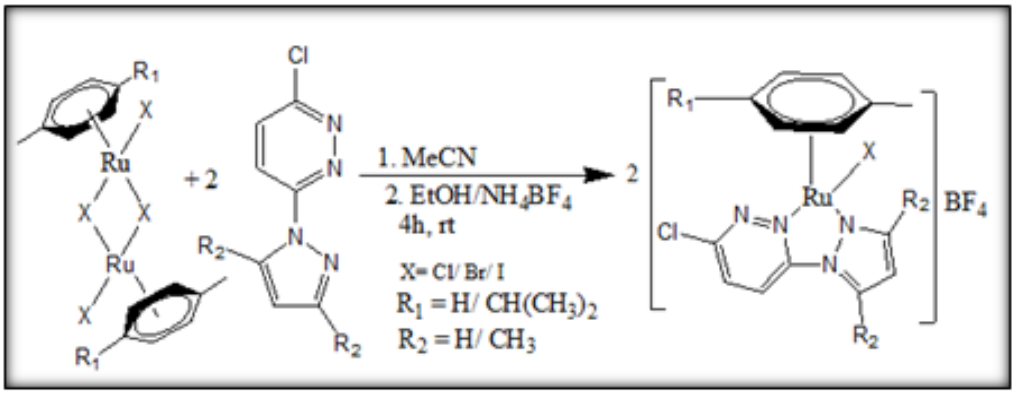

Scheme 3.3: General synthetic strategy for arene–ruthenium(II) complexes incorporating pyrazolyl–pyridazine ligands

3a (R_1 = $CH(CH_3)_2$, X = Cl & R_2 = H); **3b** (R_1 = $CH(CH_3)_2$, X = Br & R_2 = H); **3c** (R_1 = $CH(CH_3)_2$, X = I & R_2 = H); **4a** (R_1 = $CH(CH_3)_2$ & X = Cl, R_2 = CH_3); **4b** (R_1 = $CH(CH_3)_2$, X = Br & R_2 = CH_3); **4c** (R_1 = $CH(CH_3)_2$, X = I & R_2 = CH_3) and [(η^6-toluene)(pyrazol-1-yl)pyridazine)Ru(X)]BF_4: **9** (R_1 = H, X = Cl & R_2 = H).

3.6 Single-crystal X-ray Crystallography

The molecular structures of selected osmium(II) and ruthenium(II) complexes—specifically Os(II) complex **10** and Ru(II) complexes **1, 2, 3a, 3b, 4a, 4b, 6, 7**, and **9**—were determined using single-crystal X-ray diffraction analysis. Crystallographic data were obtained at low temperatures with Cu Kα radiation to enhance resolution and accuracy. Structure solution and refinement were carried out using established crystallographic software packages. All non-hydrogen atoms were refined anisotropically, while hydrogen atoms were positioned based on

idealized geometry and excluded from refinement. The final structural models were visualized using molecular modelling software for further interpretation and analysis.

3.7 Computational Modelling

Computational studies were performed to complement and interpret experimental findings. Density Functional Theory (DFT) was used to elucidate structural and electronic differences between the complexes. Molecular docking was employed to determine the preferred binding geometries within DNA and to estimate binding affinities *via* scoring functions.

3.7.1 DFT-Optimized Structures of the η^6-Arene Os(II) and Ru(II) Complexes

Ground-state DFT-optimized structures of Os(II) complex **10** and Ru(II) complexes **1, 2, 3a – c, 6,** and **7** were computed using the Gaussian 09 program suite (Frisch *et al.*, 2009). Geometry optimization employed the B3LYP functional (Becke, 1993; Lee *et al.*, 1988), with the Los Alamos National Laboratory 2 Double-ζ (LANL2DZ) basis set. DFT uses electron density as the fundamental variable instead of the many-body wave function, offering computational efficiency and reliable accuracy for systems with high electron counts, such as those containing Ru and Os (Shoeib & Sharp, 2012). Solvent effects were modelled using the conductor-like polarizable continuum model (C-PCM) in methanol (Barone & Cossi, 1998; Cossi *et al.*, 2003). Substitutional reactivity was assessed *via* HOMO–LUMO energy gaps and global reactivity descriptors such as chemical hardness (η), chemical potential (μ), electrophilicity index (ω), charge density (η), chemical potential (μ), electrophilicity (ω) (Desoize & Madoulet, 2002); (Wekesa & Jaganyi, 2014), and charge density were compared.

In general, The HOMO represents electron-donating ability, while the LUMO reflects electron-accepting capacity. A reduced HOMO–LUMO gap facilitates electron transfer from metal centres to ligands *via* π-back donation, primarily from metal *d*-orbitals (Obuah *et al.*, 2018). Chemical hardness (η) indicates a molecule's resistance to electronic deformation (Ongoma & Jaganyi, 2012), as given by:

$$\eta = (E_{LUMO} - E_{HOMO})/2 \quad (3.1)$$

High values of electron affinity ($A = -E_{LUMO}$) and ionisation potential ($I = -E_{HOMO}$) characterise soft systems, which are more reactive. Electronic chemical potential (μ) ,

representing the system's tendency to donate electrons, is defined by Equation (3.2).(Chattaraj & Maiti, 2003).

$$\mu = (E_{LUMO} + E_{HOMO})/2 \quad (3.2)$$

The electrophilicity index (ω), which quantifies a species' electron-accepting ability,(Parr *et al.*, 1999). This index is calculated based on the chemical potential and chemical hardness, as expressed in Equation (3.3).

$$\omega = \mu^2/2\eta \quad (3.3)$$

3.7.2 DNA Molecular Docking Simulations

To predict the potential interaction sites of the complexes on the DNA structure, molecular docking simulations were conducted using AutoDock Vina (Trott & Olson, 2010). This approach allowed for the identification of favourable binding regions, providing insights into the binding affinity and orientation of the complexes within the DNA grooves or intercalation sites. The DNA crystal structure (PDB ID: 1Z3F), with a resolution of 1.60 Å, was obtained from the RCSB Protein Data Bank (http://www.rcsb.org/). Before docking simulations, all water molecules and non-standard heteroatoms were eliminated from the model. Coordination environments were modelled from crystallographic data (complexes **3a, 3c**) or DFT-optimized structures (complexes **4a, 4c, 9**). Structures were converted to PDB format using GaussView 5.0. For software compatibility, Ru(II) centres were substituted with Zn(II). A grid spacing of 0.375 Å was applied, and the search space was defined to cover the entire DNA molecule. Binding modes were analysed and visualized using BIOVIA Discovery Studio Visualizer 2022.

3.8. Aqueous and DMSO Stability of η^6-Arene Ruthenium(II) Complexes

Stability of the η^6-arene Ru(II) complexes was assessed *via* UV–visible absorption in phosphate-buffered saline (PBS, pH 7.2) and DMSO at room temperature. Absorbance was monitored over 48 hours in PBS and 72 hours in DMSO. Conductivity measurements over 48 hours complemented the spectral data. Complexes **3a, 3c, 4a, 4c,** and **9** were selected for this study.

3.9. Binding Interactions Studies of (η^6-Arene)Ru(II)(3-Chloro-6-(1H-Pyrazol-1-yl)Pyridazine) Complexes with CT-DNA

The interaction of (η^6-arene)Ru(II) complexes containing the 3-chloro-6-(1H-pyrazol-1-yl)pyridazine ligand with calf thymus DNA (CT-DNA) was explored using both experimental and computational methods. Spectroscopic techniques such as UV–visible absorption and fluorescence emission were employed to monitor spectral changes upon DNA addition, offering insights into binding affinity and potential interaction modes. Electrochemical studies using cyclic voltammetry (CV) were also performed to assess changes in redox behaviour associated with DNA binding. These experimental findings were further supported by molecular docking simulations, which provided structural and energetic information about the preferred DNA binding sites of the complexes. The integrated approach allowed for a more detailed understanding of how these Ru(II) complexes interact with CT-DNA, including the strength, nature, and possible biological relevance of these interactions.

3.9.1 UV–Visible Absorption Studies of CT-DNA

Electronic absorption titrations were conducted following established procedures (Omondi *et al.*, 2020; Omondi *et al.*, 2022; Omondi *et al.*, 2021). A fixed complex concentration was titrated with increasing CT-DNA. After 5 minutes of incubation, spectra were recorded from 230–600 nm. The intrinsic binding constant (K_b) was determined using the Wolfe–Shimmer equation (3.4):

$$[DNA]/(\varepsilon_a-\varepsilon_f) = [DNA]/(\varepsilon_b-\varepsilon_f) + 1/(K_b(\varepsilon_b-\varepsilon) \quad (3.4).$$

in this context, [DNA] refers to the molar concentration of CT-DNA, expressed in base pairs. ε_a (apparent), ε_b (bound), and ε_f (free) represent molar extinction coefficients of the complex in different states. The standard Gibbs free energy change ($\Delta G°$) for DNA binding was calculated using van't Hoff equation (3.5):

$$(\Delta G)_b = -RT \ln K_b \quad (3.5),$$

where R is the universal gas constant and T is the temperature in Kelvin.

3.9.2. Fluorescence Spectroscopic Titrations/Quenching Measurements for CT-DNA

The binding interactions between the complexes and CT-DNA were further evaluated *via* fluorescence quenching of the Hoechst 33258–DNA complex. Excitation was set at 343 nm, and

emission spectra were recorded over the 375–600 nm range, following established protocols (Omondi *et al.*, 2022). The Stern-Volmer equation (3.6) was used to calculate the quenching constant (K_{SV}) from which the bimolecular quenching rate constant (k_q) was derived:

$$I_o/I = 1 + K_{sv} = 1 + k_Q\tau_0[Q] \quad (3.6).$$

Here, I_o and I represent the emission intensities in the absence and presence of the quencher (complex), respectively. [Q] denotes the quencher concentration, and τ_0 is the fluorescence lifetime of the unquenched probe.

Additionally, the Scatchard equation (3.7) was applied to determine both the binding constant (K_F) and the number of binding sites (n):

$$\text{Log } (I_o - I) / I = \log K_F + n \log[Q] \quad (3.7).$$

To correct for inner filter effects—caused by absorption of both the excitation and emitted light by the DNA–Ru(II) complexes—the observed fluorescence intensities were adjusted according to established literature methods (Parker & Rees, 1962). The correction used equation (3.8):

$$F_{corr} = F_{obs}10^{(A_{ex}+A_{em})/2} \quad (3.8),$$

Where F_{obs} and F_{corr} are the measured and corrected fluorescence intensities, respectively, while A_{ex} and A_{em} correspond to the absorbance values at the excitation and emission wavelengths.

3.9.3. Glutathione Reactivity (GSH Assay)

The interaction between selected ruthenium complexes and glutathione (GSH) was monitored by tracking changes in UV–visible absorption spectra, following the method described by (Omondi *et al.*, 2022). Absorbance measurements of the complex-GSH mixtures were taken 5 minutes after GSH addition, over the wavelength range of 230–600 nm. Spectra were recorded both in the absence and presence of GSH as a function of reaction time. To quantify the binding constant (K_b) and the number of binding sites (n), the double logarithmic regression model (equation 3.9) was employed:

$$[(A_o - A_i)/(A_f - A_o)] = \log k_b + n \log[C] \quad (3.9)$$

In this equation, A_o is the initial absorbance of the complex prior to any GSH addition, $\mathbf{A_i}$ represents the absorbance in the absence of GSH at any given time, and A_f is the absorbance after the final GSH addition. The variable [C] corresponds to the concentration of the quencher.

3.9.4. Electrochemical Properties

Cyclic voltammetry was conducted using an Epsilon Eclipse analyser with a standard three-electrode setup: glassy carbon (working), platinum wire (counter), and Ag/AgCl (reference). Measurements were done in 1.0 mM DMSO solutions with 0.10 M $TBABF_4$ under argon. Scans from –2.2 to +1.8 V at 100 mV/s characterised redox properties.

3.10. Cell Culture and Cytotoxicity Studies

A panel of human cancer cell lines was selected for *in vitro* cytotoxicity evaluation, including breast (MCF-7, T-47D, MDA-MB-231)**,** cervical (CaSki, HeLa)**,** pancreatic (CFPAC-1, PANC-1), and rhabdomyosarcoma (RH-30, RD)**.** Cells were cultured in either Roswell Park Memorial Institute medium (RPMI-1640) or Dulbecco's Modified Eagle Medium (DMEM), both from Sigma Aldrich (USA), tailored to the specific requirements of each line. The media were supplemented with 10% heat-inactivated foetal bovine serum (FBS), 100 μg/mL penicillin, and 100 μg/mL streptomycin. Cultures were maintained at 37 °C in a humidified atmosphere containing 5% CO_2, with media renewal every 48–72 hours to support optimal growth and viability.

Cytotoxicity of the synthesised η^6-arene Ru(II) complexes was evaluated across the nine cancer cell lines. Cells were seeded in 96-well plates at optimized densities: MCF-7, T-47D, CaSki, and HeLa at 4,500 cells/well; MDA-MB-231 at 3,000 cells/well; CFPAC-1 at 10,000 cells/well; PANC-1 at 8,000 cells/well; and RD and RH-30 at 6,500 cells/well. After an initial adhesion period (24 hours for CaSki, HeLa, RD, RH-30, CFPAC-1, and PANC-1; 48 hours for MCF-7, MDA-MB-231, and T-47D), cells were treated for 48 hours with the test compounds at 10 μM and 20 μM concentrations, dissolved in 0.1% DMSO. Control wells received 0.1% DMSO only.

Cell viability was assessed *via* the MTT assay, following the procedure established by (Mosmann, 1983). This colorimetric assay measures mitochondrial activity through the enzymatic reduction of MTT to insoluble purple formazan by viable cells. The conversion is mediated by cellular oxidoreductases utilizing NAD(P)H as an electron donor, thus serving as an indicator of metabolic activity (Berridge & Tan, 1993). Absorbance of the solubilized formazan was measured at 600 nm using a GloMax® Explorer Multimode Microplate Reader (GM3500, Promega). Absorbance readings were corrected against media-specific background signals from RPMI and DMEM, as described by (Welsh *et al.*, 2020; Zinman *et al.*, 2024).

3.11 Data Presentation and Statistical Analyses

All quantitative results are presented as mean values ± standard deviation (SD) or standard error of the mean (SEM), as appropriate. Statistical analyses and nonlinear regression modelling, including IC_{50} determination, were performed using GraphPad Prism (version 8.3.0, GraphPad Software Inc., CA, USA). The "log(inhibitor) *vs*. normalized response – variable slope" model was applied for dose–response curve fitting and IC_{50}

CHAPTER FOUR

RESULTS AND DISCUSSION

This chapter presents a detailed account of the results and interpretation of data obtained from the synthesis, structural characterisation, computational modelling, and biological evaluation of selected ruthenium(II) and osmium(II) arene complexes. These organometallic compounds are composed of essential components that contribute to their chemical and biological functionality. Each complex features a labile halide ligand (Cl^-, Br^-, or I^-) that can participate in substitution reactions, an η^6-coordinated arene moiety (such as *p*-cymene or toluene) that helps stabilise the oxidation state of the metal centre while enhancing cellular uptake, and a nitrogen-donor bidentate ligand designed to strengthen interactions with biomolecules like DNA. The metal core—either Ru(II) or Os(II)—belongs to the d^6 transition series and is chosen for its ability to exhibit selective reactivity and promising anticancer properties. The findings are organised into three major sections based on the structural types of the complexes: osmium(II) arene complexes with tetrafluoroborate counterions, ruthenium(II) arene complexes coordinated with bis(pyrazol-1-yl)methane ligands, and a series of ruthenium(II) complexes containing pyrazolylpyridazine ligands and halide substituents formulated as $[(\eta^6\text{-arene})(\text{pyrazol-1-yl})\text{pyridazine})\text{Ru(X)}]BF_4$, where X = Cl^-, Br^-, or I^-. Each of these categories is examined independently to explore the influence of structural and electronic features on their overall stability, reactivity, and biological performance.

4.1 Chlorido-(η^6-*Arene*)Osmium(II) Tetrafluoroborate Complexes

The chlorido-(η^6-arene)osmium(II) complexes **10, 20, 30,** and **40** were thoroughly characterised using a combination of spectroscopic, analytical, and computational techniques. Structural elucidation was achieved through UV–Visible spectroscopy, Fourier-transform infrared (FTIR) spectroscopy, and both ^1H and ^{13}C nuclear magnetic resonance (NMR) spectroscopy. Elemental analysis further confirmed the purity and composition of the synthesised compounds. Additionally, single-crystal X-ray diffraction provided unambiguous structural validation, revealing key coordination features around the osmium centre. To complement the experimental findings, post-synthetic density functional theory (DFT) calculations were performed, offering theoretical support for the observed molecular geometries and electronic

properties. Together, these techniques affirmed the successful synthesis and structural integrity of the target Os(II) complexes.

4.1.1. Syntheses and Characterisation of Os(II) Complexes

The arene Os(II) complexes shown in Scheme 3.1 (compound **10**) and Figure 4.1 (compounds **20, 30,** and **40**) were synthesised *via* a unified protocol. Specifically, a series of [(η⁶-*p*-cymene)(dpzm/pdzn-pzn)OsCl] complexes was obtained by subjecting the dinuclear precursor [(η⁶-*p*-cymene)Os(μ-Cl)Cl]₂ to ligand substitution with N,N′-donor chelators in methanol. Following the reaction, the cationic species were isolated conveniently as their tetrafluoroborate salts to facilitate further characterisation. The synthesised compounds were obtained as solid materials, exhibiting colours ranging from yellow to deep brown, and were isolated in yields between 48.1% and 78.6%, with the osmium precursor serving as the limiting reactant. Structural and compositional confirmation in solution was achieved through a comprehensive set of analytical tools such as infrared spectroscopy, NMR (^{1}H and ^{13}C), electrospray ionization mass spectrometry, and elemental composition analysis. A detailed summary of these findings is provided in Tables 4.1-4.4.

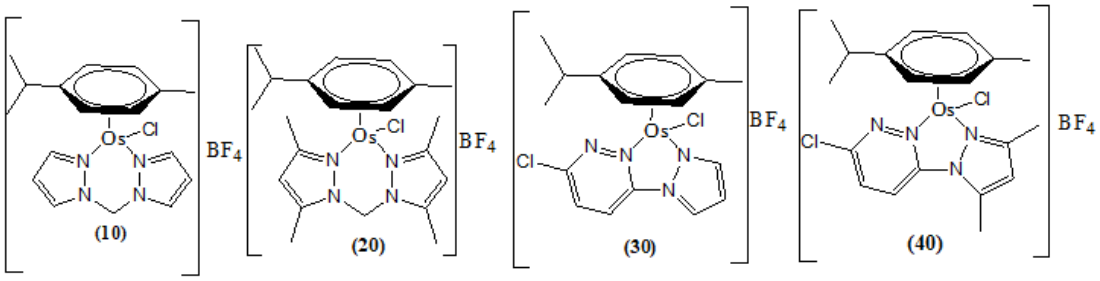

Figure 4.1: [(η⁶-*p*-cymene)(N,N′)Os(Cl)]BF_4 Complexes with Ligands **20, 30,** and **40**

Ligands: **10** = bis(pyrazol-1-yl)methane; **20** = bis(3,5-dimethylpyrazol-1-yl)methane; **30** = 3-chloro-6-(1H-pyrazol-1-yl)pyridazine; **40** = 5-chloro-2-(3,5-dimethyl-1H-pyrazol-1-yl)pyridine

[(η⁶-*p*-cymene)(bis(pyrazol-1-yl)methane)Os(Cl)]BF_4 (10):

The complex [(η⁶-*p*-cymene)(bis(pyrazol-1-yl)methane)Os(Cl)]BF_4 was synthesised by reacting 870 mg of [(η⁶-*p*-cymene)Os(μ-Cl)(Cl)]₂ with 326 mg of bis(pyrazol-1-yl)methane in the presence of 2.5 mmol of NH_4BF_4 (Mambanda *et al.*, 2022a). The reaction afforded yellow crystalline blocks in a 67.5% yield.

Table 4.1: Analytical data for [(η⁶-*p*-cymene)(bis(pyrazol-1-yl)methane)Os(Cl)]BF_4 (**10)**

Technique	**Data**
Yield	67.5%, yellow crystalline blocks
MS (ESI^+)	m/z = 509 (100%), $[C_{17}H_{22}ClN_4Os+2H]^+$
^1H NMR (500 MHz, DMSO-d_6)	δ (ppm): 8.16 (d, J = 2.1 Hz, 2H, pzn), 7.91 (d, J = 2.1 Hz, 2H, pzn), 7.12 (d, J = 14.4 Hz, 1H, pzn), 6.65 (t, J = 2.6 Hz, 2H, pzn), 6.33, 6.23 (d, J = 5.6, 5.7 Hz, 4H, η⁶-*p-cym*), 6.05 (d, J = 14.4 Hz, 1H, pzn), 2.73 (sept, J = 6.9 Hz, 1H, CH of isopropyl), 2.05 (s, 3H, CH_3 of cymene), 1.21 (d, J = 6.9 Hz, 6H, CH_3 of isopropyl)
FTIR (KBr, cm^{-1})	3132 (w, ν(C–H_arom)), 2945 (w, ν(CH_2)), 1516 (m, ν(C=N)), 1408 (m, ν(C=C)), 1281 (m, β(C=C)–CH), 1038 (s, br, ν(BF_4^-)), 830 (m, shp, ν(Os–N)), 620 (m, shp, ν(Os–Cl))
Elemental Analysis	Calculated (%): C 34.30; H 3.75; N 9.42 Found (%): C 33.98; H 3.85; N 9.14
Figures	Figures 4.10 and 4.18–4.20

w/m/s = weak/medium/strong intensity, shp/br =sharp/broad)

[(η⁶-*p*-cymene)(bis(3,5-dimethylpyrazol-1-yl)methane)Os(Cl)]BF_4 (20):

The complex [(η⁶-*p*-cymene)(bis(3,5-dimethylpyrazol-1-yl)methane)Os(Cl)]BF_4 was synthesised by reacting 870 mg of [(η⁶-*p*-cymene)Os(μ-Cl)(Cl)]$_2$ with 449.4 mg of bis(3,5-dimethylpyrazol-1-yl)methane in the presence of 2.5 mmol of NH_4BF_4. The reaction afforded a yellow solid in 77.8% yield. The compound was characterised by ESI-MS, NMR spectroscopy, FTIR, and elemental analysis, confirming the expected structure and purity.

Table 4.2: Analytical data for [(η^6-*p*-cymene)(bis(3,5-dimethylpyrazol-1-yl)methane)Os(Cl)]BF_4 **(20)**

Technique	Data
Yield	77.8%, yellow solid
MS (ESI^+)	m/z = 475 (100%), $[C_{21}H_{30}ClN_4Os+H]^+$
^1H NMR (500 MHz, DMSO-d_6)	δ (ppm): 6.57 (d, J = 15.5 Hz, 1H, pzm), 6.42 (d, J = 5.9 Hz, 2H, pzm), 6.30 (m, 4H, η^6-*p-cym*), 5.56 (d, J = 15.5 Hz, 1H, pzm), 2.68 (d, J = 6.8 Hz, 1H, CH of isopropyl), 2.47, 2.57 (s, 12H, CH_3 of pzm), 2.26 (s, 3H, CH_3 of cymene), 1.09 (d, J = 6.9 Hz, 6H, CH_3 of isopropyl)
^{13}C NMR (100 MHz, DMSO-d_6)	δ (ppm): 154.82 (C=N), 142.74 (C–N), 108.11 (C=C, pzm), 96.91, 91.50, 75.82, 73.30 (Ar, *p-cym*), 56.65 (CH_2-pzm), 31.28 (CH of cymene), 22.23 (CH_3 of cymene), 17.78 (Me_2 of cymene), 15.20, 10.56 (CH_3-pzm)
FTIR (KBr, cm^{-1})	3061 (w, ν(C–H_arom)), 2955 (w, ν(CH_2)), 1556 (m, ν(C=N)), 1466 (m, ν(C=C)), 1290 (m, β(C=C)–CH), 1054 (s, br, ν(BF_4^-)), 830 (m, shp, ν(Os–N))
Elemental Analysis	Calculated (%): C 44.89; H 5.38; N 9.97 Found (%): C 45.09; H 5.11; N 10.16
Figures	Figures 4.2–4.4

w/m/s = weak/medium/strong intensity, shp/br =sharp/broad)

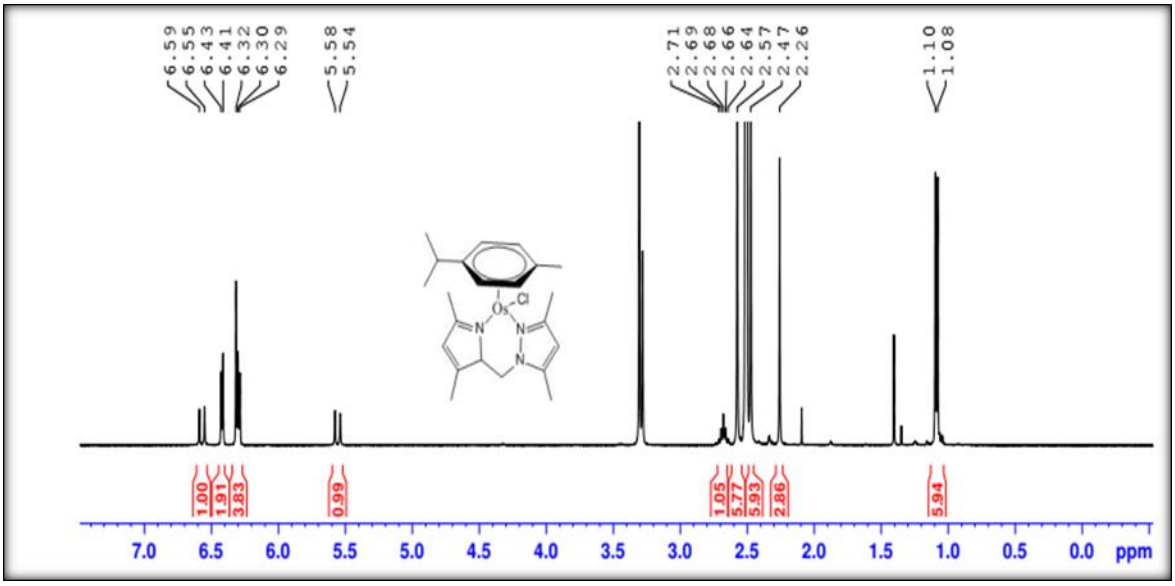

Figure 4.2: ^{1}H NMR spectrum (500 MHz, DMSO-d_6) of complex **20**

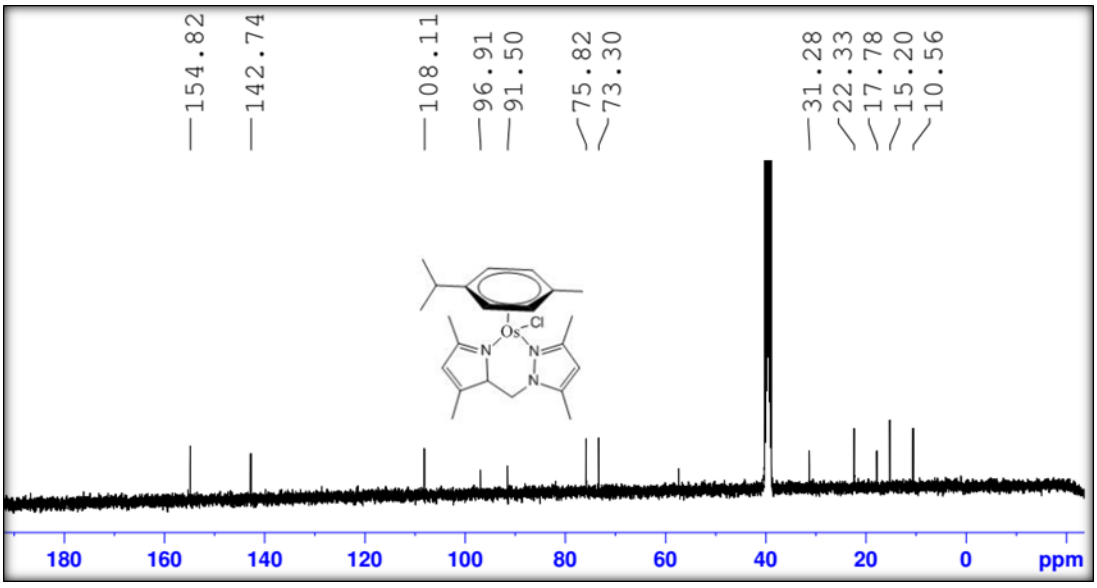

Figure 4.3: ^{13}C NMR spectrum (100 MHz, DMSO-d_6) of complex **20**

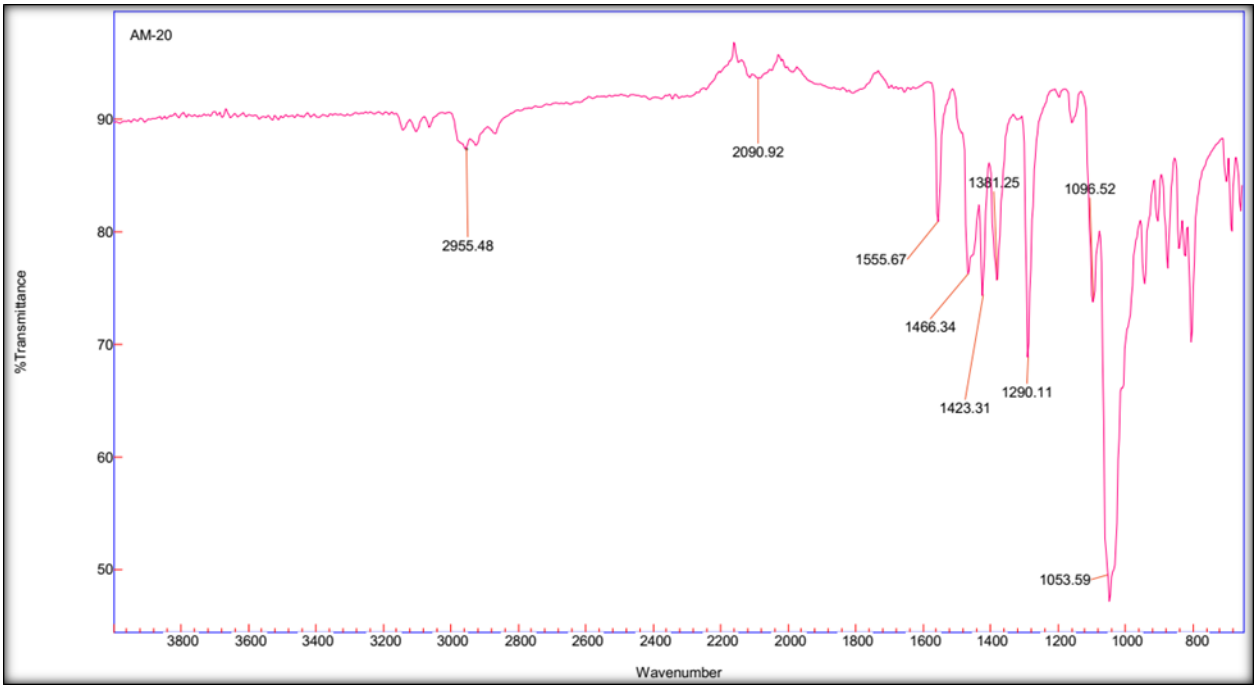

Figure 4.4: FTIR spectrum (dispersed in KBr) of complex **20**

[(η^6-*p*-cymene)(3-chloro-6-(1H-pyrazol-1-yl)pyridazine)Os(Cl)]BF_4 (30):

The complex [(η^6-*p*-cymene)(pdzn-pzm)Os(Cl)]BF_4 (**30**) was synthesised by reacting 870 mg of [(η^6-*p*-cymene)Os(μ-Cl)(Cl)]$_2$ with 399.4 mg of 3-chloro-6-(1H-pyrazol-1-yl)pyridazine (pdzn-pzm) in the presence of 2.5 mmol of NH_4BF_4. The reaction afforded a yellow solid in 78.6% yield. The product was characterized by ESI-MS, NMR (^{1}H and ^{13}C), FTIR spectroscopy, and elemental analysis. The spectral and analytical data confirmed the proposed formulation and structural integrity.

Table 4.3: Analytical data for [(η⁶-*p*-cymene)(3-chloro-6-(1H-pyrazol-1-yl)pyridazine)Os(Cl)]BF_4 **(30)**

Technique	Data
Yield	78.6%, yellow solid
MS (ESI^+)	m/z = 541 (100%), $[C_{17}H_{19}ClN_4OsCl+2H]^+$
^1H NMR (500 MHz, DMSO-d_6)	δ (ppm): 9.17 (d, J = 3.2 Hz, 1H, pzn), 8.91 (m, 2H, pzn), 8.57 (d, J = 9.3 Hz, 1H, pdzn), 7.18 (dd, J = 3.2, 2.2 Hz, 1H, pdzn), 6.38, 6.30, 6.16, 6.03 (d, J ≈ 5.7–5.9 Hz, 4H, Ar-H of cymene), 2.67 (p, J = 6.9 Hz, 1H, CH of isopropyl), 2.18 (s, 3H, CH_3 of cymene), 1.12 (dd, J = 6.9, 2.3 Hz, 6H, CH_3 of isopropyl)
^{13}C NMR (100 MHz, DMSO-d_6)	δ (ppm): 154.43 (N–C–N, pdzn), 151.76 (N=C–Cl, pdzn), 148.58, 134.54 (C=N, pzn), 133.60, 121.51 (C=C, pdzn), 113.40 (C=C, pzn), 96.3, 94.6, 79.3, 78.8, 76.1, 75.8 (Ar–C, cymene), 30.76 (CH, isopropyl), 22.04 (CH_3, isopropyl), 18.20 (CH_3, cymene)
FTIR (KBr, cm^{-1})	3085 (w, ν(C_ar–H)), 2955 (w, ν(C–H_aliphatic), br), 2090 (ν(N=N), pdzn), 1556 (w, sharp, ν(C=N), pdzn/pzn), 1466, 1423 (s, sharp, ν(C=C), cymene/pzn/pdzn), 1290 (m, sharp, β(C–H), cymene), 1056 (vs, sharp, ν(BF_4^-)), 820–650 (m, sharp, ν(Os–N, Os–C_centroid, Os–Cl))
Elemental Analysis	Calculated (%): C 37.94; H 3.56; N 10.41 Found (%): C 37.85; H 3.57; N 10.50
Figures	Figures 4.14–4.15 and 4.21

w/m/s = weak/medium/strong intensity, shp/br =sharp/broad)

[(η⁶-*p*-cymene)(3-chloro-6-(3,5-dimethyl-1H-pyrazol-1-yl)pyridazine)Os(Cl)]BF_4 (40):

The complex [(η⁶-*p-cymene*)(3-chloro-6-(3,5-dimethyl-1H-pyrazol-1-yl)pyridazine)Os(Cl)]BF_4 was synthesised by reacting 870 mg of [(η⁶-*p-cymene*)Os(μ-Cl)(Cl)]$_2$ with 457 mg of 5-chloro-2-(3,5-dimethyl-1H-pyrazol-1-yl)pyridine in the presence of 2.5 mmol of NH_4BF_4. The reaction yielded a red-brown solid with a yield of 48.1%.

Table 4.4: Analytical data for complex [(η^6-*p*-cymene)(3-chloro-6-(3,5-dimethyl-1H-pyrazol-1-yl)pyridazine)Os(Cl)]BF_4 **(40)**

Technique	Data
Yield	48.1%, red-brown solid
MS (ESI^+)	m/z = 569 (100%); $[C_{19}H_{24}ClN_4OsCl+H]^+$
^1H NMR (500 MHz, DMSO-d_6)	δ (ppm): 1.05 (dd, J = 15.7, 6.9 Hz, 6H, CH_3 isopropyl, *p-cym*), 2.17 (s, 3H, CH_3 *p-cym*), 2.64 (m, 1H, CH isopropyl, *p-cym*), 2.72 & 2.78 (s, 3H each, CH_3, pyrazolyl), 5.97–6.74 (m, 5H, Ar–*p-cym*), 7.20 (s, 1H), 8.40 (d, J = 2.8 Hz, 1H)
^{13}C NMR (100 MHz, DMSO-d_6)	δ (ppm): 13.6, 15.8 (CH_3, pyrazolyl), 18.3, 21.7, 22.5, 30.6 (CH/CH_3, *p-cym*), 73.2, 74.2, 76.93, 80.8, 96.6, 98.6 (Ar–*p-cym*), 113.8, 122.2, 133.1, 146.0, 151.5 (C=C, pyrazolyl), 153.0 (N=C–Cl), 156.8 (N–C–N)
FTIR (KBr, cm^{-1})	3103 (w, ν(C–H_arom)), 2977 (w, br, ν(C–H_aliph)), 2085 (ν(N=N_pyrazolyl)), 1577 (w, sharp, ν(C=N)), 1433 (s, sharp, ν(C=C_arom)), 1284 (m, sharp, Ar–β–CH), 1042 (vs, sharp, ν(BF_4^-)), 820–850, 780, 650 (m, sharp, ν(Os–N), ν(Os–C), ν(Os–Cl))
Elemental Analysis	Calculated (%): C 47.60, H 4.84, N 11.69 Found (%): C 47.47, H 4.71, N 11.59
Figures	Figures 4.5 - 4.8.

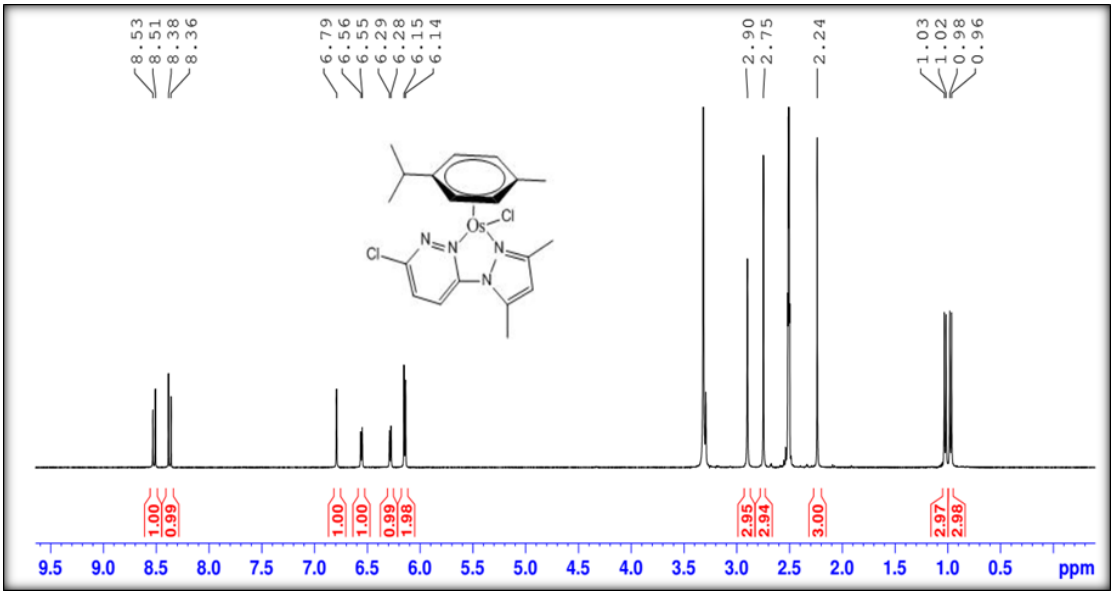

Figure 4.5: ^{1}H NMR spectrum (500 MHz, DMSO-d_6) of complex **40**

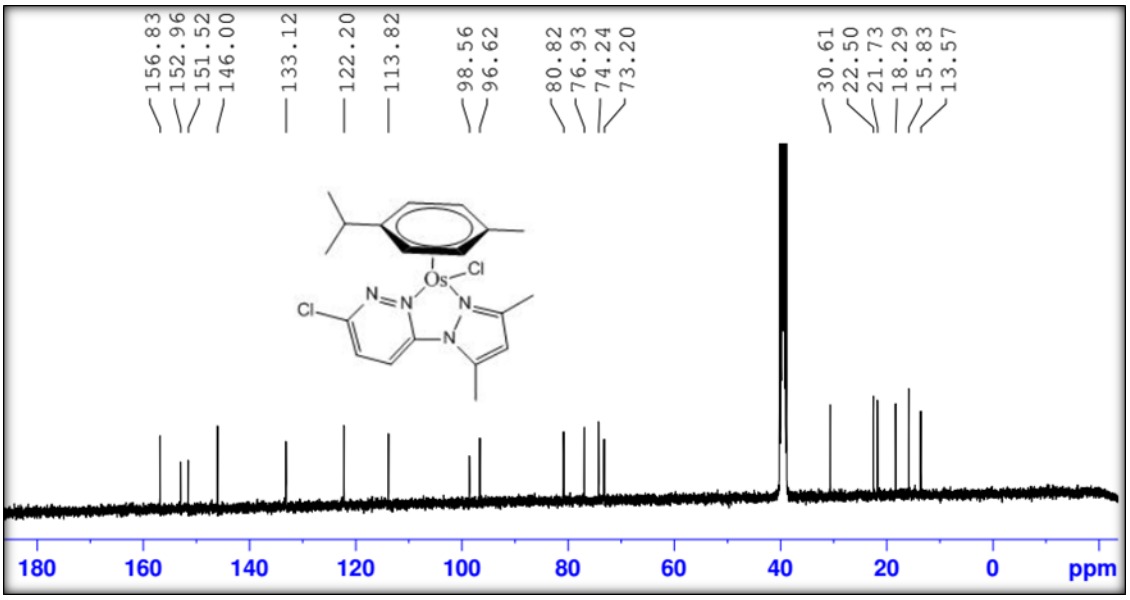

Figure 4.6: ^{13}C NMR spectrum (100 MHz, DMSO-d_6) of complex **40**

Figure 4.7: FTIR spectrum (dispersed in KBr) of complex **40**

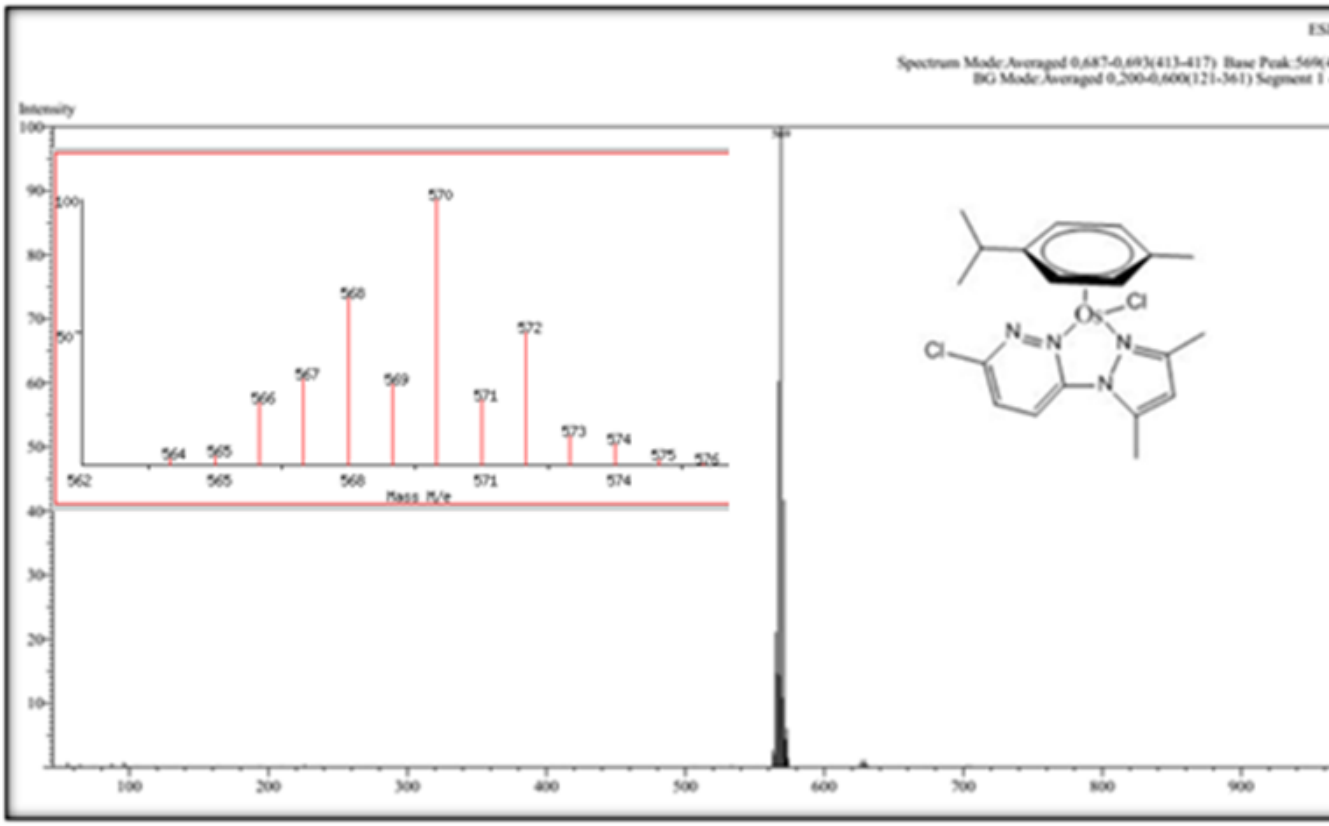

Figure 4.8: Low-resolution mass spectrum of **40**, showing the *m/z* of 569 (100%) of the pseudo-molecular ion peak, $[C_{17}H_{19}ClN_4OsCl+H]^+$. Inset: Predicted isotopic distribution pattern for complex **40** generated using the SIS Isotope Distribution Calculator (accessed December 13, 2024; https://www.sisweb.com/mstools/isotope.htm).

4.1.2 X-ray Crystallography of Complex 10 ($C_{17}H_{22}BClF_4N_4Os$)

The molecular structure of complex **10** was elucidated through single-crystal X-ray diffraction analysis. The ORTEP diagram (Figure 4.9) illustrates the atomic numbering within the asymmetric unit, while the crystal packing arrangement is depicted in Figure 4.10. In this complex, the osmium centre exhibits a distorted octahedral geometry, commonly referred to as a "piano-stool" configuration. This coordination environment arises from the presence of three distinct ligands: an η^6-arene moiety and two nitrogen-donor ligands that coordinate in a bidentate manner, forming six-membered chelate rings. The observed bite angles between the coordinating nitrogen atoms are approximately 83°, consistent with the structural constraints imposed by the ligand framework.

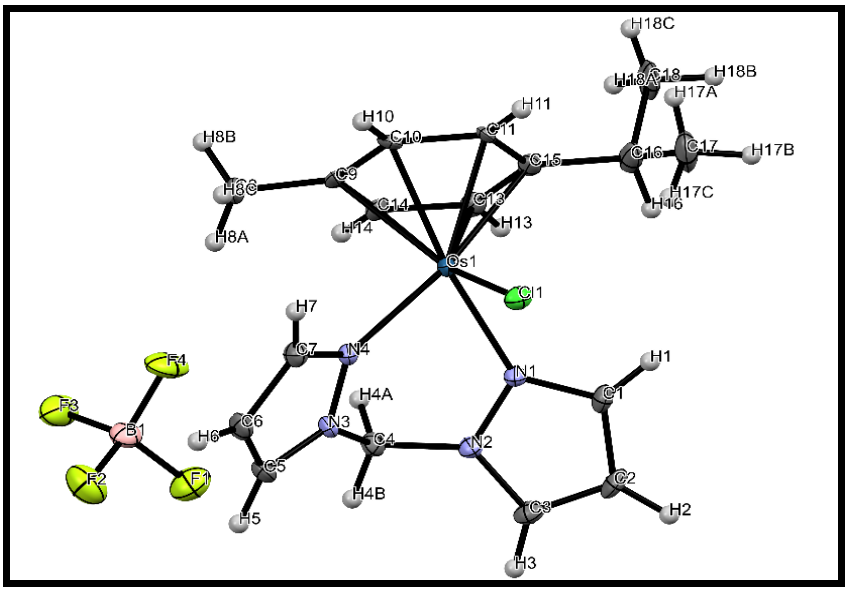

Figure 4.9: The Ortep diagram of **10** ($C_{17}H_{22}BClF_4N_4Os$).

The diagram illustrates the asymmetric unit of complex 10. Thermal ellipsoids are drawn at the 50% probability level.

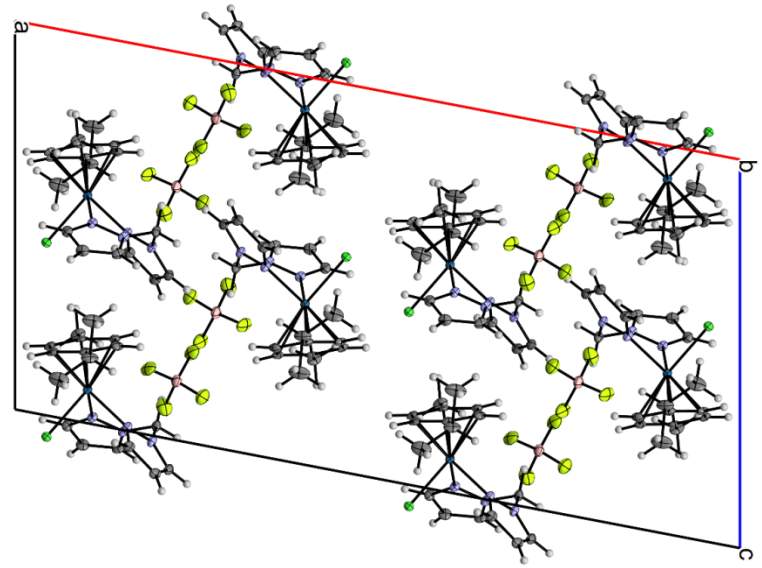

Figure 4.10: Unit cell and crystal packing of complex **10** ($C_{17}H_{22}BClF_4N_4Os$).

A summary of the crystallographic data and refinement statistics for complex **10** is presented in Table 4.5. Table 4.6 lists key bond distances (in Å) and bond angles (in degrees) relevant to the coordination environment. Additional crystallographic details—such as atomic coordinates (scaled by $\times 10^4$), equivalent isotropic displacement factors ($Å^2 \times 10^3$), and further

selected bond metrics—are provided in Tables a–c in the appendix section of the supplementary material.

Table 4.5: Detailed crystallographic data and refinement parameters for **10** ($C_{17}H_{22}BClF_4N_4Os$).

Identification code for 10	**cu_am_ro_am_10_5_0m**
Crystal (Colour /Shape)	Yellow /Block
Formula Weight	594.84
Temperature (K)	102.22
Crystal system	Monoclinic
Space group	C2/c
a (Å)	27.4619(7)
b (Å)	10.2573(3)
c (Å)	14.4399(4)
α (°)	90
β (°)	100.8160(10)
Γ (°)	90
Volume ($Å^3$)	3995.24(19)
Z	8
ρ_{calc}, g/cm^3	1.978
M (mm^{-1})	13.718
F(000)	2288
Crystal size (mm^3)	0.475 × 0.33 × 0.15
Radiation source, λ (Å)	Cu(K_α), λ = 1.54178
2θ range for data collection (°)	6.554 to 136.734
Index ranges	$-32 \le h \le 32$, $-12 \le k \le 12$, $-17 \le l \le 16$
Reflections collected	17267
Independent reflections	3581 [R_{int} = 0.0446, R_σ = 0.0383]
Data/restraints/parameters	3581/0/256
Goodness-of-fit on F^2	1.245
Final R indexes [I ≥ 2σ(I)]	R_1 = 0.0275, wR_2 = 0.0659
Final R indexes [all data]	R_1 = 0.0277, wR_2 = 0.0661

Largest diff. peak/hole / e $Å^{-3}$	0.70/−1.68

Table 4.6: Selected bond lengths (Å) and bond angles (°) for complex **10** ($C_{17}H_{22}BClF_4N_{40}$).

Length, (Å)	
Os1-Cl1	2.3982(8)
Os1-N1	2.122(3)
Os1-N4	2.105(3)
Angles/°	
N4-Os1-Cl1	84.71(9)
N4-Os1-N1	83.17(11)
N1-Os1-Cl1	83.84(9)

4.1.3. Discussion

Evaluations of half-sandwich η^6-arene Os(II) complexes as prospective anticancer metallodrugs have been documented in earlier studies (Păunescu *et al.*, 2015; Peacock *et al.*, 2007; van Rijt *et al.*, 2009), which served as a basis for the current investigation. Nonetheless, studies involving η^6-arene Os(II) complexes coordinated with flexible *N,N′*-donor ligands remain limited, aside from a few recent accounts focusing on Ru(II) analogues (Gichumbi *et al.*, 2020; Thangavel *et al.*, 2016).

In the ^{1}H NMR spectrum of complex **10** (Figure 4.12), the chemical shifts, integration values, and splitting patterns clearly correspond to the distinct proton environments of the dpzm and *p*-cymene ligands. Compared to the free ligands (Figure 4.11), the proton resonances in the complex are noticeably downfield-shifted, which is consistent with ligand-to-metal σ- and π-donation to the Os(II) centre

. Despite this deshielding, a spin–orbit (SO) shielding influence from the heavy osmium atom is observed, particularly affecting the protons on the arene ring. This phenomenon is likely attributed to an increase in electron density around the donor atoms, influenced by the relativistic effects associated with osmium. Additional evidence for coordination of the dpzm ligand is provided by the clear splitting pattern observed for the geminal methylene protons (C4) on each arm of the ligand. These protons appear as two distinct doublets at δ 7.12 ppm and 6.05 ppm, consistent with the characteristics of an A(B)X spin system. The loss of conformational

flexibility upon coordination gives rise to diastereotopic behaviour of these methylene protons, as the two hydrogen atoms become magnetically non-equivalent due to their differing spatial environments.

This diastereotopicity is well-resolved on the NMR timescale and aligns with similar behaviour observed in other multidentate ligands containing methylene bridges, as previously reported in related systems (Marchetti *et al.*, 2008). The η^6-*p*-cymene protons (Figure 4.11) give rise to two different sets of resonances at $\delta_{(ppm)}$ values of 6.33 (C10/12) and 6.23 (C9/13) due to their XA(A')-XB(B') spin systems. *p*-Cymene also exhibits the aliphatic protons at 2.73 ppm, C15 (*sept*, $1H_{CH(CH3)2}$, 2.05 ppm, C15 (*s*, $3H_{methyl}$), and 1.21 ppm, C16/17 (*dd*, $2 \times 3H_{methyl\ isopropyl}$).

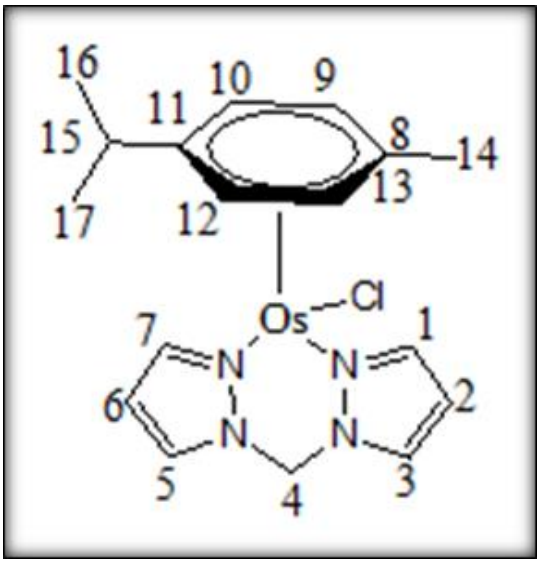

Figure 4.11: Carbon number system for complex **10**

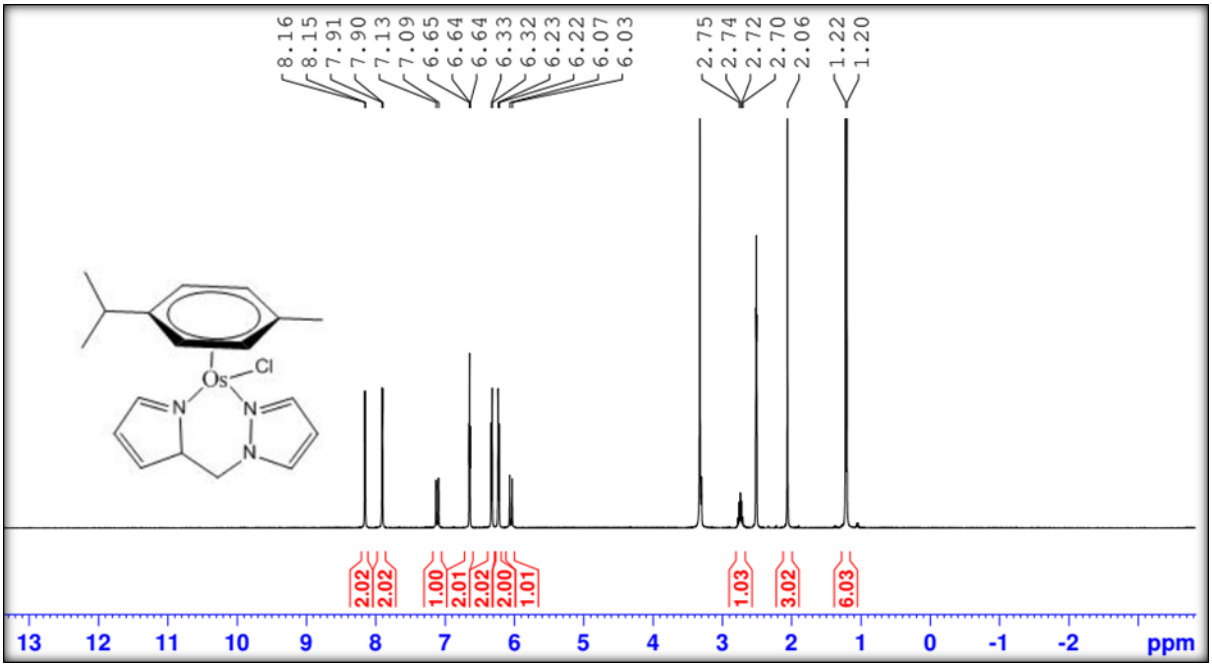

Figure 4.12: ^{1}H NMR spectrum (500 MHz, DMSO-d_6) of complex **10**.

The ^{1}H NMR spectrum of the complex **20** (Figure 4.2) and **10** are similar for arene and *N,N'* bidentate ligands; however, they are slightly lower due to the influence of the methyl substitution on C1/3/5/7 (2.47, 2.57 ppm). The C_2 symmetry of the η^6-*p*-cymene ligand, when coordinated in a facial manner, maintains the chemical equivalence of the four aromatic protons (C9, C10, C12, and C13). This symmetry remains unaffected by any potential spin–spin interactions with the diastereotopic methyl protons on the isopropyl substituent, indicating that the coupling is either negligible or averaged out under the experimental conditions. In contrast, the methylene protons at position C4 of the dpzm ligand display clear diastereotopic splitting, appearing as two distinct doublets at δ 6.59 ppm and 5.56 ppm. This splitting pattern is characteristic of an A(B)X spin system, further supporting the restricted rotational freedom and asymmetry introduced upon coordination to the Os(II) centre.

The ^{1}H NMR spectrum of complex **30** (Figure 4.14) reveals a series of five distinct downfield signals between δ = 7.18–9.18 ppm, corresponding to the aromatic protons of both the pzn and pdzn ligands. These resonances are assigned to protons positioned on C=N, C–N, and C=C moieties. Compared to the uncoordinated ligands, whose chemical shifts typically fall within δ = 6.69–8.80 ppm, the observed downfield shift indicates a deshielding effect induced by coordination to the Os(II) centre. Additionally, four distinct signals are observed in the δ = 6.00–

6.38 ppm region, corresponding to the aromatic protons of the η⁶-p-cymene moiety. In the case of complex 30, the typical C_2 symmetry of the cymene ligand appears disrupted. This loss of symmetry is attributed to spin–spin coupling interactions between the aromatic protons of the cymene ring and the magnetically non-equivalent methyl protons within the isopropyl group, leading to differentiated chemical environments.

Moreover, the asymmetric arrangement of ligands around the Os(II) centre creates a chiral environment, with the metal adopting a coordination geometry that resembles a distorted octahedron typical of arene–metal complexes. As a result, the complex exists as stereoisomers, and this stereochemical complexity contributes to the loss of C_2 symmetry in the cymene ligand, which is reflected in the splitting of its proton signals. This behaviour aligns with previous observations in structurally related Os(II) arene complexes (Gupta *et al.*, 2009). As expected, the aliphatic protons of the cymene appear at 2.67 ppm (*m*, $1H_{CH(CH3)2}$, 2.18 ppm (*s*, $3H_{methyl}$), and 1.12 ppm (*dd*, $2 \times 3H_{methyl\ isopropyl}$). The correlation of each proton was observed in the ^1H-^1H COSY spectrum, Figure 4.16 and Table 4.7, which distinguishes the protons in different positions, C16/17 (1.20 ppm) *vs.* C15 (2.97 ppm); C2 (7.17 ppm) *vs.* C15 (8.94 ppm); C2 *vs.* C1 (9.20 ppm) and C6 (8.55 ppm) *vs.* C5 (8.78 ppm) as defined in the structure in Figure 4.6. Proton–carbon correlations were further investigated using HSQC NMR spectroscopy (Figure 4.17 and Table 4.7) of complex **30** showed a good correlation between the protons and the associated carbons. This 2D-NMR was used as a representative of Os(II) complexes. This data was also very close the ruthenium(II) analogue of complex **30** published as **Ru1** (Mambanda *et al.*, 2022b)**.**

In the ¹H NMR spectrum of complex **40** (Figure 4.48), three distinct resonance signals between chemical shift (δ) 6.74 and 8.40 ppm are observed, attributable to aromatic protons on the C=C and C=N units of the coordinated pyrazole and pyridazine ligands**.** Meanwhile, the aromatic protons associated with the η⁶-*p*-cymene ligand produce a multiplet between δ 5.97 and 6.29 ppm, exhibiting a pattern consistent with overlapping doublet-of-doublets, indicative of the complex coupling environment. This complex splitting pattern likely arises from scalar coupling with the diastereotopic methyl protons of the isopropyl group**,** which interact asymmetrically due to the chiral environment around the Os(II) centre—a result of coordination by four chemically distinct donor atoms, as similarly noted by (Prasad *et al.*, 2008).

When comparing the chemical shifts of complexes **40** and **30**, the proton signals in **40** appear slightly upfield, suggesting a greater shielding effect. This behaviour is likely influenced by the electron-donating effect of the methyl groups on the pzn-pdzn rings, which enhance electron density within the ligand system and mitigate deshielding effects upon coordination to the metal centre. Beyond the aromatic region, complex **40** exhibits a singlet between δ 2.64 and 2.78 ppm, attributed to methyl protons on the coordinated heterocyclic ligands. Additional features include two doublets at δ 1.05 ppm, corresponding to the diastereotopic methyl groups of the isopropyl substituent, a multiplet near δ 2.17 ppm assigned to the methine proton of the isopropyl unit, and another singlet at δ 2.17 ppm, indicative of the methyl protons on the p-cymene ring.

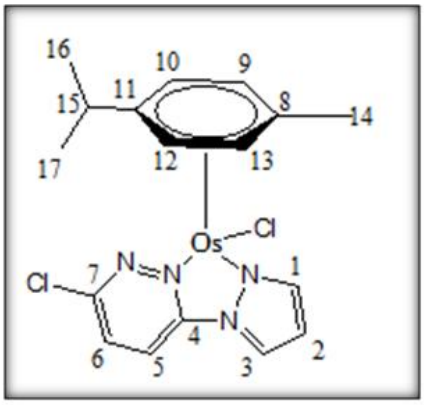

Figure 4.13: Carbon number system for **30**

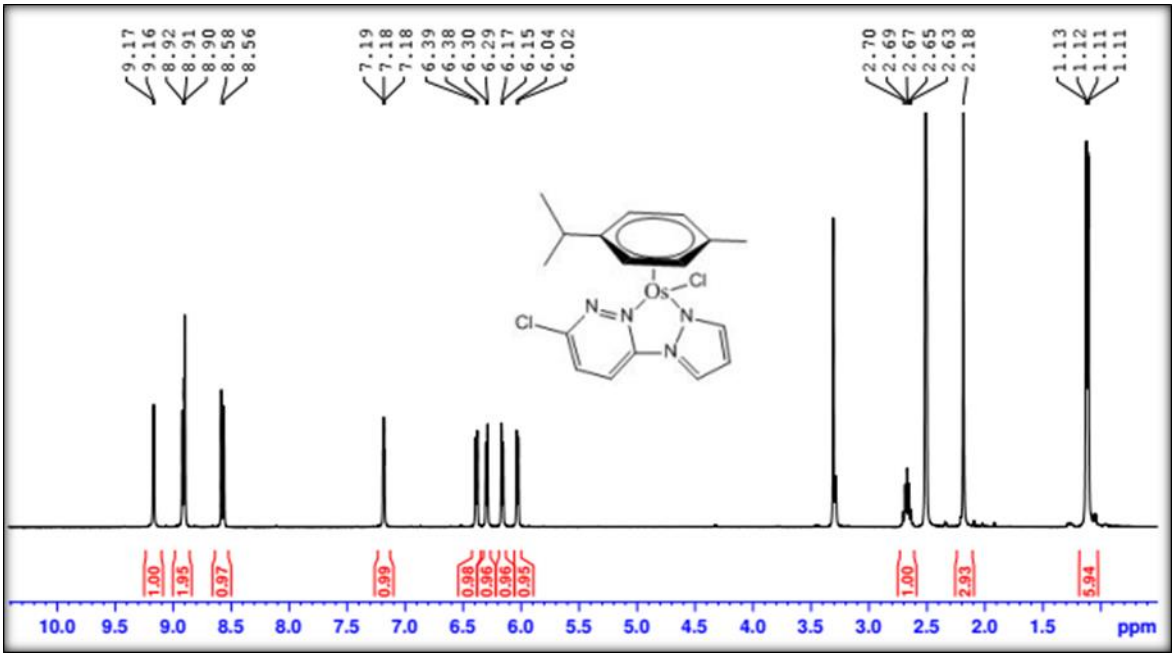

Figure 4.14: ^{1}H NMR spectrum (500 MHz, DMSO-d_6) of complex **30**

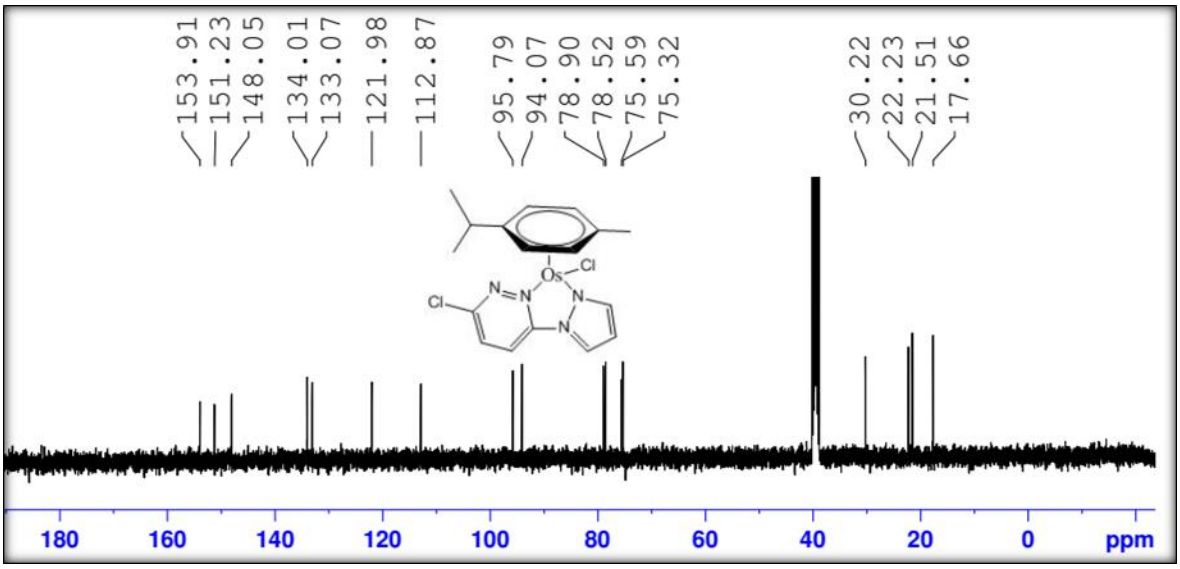

Figure 4.15: ^{13}C NMR spectrum (100 MHz, DMSO-d_6) of complex **30**

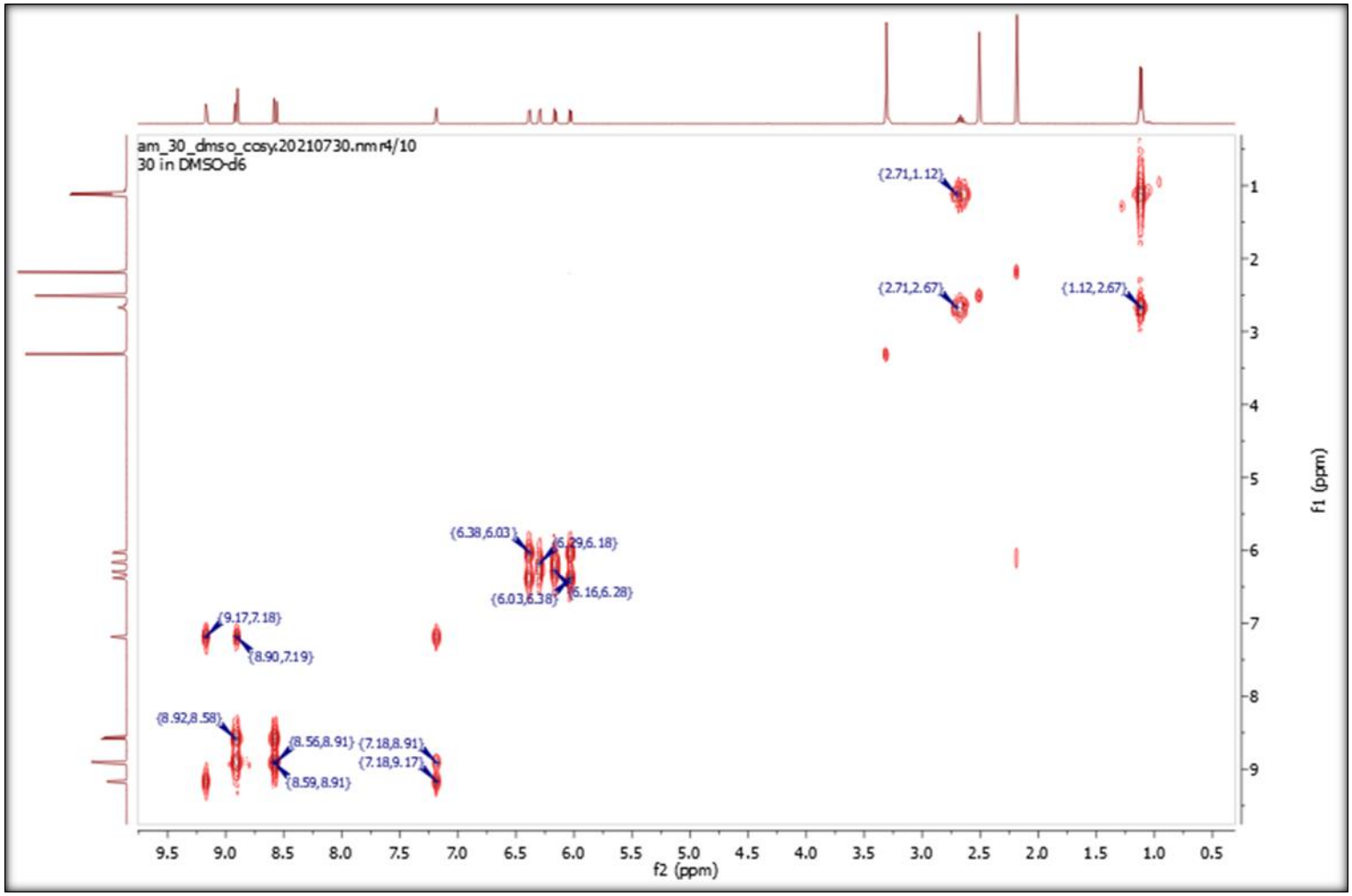

Figure 4.16: ^{1}H–^{1}H COSY Spectrum of Complex **30**

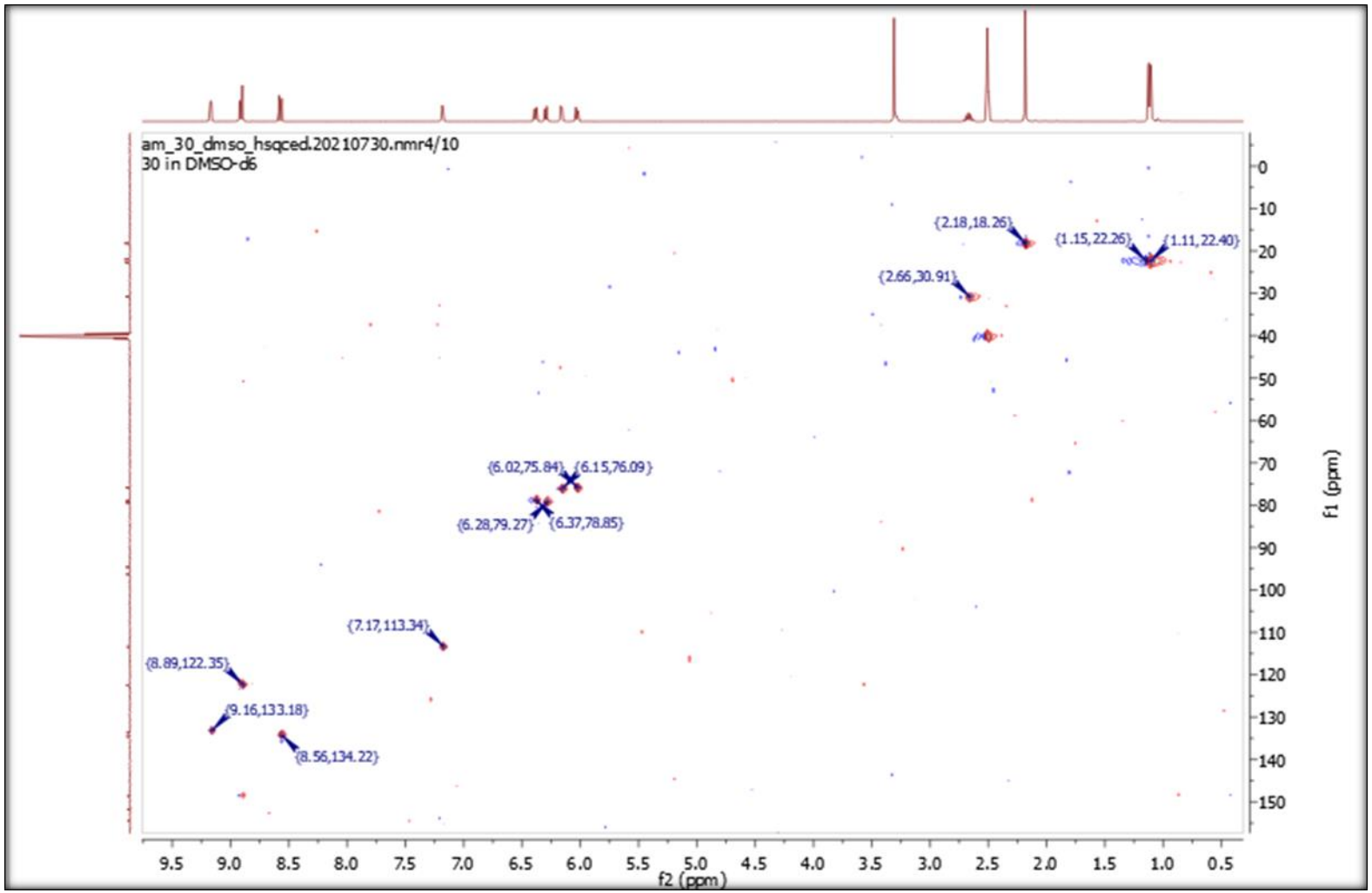

Figure 4.17: ^{1}H–^{13}C HSQC Spectrum of Complex **30**

Table 4.7: 2D NMR (HSQC and COSY) data for complex **30**

	HSQC (see Figure 4.17**)**		**COSY** (see Figure 4.16)	
Carbon Number	chemical shifts of correlated nuclei		chemical shifts (splitting pattern, and ^{3}J coupling constants, Hz) of the correlated nuclei	
	^{3}C (ppm)	^{1}H (ppm)	F1 ^{1}H (ppm)	F2 ^{1}H (ppm)
14	18.26	2.18		
15	22.26	1.15	1.12 (dd, 6.9)	2.71 (p; 6.9)
17	22.40	1.11		
16	30.91	2.66	2.67 (p; 6.9)	1.12 (dd, 6.9)
12	75.84	6.02	6.03 (d; 5.7)	6.38 (d; 5.7)
10	76.09	6.15	6.18 (d; 5.9)	6.29 (d; 5.9)
13	78.85	6.37	6.28 (d; 5.9)	6.16 (d; 5.9)
9	79.27	6.28	6.38 (d; 5.7)	6.03 (d; 5.7)
11	94.60			
8	96.32			
2	113.34	7.17	7.18 (dd, 3.2, 2.2)	9.17 (d; 3.2)
5	122.35	8.89	8.91 (m)	8.56 (d; 9.3)
1	133.18	9.19	9.17 (d; 3.2)	7.18 (dd, 3.2, 2.2)
6	134.22	8.56	8.58 (d; 9.3)	8.90 (m)
3	143.58	8.91	8.91 (m)	7.18 (dd, 3.2, 2.2)
7	151.76			
4	153.5			

The FTIR spectrum of complex **10** (Figure 4.18) reveals distinct vibrational features corresponding to functional groups present in both the parent dpzm and η^6-p-cymene ligands. Key absorption bands are observed at 3131 cm^{-1} for aromatic C–H stretching and at 2945 cm^{-1} for methylene C–H vibrations. Additionally, stretching modes related to the C=N and C=C bonds appear at 1516, 1408, and 1281 cm^{-1}. Upon coordination, several of these signals—particularly those associated with the dpzm moiety—undergo notable shifts in wavenumber compared to the

spectra of the uncoordinated ligands, indicating ligand–metal interaction. These changes are most prominent near vibrational modes involving atoms close to the Os–N coordination sites (notably N1 and N4), indirectly supporting the formation of metal–ligand bonds upon coordination with Os(II). In contrast, the vibrational frequencies linked to the *p*-cymene ligand remain relatively unchanged. This limited shift may result from electron delocalisation within the aromatic ring, which stabilizes the ligand and minimises the impact of coordination on its vibrational behaviour. Additionally, the substituents on *p*-cymene are positioned far from the π-donor Os–C interaction, further reducing any perturbation in their vibrational frequencies. A sharp band observed at 1032 cm^{-1} is assigned to the stretching vibration of the BF_4^- counterion, confirming its presence in the complex. Complex **20** (Figure 4.4) has slightly higher wavenumber values than **10**; this may be due to the influence of methyl substitution on the pyrazole ligand. For example, ν_{B-F} (1053 cm^{-1}), $\nu_{C=N}$ (1556 cm^{-1}) and, $\nu_{C=C}$ (1423, 1290cm^{-1}).

As illustrated in Figure 4.82, the FTIR profile of complex **40** exhibits distinct shifts in the vibrational frequencies of the coordinated N,N' bidentate ligand pzn-pdzn ligands compared to their metal-free counterparts. These frequency shifts provide clear evidence of ligand coordination to the Os(II) centre. Prominent absorption bands in the spectrum can be ascribed to the coordinated pzn-pdzn ligands, the η^6-*p*-cymene ring, and the BF_4^- anion, each contributing characteristic vibrational signals. For example, C–H stretching vibrations appear as weak bands at 3103 cm^{-1} and 2977 cm^{-1}, corresponding to aromatic and aliphatic stretches, respectively. A medium-intensity band at 1578 cm^{-1} reflects the stretching frequency associated with the C=N moiety of the pyrazolyl/pyridazine rings, confirming their involvement in metal coordination. The *p*-cymene ligand shows two strong absorptions at 1479 cm^{-1} and 1404 cm^{-1}, consistent with C=C ring stretching vibrations. Additionally, sharp bands within the 1200–1400 cm^{-1} region are associated with asymmetric C=C stretching modes from the pzn-pdzn ligand framework. A strong absorption band observed at 1042 cm^{-1} is associated with the B–F stretching vibration of the BF_4^- anion, indicating its presence in the complex. Below 800 cm^{-1}, multiple medium-intensity bands are observed, which can be assigned to metal–ligand vibrational modes, including Os–C, Os–N(pzn/pdzn), and Os–Cl stretches. These low-frequency vibrations fall within expected ranges reported for structurally similar Os(II) complexes (Peacock *et al.*, 2007), further supporting the proposed coordination environment in complex **40**.

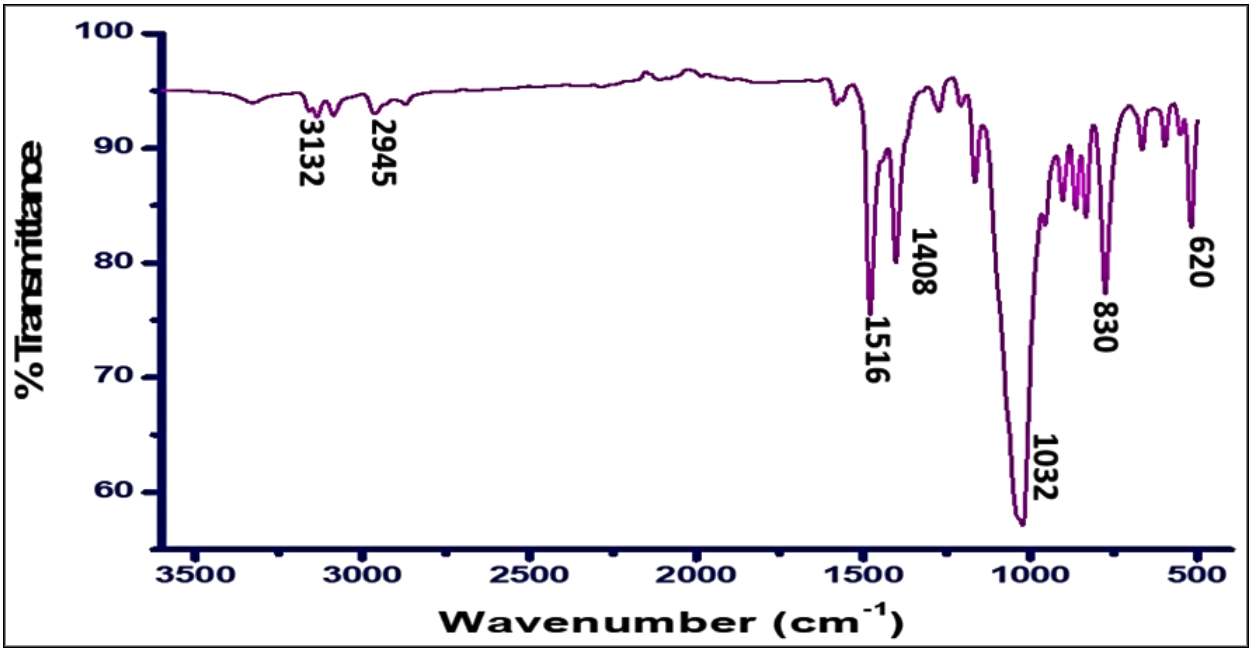

Figure 4.18: FTIR spectrum of complex **10** (KBr pellet method)

The electronic absorption spectrum of complex **10** (Figure 4.19) displays a prominent band in the ultraviolet region, below 300 nm. This feature is indicative of π–π* transitions, which are commonly associated with the aromatic rings present in the coordinated ligands. A less intense shoulder near 350 nm suggests the presence of n–π* transitions, likely originating from non-bonding electrons on heteroatoms such as nitrogen in the pyrazole-pyridazine framework. A broad, low-intensity band spanning the 350–500 nm region is a characteristic of a MCLT (metal-to-ligand charge transfer) process. This feature is commonly observed in arene-based organometallic compounds incorporating Os^{2+} and Ru^{2+} centres, as previously described by (Vajpayee *et al.*, 2011). Altogether, the spectral profile of complex **10** reflects typical behaviour of nitrogen-donor ligand complexes**,** where ligand-centred π–π* transitions dominate the ultraviolet region, while MLCT absorptions appear at longer wavelengths in the visible range, confirming the coordination and electronic characteristics expected for this class of compounds.

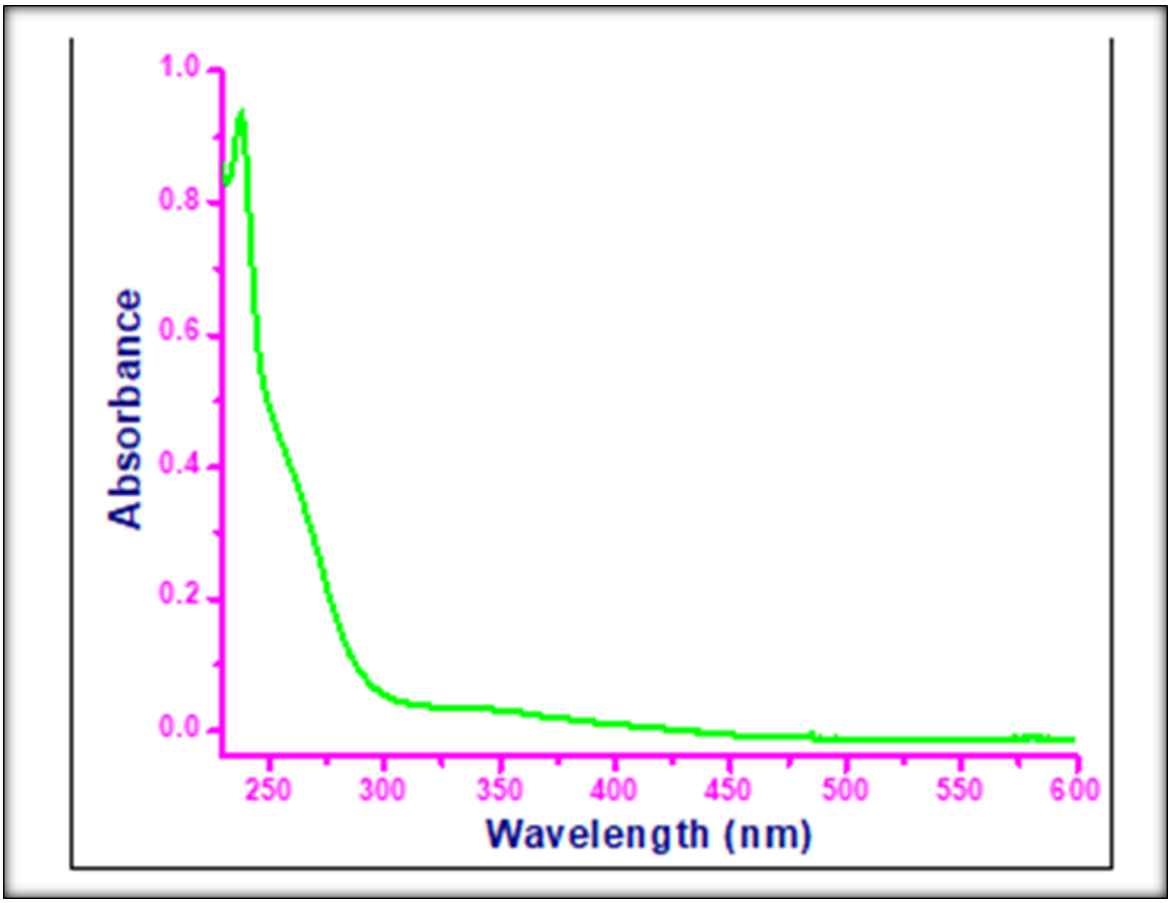

Figure 4.19: UV-Vis absorption spectrum of complex **10** in methanol (1.0×10^{-5} M)

ESI mass spectrometry was employed to confirm the molecular compositions of complexes **10** through **40**. The measurements were carried out using methanolic solutions buffered with 0.1% formic acid/formate, delivered *via* direct electro-spray ionization. The resulting low-resolution mass spectra displayed prominent peaks at m/z 509, 564, 541, and 569 for complexes **10, 20, 30**, and **40**, respectively (Figures 4.8, 4.20, and 4.21). Each of these peaks appeared with 100% relative intensity, indicating they represent the most stable ionized species under the experimental conditions. These *m/z* values correspond to the expected pseudo-protonated molecular ions: $[C_{17}H_{22}ClN_4Os+2H]^+$ (for **10**), $[C_{21}H_{30}ClN_4Os+H]^+$ (for **20**), $[C_{17}H_{19}ClN_4OsCl+2H]^+$ (for **30**), and $[C_{19}H_{24}ClN_4OsCl+H]^+$ (for **40**). The isotopic patterns observed in the expanded views of each spectrum closely matched the theoretically calculated distributions for their respective molecular formulas, as illustrated in the inset panels of the figures. This high level of agreement between experimental and predicted isotopic fingerprints

provides strong confirmation of both the molecular identity and successful synthesis of the Os(II) complexes.

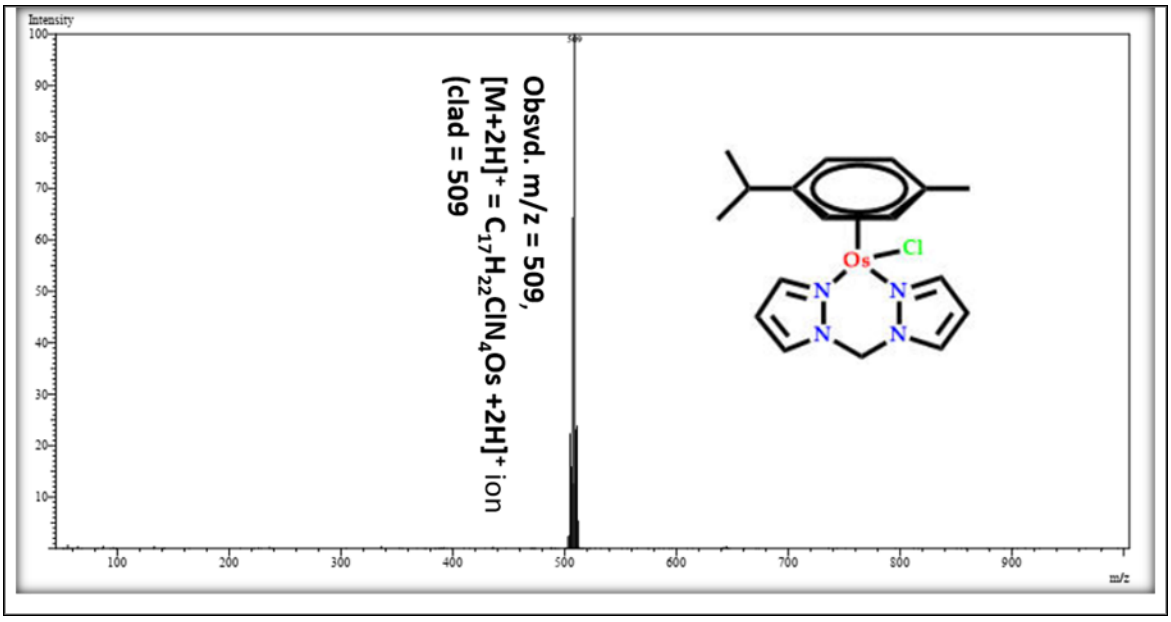

(a)

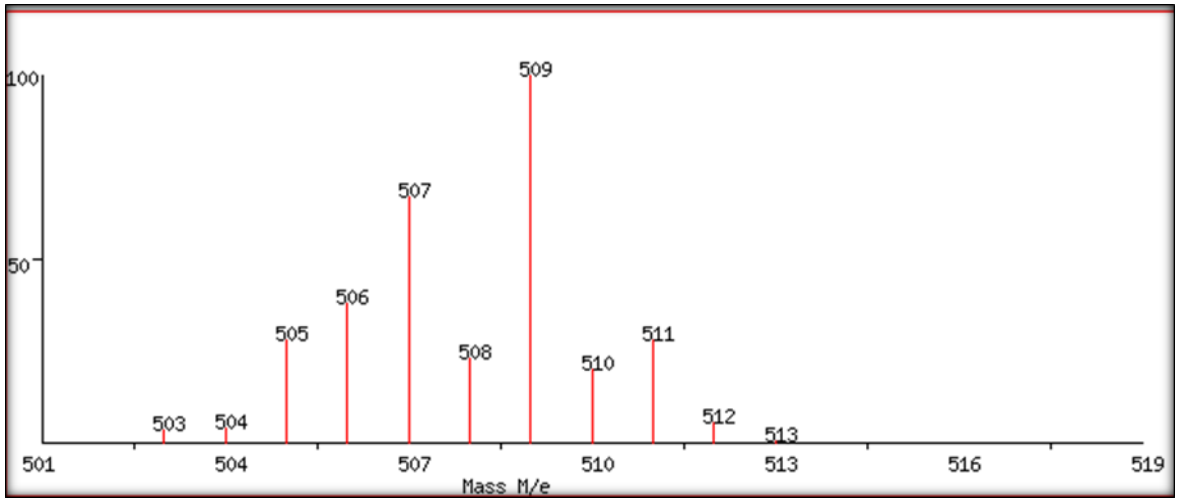

(b)

Figure 4.20: Mass spectrometric analysis of complex **10**

(a) Low-resolution mass spectrum of complex 10 showing the pseudo-molecular ion peak at m/z = 509, corresponding to the protonated species $[C_{17}H_{22}ClN_4Os+2H]^+$ (100% intensity). (b) Predicted isotopic distribution pattern of complex **10** generated using the SIS isotope distribution calculator (accessed December 13, 2024; https://www.sisweb.com/mstools/isotope.htm).

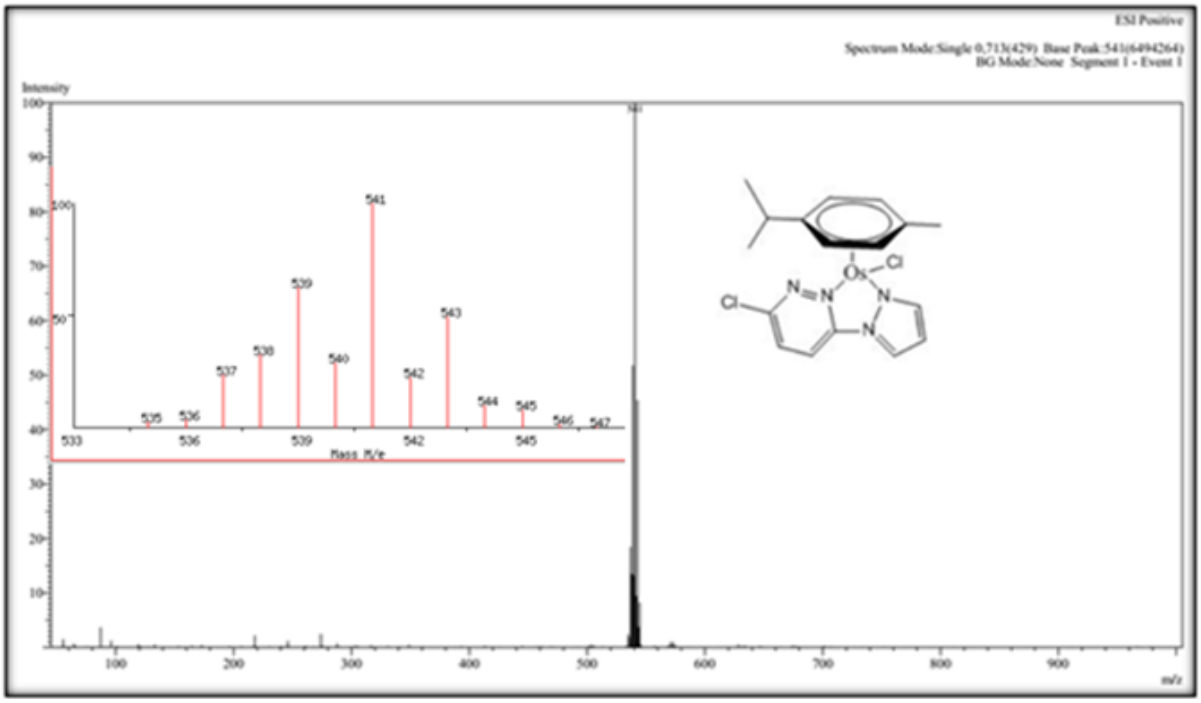

Figure 4.21: Mass spectrometric analysis of complex **30**

Low-resolution mass spectrum of complex **30** showing the pseudo-molecular ion peak at m/z = 541 (100%), corresponding to the protonated species $[C_{17}H_{19}ClN_4OsCl+2H]^+$. Inset: Predicted isotopic distribution pattern generated using the SIS isotope distribution calculator (accessed December 13, 2024; https://www.sisweb.com/mstools/isotope.htm).

The experimental elemental (CHN) data of the complexes were in agreement with their calculated percentage values, as listed in the results section, Tables 4.1-4.4. The purity of the crystalline blocks of **10** - **40** was, thus confirmed. Crystallographic data of complex **10** has already been published (Mambanda *et al.*, 2022a).

The crystal blocks of **10** ($C_{17}H_{22}BClF_4N_4Os$) were further analysed by single-crystal X-ray diffraction analysis, and details are given in the experimental section. The asymmetric unit of **10** (see Figure 4.9 for a perspective) comprises an [Os(II)(dpzm(η^6-*p*-cym)Cl]$^+$ cation and a tetrafluoroborate as an anion. The cation is formed by the η^6–π-coordination of a *p-cym* and two N and Cl donor atoms to an Os(II) ion, leading to the pseudo-octahedral "three-leg piano stool" geometry (Gichumbi *et al.*, 2020; Păunescu *et al.*, 2015; Peacock *et al.*, 2007; Thangavel *et al.*, 2016; van Rijt *et al.*, 2009). For this geometry, the η^6-*p*-cymene constitutes the pseudo 'seat' of the stool and is π-bonded to Os(II) at the Os–C bond distances (Os1—(C9, C10,…..C15) ranging

from 2.161(4) to 2.214(4) Å, making a centroid (*p*-cym ring-Os1) distance of 1.671 Å. The metal centre is σ-bonded to the flexible dpzm chelate at asymmetric bond distances of 2.122(3) Å (Os1—N1) and 2.105(3) Å (Os1—N4). The chlorido co-ligand is bonded at a distance of 2.3982(9) Å (Os1—Cl1). These bond distances are close to those reported for related Os(II) complexes (Păunescu *et al.*, 2015; Schreiber *et al.*, 2013). The N1, N4, and Cl1 donor atoms are staggered relative to the carbon atoms of the cymene forming the pseudo legs of the piano-stool structure. The bond angles (∠s) are typical of octahedral half-sandwiches bearing flexible N, N-bidentate chelates and are 83.83(9)° (∠N1—Os1—Cl1), 83.17(12) (∠N1—Os1—N4) and 84.71(9)° (∠ N4—Os1—Cl1). They do not differ by more than 8° from 90° for an ideal octahedral geometry. However, the flexibility foisted by the methylene carbon of the chelate makes the N1—Os1—N4 angle significantly larger than those of other complexes chelated by rigid and aromatic N, N-ligands. All C—C, C—N, and B—F bond lengths and associated angles are in the expected ranges for N, N/*O*-chelated *p*-cym ring Os(II) complexes (Schreiber *et al.*, 2013).

When viewed along the *b*-axis (see Figures 4.10 and 4.22), the cations of **10** are packed as complementary columnar duets along the *c*-axis and are stabilized by Cl1…..H1—C (2.640 Å) short contacts. As shown in Figure 4.22, these dimeric stacks are together through bridged tetra-furcated short-range interactions involving the fluorine and boron atoms of the tetrafluoroborate anions as hydrogen bond donors and acceptors, respectively. The quadruped and short range-interactions are the F1…..H13—C13 (2.636Å); F3…..H14—C13 (2.481Å); F4…..H8—C8 (2.235 Å) and C5 (π edge)…..B1 (3.574 Å). Numerous other short contacts further stabilised these cationic columns into a stable 3D structure.

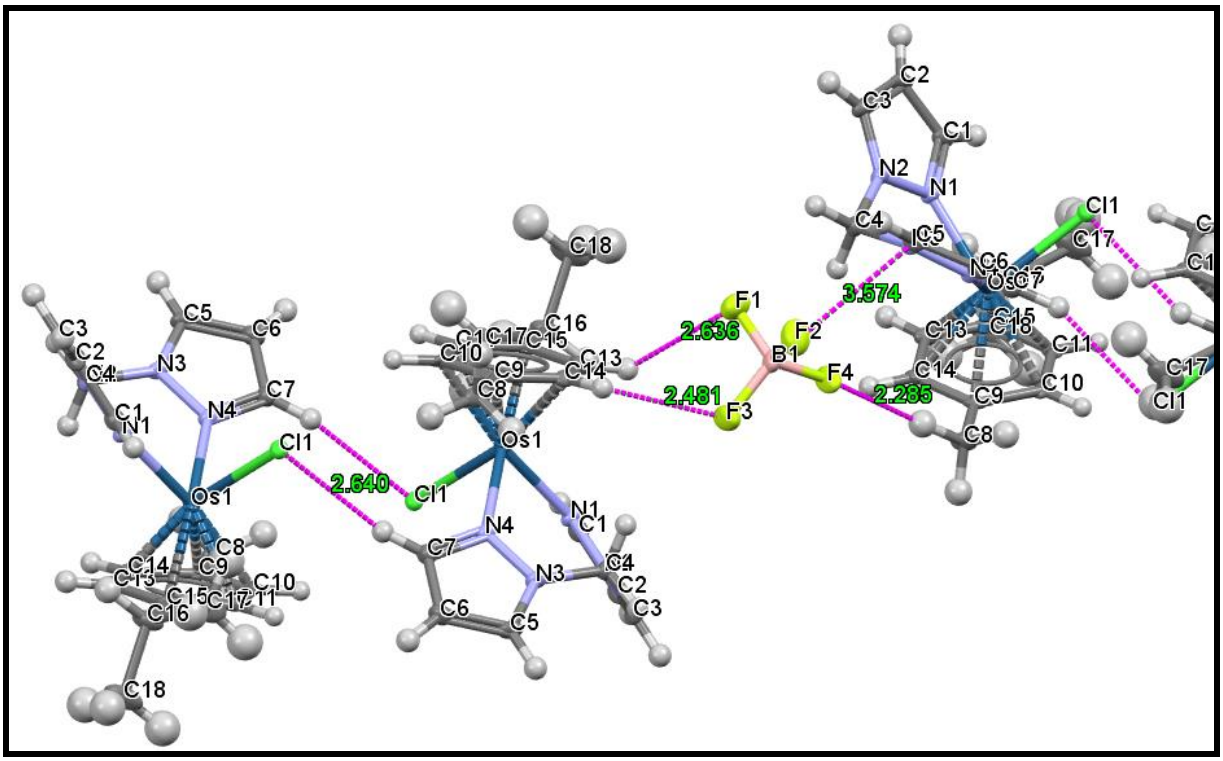

Figure 4.22: A view along the *b*-axis, showing the 1D-short contacts that support the columnar stacking of dimers of **10** ($C_{17}H_{22}BClF_4N_4Os$), projected along the *ab*-plane.

Computational modelling was undertaken using DFT methods for complex **10** to further explore its electronic structure and optimised molecular geometry. The fully optimised ground-state structure, calculated in methanol as the solvent, is summarised in Table 4.9, with key geometric parameters highlighted in Tables 4.8 and 4.10. In this complex, the N,N'-donor pyrazolyl–pyridazine (pzn-pdzn) ligand chelates the Os(II) centre through two nitrogen atoms, generating a six-membered metallacyclic ring. The structural flexibility of the heteroaryl backbone permits the ring to adopt non-planar conformations, accommodating minor distortions without compromising coordination stability. The *p*-cymene moiety, coordinated in an η^6-fashion, along with a chlorido ligand, completes the coordination framework exhibits a pseudo-octahedral configuration about the metal ion. However, subtle deviations from ideal octahedral geometry arise due to ligand asymmetry and steric factors within the coordination sphere.

Frontier molecular orbital (FMO) analysis of complex **10** reveals distinct patterns of electron delocalisation across the molecule's key components (Table 4.9). A major portion of the

electron density in the HOMOs is centred around the Os(II) metal centre, the η^6-bound arene ring, and one of the pyrazole units within the coordinated bidentate ligand. Meanwhile, the lowest unoccupied molecular orbitals (LUMOs) show partial delocalisation across the metal centre, the arene ring, and—more weakly—over one of the pyrazole rings. This distribution suggests that the metal centre can participate in limited π-backbonding interactions, particularly toward the π*-orbitals of the arene and the proximal pyrazole unit. However, the overlap with the ligand's π*-system is minimal, indicating a weak back-donation interaction, consistent with expectations for osmium(II) arene complexes.

These electronic features correlate well with the UV–visible spectral data, which also reflect transitions characteristic of ligand-centre and MLCT-type electronic transitions. The nature of the HOMO–LUMO distribution supports the idea that coordination influences are localised and directional, supporting the observed stability and reactivity patterns of complex **10**.

Table 4.8: Comparative analysis of selected geometric parameters from DFT optimization and single-crystal X-ray data for complex **10**

Bond lengths	DFT (Theoretical)	Cryst.	%RE
Os-‡ Cl	2.4680	2.3982	2.9
Os-$C_{Cym(centroid)}$	1.7930	1.6710	7.3
Os-N1	2.0881	2.1215	1.5
Os-N4	2.0853	2.1046	0.9

Theoret. = DFT-calculated data; Cryst = crystal data taken as accurate data; percentage relative error (RE %) = {(DFT Theoret. - Cryst)/Cryst}*100.

An overlay comparison between the DFT-optimized geometry of complex **10** (in methanol) and its experimentally determined X-ray crystal structure demonstrates strong structural agreement, with a root-mean-square deviation (RMSD) of approximately 2%. Superimposed views of the structures are shown in Table 4.9 (first column), clearly showing the geometric congruence between the theoretical and solid-state models. Key geometric descriptors—such as bond distances, angular orientations, and metal–ligand coordination lengths—derived from DFT optimization show excellent agreement with crystallographic data,

differing by less than 10%. This close correlation confirms the reliability of the theoretical models in reproducing the experimentally observed molecular structures (see Appendix Tables a–c). This high level of consistency underscores the reliability of the theoretical approach used to model the complex and validates the computational methods applied to evaluate its electronic and geometric features.

Table 4.9: Structural overlays and frontier molecular orbital (HOMO–LUMO) electron density maps for complexes **10** (Os) and **1** (Ru)

	DFT-Optimized (Blue); Crystal Structure (Red)	HOMO	LUMO
10	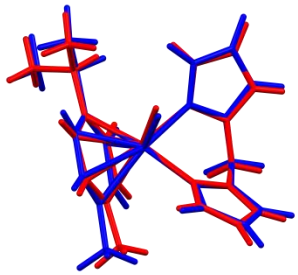	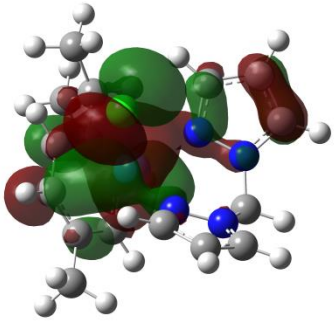	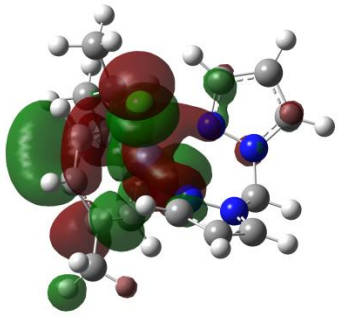
1	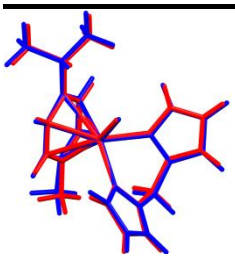	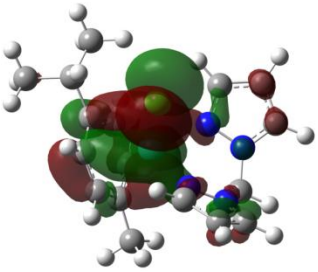	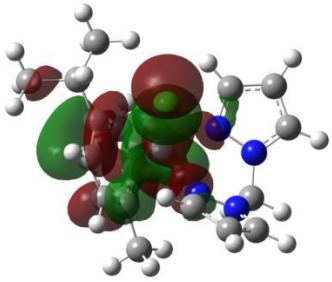

Table 4.10: DFT-calculated electronic and geometric parameters for complexes **10** and **1**

Parameter	**10 (Os)**	**1 (Ru)**
HOMO-LUMO energy/eV		
−(LUMO), eV	1.671	2.330
−(HOMO), eV	6.323	6.398
Band gap, ΔE, eV	4.652	4.069
Global electrochemical parameter		
Chemical hardness (η)	2.326	2.034

Chemical potential (μ)	−3.997	−4.364
Chemical softness (σ)	0.430	0.492
Electronegativity (χ)	4.702	4.838
Electrophilicity index (ω)	3.435	4.681
Nucleophilicity (ε)	0.291	0.214
Dipole moments	7.953	7.8202
(NBO) charge		
Ru/Os	+0.004	-0.032
Cl	−0.297	−0.299
N1	−0.251	−0.237
N4	−0.254	−0.235

The ruthenium(II) complex (**1**) was included in Table 4.10 for comparative purposes, as it is structurally analogous to complex **10**, with the only difference being the metal centre (Ru *vs.* Os).

From the NBOs charges (Table 4.10), the effective charge on the Os(II) > Ru(II), these findings indicate that the overall charge distribution within the complexes is influenced by both the identity of the central metal ion and the electronic characteristics of the N,N'-bidentate ligand substituents. However, it is the electrophilicity indices that determine reactivity, not the charge on the metal (Wekesa & Jaganyi, 2014). The calculated electrophilicity indices follow the trend Ru(II) > Os(II), indicating that the ruthenium(II) centre exhibits greater reactivity compared to its osmium(II) counterpart. The Ru(II) complex has a lower HOMO-LUMO energy gap, which renders it more reactive (Dhariyal *et al.,* 2023). The DFT findings suggest that the Ru(II) analogue exhibits a higher electrophilic character, making it more receptive to nucleophilic attack**.** This increased ability to accept electron density promotes π-backdonation**,** particularly between the metal centre and the coordinated ligands. It is evident from the results that the metal centre's electronic configuration is a critical factor in determining the complex's chemical behaviour and charge distribution, highlighting its influence on ligand–metal interactions and potential biological or catalytic behaviour.

4.2 Half Sandwich η^6-Arene Ruthenium(II) Complexes with Bis(pyrazol-1-yl)methane Ligands

Complexes **1, 2, 6,** and **7**, as shown in Figure 4.23, are a class of half-sandwich ruthenium(II) compounds characterised by an η^6-coordinated arene ligand—either *p*-cymene or toluene—serving as the "cap" of the piano-stool architecture. These complexes incorporate N,N'-bidentate bis(pyrazol-1-yl)methane ligands, which possess either hydrogen or methyl groups as substituents on the pyrazole rings. The variation in both the arene moiety and the substituents on the bidentate ligand provides structural diversity and offers insights into how such modifications influence the coordination behaviour, electronic environment, and overall physicochemical properties of the Ru(II) centre.

4.2.1 Syntheses and Spectral Data for the Complexes

The [(*p*-cymene/toluene)Ru(N,N')Cl]BF_4 derivatives corresponding to complexes **1, 2, 6,** and **7** were successfully synthesised, as illustrated in Figure 4.23. Well-defined single crystals appropriate for X-ray crystallographic analysis were obtained by allowing slow vapour diffusion to proceed over a period of 1 to 2 weeks from methanol/diethyl ether solutions of the respective complexes. These complexes were isolated as orange-coloured solids, with yields ranging from 40% to 82%.

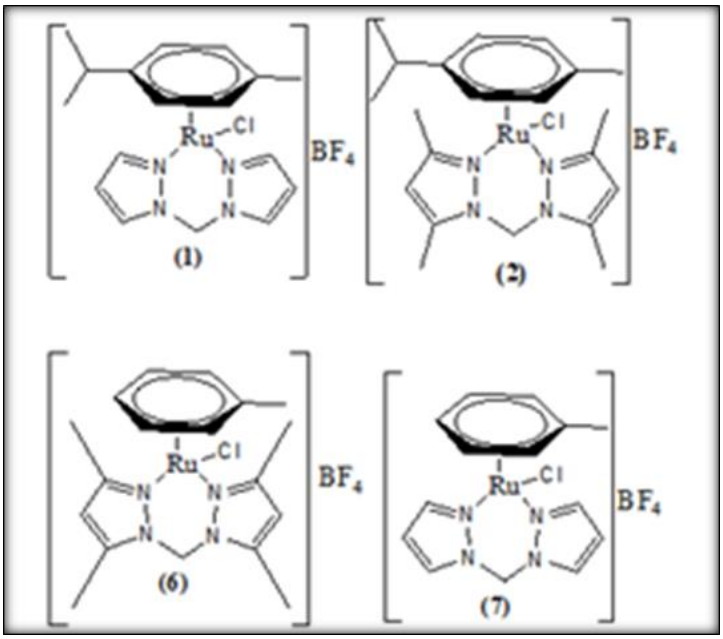

Figure 4.23: Chemical structures of the η6-arene ruthenium(II) complexes bearing bis(pyrazol-1-yl)methane ligands.

The identity and structure of the synthesised complexes were validated through a comprehensive set of characterisation techniques, such as NMR spectroscopy, elemental analysis, FTIR, UV–Visible spectroscopy, and mass spectrometry. The corresponding analytical data are compiled and summarised in Tables 4.11 to 4.14.

[(η^6-*p*-cymene)(bis(pyrazol-1-yl)methane)Ru(Cl)]BF_4, [RudpzmcymCl]BF_4 (1):

Complex **1**, denoted as [(η^6-*p*-cymene)(bis(pyrazol-1-yl)methane)Ru(Cl)]BF_4, was synthesised by reacting 674 mg of the dimeric precursor [(η^6-*p*-cymene)Ru(μ-Cl)(Cl)]$_2$ with 326 mg of dpzm in the presence of 2.5 mmol of NH_4BF_4. The reaction afforded orange crystalline solids in 40% yield.

Table 4.11: Analytical data for [(η^6-*p*-cymene)(bis(pyrazol-1-yl)methane)Ru(Cl)]BF_4 (**1**)

Technique	**Data**
Yield	40%, orange crystalline solid
MS (ESI^+)	m/z = 419 (100%), $[C_{17}H_{22}ClN_4Ru+H]^+$
^1H NMR (500 MHz, DMSO-d_6)	δ (ppm): 8.22 (d, J = 2.1 Hz, 2H, pzm), 8.00 (d, J = 2.1 Hz, 2H', pzm), 7.07 (d, J = 14.4 Hz, 1H, pzm), 6.63 (t, J = 2.6 Hz, 2H, pzm), 6.25, 5.95 (d, J = 5.6, 5.7 Hz, 4H, Ar–*p-cym*), 6.08 (d, J = 14.4 Hz, 1H, pzm), 2.85 (septet, J = 6.9 Hz, 1H, CH–isopropyl, *p-cym*), 2.02 (s, 3H, CH_3, *p-cym*), 1.23 (d, J = 6.9 Hz, 6H, isopropyl CH_3, *p-cym*)
FTIR (KBr, cm^{-1})	3132 (w, ν(C–H_arom)), 2945 (w, ν(CH_2, methylene)), 1516 (m, ν(C=N)), 1408 (m, ν(C=C)), 1281 (m, β(C=C)–CH), 1038 (s, br, ν(BF_4^-))
Elemental Analysis	Calculated (%): C 40.38; H 4.38; N 11.08 Found (%): C 40.18; H 4.24; N 11.40
Figures	See Figures 4.24–4.25 for spectral data

w/m/s = weak/medium/strong intensity, shp/br =sharp/broad)

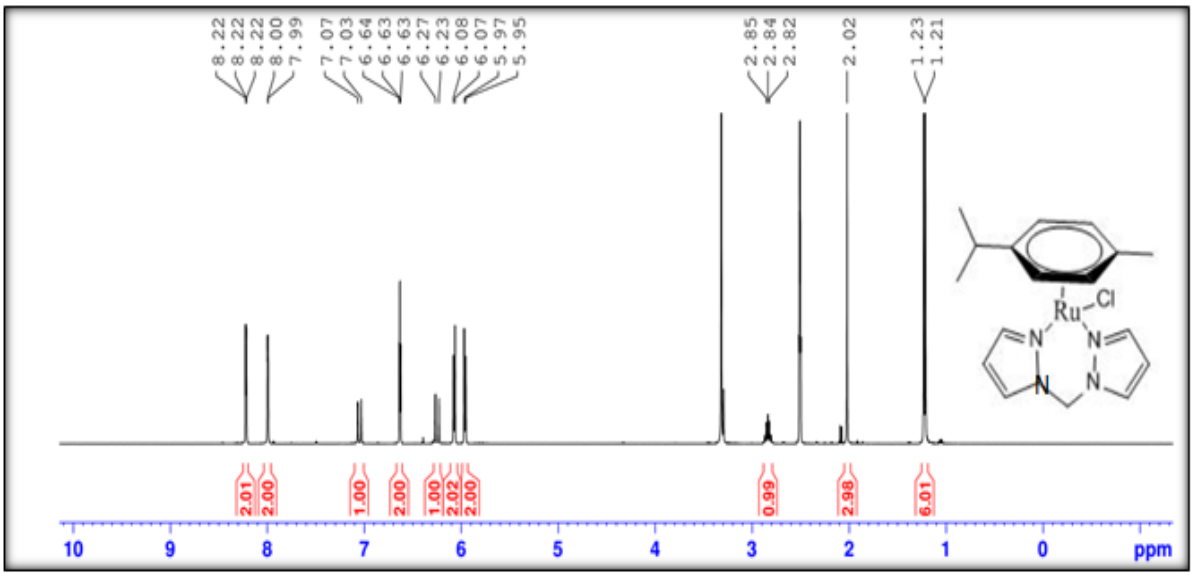

Figure 4.24: ^1H NMR spectrum (500 MHz, DMSO- d_6) of complex **1**

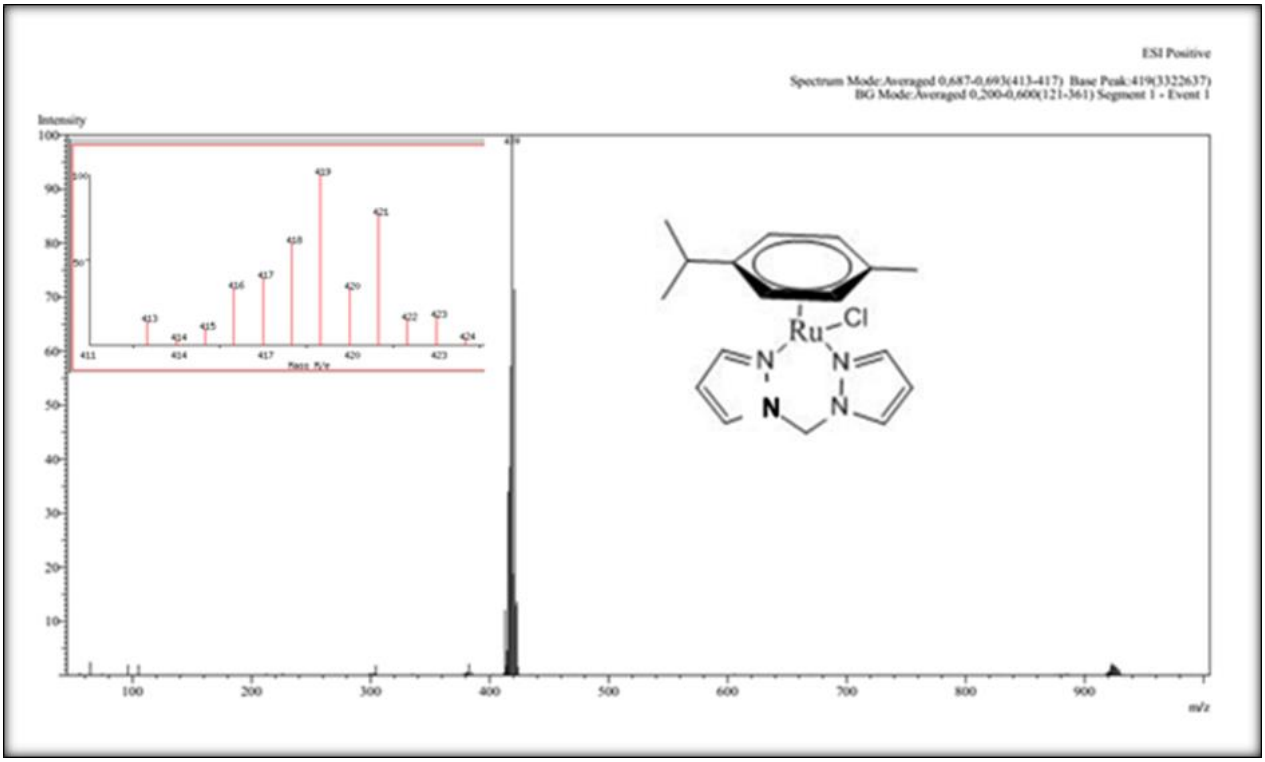

Figure 4.25: Mass spectrometric analysis of complex **1**

Low-resolution mass spectrum of complex **1** showing the pseudo-molecular ion peak at m/z = 419 (100%), corresponding to the protonated species $[C_{17}H_{22}N_4RuCl+H]^+$. Inset: Predicted isotopic distribution pattern generated using the SIS isotope distribution calculator (accessed December 13, 2024; *https://www.sisweb.com/mstools/isotope.htm*).

[(η^6-*p*-cymene)(bis(3,5-dimethylpyrazol-1-yl)methane)Ru(Cl)]BF_4, [RubdmpzmcymCl]BF_4 (2):

The complex [(η^6-*p*-cymene)(bis(3,5-dimethylpyrazol-1-yl)methane)Ru(Cl)]BF_4 was synthesised by reacting 674 mg of [(η^6-*p*-cymene)Ru(μ-Cl)(Cl)]$_2$ with 449.4 mg of bdmpzm, in the presence of an excess of 2.5 mmol NH_4BF_4. The reaction yielded an orange crystalline product in 84% yield.

Table 4.12: Analytical data for [(η^6-*p*-cymene)(bis(3,5-dimethylpyrazol-1-yl)methane)Ru(Cl)]BF_4 **(2)**

Technique	Data
Yield	84%, orange crystalline solid
MS (ESI^+)	m/z = 475 (100%), $[C_{21}H_{30}ClN_4Ru+H]^+$
^1H NMR (500 MHz, DMSO-d_6)	δ (ppm):6.52 (d, J = 15.5 Hz, 1H, pzm), 6.27 (s, 2H, pzm), 6.08, 6.00 (d, J = 6.2 Hz, 4H, Ar–*p-cym*), 5.81 (d, J = 15.5 Hz, 1H, pzm), 2.77 (d, J = 6.6 Hz, 1H, CH–isopropyl, *p-cym*), 2.48 (d, J = 9.5 Hz, 12H, CH_3–pzm), 2.23 (s, 3H, CH_3–*p-cym*), 1.09 (d, J = 6.9 Hz, 6H, isopropyl CH_3–*p-cym*)
^{13}C NMR (100 MHz, DMSO-d_6)	δ (ppm): 155.80 (C=N, pzm), 143.41 (C–N, pzm), 108.54, 106.44, 99.62 (C=C, pzm), 84.52, 81.14 (Ar, *p-cym*), 56.65 (CH_2, pzm), 30.89 (CH, isopropyl), 21.94 (CH_3, *p-cym*), 17.76 (Me_2–*p-cym*), 15.14, 10.72 (CH_3–pzm)
FTIR (KBr, cm^{-1})	3061 (w, ν(C–H_arom)), 2953 (w, ν(CH_2, methylene)), 1555 (m, ν(C=N)), 1467 (m, ν(C=C)), 1291 (m, β(C=C)–CH), 1050 (s, br, ν(BF_4^-)), 830 (m, sharp, ν(Ru–N))
Elemental Analysis	Calculated (%): C 44.89; H 5.38; N 9.97 Found (%): C 45.09; H 5.11; N 10.16
Figures	See Figures 4.26, 4.34–4.35, and 4.38 for spectral data

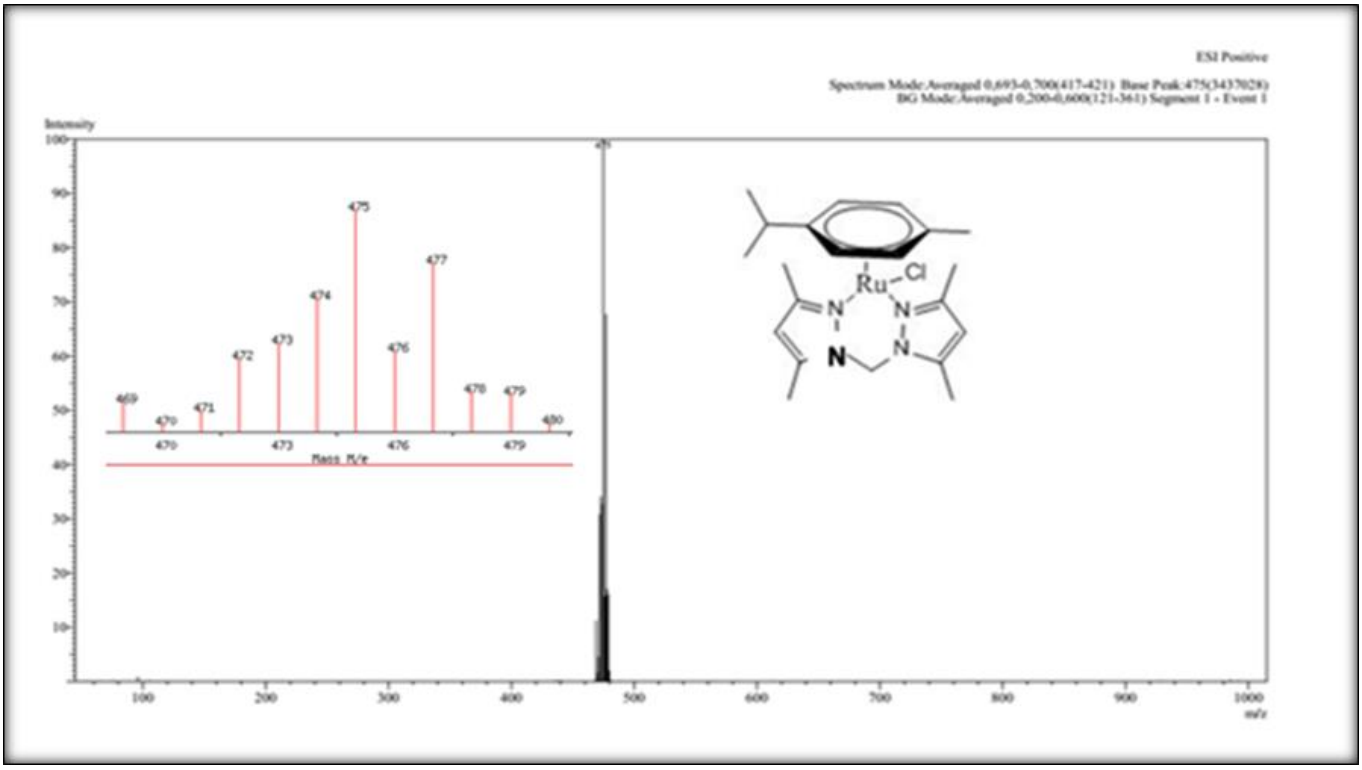

Figure 4.26: Mass Spectrometric Analysis of Complex **2**

Low-resolution mass spectrum of complex 2 showing the pseudo-molecular ion peak at m/z = 475 (100%), corresponding to the protonated species $[C_{21}H_{30}N_4RuCl+H]^+$. Inset: Predicted isotopic distribution pattern generated using the SIS Isotope Distribution Calculator (accessed December 13, 2024; https://www.sisweb.com/mstools/isotope.htm).

[(η^6-toluene)(bis(3,5-dimethylpyrazol-1-yl)methane)Ru(Cl)]BF_4, [RubdmpzmtolCl]BF_4 (6):

The complex [(η^6-toluene)(bis(3,5-dimethylpyrazol-1-yl)methane)Ru(Cl)]BF_4 was synthesised by reacting 581 mg of [(η^6-toluene)Ru(μ-Cl)(Cl)]$_2$ with 449.4 mg of bdmpzm in the presence of 2.5 mmol of NH_4BF_4. The reaction afforded an orange crystalline product in 84% yield, table 4.13.

Table 4.13: Analytical data for [(η^6-toluene)(bis(3,5-dimethylpyrazol-1-yl)methane)Ru(Cl)]BF_4 (**6**)

Technique	Data
Yield	84%, orange crystalline solid
MS (ESI^+)	m/z = 433 (100%), $[C_{18}H_{24}ClN_4Ru+H]^+$
^1H NMR (500 MHz, DMSO-d_6)	δ (ppm): 6.50 (d, J = 16 Hz, 1H, pzm), 6.26 (s, 2H, pzm), 6.18, 5.94 (d, J = 12 Hz, 4H, Ar–tol), 6.04 (d, J = 16 Hz, 1H, pzm), 2.48 (d, J = 9.5 Hz, 12H, CH_3–pzm), 2.19 (s, 3H, CH_3–tol)
^{13}C NMR (100 MHz, DMSO-d_6)	δ (ppm): 155.45 (C=N, pzm), 143.40 (C–N, pzm), 108.44 (C=C, pzm), 104.59, 81.50, 78.88 (Ar, tol), 56.88 (CH_2, pzm), 18.52 (CH_3, tol), 15.14, 10.72 (CH_3, pzm)
FTIR (KBr, cm^{-1})	3061 (w, ν(C–H_arom)), 2953 (w, ν(CH_2)), 2094, 1920, 1559 (m, ν(C=N)), 1422 (m, ν(C=C)), 1284 (m, β(C=C)–CH), 1034 (s, br, ν(BF_4^-)), 830 (m, shp, ν(Ru–N)), 620 (m, shp, ν(Ru–Cl))
Elemental Analysis	Calculated (%): C 41.60; H 4.65; N 10.78 Found (%): C 41.76; H 4.69; N 10.84
Figures	See Figures 4.27–4.29 for spectral data

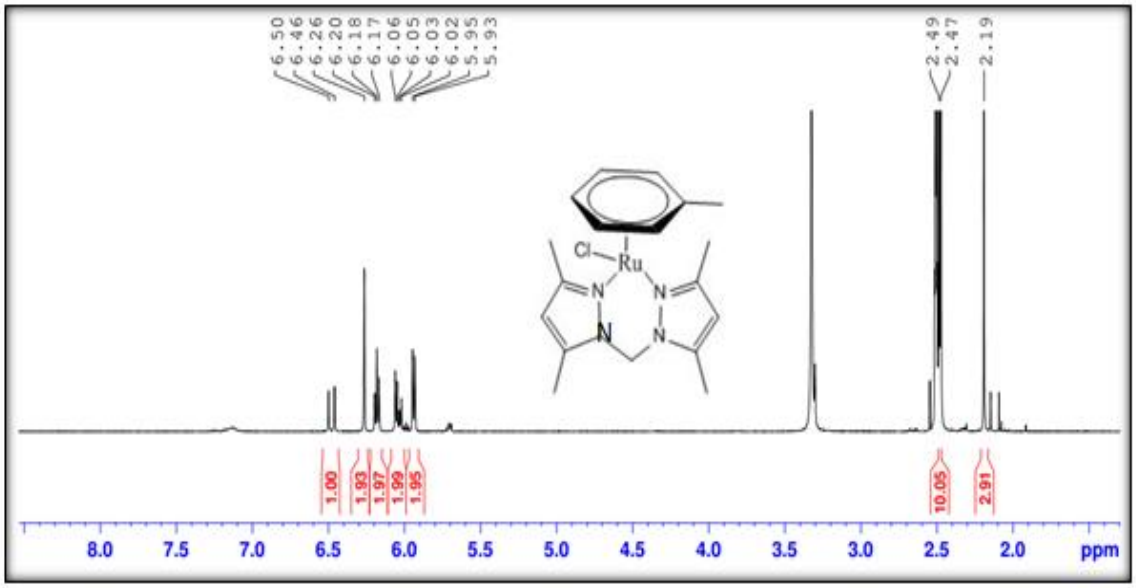

Figure 4.27: ^1H NMR spectrum (500 MHz, DMSO- d_6) of complex **6**

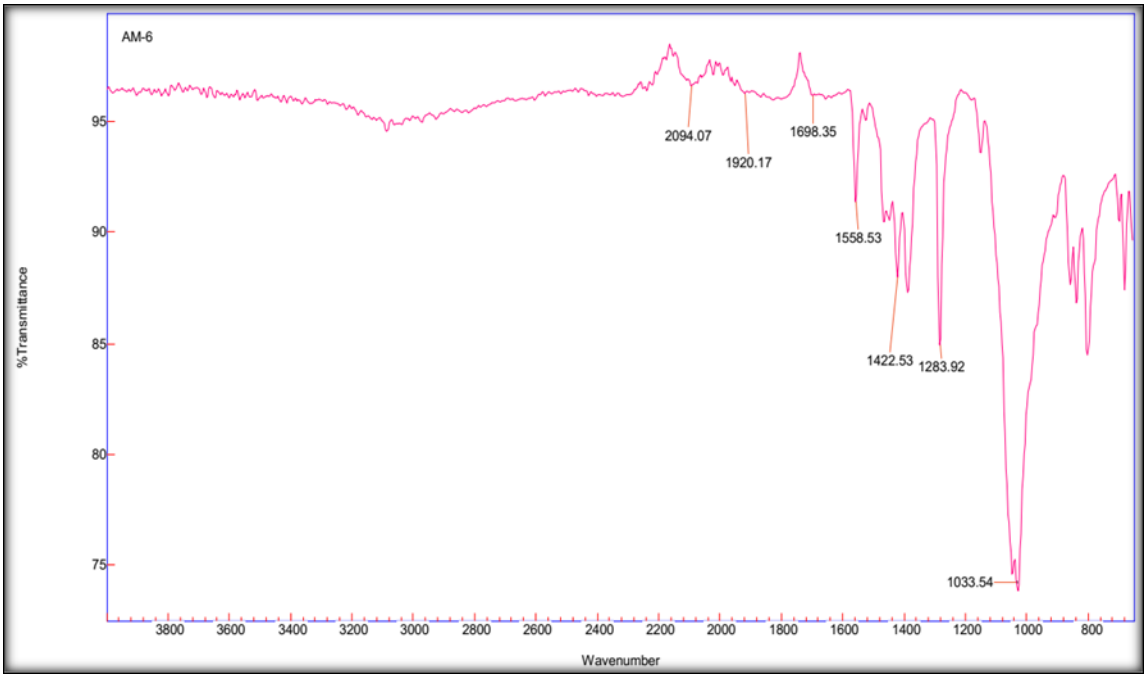

Figure 4.28: FTIR spectrum (dispersed in KBr) of complex **6**

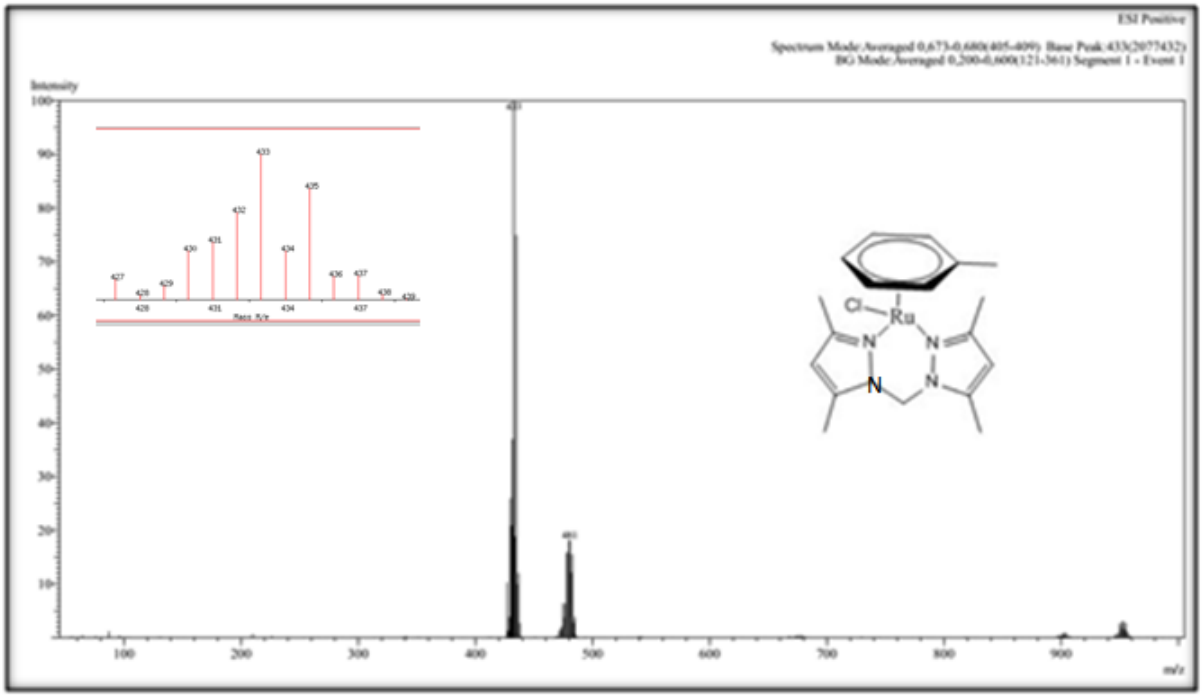

Figure 4.29: Mass spectrometric analysis of complex **6**

Low-resolution mass spectrum of complex **6** showing the pseudo-molecular ion peak at m/z = 433 (100%), corresponding to the protonated species $[C_{18}H_{24}N_4RuCl+H]^+$. Inset: Predicted

isotopic distribution pattern generated using the SIS Isotope Distribution Calculator (accessed December 13, 2024; https://www.sisweb.com/mstools/isotope.htm).

[(η^6-toluene)(bis(pyrazol-1-yl)methane)Ru(Cl)]BF_4, [RudpzmtolCl]BF_4 (7):

The complex [(η^6-toluene)(bis(pyrazol-1-yl)methane)Ru(Cl)]BF_4 was synthesised by reacting 581 mg of [(η^6-toluene)Ru(μ-Cl)(Cl)]$_2$ with 326 mg of dpzm in the presence of 2.5 mmol of NH_4BF_4. The reaction afforded orange crystalline solids in 84.1% yield, Table 4.14.

Table 4.14: Analytical data for [(η^6-toluene)(bis(pyrazol-1-yl)methane)Ru(Cl)]BF_4 (**7)**

Technique	Data
Yield	84.1%, orange crystals
MS (ESI^+)	m/z = 377 (100%), $[C_{14}H_{16}ClN_4Ru+H]^+$
^1H NMR (500 MHz, DMSO-d_6)	δ (ppm): 8.22 (d, J = 4 Hz, 2H, pzm), 8.07 (d, J = 4 Hz, 2H, pzm), 7.08 (d, J = 14.4 Hz, 1H, pzm), 6.63 (t, J = 2.3 Hz, 2H, pzm), 6.34 (d, J = 14.4 Hz, 1H, pzm), 6.14, 6.03, 5.96 (d, J = 5.6–5.9 Hz, 5H, Ar–tol), 2.12 (s, 3H, CH_3–tol)
^{13}C NMR (100 MHz, DMSO-d_6)	δ (ppm): 148.58 (C=N, pzm), 135.54 (C–N, pzm), 108.56 (C=C, pzm), 106.69, 90.26, 89.73, 85.31, 82.16, 79.72 (Ar–tol), 62.65 (CH_2, pzm), 19.05 (CH_3, tol)
FTIR (KBr, cm^{-1})	3133 (w, ν(C–H_arom)), 2945 (w, ν(CH_2)), 2109, 1516 (m, ν(C=N)), 1408 (m, ν(C=C)), 1282 (m, β(C=C)–CH), 1038 (s, br, ν(BF_4^-))
Elemental Analysis	Calculated (%): C 37.64; H 4.00; N 11.70 Found (%): C 37.50; H 3.86; N 12.08
Figures	Figures 4.30–4.33

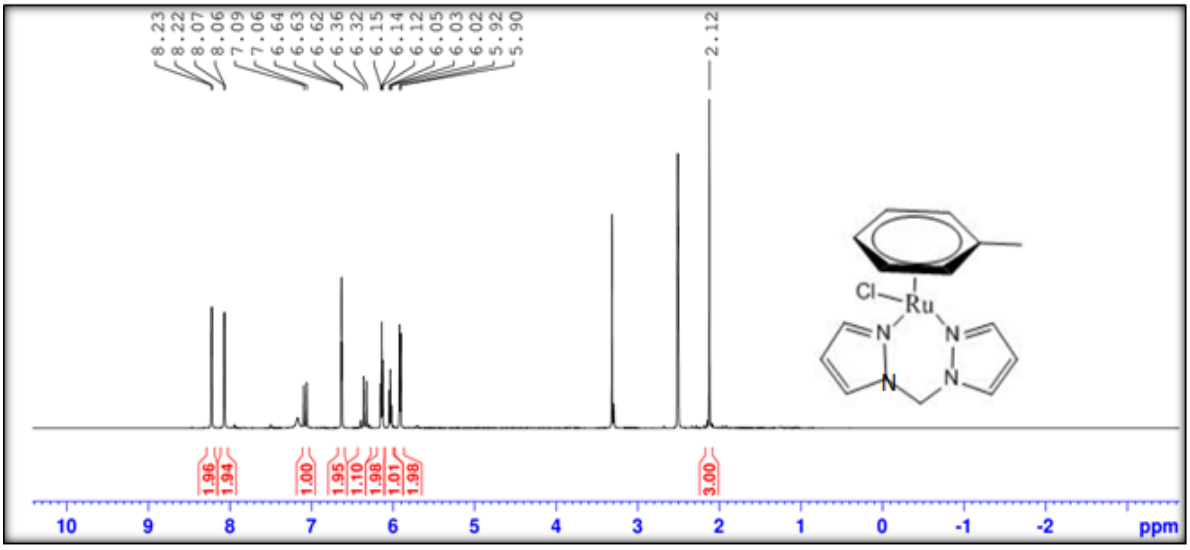

Figure 4.30: ^{1}H NMR spectrum (500 MHz, DMSO-d_6) of complex **7**

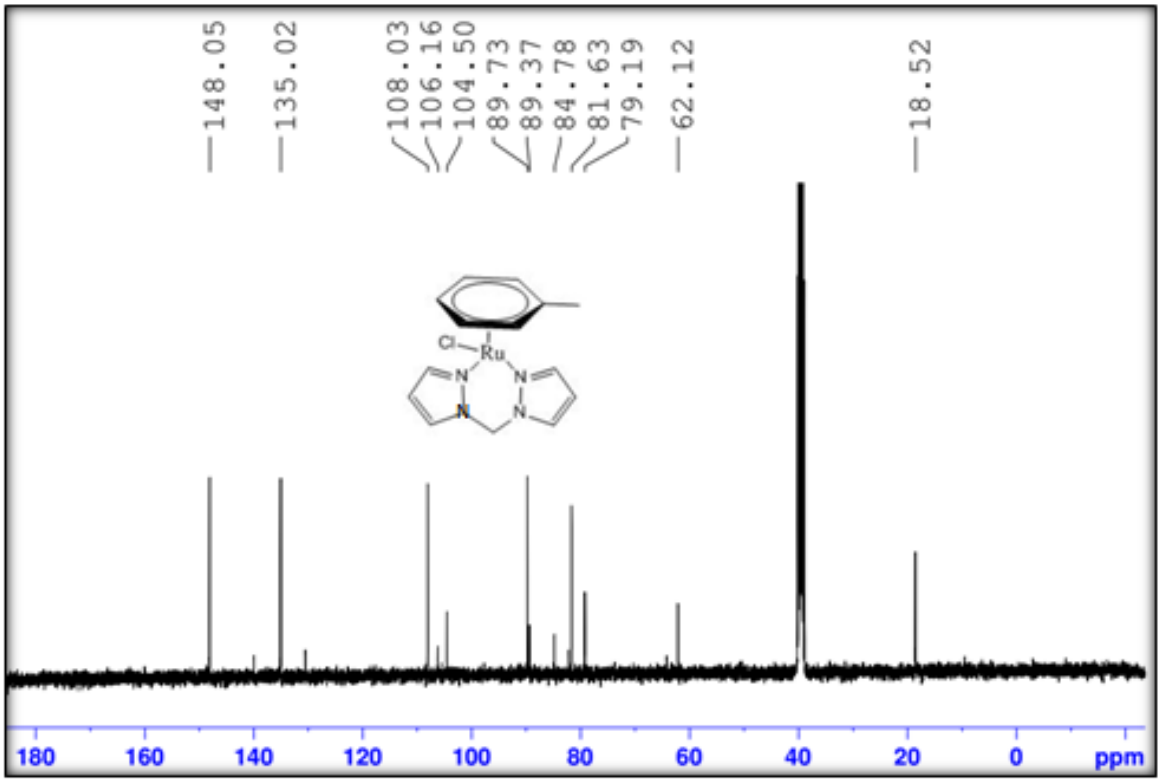

Figure 4.31: ^{13}C NMR spectrum (100 MHz, DMSO-d_6) of complex **7**

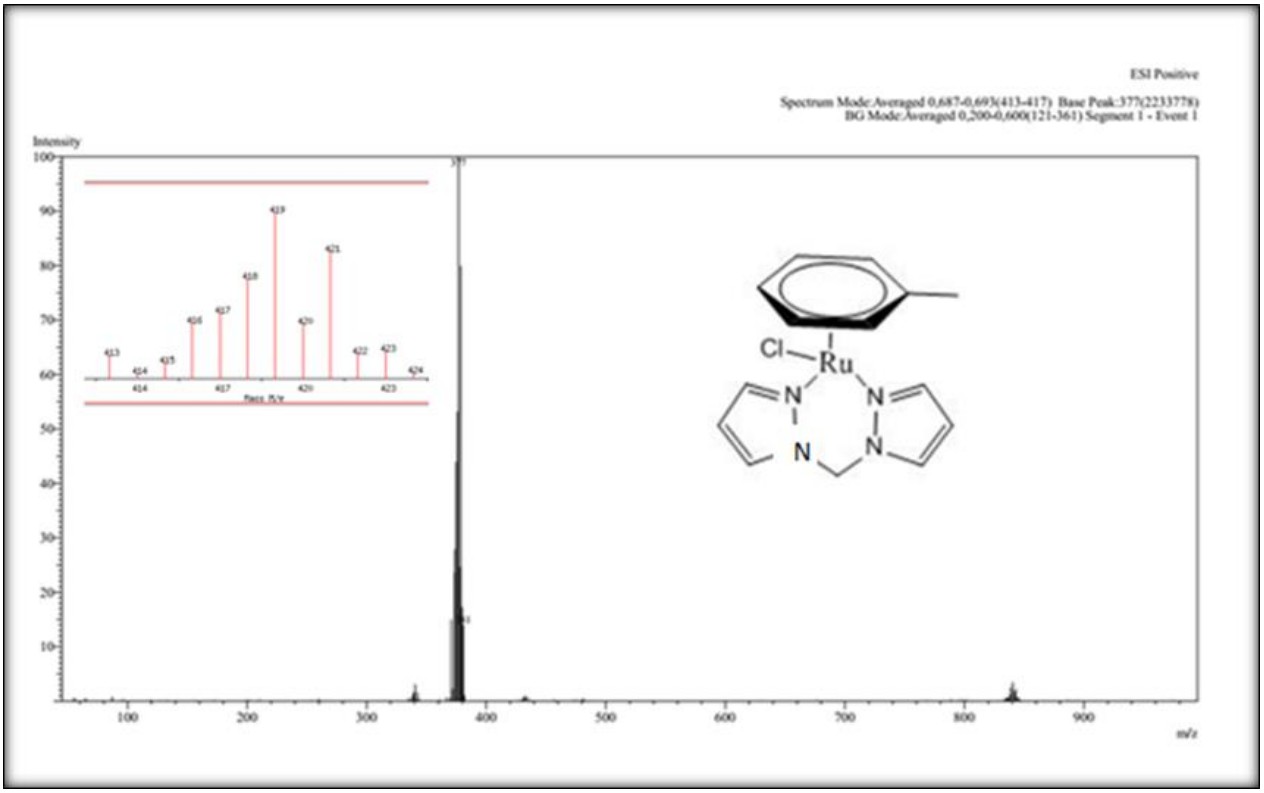

Figure 4.33: Mass Spectrometric Analysis of Complex **7**

Low-resolution mass spectrum of complex **7** showing the pseudo-molecular ion peak at m/z = 377 (100%), corresponding to the protonated species $[C_{14}H_{16}N_4RuCl+H]^+$. Inset: Predicted isotopic distribution pattern generated using the SIS isotope distribution calculator (accessed December 13, 2024; https://www.sisweb.com/mstools/isotope.htm).

4.2.2. Molecular Structures/X-ray Diffraction Studies

The solid-state structures of complexes **1, 2, 6,** and **7** were determined through single-crystal X-ray diffraction analysis. The refined crystallographic parameters, including representative bond distances and angles, are summarised in Tables 4.15 and 4.16. These data provide conclusive structural evidence and detailed information regarding the coordination environments within the complexes.

Table 4.15: Key crystallographic and refinement metrics for complexes **1, 2, 6,** and **7**

	1	**2**	**6**	**7**
Empirical formula	$C_{34}H_{44}B_2Cl_2F_8N_8Ru_2$	$C_{21}H_{30}BClF_4N_4Ru$	$C_{36}H_{48}B_2Cl_2F_8N_8Ru_2$	$C_{14}H_{16}BClF_4N_4Ru$
Colour	Orange	Orange	Orange	Yellow
Formula weight	1011.43	561.82	1039.48	463.64
Temperature/K	99.95	102.36	100.01	103.17
Crystal system	triclinic	monoclinic	triclinic	monoclinic
Space group	*P*-1	$P2_1/n$	*P*-1	$P2_1/c$
a/Å	9.9969(2)	9.7370(3)	13.0289(2)	7.0627(2)
b/Å	13.8338(3)	24.5694(7)	13.8249(2)	19.5075(5)
c/Å	14.2960(3)	9.9199(3)	14.0532(2)	12.0646(3)
α/°	87.5770(10)	90	109.4400(10)	90
β/°	89.5590(10)	99.0130(10)	115.09	96.6580(10)
γ/°	85.0700(10)	90	100.26	90
Volume/$Å^3$	1967.98(7)	2343.86(12)	2004.98(5)	1651.00(8)
Z	2	4	2	4
$\rho_{calc}g/cm^3$	1.707	1.592	1.722	1.865
μ/mm^{-1}	8.132	6.89	8	9.627
F(000)	1016	1144	1048	920
Crystal size/mm^3	0.23 × 0.17 × 0.125	0.125 × 0.105 × 0.06	0.335 × 0.205 × 0.205	0.215 × 0.075 × 0.04
Radiation	CuKα (λ = 1.54178)	CuKα (λ = 1.54178)	CuKα (λ = 1.54178)	CuKα (λ = 1.54178)
2Θ range for data collection/°	6.188 to 134.354	7.196 to 136.53	7.31 to 143.952	8.66 to 136.284
Index ranges	-11 ≤ h ≤ 11, -16 ≤ k ≤ 16, -17 ≤ l ≤ 17	-9 ≤ h ≤ 11, -29 ≤ k ≤ 29, -11 ≤ l ≤ 11	-15 ≤ h ≤ 15, -16 ≤ k ≤ 16, -16 ≤ l ≤ 15	-7 ≤ h ≤ 7, -23 ≤ k ≤ 23, -14 ≤ l ≤ 14
Reflections collected	56434	32378	49369	23923
Independent reflections	6893 [R_{int} = 0.0271,	4179 [R_{int} =	7309 [R_{int} = 0.0260,	2934 [R_{int} =

	R_{sigma} = 0.0141]	0.0302, R_{sigma} = 0.0165]	R_{sigma} = 0.0151]	0.0253, R_{sigma} = 0.0142]
Data/restraints/parameters	6893/0/511	4179/0/296	7309/0/553	2934/0/247
Goodness-of-fit on F^2	1.162	1.042	1.133	1.061
Final R indexes [I>=2σ (I)]	R_1 = 0.0199, wR_2 = 0.0491	R_1 = 0.0182, wR_2 = 0.0448	R_1 = 0.0238, wR_2 = 0.0593	R_1 = 0.0161, wR_2 = 0.0411
Final R indexes [all data]	R_1 = 0.0202, wR_2 = 0.0494	R_1 = 0.0190, wR_2 = 0.0452	R_1 = 0.0240, wR_2 = 0.0595	R_1 = 0.0166, wR_2 = 0.0415
Largest diff. peak/hole / e $Å^{-3}$	0.26/-0.61	0.29/-0.38	0.48/-0.96	0.31/-0.32

Table 4.16: Selected lengths (Å) and angles (°) derived from X-ray structures of the complexes

Atom	**Length/Å**		**Atom**	**Length/Å**	
Complex	1	6		**2**	7
Ru1-Cl1	2.4016(5)	2.3904(5)	Ru1-Cl1	2.4013(4)	2.4089(4)
Ru1-N1	2.0974(16)	2.1194(18)	Ru1-N3	2.1270(14)	2.0985(14)
Ru1-N4	2.1037(16)	2.1208(19)	Ru1-N1	2.1121(13)	2.0878(14)
Ru2-Cl2	2.3886(5)	2.4066(5)			
Ru2-N7/8	2.1065(16)	2.1177(18)			
Ru2-N5	2.0978(17)	2.1264(18)			
Complex	1	6	2	7	
	Angle/°				
N1-Ru1-Cl1	86.90(5)	84.88(5)			
N1-Ru1-N4	84.40(6)	85.98(7)			
N4-Ru1-Cl1	85.51(5)	86.12(5)			
N5-Ru2-Cl2	85.31(5)	85.81(5)			
N5-Ru2-N7/8	83.55(6)	86.87(7)			
N7/8-Ru2-Cl2	85.17(5)	85.64(5)			
N3-Ru1-Cl1			84.38(4)	84.78(4)	
N1-Ru1-Cl1			84.56(4)	85.10(4)	

N1-Ru1-N3	87.68(5)	85.72(5)

4.2.3 Discussion

The ^{1}H and ^{13}C NMR spectra acquired in DMSO-d_6 revealed distinct chemical shifts attributable to both the η^6-bound arene ligands (*p*-cymene or toluene) and the coordinated N,N′-bidentate ligands. The spectral features were sharp and well-defined, suggesting a uniform coordination environment and the presence of a single dominant species in solution. These findings are consistent with the expected half-sandwich ("piano-stool") configuration, as illustrated in Figures 4.25, 4.27, 4.30–31, and 4.34–35. To further confirm proton correlations and carbon assignments, 2D-NMR techniques such as COSY and HSQC were employed, with complex **2** serving as a representative model (Table 4.17; Figures 4.36 & 4.37). Notably, in the ^{1}H NMR spectra, the geminal methylene protons originating from the bdmpzm or dpzm ligands exhibited clearly resolved spin patterns that varied with the specific complex. These protons displayed distinct chemical shifts and coupling behaviours, reflecting differences in their coordination environments and indicating successful metal–ligand interaction. Compounds **1** and **7** displayed chemical shift patterns consistent with an AB spin system (δ = 6.25–6.34 and 7.05–7.08 ppm), whereas compounds **2** and **6** exhibited features indicative of an AX spin system (δ = 5.84–6.04 and 6.25–6.34 ppm). These differences arise from variations in the structural symmetry and conformational flexibility of the ligand framework surrounding the metal ion.

The two resonances observed for the bridging -CH_2- indicate a diastereotopic nature of H groups, axial and equatorial. In addition, compounds **1** and **7** have three resonances in the region δ = 6.63-8.22 ppm, whereas compounds **2** and **6** have one at δ = 6.26-7 in the aromatic region of dpzm and bdmpzm, respectively. Besides these, bdmpzm in **2** and **6** shows a singlet in the region δ = 2.48, which corresponds to the methyl protons. The findings suggest that the nature of the arene ligand exerts minimal influence on the chemical environment of the bdmpzm N,N′-donor framework. In the spectra of complexes **2** and **6**, the observed AA′BB′ spin pattern produced two well-separated aromatic proton signals within the δ = 6.00–6.18 ppm range. This splitting pattern is characteristic of η^6-arene–ruthenium complexes possessing a symmetrical coordination environment, consistent with literature reports for related systems (Fernández *et al*., 2004; Peacock *et al*., 2007). While the toluene has three peaks associated with the arene group in the range of δ = 5.91-6.18 ppm (**6** and **7**). For complexes **1** and **2,** the ^{1}H NMR spectra reveal

characteristic signals from the isopropyl group ($CH(CH_3)_2$) attached to the *p*-cymene moiety, showing as a doublet for the methyl protons and a multiplet for the central methine proton. Additionally, the methyl groups on the cymene and toluene rings produce singlet or narrowly split resonances within the chemical shift window of δ = 1.09–1.22 ppm (2 × 3H, isopropyl CH_3), 2.02–2.23 ppm (3H, cymene CH_3), 2.77–2.83 ppm (1H, $CH(CH_3)_2$), and 2.12–2.19 ppm (3H, toluene CH_3), confirming the identity and integrity of the arene ligands in solution.

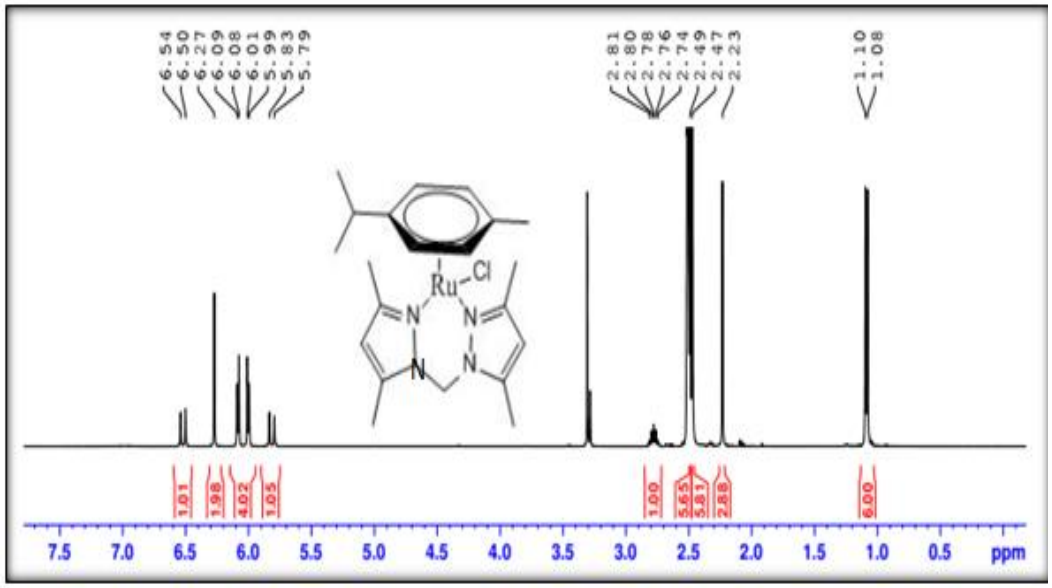

Figure 4.34: ^{1}H NMR spectrum (500 MHz, DMSO-d_6) of complex **2**

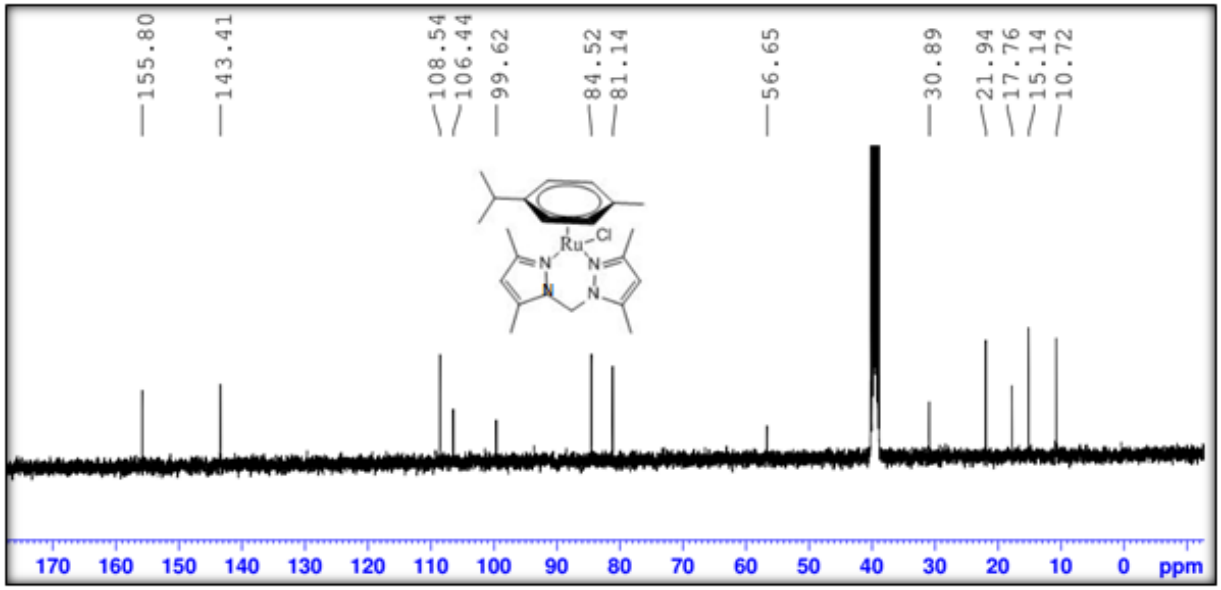

Figure 4.35: ^{13}C NMR spectrum (100 MHz, DMSO-d_6) of complex **2**

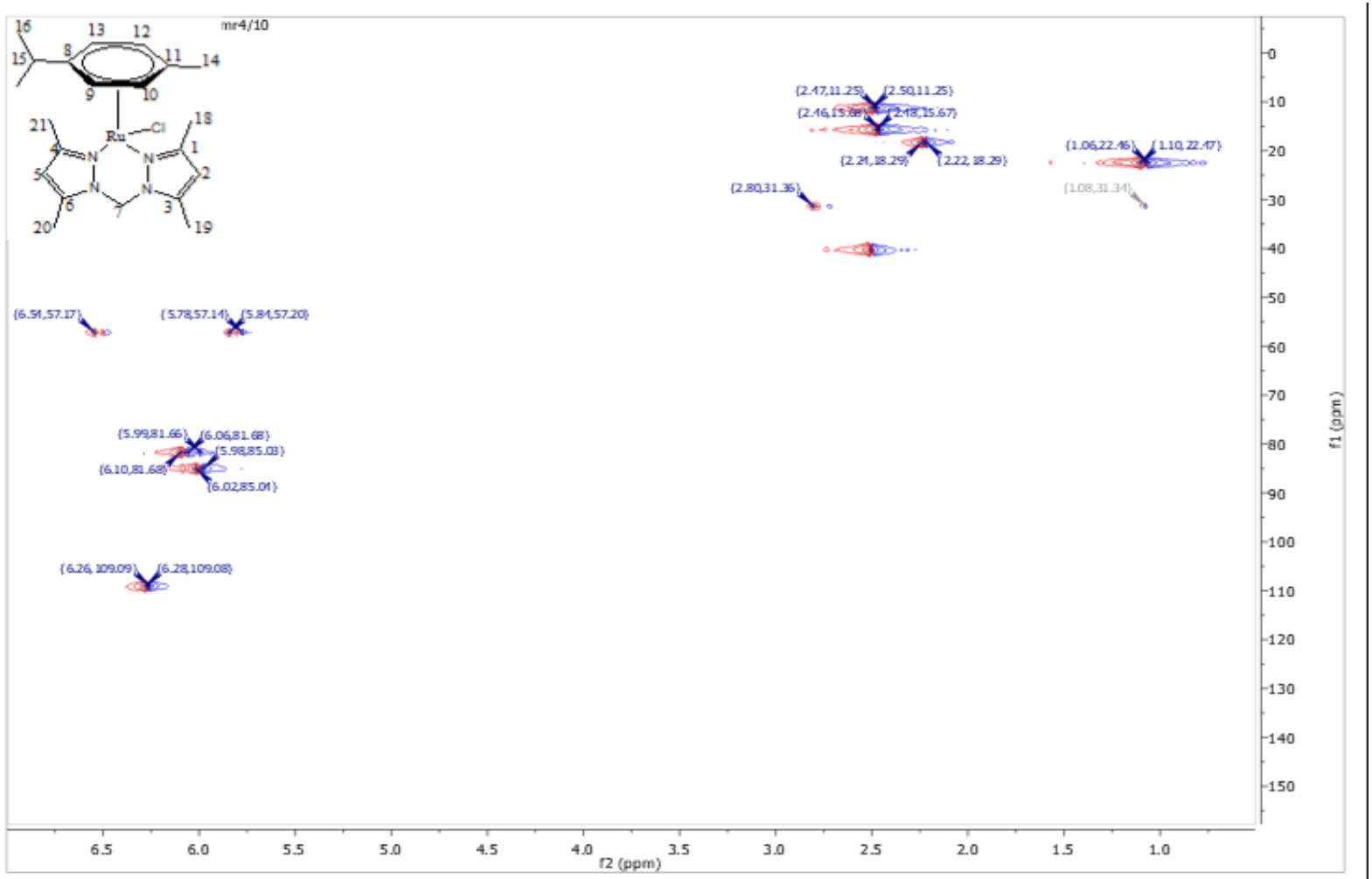

Figure 4.36: HSQC Spectrum of Complex **2**

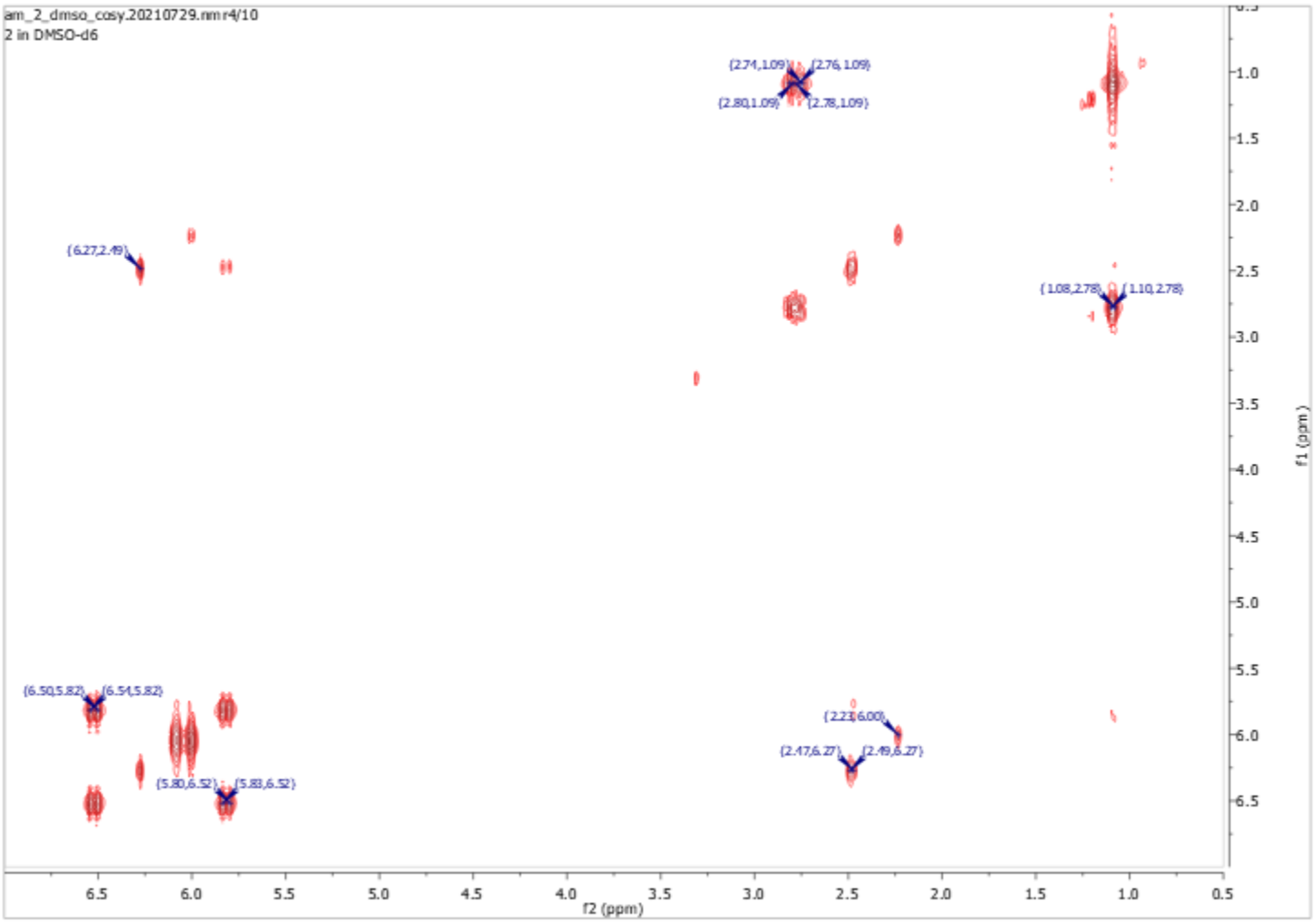

Figure 4.37: COSY Spectrum of Complex **2**

Table 4.17: Summary of 2D NMR data (HSQC and COSY) for complex **2**

HSQC (see Figure 4.36**)**			**COSY** (see Figure 4.37)	
Carbon Number	Chemical shifts of correlated nuclei		Chemical shifts (splitting pattern, and ^{3}J coupling constants, Hz) of the correlated nuclei	
	^{3}C (ppm)	^{1}H (ppm)	F1 ^{1}H (ppm)	F2 ^{1}H (ppm)
18/21	10.72	2.48		
19/20	15.14	2.48	1.09 (d, 6.9)	2.77 (d; 6.6)
14	17.76	2.23	2.48 (d; 7.5)	6.27 (s)
16/17	21.94	1.09	5.81 (d; 15.5)	6.52 (d, 15.5)
15	30.89	2.77	6.00 (d; 6.2)	2.23 (s)
7	56.65	6.52, 5.81	6.27 (s)	2.47 (d; 9.5)
9/13	81.14	6.08	6.52 (d; 15.5)	5.80 (d; 5.9)
10/12	84.52	6.00		
11	99.62			
8	106.44			
2/5	108.54	6.27		
3/6	143.41			
1/4	155.80			

The FTIR spectra (Figures 4.28, 4.32 and 4.38) of the complexes revealed C–H stretching vibrations, corresponding to aromatic and aliphatic groups, typically observed in the higher wavenumber region (3133 and 2950 cm^{-1}). Characteristic C=N stretching bands appeared sharply between 1516 and 1559 cm^{-1}**,** while C=C vibrations from the pyrazole rings were evident in the range of 1200–1422 cm^{-1}**,** consistent with known ring-stretching modes (Potapov & Khlebnikov, 2006). A distinct and sharp absorption band attributed to the B–F stretching vibration of the BF_4^- counterion was also observed, appearing at ~1030 cm^{-1} for complexes **6** and **7** and ~1050 cm^{-1} for complexes **1** and **2.**

Further confirmation of the molecular composition was obtained from elemental analysis and ESI-MS data**,** both of which matched the theoretical values for the proposed molecular formulas. Well-defined molecular ion signals were observed, with *m/z* values that align with the expected

molecular weights of the respective complexes (Figures 4.25–26, 4.29, and 4.33), further validating the identity and purity of the synthesised complexes.

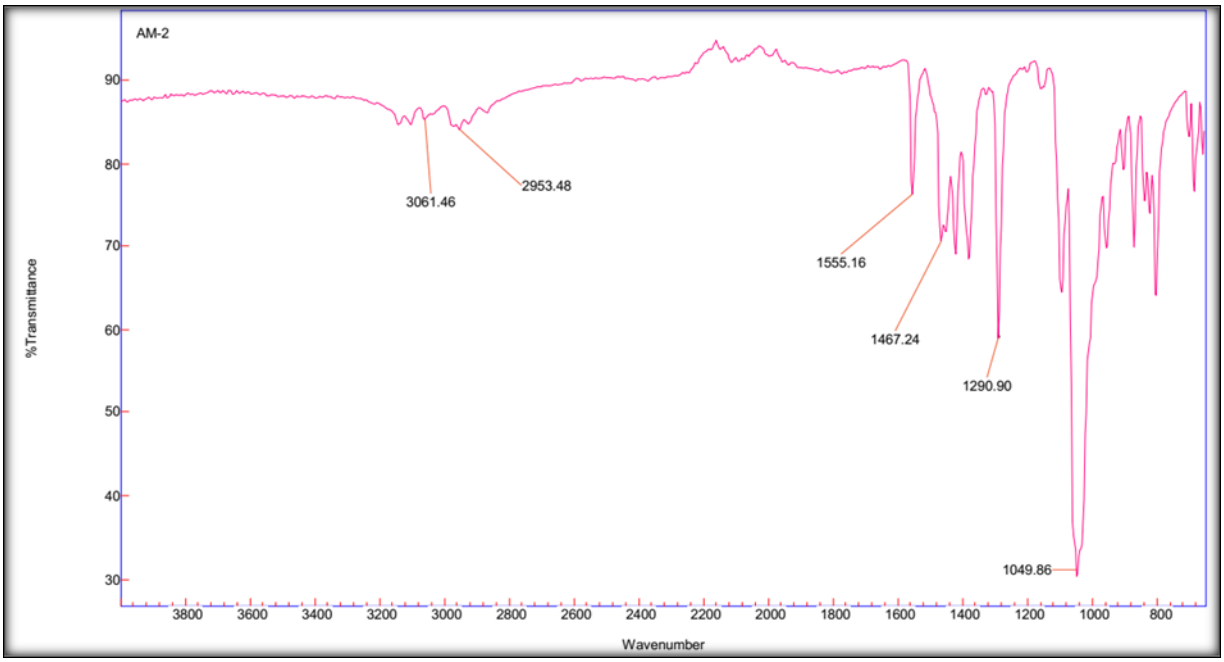

Figure 4.38: FTIR spectrum (dispersed in KBr) of complex **2**

Complex **1** was obtained as a mononuclear ionic species that crystallizes in the triclinic crystal system with space group *P*-1, as illustrated in Figure 4.39. The Ru(II) centre displays a six-coordinate arrangement, typical of a half-sandwich architecture. In this structure, the coordination sphere comprises two nitrogen donors from the chelating ligand, a single chloride ligand, and an η^6-coordinated *p*-cymene ring functioning as the arene base of the "piano-stool" motif. Key bond angles around the Ru centre reflect slight deviations from ideal octahedral geometry: N1–Ru1–N4: 83.40(6)°, N5–Ru2–N7: 83.55(6)°, N1–Ru1–Cl1: 86.90(5)°, N4–Ru1–Cl1: 85.51(5)°, N5–Ru2–Cl2: 85.31°, and N7–Ru2–Cl2: 85.17(5)°. The *p*-cymene ligand is nearly planar, coordinating through its aromatic π-system, with Ru–C bond distances ranging between 2.1753(18) and 2.2261(19) Å. The centroid of the aromatic ring is positioned at a distance of 1.676 Å from the ruthenium centre, consistent with typical η^6-arene metal interactions. The Ru atoms are coordinated through two nitrogen atoms of bis(pyrazolyl)methane moieties, Ru1-N1, Ru1-N4, Ru2-N7, and Ru2-N5, which are almost identical *.i.e.,* 2.0974 (16), 2.1037 (16), 2.1065 (16) and 2.0978 (17). The Ru–Cl bond distances, measured at 2.4016(5) Å

for Ru1–Cl1 and 2.3886(5) Å for Ru2–Cl2, are consistent with those typically observed in cationic η^6-arene ruthenium(II) complexes (Field *et al.*, 2001). The bpzm ligand adopts a bidentate chelating coordination mode, forming a stable five-membered ring with the metal centre. Interestingly, a change in reaction solvent polarity significantly contributes to the coordination behaviour. For instance, replacing acetonitrile with methanol in reactions involving $[Ru(p\text{-cym})Cl_2]_2$ and bis(imidazol-1-yl)methane leads to the formation of binuclear cyclic complexes, where the ligand bridges two ruthenium centres in an N,N′-bidentate fashion (Matveevskaya *et al*., 2021). This highlights the significant impact of solvent environment on the final architecture of ruthenium coordination compounds. The interatomic distances involving Ru–N, Ru–Cl, and Ru–C bonds in the bridging bidentate ligands are comparable to those observed in complex **1**. Significantly, hydrogen bonds were observed involving the chloride anions and the *p*-cymene/bis(pyrazolyl)methane moieties, including: C1–H1···Cl1 (2.931 Å), C8B–H8B···Cl2 (2.833 Å), C31–H31···Cl2 (2.644 Å), and C25B–H25B···Cl1 (2.880 Å). These short contacts further support the presence of non-covalent interactions: Cl1···H1 (2.934 Å), Cl1···H25B (2.880 Å), Cl2···H8B (2.833 Å), and Cl2···H31 (2.644 Å). Figure 4.39b illustrates that the crystallographic unit cell of complex 1 contains four separate molecules.

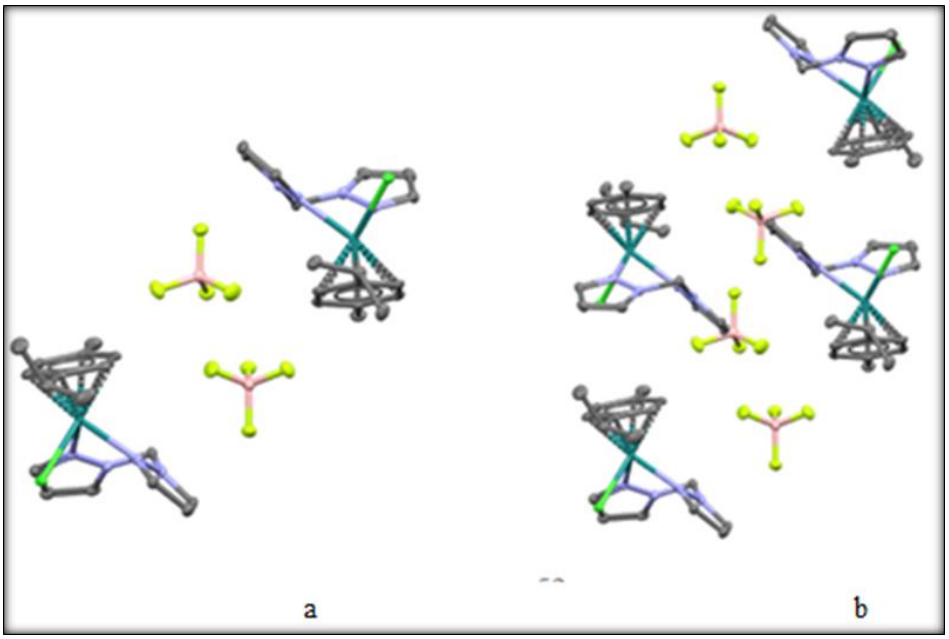

Figure 4.39: Crystal packing view of complex **1** along the *a*-axis*

As depicted in Figure 4.40, the crystal structure of complex **2** belongs to the monoclinic system ($P2_1/n$ space group), with one distinct molecule per asymmetric unit. The ruthenium centre exhibits a typical η^6-arene coordination with the *p*-cymene ligand, forming a pseudo-octahedral geometry. The Ru–C bond distances to the arene ring fall within 2.1804(16)–2.2317(16) Å**,** consistent with reported values for similar complexes. Coordination to the chloride ligand occurs exhibiting a Ru–Cl bond distance measuring 2.4013(4) Å**,** which aligns well with those observed in related η^6-arene-Ru(II) systems (Matveevskaya *et al.*, 2021). The dpzm ligand coordinates through both pyrazole nitrogen atoms, with Ru–N1 and Ru–N3 bond lengths of 2.1121(13) Å and 2.1270(14) Å**,** respectively. Significant hydrogen bond interactions were observed between the chloride anion and hydrogen atoms on the coordinated ligand framework, including H(12)…Cl(1) at 2.8132 Å and H(1)…Cl(1) at 2.7912 Å**,** contributing to the overall crystal packing stability.

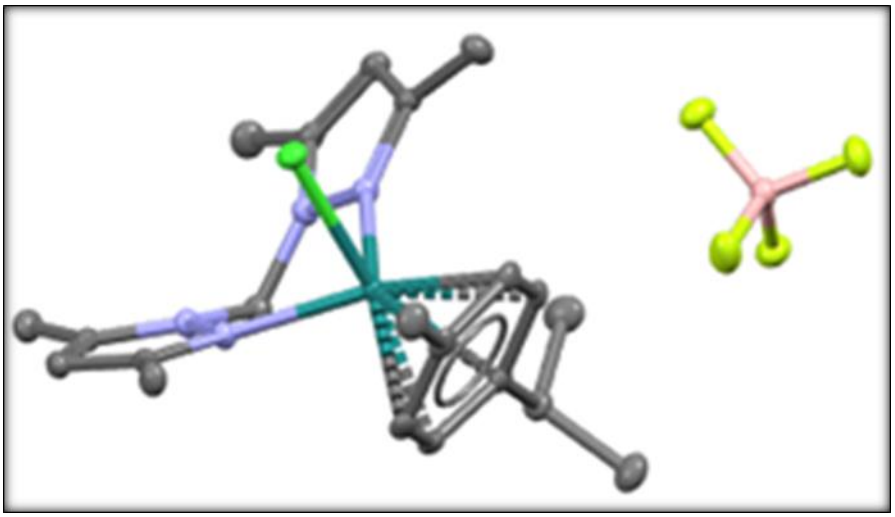

Figure 4.40: Crystal packing view of complex **2** along the *a*-axis*

As shown in Figure 4.41, the crystal structure of compound **6** corresponds to the triclinic crystal system and belongs to the *P*–1 space group. The ruthenium centres display coordination geometries typical of η^6-arene-Ru(II) complexes. The Ru–N bond lengths are measured as follows: 2.1206(19) Å for Ru1–N1, 2.1192(18) Å for Ru1–N4, 2.1263(18) Å for Ru2–N5, and 2.1176(18) Å for Ru2–N7. The observed Ru–Cl separations measure approximately 2.3903(5) Å for Ru1–Cl1 and 2.4066(5) Å for Ru2–Cl2, which fall within the expected range for mononuclear chlorido Ru(II) complexes. Meanwhile, the Ru–C distances between the metal

centres and the coordinated arene ligands span 2.184(2)–2.227(2) Å, further support the formation of a half-sandwich "piano-stool" geometry typical of η⁶-arene-ruthenium species.

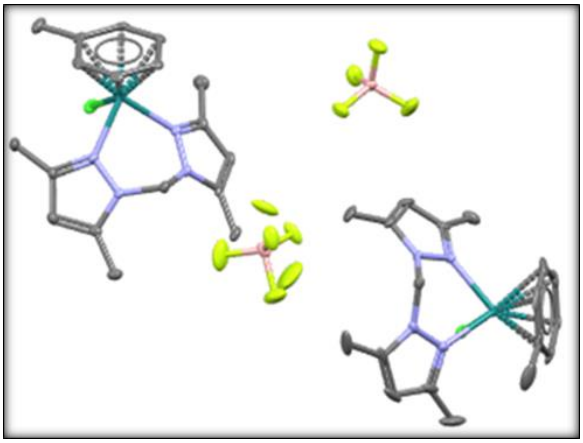

Figure 4.41: Crystal packing view of complex **6** along the *b*-axis

Complex **7** crystallises in the monoclinic crystal system with space group $P2_1/c$ (Figure 4.42). The Ru–N bond lengths are measured at 2.0985(14) Å for Ru1–N1 and 2.0878(14) Å for Ru1–N4, indicating effective binding of the bidentate ligand to the Ru(II) ion. The Ru–Cl bond is observed at 2.4089(4) Å**,** which aligns well with bond lengths typically reported for chlorido ligands in similar η⁶-arene-Ru(II) complexes. These structural features are consistent with the formation of a stable half-sandwich ("piano-stool") geometry.

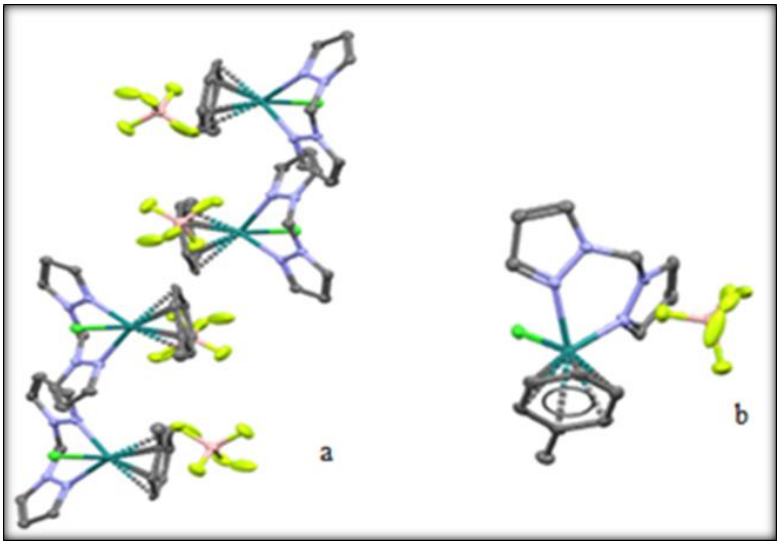

Figure 4.42: Crystal packing of complex **7**: (a) packing diagram of complex **7** within the unit cell. (b) Projection along the *c*-axis

All four ruthenium complexes (**1, 2, 6,** and **7**) feature a six-coordinate metal centre and adopt a pseudo-octahedral geometry characteristic of a half-sandwich "piano-stool" configuration. Bite angles involving the two nitrogen atoms and ruthenium were found to lie between from 83.55(6)° to 87.68(5)°, deviating from the ideal 90° due to the constrained bite of the chelating bis(pyrazolyl)methane ligands. These deviations are consistent with a distorted octahedral geometry and align with values reported for similar η^6-arene–ruthenium(II) complexes (Marchetti *et al.*, 2008; Mishra & Mukherjee, 2006). The Ru–N and Ru–Cl bond lengths fall within expected ranges and are comparable to those reported for analogous cationic η^6-arene–Ru(II) complexes (Tripathy *et al.*, 2015). Coordination distances from Ru to the centroid of the η^6-arene ring were observed to be 1.676 Å (1), 1.688 Å (2), 1.676 Å (6), and 1.673 Å (7), closely matching values in previously characterised structures (Mishra & Mukherjee, 2006). Complexes containing the bulkier bdmpzm ligands (**2** and **6**) exhibit slightly longer Ru–$C_{centroid\ bonds}$ compared to those with dpzm ligands (**1** and **7**), *i.e.*, **2** > **1** and **6** > **7**. The arene complexes follow a consistent trend, as reflected in the Ru–cymene bond parameters (in **1** and **2**) are longer than those with Ru–toluene (in **6** and **7**), suggesting that methyl substituents on the arene or ligand enhance electron donation to the Ru centre. This increases σ-donation, reduces π-backdonation, and ultimately elongates the Ru–arene bond.

The bis(pyrazolyl)methane ligands form flexible six-membered chelate rings that can adopt boat or chair conformations due to the methylene bridge between the pyrazole rings. In this

arrangement, the two donor atoms from the chelating ligand and the chloride ion serve as the 'legs' of the half-sandwich architecture, while the tetrafluoroborate counterion remains uncoordinated in the outer coordination sphere. Across the series, structural differences are minimal and primarily attributed to the impact of both the size and electron-donating/withdrawing nature of substituents on the ligands and arenes. In general, complexes **1** and **7** exhibit slightly stronger metal–ligand interactions, as inferred from their shorter Ru–ligand bond distances, relative to their more sterically hindered counterparts (**2** and **6**).

In addition to primary coordination geometry, the crystal structures reveal a network of secondary interactions. All four complexes exhibit C–H···Cl hydrogen bonding with adjacent chloride ligands. For example, in complex **1**, Cl1···H1 = 2.934 Å, Cl1···H25B = 2.880 Å, and Cl2···H31 = 2.883 Å. Complex **2** features contacts such as C1–H1···Cl1 = 2.791 Å and C12–H12···Cl1 = 2.813 Å, while complex **6** shows C12B–H1···Cl2 = 2.705 Å and C22–H22A···Cl2 = 2.756 Å. Complex **7** includes a Cl1···H1 interaction at 2.766 Å. These distances fall within the hydrogen bond range reported in the literature (2.569–2.944 Å) (Kapoor *et al.*, 2004; Singh *et al.*, 2004; Taylor & Kennard, 1982). These are intermediate contacts (2.41-2.73 Å), and are less than the combined van der Waals radii of neutral hydrogen atoms and chlorine atoms (2.95 Å) (Aakeröy *et al.*, 1999), indicating moderately strong hydrogen bonding. Additional short contacts support the role of electron-deficient C–H groups in facilitating intermolecular interactions. Notable examples include: C18–H18···F4 = 2.543 Å, C18–H18···F2 = 2.622 Å, C5–H5···H7 = 2.286 Å, N1···H22A = 2.643 Å, and Ru1···H12C = 3.156 Å in complex 2; and H4B···F1 = 2.311 Å and H4B···F4 = 2.563 Å in complex **7**. These interactions suggest partial electron withdrawal from the aromatic rings, enhancing the acidity of adjacent C–H bonds and promoting hydrogen bonding.

Among the four complexes, complex **7** displays the longest observed bond between Ru and C at 2.4089(4) Å, implying high probility of a greater lability and increased susceptibility to aquation. This enhanced aquation may reduce biological activity by promoting nonspecific binding to cellular biomolecules and increasing off-target toxicity. Density functional theory (DFT) calculations corroborate this interpretation, showing that complex **7** exhibits the lowest natural bond orbital (NBO) charge on the ruthenium centre (–0.046), indicative of reduced π-backdonation and weaker metal–ligand bonding.

4.2.3 DFT Results

To elucidate the electronic structure and geometry of the Ru(II) complexes bearing either dpzm or bdmpzm as N,N'-chelating ligands, density functional theory (DFT) calculations were performed. Theoretical modelling offers critical insights into how the electronic configuration and three-dimensional arrangement of donor atoms influence the complexes' stability and potential reactivity. Optimized molecular structures derived from DFT calculations are depicted in Table 4.18, while key geometric and electronic descriptors—such as bond metrics, HOMO–LUMO gaps, and charge distributions—are compiled in Tables 4.19 and 4.20, respectively.

Table 4.18: Structural correlation between optimized and experimental models with HOMO and LUMO representations for selected complexes

DFT-optimized (blue); Crystal structure (red)	**HOMO**	**LUMO**
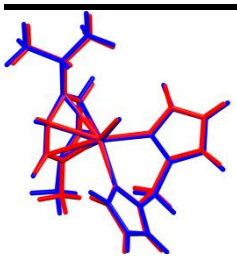 **1**	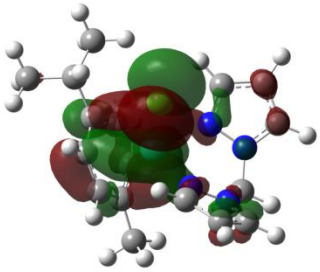	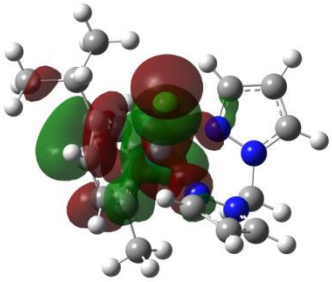
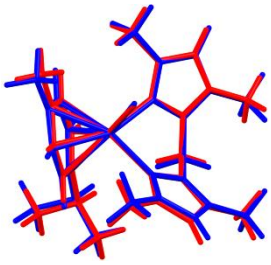 **2**	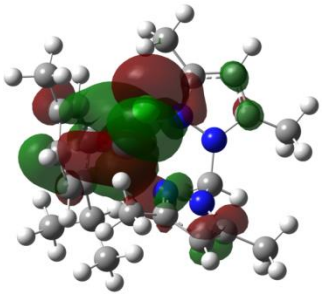	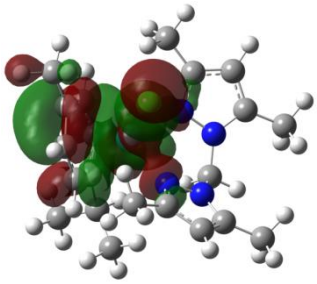

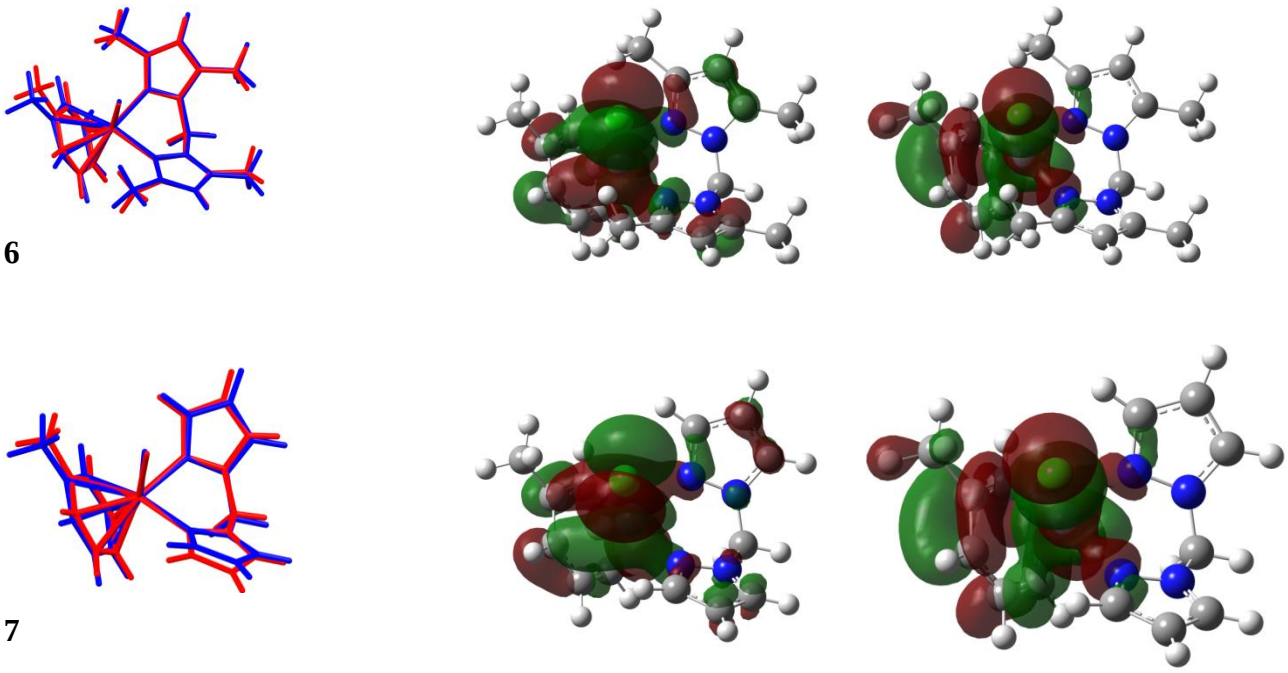

6

7

Table 4.19: Summary of DFT-calculated parameters for optimized complexes **10, 1, 2, 6,** and **7**

Parameter	**10**	**1**	**2**	**6**	**7**
HOMO-LUMO energy/eV					
- (LUMO), eV	1.671	2.330	2.338	2.403	2.420
-(HOMO), eV	6.323	6.398	6.330	6.374	6.468
Band gap, ΔE, eV	4.652	4.068	3.992	3.971	4.048
Global electrochemical parameters					
Chemical hardness (η)	2.326	2.034	1.996	1.986	2.024
Chemical potential (μ)	−3.997	−4.364	-4.334	−4.389	−4.444
Chemical softness (σ)	0.430	0.492	0.501	0.504	0.494
Electronegativity (χ)	4.702	4.364	4.334	4.389	4.444
Electrophilicity index (ω)	3.435	4.681	4.705	4.850	4.879
Nucleophilicity (ε)	0.291	0.214	0.213	0.206	0.205
Dipole moments	7.953	7.8202	6.6336	6.8039	7.0519
(NBO) charge					
Ru/Os	+0.004	-0.032	-0.019	−0.035	−0.046
Cl	−0.297	−0.299	-0.312	−0.303	−0.289
N1	−0.251	−0.237	-0.253	−0.256	−0.235

N3/N4	−0.254	−0.235	-0.257	−0.215	−0.232

Table 4.18 shows the molecular orbital representations of the complexes. For all the Ru complexes, the HOMO and LUMO reside on the metal. This indicates weak MLCT; these results align with the experimental UV-visible results of **10**, which is an analogue of complex **1**. The HOMO-LUMO energy gap has proven to be a useful tool in determining a molecule's kinetic stability and chemical reactivity. A lower energy gap is an appropriate condition in which a molecule can easily exit, whereas a higher energy gap leads to higher kinetic stability but lower chemical reactivity of the molecule (Obuah *et al.*, 2018). Therefore, the energy gap for the complexes follows the order **1** > **7** > **2** > **6**, with complex **6** having the lowest HOMO-LUMO energy gap among these complexes. The results indicated that **6** is a promising candidate for use as an anticancer agent because of its small energy gap, low chemical hardness (1.986 eV), and higher softness (0.504 eV), as seen in Table 4.19. The σ-donor and π-acceptor properties of pyrazole ligands can be modulated by introducing substituents at the 3- and -5-positions (Khusi, 2015). As expected, increased electron donation to the metal centre induces a reduction of the HOMO–LUMO energy gap, as observed in the comparison of complex **2** with **1**, and complex **7** with **6** (Table 4.19). Furthermore, LUMO energies show a high value for **1** (-2.330 eV) in comparison to **2** (-2.338 eV), **6** (-2.403 eV), and **7** (-2.420 eV), making it the poorest π-acceptor, resulting in more dampening of **1**'s general reactivity compared to the others. From the results, it is therefore expected that the methyl substituted bidentate ligands for **2** and **6** complexes would be more active. Lewis acids have a high electronegativity (χ), while Lewis bases have a low electronegativity. As a result, **7** > **6** > **1** > **2,** which indicates that complex **7** is more Lewis acid and **2** is more Lewis base.

The NBO charges on the Ru atom in complexes are -0.032, -0.019, -0.035, and -0.046 (**1**, **2**, **6**, and **7,** respectively) which are significantly lower than the formal charge of +2. Furthermore, a lower negative charge on Cl in complex **7** indicates that it receives less charge transfer than the other complexes, resulting in an accumulation of a higher negative charge at the Ru. Variations in the electron-donating or -withdrawing nature of groups attached at the 3,5-positions of the pyrazole scaffolds, in conjunction with the metal coordination framework, play a pivotal role in tuning the overall electronic behaviour of the complexes. Substituting the arene ring from cymene to toluene (*e.g.*, **1** *vs.* **7** and **2** *vs.* **6**) leads to noticeable changes in the

electronic distribution. Specifically, a smaller HOMO–LUMO energy gap combined with a more positive natural bond orbital (NBO) charge on the ruthenium centre corresponds to increased electrophilicity. Additionally, the dipole moment values reflect the electronic effects of the substituents on the bidentate ligands. In this study, complexes without electron-donating groups (**1** and **7**) exhibited higher dipole moments than their substituted analogues (**2** and **6**), highlighting the impact of ligand electronics on the overall polarity of the complexes.

Chemical hardness (η) provides an estimate of a compound's intrinsic resistance to electronic perturbations and serves as an indicator of its overall thermodynamic stability (Li *et al.*, 2009). As presented in Table 4.19, the Ru(II) complexes incorporating the dpzm ligand—specifically complexes **1** and **7**—exhibit higher chemical hardness values (2.034 and 2.024 eV, respectively), suggesting a lower tendency toward reactivity relative to their bdmpzm-based counterparts (complexes **2** and **6**). In addition, the electrophilicity index (ω), which reflects the tendency of a species to accept electrons, is higher for complexes with more electrophilic metal centres, indicating a greater potential for engaging in electron-accepting interactions (Obuah *et al.*, 2018). The high electrophilicity index for **7** illustrates that this compound is capable of creating significant interactions with biological macromolecules such as DNA. The highest occupied molecular orbitals (HOMOs) in these complexes are primarily composed of ruthenium d-orbital character. A smaller HOMO–LUMO energy gap enhances the potential for electron density delocalisation from the metal into the π orbitals of the ligand system thereby increasing the electrophilic character of the metal. Computational results indicate that complexes bearing 3,5-methyl substituents on the pyrazole rings exhibit narrower HOMO–LUMO gaps compared to their unsubstituted counterparts, suggesting that these substituted complexes possess greater electrophilicity.

The geometric parameters, encompassing measurements of interatomic distances and angular relationships within the DFT-optimised structures, are summarised in Table 4.20. The theoretical geometric parameters show a high level of consistency with those determined experimentally through single-crystal X-ray diffraction analysis, supporting the robustness of the computational protocol applied, which utilised the B3LYP functional with the 6-31G basis set for non-metal atoms and the LanL2DZ pseudopotential for ruthenium. The close agreement between the computed and experimental structural data affirms the reliability of the employed theoretical framework in capturing the key molecular characteristics of the complexes. Analysis

of the computed electrophilicity indices suggests a reactivity sequence progressing from complex **1** through to complex **7**, in the order: **1 < 2 < 6 < 7**.

Table 4.20: Comparison of selected DFT-optimized structural parameters with single-crystal X-ray data for complexes **1, 2, 6,** and **7**

	1			**2**			**6**			**7**	
Bond lengths	Theoret.	Cryst.	%RE	Theoret.	Cryst	%RE	Theoret.	Cryst.	%RE	Theoret	Crys
Ru-‡ Cl	2.4468	2.4015	1.9	2.4598	2.4012	2.4	2.4541	2.3905	2.7	2.468	2.40
Ru-$C_{centroid}$	1.850	1.676	10.4	1.860	1.688	10.2	1.873	1.676	11.8	1.864	1.67
Ru-N1	2.0915	2.1037	0.6	2.0952	2.112	0.8	2.1025	2.1206	0.9	2.0826	2.09
Ru-N3	2.0848	2.0975	0.6	2.1075	2.1270	0.9	2.0937	2.1192	1.2	2.0853	2.08

Theoret. = DFT-calculated data; Cryst = crystal data taken as the accurate data; % % relative error (RE) = {(DFT Theoret. − Cryst)/Cryst} × 100.

4.2.4 Cytotoxicity Evaluation of Complexes 1, 2, 6, and 7 against Various Cancer Cell Lines

The cytotoxic activities of complexes **1, 2, 6,** and **7** were systematically assessed against a broad spectrum of human cancer cell lines, including cervical (HeLa, CaSki), breast (MCF-7, T-47D, MDA-MB-231), pancreatic (PANC-1, CFPAC-1), and rhabdomyosarcoma (RD, RH-30) models. Cytotoxicity assessments were conducted using the MTT assay following a 48-hour incubation period with the complexes. Cytotoxic screening revealed that the evaluated complexes exhibited low antiproliferative potency, with most half-maximal inhibitory concentration (IC_{50}) values approaching or exceeding 100 μM. This trend persisted even after exposure to 20 μM concentrations. Cisplatin (CDDP) was included as a reference standard for benchmarking the activity. The detailed IC_{50} outcomes are illustrated in Figures 4.43–4.46 and tabulated in Table 4.21.

In a related study, (Domínguez-Jurado *et al.*, 2024) examined the anticancer efficacy of structurally analogous η^6-arene ruthenium(II) complexes featuring variations on the methylene linker of their bidentate ligands. This evaluation incorporated a diverse panel of breast cancer cell lines, including triple-negative subtypes (BT549 and MDA-MB-231), HER2-overexpressing (SKBR3), and hormone receptor-positive (MCF-7) models. The cytotoxic efficacy of the test compounds was systematically compared against established benchmarks—UNICAM-1 and

cisplatin—representing standard metal-based chemotherapeutic agents. Notably, these modified complexes exhibited significantly enhanced cytotoxicity, with half-maximal inhibitory concentration (IC_{50}) values observed in the range of 4 to 18 µM. These findings highlight the pivotal role of ligand architecture—particularly substituents on the methylene bridge—in modulating the biological performance of arene–ruthenium(II) frameworks.

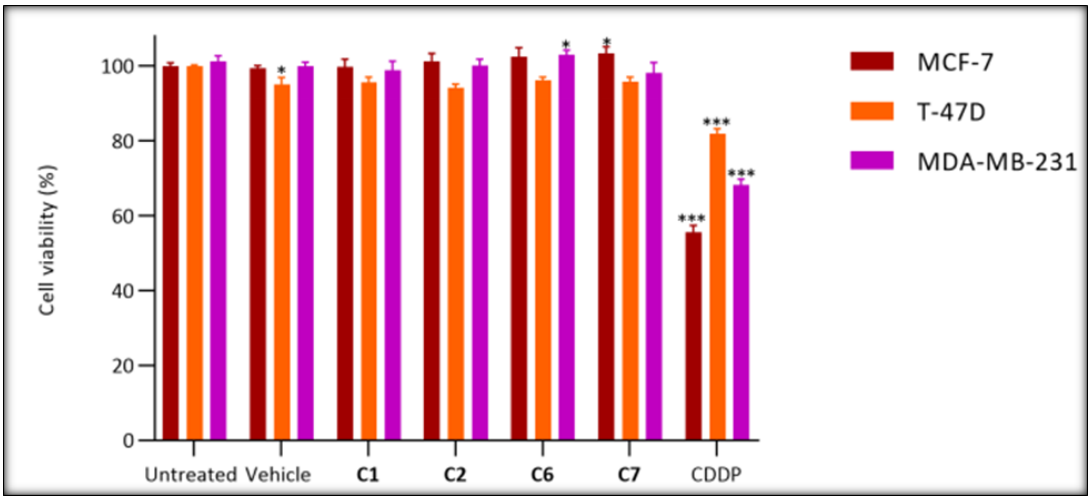

Figure 4.43: Cell viability (%) of human breast cancer cell lines (MCF-7, T-47D, and MDA-MB-231) following 48-hour exposure to 20 µM of complexes **1, 2, 6,** and **7**, as determined by the MTT assay.

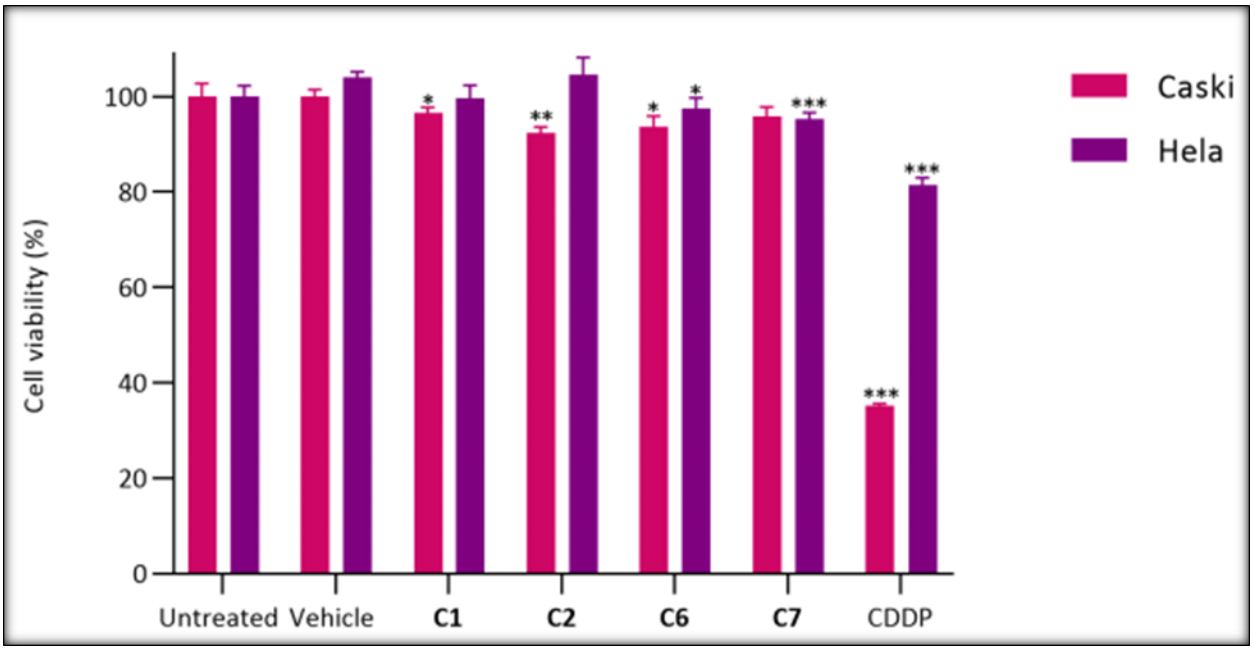

Figure 4.44: Cell viability (%) of human cervical cancer cell lines (CaSki and HeLa) after 48-hour treatment with 20 µM of complexes **1, 2, 6,** and **7,** assessed using the MTT assay.

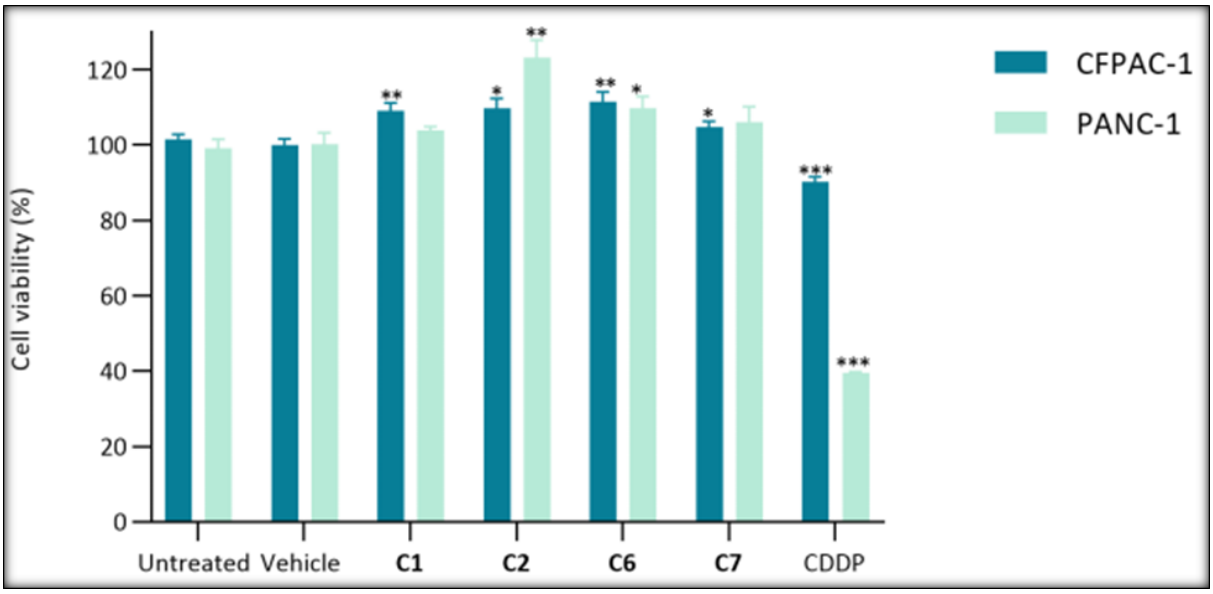

Figure 4.45: Cell viability (%) of human pancreatic cancer cell lines (CFPAC-1 and PANC-1) following 48-hour exposure to 20 µM of complexes **1, 2, 6,** and **7**, as evaluated by the MTT assay.

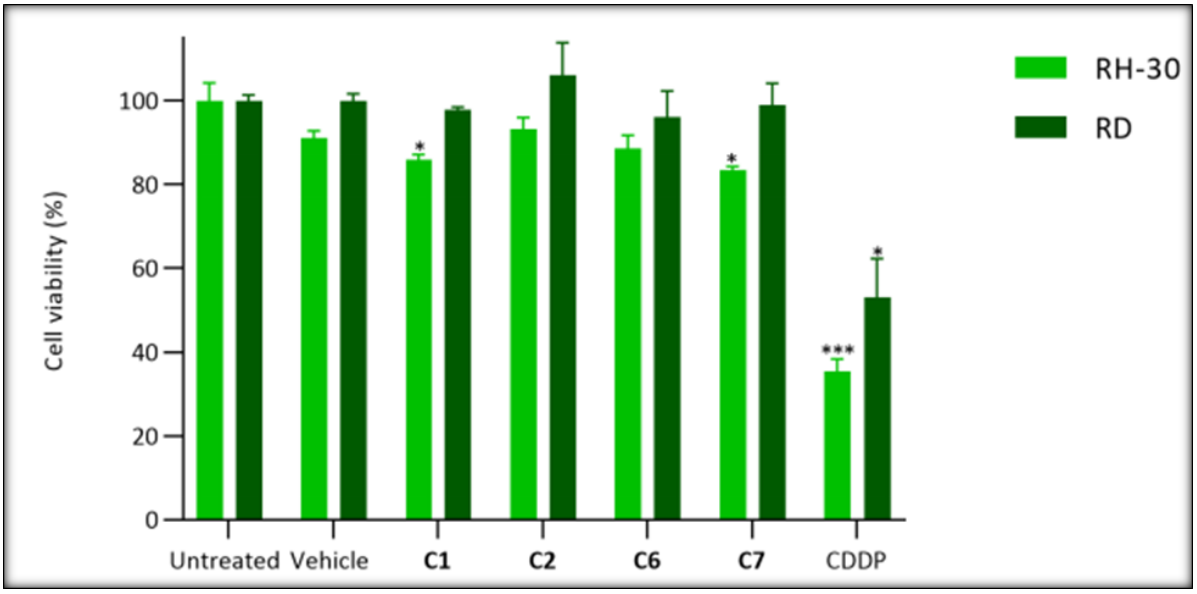

Figure 4.46: Cell viability (%) of human rhabdomyosarcoma cell lines (RH-30 and RD) after 48-hour treatment with 20 µM of complexes **1, 2, 6,** and **7**, determined using the MTT assay.

Table 4.21: IC_{50} values (µM) of synthesised complexes **1, 2, 6,** and **7** after 24-hour exposure to various cancer cell lines.

Cancer Type	Cell Line	Complex 1	Complex 2	Complex 6	Complex 7
Breast	MCF-7	—	—	—	—
	T-47D	—	—	—	—
	MDA-MB-231	—	—	—	—
Cervical	CaSki	—	—	—	—
	HeLa	—	—	—	—
Pancreatic	CFPAC-1	—	—	—	—
	PANC-1	—	—	—	—
Rhabdomyosarcoma	RH-30	—	—	—	—
	RD	—	—	—	—

None of the compound was active

4.3 [(η^6-Arene)(pyrazol-1-yl)pyridazine)Ru(X)]BF_4 Complexes

The molecular structures of the synthesised complexes are presented in Figure 4.47, encompassing compounds **3a** (X = Cl), **3b** (X = Br), **3c** (X = I), **4a** (X = Cl), **4b** (X = Br), **4c** (X = I), and **9** (X = Cl). Complexes in the **3**-series (featuring a *p*-cymene arene) and complex **9** (bearing a toluene arene) incorporate the pdzn-pzn ligand. In contrast, the **4**-series (also *p*-cymene-based) utilises a 3-chloro-6-(3,5-dimethyl-1H-pyrazol-1-yl)pyridazine ligand. For biological evaluation, five representative complexes—**3a, 3c, 4a, 4c,** and **9**—were selected to systematically assess the influence of halide substitution (Cl *vs*. I) and arene identity (*p*-cymene *vs.* toluene) on DNA binding affinity and cytotoxic potential, as reported in (Kanyora *et al.*, 2024).

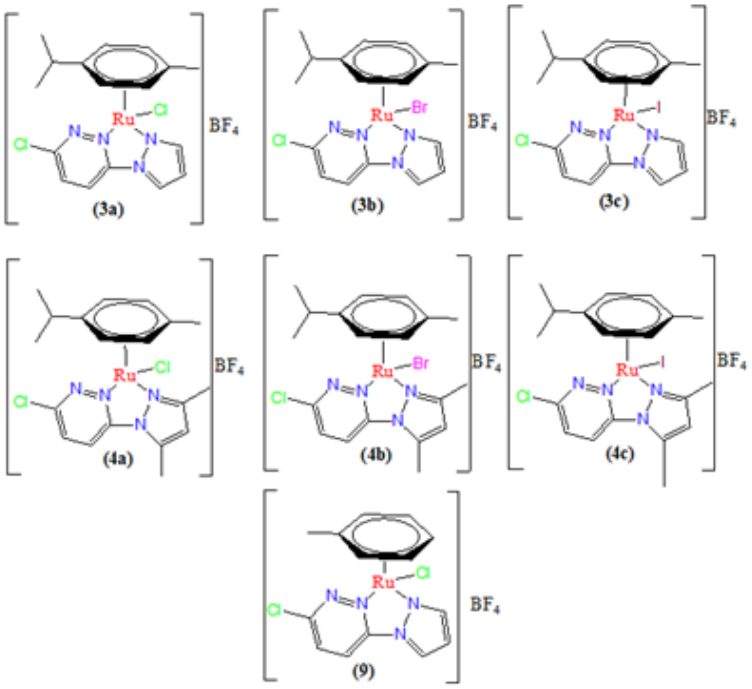

Figure 4.47: Chemical structures of η⁶-arene ruthenium(II) complexes featuring pyrazol-1-yl)pyridazine-based ligands.

4.3.1 Syntheses and Spectral Data of the η^6-Arene Ru(II) Complexes

The complexes were isolated as orange to yellow solids in yields ranging from 40% to 82%. Their identities were confirmed through a combination of spectroscopic and analytical

techniques, including NMR spectroscopy, elemental analysis, FTIR, and UV–Visible spectroscopy, as summarised below.

3-chloro-6-(1H-pyrazol-1-yl)pyridazine (*N,N'*):

White powder. ^{1}H NMR (500 MHz, d_6-DMSO, δ in ppm): 8.80 (d, J = 2.5 Hz, $1H_{pzn}$), 8.27 (d, J = 9.0 Hz, $1H_{pzn}$), 8.08 (d, J = 9.0 Hz, $1H_{pdzn}$), 7.98 (d, J = 1.4 Hz, $1H_{pdzn}$), 6.70 (dd, J = 4.3 Hz, $1H_{pzn}$). ^{13}C (100 MHz, δ in ppm): 154.1 (N-C-N_{pdzn}), 153.7 (N=C-Cl, $_{pdzn}$), 143.7 (C=N, $_{pzn}$), 131.8 (C=C_{pdzn}), 127.8 (C=N_{pzn}), 120.9 (C=C_{pdzn}), 109.7 (C=C_{pzn}) (see Figure 4.48).

3-chloro-6-(3,5-dimethyl-1H-pyrazol-1-yl)pyridazine (*N,N'*):

^{1}H NMR (500 MHz, d_6-DMSO δ in ppm): 8.15 (d, J = 2.8 Hz, $1H_{pzn}$), 8.0 (d, J = 9.0 Hz, $1H_{pzn}$), 6.24 (s, $1H_{pzn}$), 2.61 (s, 3H, -CH_{3pzn}), 2.22 (s, 3H, -CH_{3pzn}). ^{13}C (100 MHz, δ in ppm) 155.8 (N-C-N_{pdzn}), 153.3 (N=C-Cl, $_{pdzn}$), 151.0 (C=N_{pzn}), 141.8 (N-C=C_{pzn}), 131.2 (C=N_{pdzn}), 123.5 (C=C_{pdzn}), 110.4 (C=C_{pzn}), 14.3 (-CH_{3pzn}), 13.3 (-CH_{3pzn}) (see Figure 4.49).

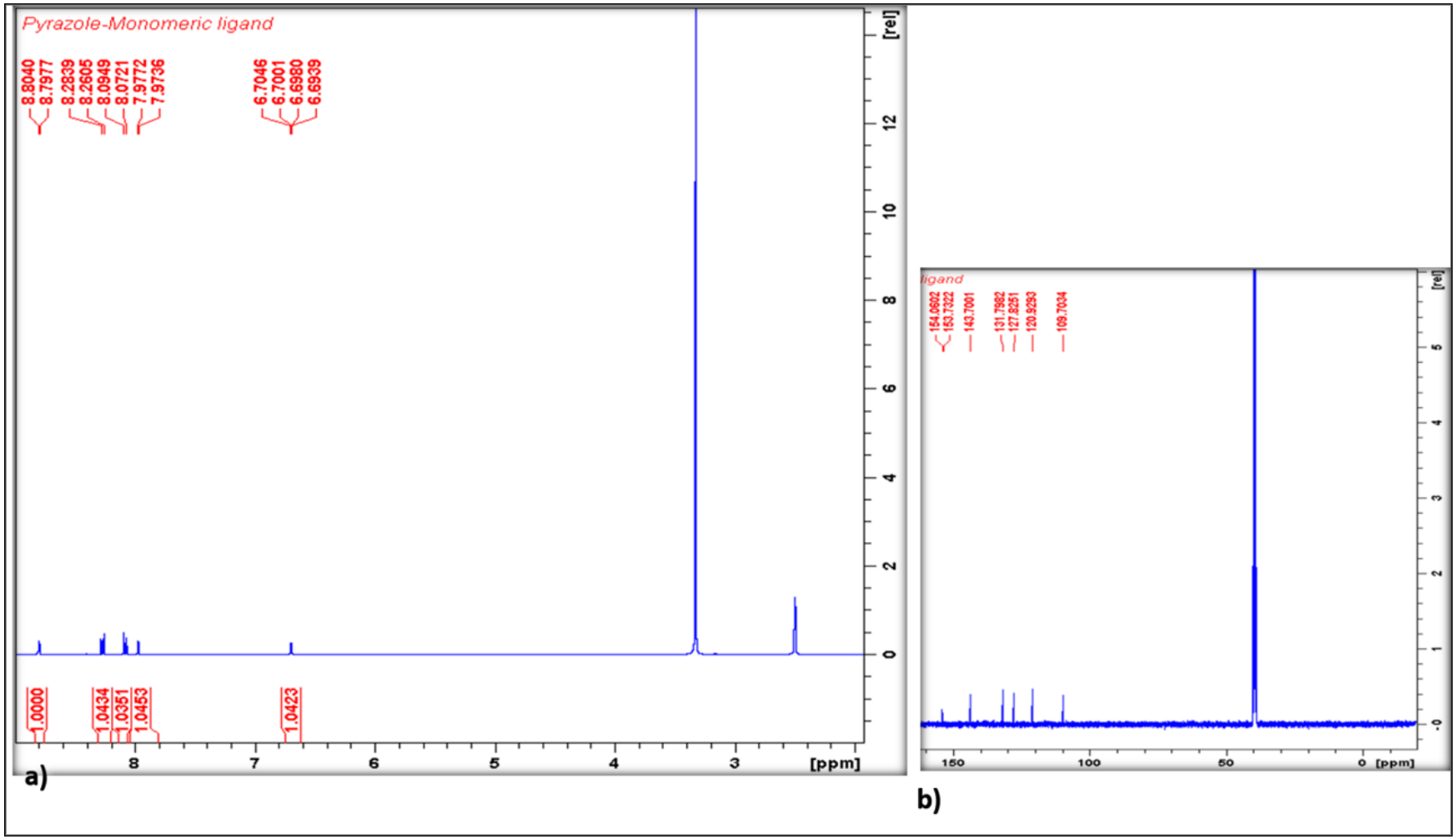

Figure 4.48: a) ^{1}H NMR spectrum (500 MHz) and b) ^{13}C NMR spectrum (100 MHz) spectra of 3-chloro-6-(1H-pyrazol-1-yl)pyridazine recorded in DMSO-d_6

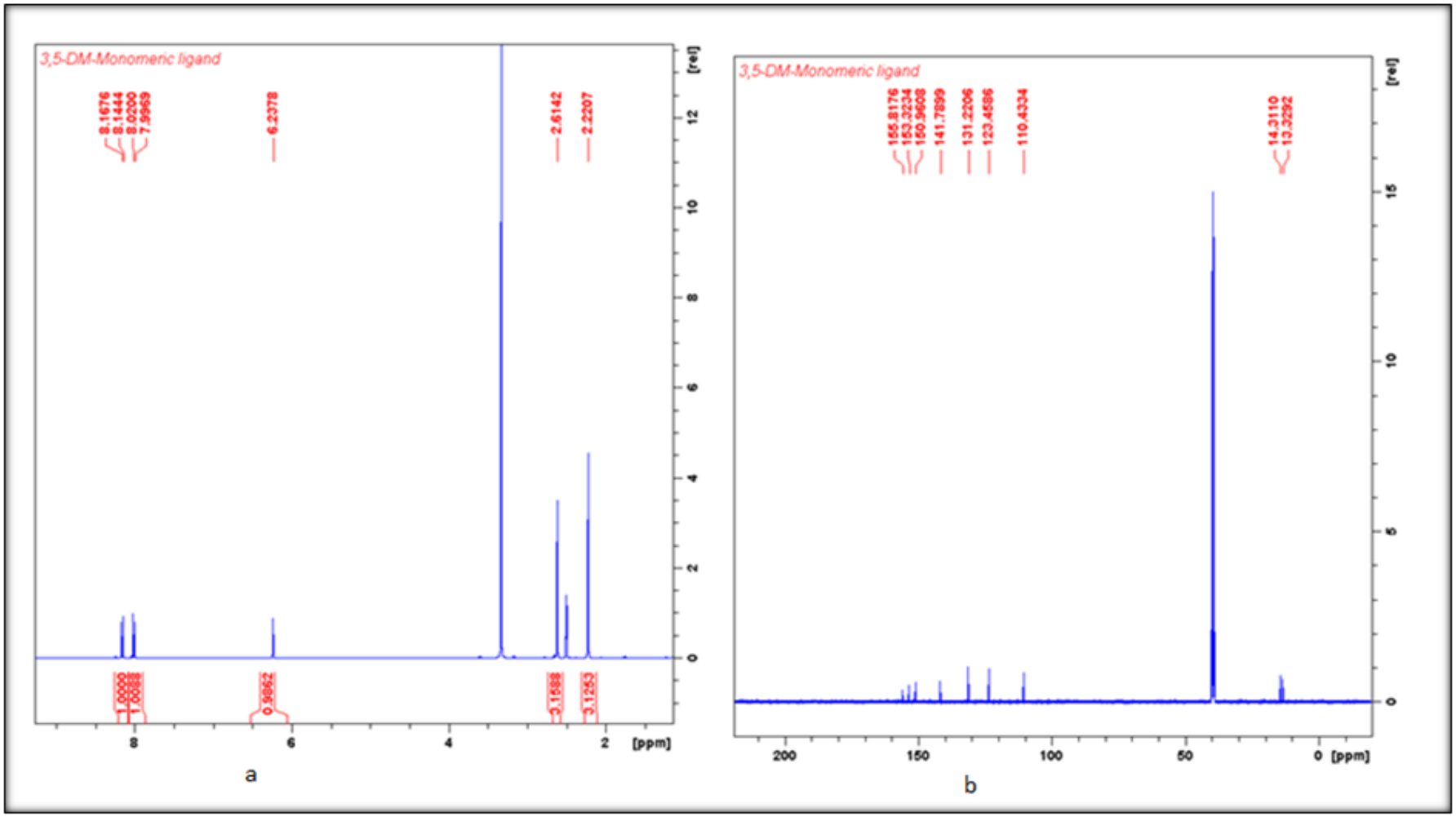

Figure 4.49: a) 1H NMR spectrum (500 MHz) and b) 13C NMR spectrum (100 MHz) of 3-chloro-6-(3, 5-dimethyl-1H-pyrazol-1-yl)pyridazine recorded in DMSO-d_6

[(η^6-*p*-cymene)(3-chloro-6-(1H-pyrazol-1-yl)pyridazine)Ru(Cl)]BF_4 (3a):

The complex [(η^6-*p*-cymene)(3-chloro-6-(1H-pyrazol-1-yl)pyridazine)Ru(Cl)]BF_4 was synthesised by reacting 674 mg of [(η^6-*p*-cymene)Ru(μ-Cl)(Cl)]$_2$ with 399.4 mg of 3-chloro-6-(1H-pyrazol-1-yl)pyridazine in the presence of 2.5 mmol of NH_4BF_4 in an appropriate solvent system. The reaction afforded orange crystals in 74.2% yield.

Table 4.22: Analytical data for complex [(η^6-*p*-cymene)(3-chloro-6-(1H-pyrazol-1-yl)pyridazine)Ru(Cl)]BF_4 (**3a**)

Technique	Data
Yield	74.2%, orange crystals
MS (ESI^+)	m/z = 451 (100%); $[C_{17}H_{19}ClN_4RuCl+H]^+$
^{1}H NMR (500 MHz, DMSO-d_6)	δ (ppm): 9.18 (d, J = 3.2 Hz, 1H, pyrazolyl), 9.02 (d, J = 2.2 Hz, 1H, pyrazolyl), 8.80 (d, J = 9.3 Hz, 1H, pyridazinyl), 8.58 (d, J = 9.3 Hz, 1H, pyridazinyl), 7.17 (dd, J = 3.2, 2.2 Hz, 1H, pyrazolyl), 6.17 (ddd, J = 12.1, 6.2, 1.1 Hz, 2H, Ar–*p-cym*), 5.99 (dd, J = 6.1, 1.1 Hz, 1H, Ar–*p-cym*), 5.87 (dd, J = 6.2, 1.1 Hz, 1H, Ar–*p-cym*), 2.79 (p, J = 13.8, 6.9 Hz, 1H, CH isopropyl, *p-cym*), 2.12 (s, 3H, CH_3, *p-cym*), 1.15 (t, J = 6.9 Hz, 6H, CH_3 isopropyl, *p-cym*)
^{13}C NMR (100 MHz, DMSO-d_6)	δ (ppm): 153.7 (N–C–N, pdzn), 150.9 (C=N, pzn), 148.8 (N=C–Cl, pdzn), 134.0 (C=C, pdzn), 132.9 (C=N, pzn), 121.9 (C=C, pdzn), 112.8 (C=C, pzn), 105.0, 101.9, 86.7, 86.6, 84.2, 84.1 (Ar–*p-cym*), 30.3 (CH, isopropyl, *p-cym*), 21.9 (CH_3, *p-cym*), 21.3, 17.8 (CH_3 isopropyl, *p-cym*)
FTIR (KBr, cm^{-1})	3085 (w, ν(C–H_arom)), 2959 (w, br, ν(C–H_aliph)), 2085 (ν(N=N, pdzn)), 1582 (w, sharp, ν(C=N, pdzn/pzn)), 1480, 1404 (s, sharp, ν(C=C, cym/pzn/pdzn)), 1284 (m, sharp, Ar–β–CH, cym), 1050 (vs, sharp, ν(BF_4^-)), 820–850, 780, 650 (m, sharp, ν(Ru–N, Ru–C_centroid, Ru–Cl))
Elemental Analysis	Calculated (%): C 37.94, H 3.56, N 10.41 Found (%): C 37.82, H 3.56, N 10.50
Figures	Figures 4.50-51

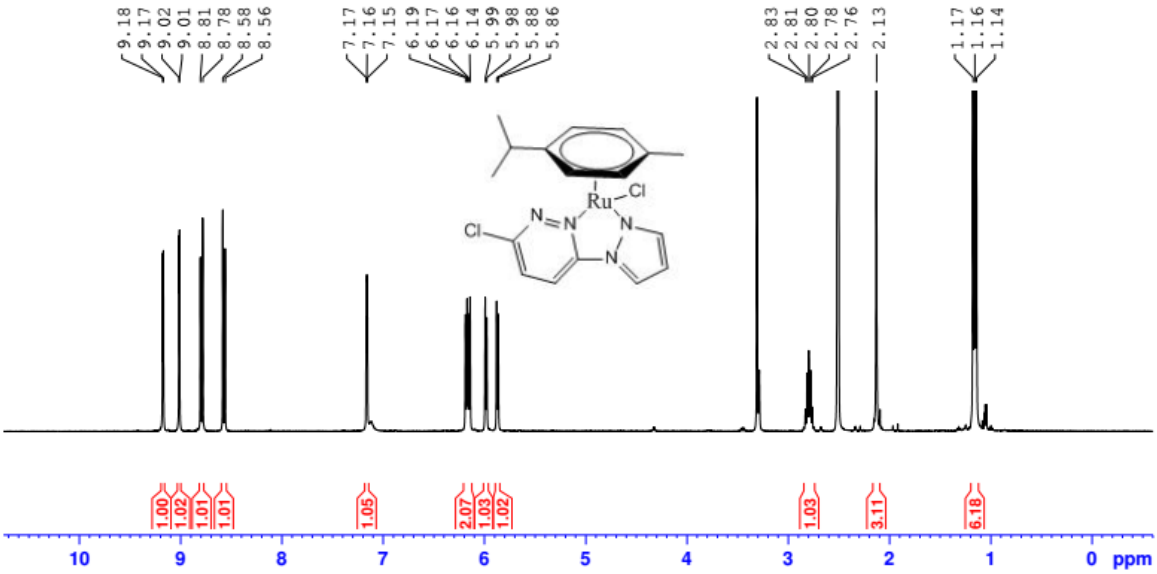

Figure 4.50: ^{1}H NMR spectrum (500 MHz, DMSO-d_6) of complex **3a.**

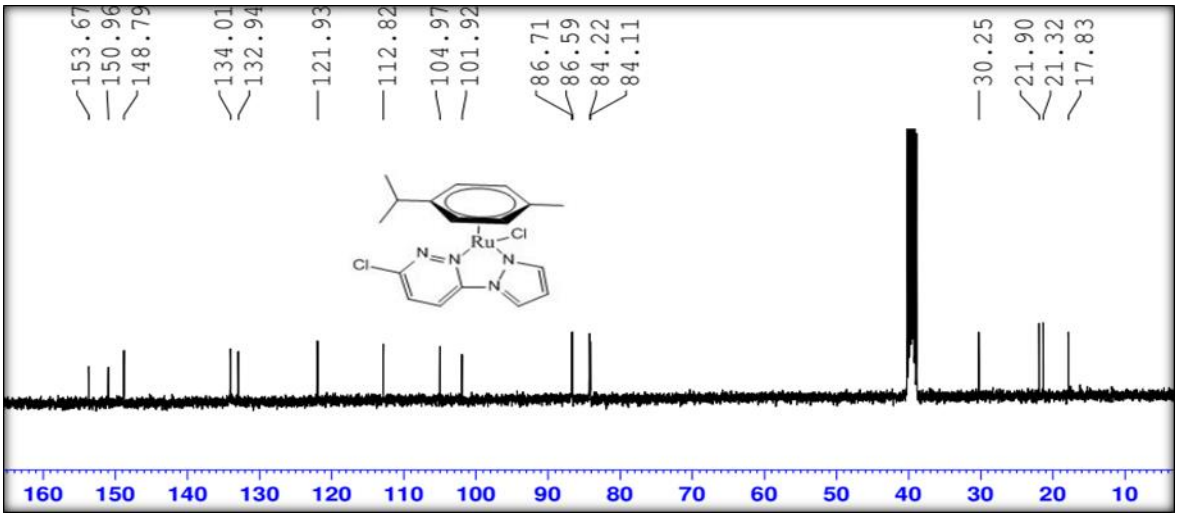

Figure 4.51: ^{13}C NMR spectrum (100 MHz, DMSO-d_6) of complex **3a**

[(η^6-*p*-cymene)(3-chloro-6-(1H-pyrazol-1-yl)pyridazine)Ru(Br)]BF_4 (3b):

The complex [(η^6-*p*-cymene)(3-chloro-6-(1H-pyrazol-1-yl)pyridazine)Ru(Br)]BF_4 was synthesised by reacting 718.4 mg of [(η^6-*p*-cymene)Ru(μ-Br)(Br)]$_2$ with 399.4 mg of 3-chloro-6-(1H-pyrazol-1-yl)pyridazine in the presence of 2.5 mmol of NH_4BF_4. The reaction afforded orange crystals in 75.5% yield.

Table 4.23: Analytical data for complex [(η⁶-*p*-cymene)(3-chloro-6-(1H-pyrazol-1-yl)pyridazine)Ru(Br)]BF_4 (**3b**)

Technique	Data
Yield	75.5%, orange crystals
MS (ESI^+)	m/z = 497 (100%); $[C_{17}H_{19}ClN_4RuBr+H]^+$
^1H NMR (500 MHz, DMSO-d_6)	δ (ppm): 9.18 (d, J = 3.2 Hz, 1H, pzn), 8.99 (d, J = 2.1 Hz, 1H, pzn), 8.78 (d, J = 9.3 Hz, 1H, pdzn), 8.57 (d, J = 9.3 Hz, 1H, pdzn), 7.17 (dd, J = 3.2, 2.1 Hz, 1H, pzn), 6.16 (m, 2H, Ar–*p-cym*), 5.99 (m, 1H, Ar–*p-cym*), 5.88 (dd, J = 6.3, 1.2 Hz, 1H, Ar–*p-cym*), 2.86 (h, J = 6.9 Hz, 1H, CH isopropyl, *p-cym*), 2.17 (s, 3H, CH_3, *p-cym*), 1.17 (dd, J = 8.6, 6.9 Hz, 6H, CH_3 isopropyl, *p-cym*)
^{13}C NMR (100 MHz, DMSO-d_6)	δ (ppm): 153.6 (N–C–N, pdzn), 150.8 (C=N, pzn), 149.1 (N=C–Cl, pdzn), 133.9 (C=C, pdzn), 132.9 (C=N, pzn), 121.8 (C=C, pdzn), 112.9 (C=C, pzn), 105.4, 101.8, 86.6, 84.6, 84.5 (Ar–*p-cym*), 30.3 (CH, isopropyl), 21.9 (CH_3, *p-cym*), 21.3, 17.8 (CH_3 isopropyl, *p-cym*)
FTIR (KBr, cm^{-1})	3083 (w, ν(C–H_arom)), 2875–3 (w, br, ν(C–H_aliph)), 1582 (w, sharp, ν(C=N, pdzn/pzn)), 1480, 1403 (s, sharp, ν(C=C, cym/pzn/pdzn)), 1168 (m, sharp, Ar–β–CH, cym), 1021 (vs, sharp, ν(BF_4^-)), 820–850, 780, 650 (m, sharp, ν(Ru–N, Ru–C_centroid, Ru–Cl))
Elemental Analysis	Calculated (%): C 35.05, H 3.29, N 9.62 Found (%): C 35.72, H 3.08, N 9.48
Figures	Figures 4.52-55

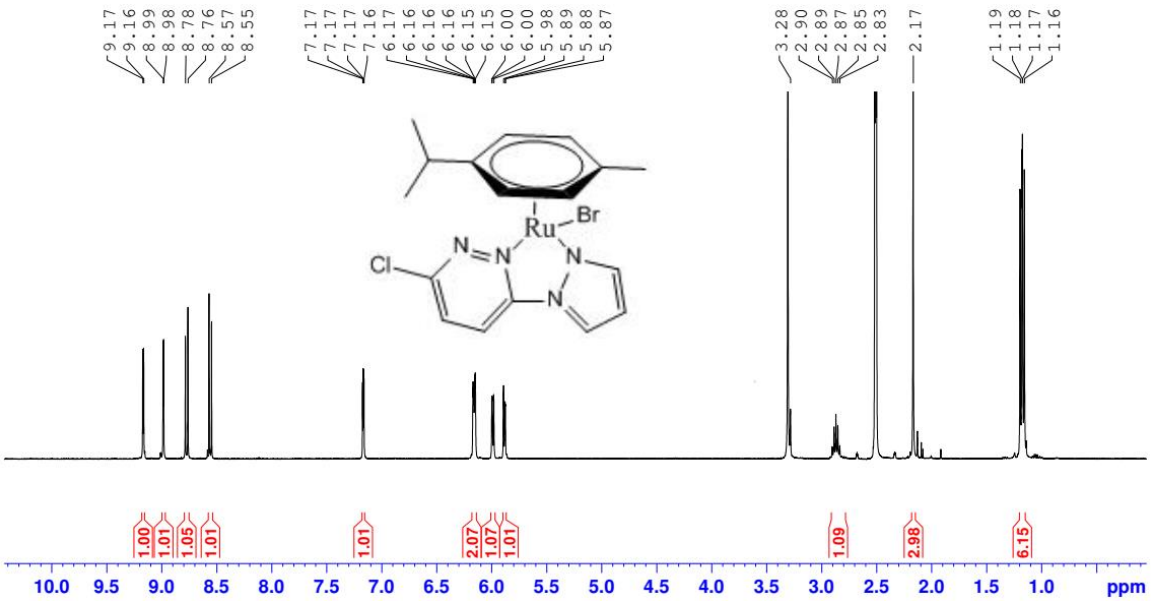

Figure 4.52: ^{1}H NMR spectrum (500 MHz, DMSO-d_6) of complex **3b.**

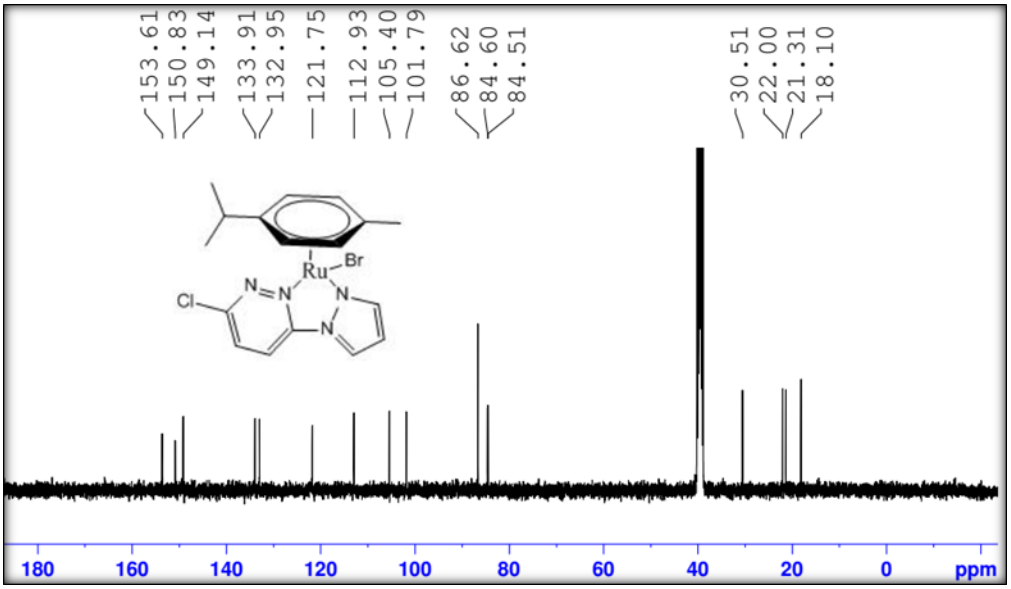

Figure 4.53: ^{13}C NMR spectrum (100 MHz, DMSO-d_6) of complex **3b.**

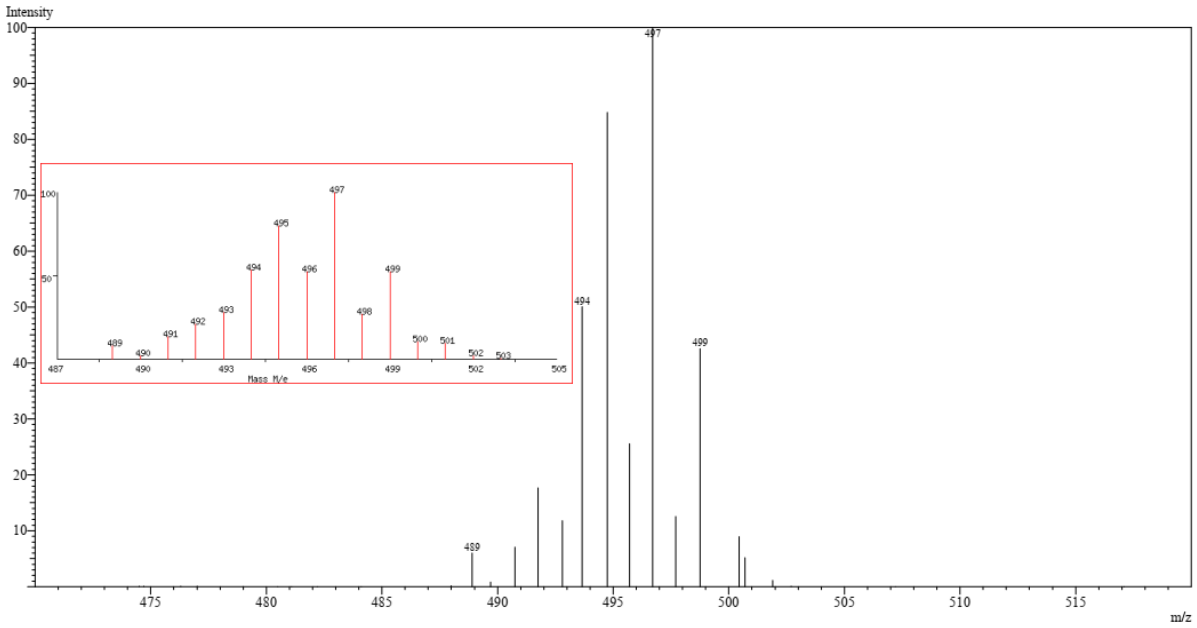

Figure 4.54: Low-resolution ESI$^+$ mass spectrum of complex 3b, showing a base peak at *m/z* 497 corresponding to the $[C_{17}H_{19}ClN_4RuBr+H]^+$ pseudomolecular ion. *Inset:* Predicted isotopic distribution generated using SIS Isotope Pattern Calculator (https://www.sisweb.com/mstools/isotope.htm, accessed December 13, 2024).

Figure 4.55: FTIR spectrum of complex **3b** (dispersed in KBr).

[(η^6-*p*-cymene)(3-chloro-6-(1H-pyrazol-1-yl)pyridazine)Ru(I)]BF_4 (3c):

The complex [(η^6-*p*-cymene)(3-chloro-6-(1H-pyrazol-1-yl)pyridazine)Ru(I)]BF_4 was synthesised by reacting 1076 mg of [(η^6-cymene)Ru(μ-I)(I)]$_2$ with 399.4 mg of 3-chloro-6-(1H-pyrazol-1-yl)pyridazine in the presence of 2.5 mmol of NH_4BF_4. The reaction yielded orange crystals in 40% yield.

Table 4.24: Analytical data for complex [(η^6-*p*-cymene)(3-chloro-6-(1H-pyrazol-1-yl)pyridazine)Ru(I)]BF_4 (**3c**)

Technique	Data
Yield	40%, orange crystals
MS (ESI^+)	m/z = 543 (100%); $[C_{17}H_{19}ClN_4RuI+H]^+$
^{1}H NMR (500 MHz, DMSO-d_6)	δ (ppm): 9.19 (d, J = 3.2 Hz, 1H, pzn), 8.94 (d, J = 2.2 Hz, 1H, pzn), 8.78 (d, J = 9.3 Hz, 1H, pdzn), 8.55 (d, J = 9.3 Hz, 1H, pdzn), 7.17 (dd, J = 3.2, 2.2 Hz, 1H, pzn), 6.21 (dd, J = 6.4, 1.3 Hz, 1H, Ar–*p-cym*), 6.14 (dd, J = 6.2, 1.2 Hz, 1H, Ar–*p-cym*), 5.99 (dd, J = 6.4, 1.3 Hz, 1H, Ar–*p-cym*), 5.94 (dd, J = 6.2, 1.2 Hz, 1H, Ar–*p-cym*), 2.97 (h, J = 6.9 Hz, 1H, CH isopropyl, *p-cym*), 2.21 (s, 3H, CH_3, *p-cym*), 1.19 (d, J = 11.0, 6.9 Hz, 6H, CH_3 isopropyl, *p-cym*)
^{13}C NMR (100 MHz, DMSO-d_6)	δ (ppm): 153.5 (N–C–N, pdzn), 150.3 (N=C–Cl, pdzn), 149.8 (C=N, pzn), 133.7 (C=N, pzn), 133.0 (C=C, pdzn), 121.5 (C=C, pdzn), 113.5 (C=C, pzn), 106.0, 102.2, 86.8, 86.5, 85.5, 84.9 (Ar–*p-cym*), 31.1 (CH isopropyl, *p-cym*), 22.8 (CH_3, *p-cym*), 21.9, 19.1 (CH_3 isopropyl, *p-cym*)
FTIR (KBr, cm^{-1})	3107 (w, ν(C–H_arom)), 2976 (w, br, ν(C–H_aliph)), 2085 (ν(N=N, pdzn)), 1581 (w, sharp, ν(C=N, pdzn/pzn)), 1433 (s, sharp, ν(C=C, cym/pzn/pdzn)), 1284 (m, sharp, Ar–β–CH, cym), 1030 (vs, sharp, ν(BF_4^-)), 820–850, 780, 650 (m, sharp, ν(Ru–N, Ru–C_centroid, Ru–Cl))
Elemental Analysis	Calculated (%): C 32.43, H 3.04, N 8.90 Found (%): C 32.92, H 3.32, N 9.07
Figures	Figures 4.56 – 57

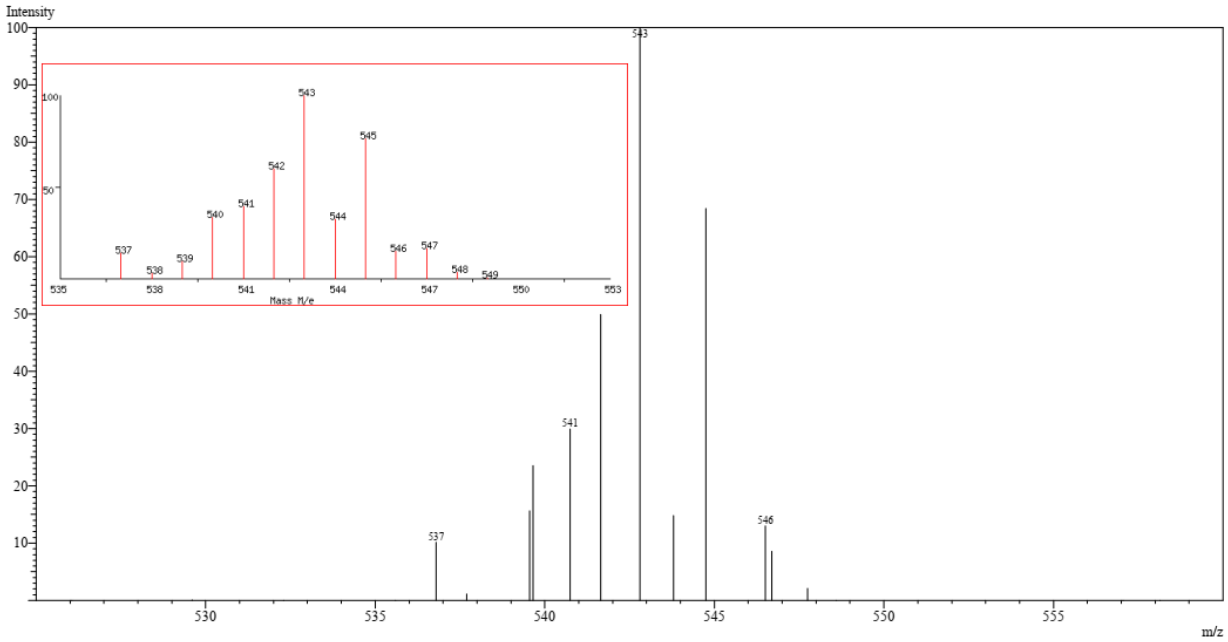

Figure 4.56: Low-resolution ESI$^+$ mass spectrum of complex **3c**, showing a base peak at m/z 543, corresponding to the $[C_{17}H_{19}ClN_4RuI+H]^+$ pseudomolecular ion (100%). Inset: Predicted isotopic distribution generated using the SIS Isotope Pattern Calculator (https://www.sisweb.com/mstools/isotope.htm, accessed December 13, 2024).

Figure 4.57: FTIR spectrum of complex **3c** (dispersed in KBr).

[(η^6-*p*-cymene)(3-chloro-6-(3,5-dimethyl-1H-pyrazol-1-yl)pyridazine)Ru(Cl)]BF_4 (4a):

The complex [(η^6-*p*-cymene)(3-chloro-6-(3,5-dimethyl-1H-pyrazol-1-yl)pyridazine)Ru(Cl)]BF_4 was synthesised by reacting 674 mg of [(η^6-*p*-cymene)Ru(μ-Cl)(Cl)]$_2$ with 457 mg of 5-chloro-2-(3,5-dimethyl-1H-pyrazol-1-yl)pyridine in the presence of 2.5 mmol of NH_4BF_4. The reaction yielded orange crystals in 82% yield.

Table 4.25: Analytical data for complex [(η^6-*p*-cymene)(3-chloro-6-(3,5-dimethyl-1H-pyrazol-1-yl)pyridazine)Ru(Cl)]BF_4 (**4a**)

Technique	Data
Yield	82%, orange crystals
MS (ESI^+)	m/z = 480 (100%); $[C_{19}H_{24}ClN_4RuCl+H]^+$
^{1}H NMR (500 MHz, DMSO-d_6)	δ (ppm): 1.05 (dd, J = 15.7, 6.9 Hz, 6H, CH_3 isopropyl, *p-cym*), 2.17 (s, 3H, CH_3, *p-cym*), 2.64 (m, 1H, CH isopropyl, *p-cym*), 2.72 (s, 3H, CH_3, pzn), 2.78 (s, 3H, CH_3, pzn), 5.97 (m, 2H, Ar–*p-cym*), 6.11 (dd, J = 6.3, 1.2 Hz, 1H, Ar–*p-cym*), 6.29 (dd, J = 6.2, 1.2 Hz, 1H, Ar–*p-cym*), 6.74 (s, 1H, pzn), 7.20 (s, 1H, pdzn), 8.40 (d, J = 2.8 Hz, 1H, pdzn)
^{13}C NMR (100 MHz, DMSO-d_6)	δ (ppm): 14.3, 16.1 (CH_3, pzn), 18.9 (CH_3, *p-cym*), 21.8, 22.7 (CH_3 isopropyl, *p-cym*), 30.9 (CH, isopropyl, *p-cym*), 83.6, 84.3, 85.7, 89.4, 105.1, 105.5 (Ar–*p-cym*), 114.7, 122.8, 133.6 (C=C, pzn), 146.5, 151.8 (C=C, pdzn), 153.2 (N=C–Cl, pdzn), 158.0 (N–C–N, pdzn)
FTIR (KBr, cm^{-1})	3100 (w, ν(C–H_arom)), 2970 (w, br, ν(C–H_aliph)), 2085 (ν(N=N, pdzn)), 1578 (w, sharp, ν(C=N, pdzn/pzn)), 1431 (s, sharp, ν(C=C, cym/pzn/pdzn)), 1284 (m, sharp, Ar–β–CH, cym), 1053 (vs, sharp, ν(BF_4^-)), 820–850, 780, 650 (m, sharp, ν(Ru–N, Ru–C_centroid, Ru–Cl))
Elemental Analysis	Calculated (%): C 47.60, H 4.84, N 11.69 Found (%): C 47.48, H 4.73, N 11.58
Figures	Figures 4.58-59

w/m/$s_{shrp/br}$ (= weak/ medium/ strong/ sharp/ broad $\nu_{(funct.\ gr)}$)

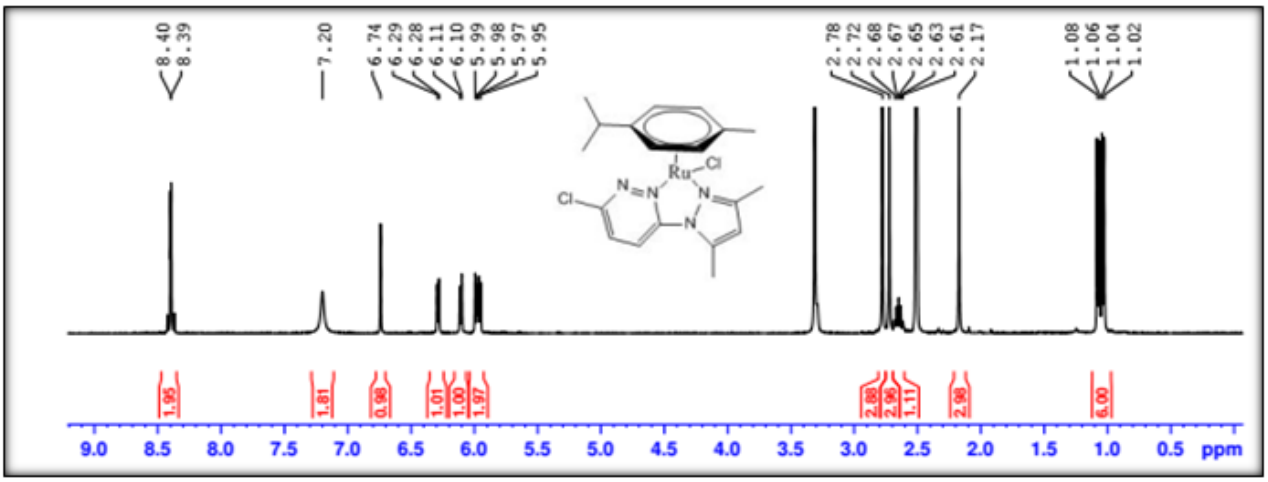

Figure 4.58: ^{1}H NMR spectrum (500 MHz, DMSO-d_6) of complex **4a**

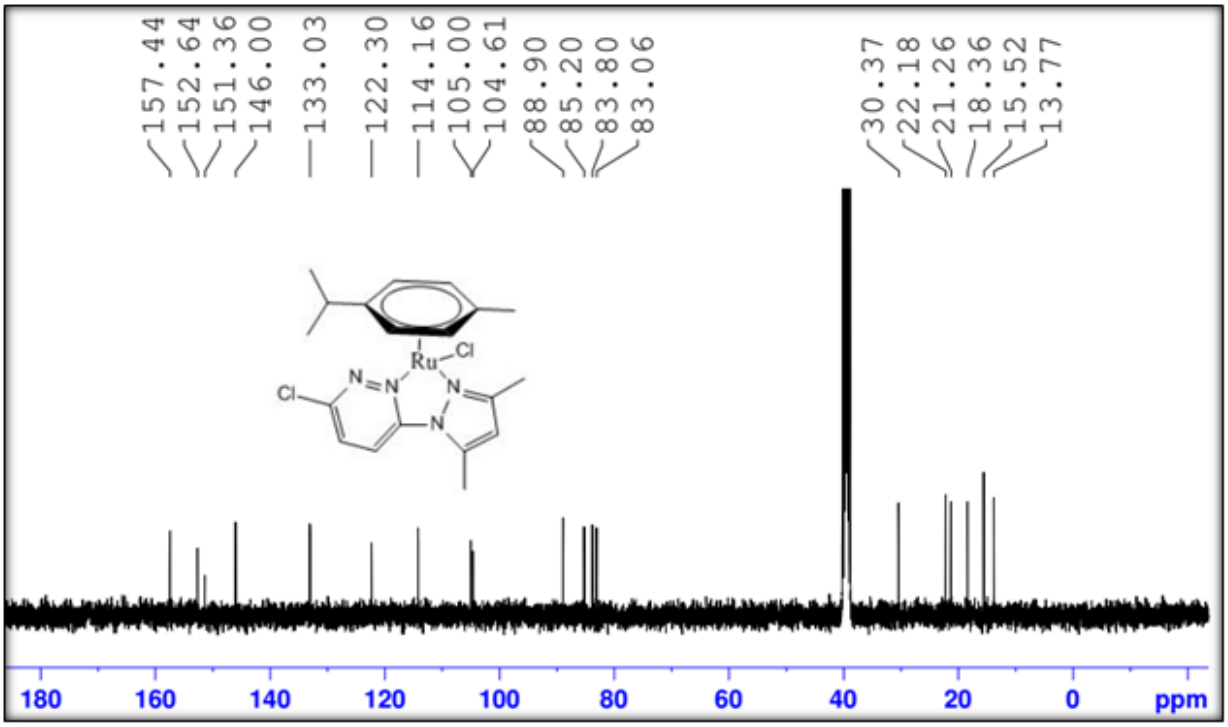

Figure 4.59: ^{13}C NMR spectrum (100 MHz, DMSO-d_6) of complex **4a**

[(η^6-*p*-cymene)(3-chloro-6-(3,5-dimethyl-1H-pyrazol-1-yl)pyridazine)Ru(Br)]BF_4 (4b):

The complex [(η^6-*p*-cymene)(3-chloro-6-(3,5-dimethyl-1H-pyrazol-1-yl)pyridazine)Ru(Br)]BF_4 was synthesised from 718.4 mg of [(η^6-*p*-cymene)Ru(μ-Br)(Br)]$_2$, 457 mg of 5-chloro-2-(3,5-dimethyl-1H-pyrazol-1-yl)pyridine, and 2.5 mmol of NH_4BF_4. The reaction afforded an orange solid in 70% yield.

Table 4.26: Analytical data for complex [(η^6-*p*-cymene)(3-chloro-6-(3,5-dimethyl-1H-pyrazol-1-yl)pyridazine)Ru(Br)]BF_4 **(4b)**

Technique	Data
Yield	70%, orange solid
MS (ESI^+)	m/z = 525 (100%); $[C_{19}H_{24}ClN_4RuBr+H]^+$
^{1}H NMR (500 MHz, DMSO-d_6)	δ (ppm): 1.07 (dd, J = 16.6, 6.9 Hz, 6H, CH_3 isopropyl, *p-cymene*), 2.26 (s, 3H, CH_3, *p-cymene*), 2.64 (m, 1H, CH isopropyl, *p-cymene*), 2.74 (s, 6H, CH_3, pzn), 5.98 (dd, J = 18.5, 6.3 Hz, 2H, Ar–*p-cymene*), 6.09 (m, 1H, Ar–*p-cymene*), 6.25 (d, J = 6.3 Hz, 1H, Ar–*p-cymene*), 6.74 (s, 1H, Ar–*p-cymene*), 7.09 (s, 1H, pzn), 8.38 (m, 2H, pdzn)
^{13}C NMR (100 MHz, DMSO-d_6)	δ (ppm): 14.3, 16.4 (CH_3, pzn), 19.5 (CH_3, *p-cymene*), 21.7, 22.8 (CH_3 isopropyl, *p-cymene*), 31.1 (CH isopropyl, *p-cymene*), 84.2, 84.8, 85.7, 89.2, 104.5, 106.3 (Ar–*p-cymene*), 114.7, 122.6, 133.5 (C=C, pzn), 146.6, 153.1 (C=C, pdzn), 153.2 (N=C–Cl, pdzn), 158.4 (N–C–N, pdzn)
FTIR (KBr, cm^{-1})	3100 (w, ν(C–H_arom)), 2970 (w, br, ν(C–H_aliph)), 2085 (ν(N=N, pdzn)), 1578 (w, sharp, ν(C=N, pdzn/pzn)), 1431 (s, sharp, ν(C=C, cym/pzn/pdzn)), 1284 (m, sharp, Ar–β–CH, cym), 1053 (vs, sharp, ν(BF_4^-)), 820–850, 780, 650 (m, sharp, ν(Ru–N, Ru–C_centroid, Ru–Cl))
Elemental Analysis	Calculated (%): C 47.54; H 4.83; N 11.65 Found (%): C 47.45; H 4.69; N 11.60
Figures	Figures 4.60-63

w/m/$s_{shrp/br}$ (= weak/medium/strong/sharp/broad $\nu_{(funct.\ gr)}$)

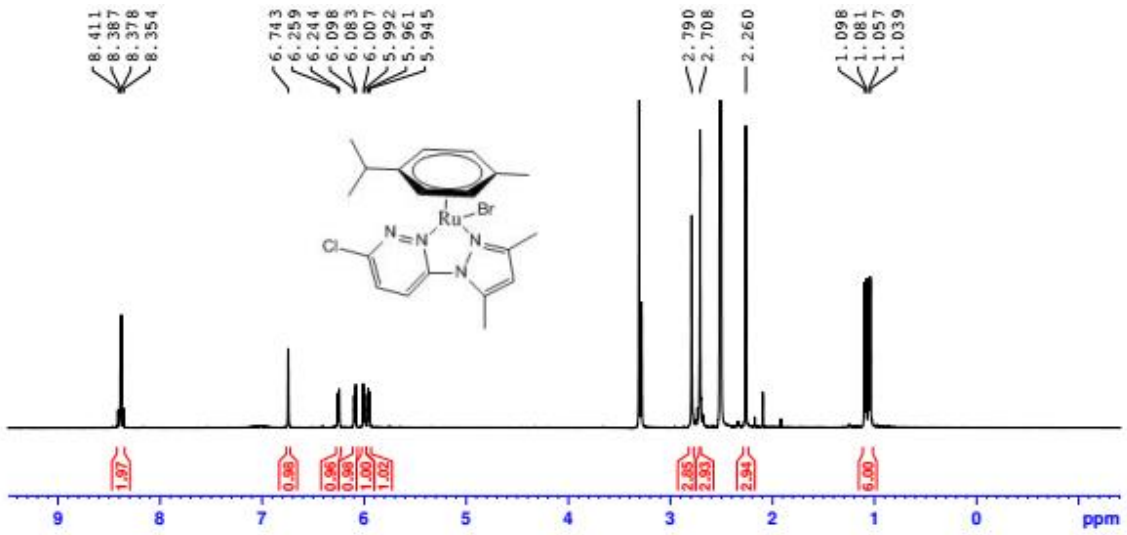

Figure 4.60: [1]HNMR spectrum (500 MHz, DMSO-d_6) of complex **4b**

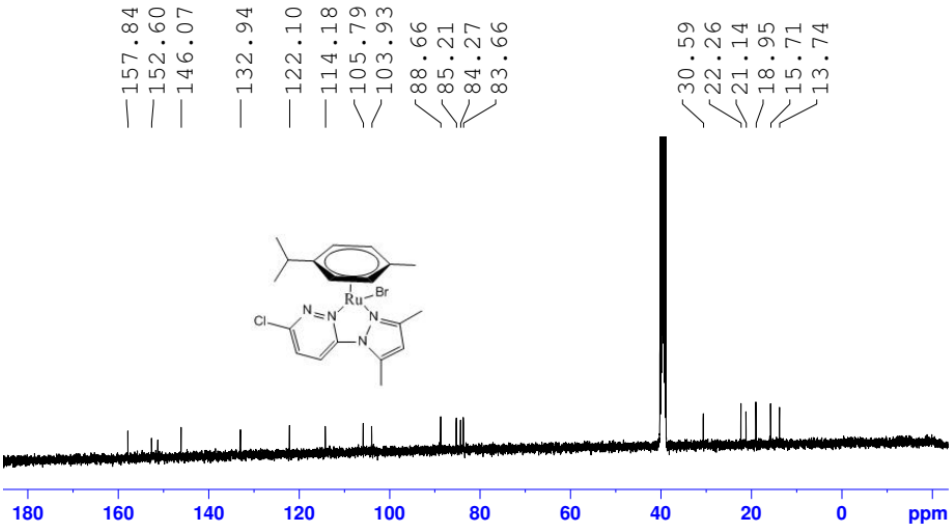

Figure 4.61: [13]C NMR spectrum (100 MHz, DMSO-d_6) of complex **4b**

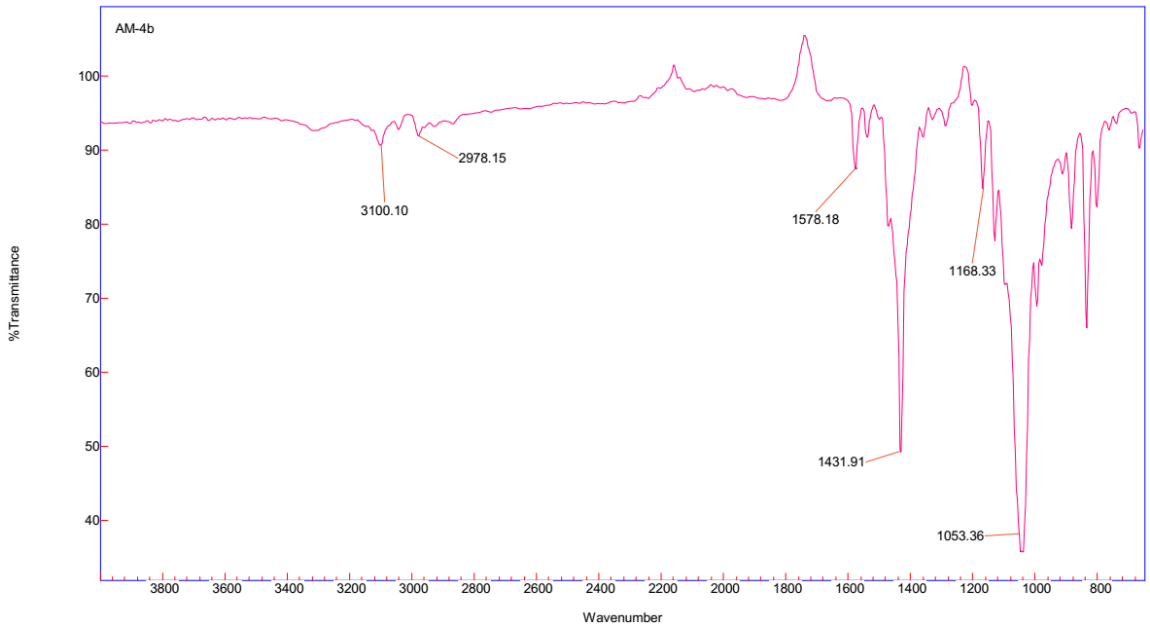

Figure 4.62: FTIR spectrum of complex **4b** recorded in KB

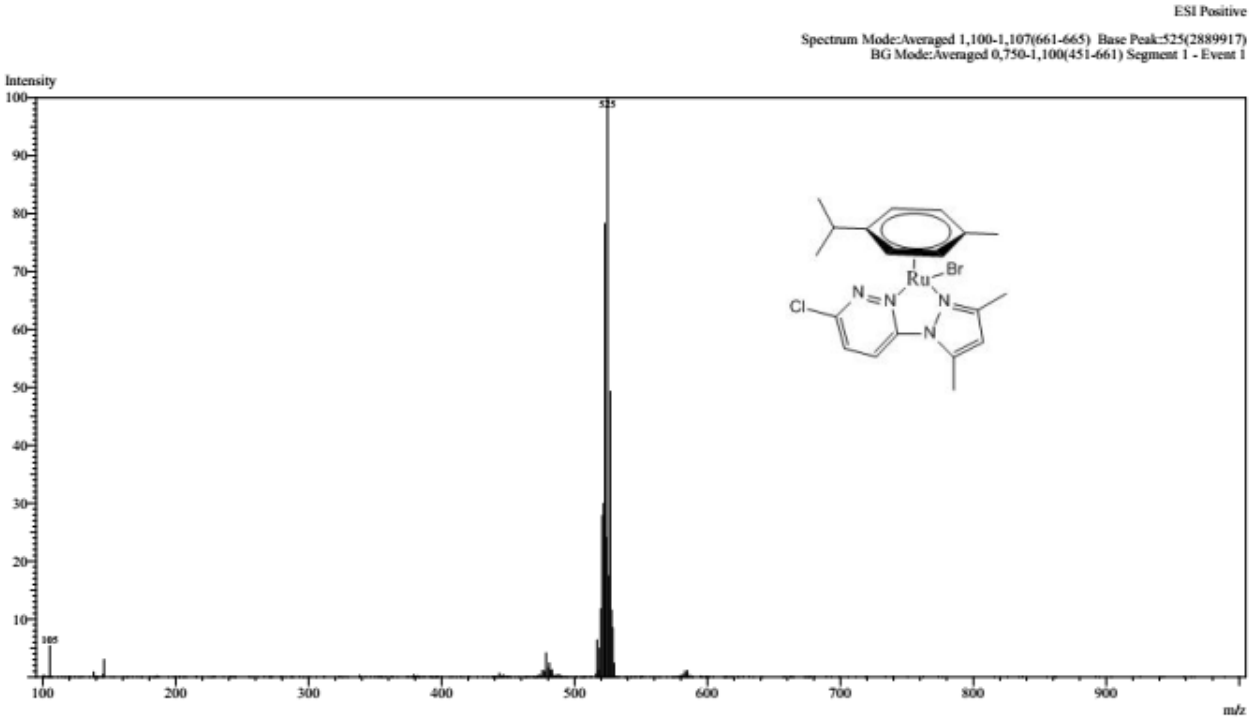

Figure 4.63: Low-resolution mass spectrum of complex **4b**, showing a base peak at *m/z* 525 (100%) corresponding to the $[C_{18}H_{22}ClN_4RuBr+H]^+$ pseudo-molecular ion.

[(η^6-*p*-cymene)(3-chloro-6-(3,5-dimethyl-1H-pyrazol-1-yl)pyridazine)Ru(I)]BF_4 (4c):

The complex [(η^6-*p*-cymene)(3-chloro-6-(3,5-dimethyl-1H-pyrazol-1-yl)pyridazine)Ru(I)]BF_4 was synthesised from 1076 mg of [(η^6-*p*-cymene)Ru(μ-I)(I)]$_2$, 457 mg of 5-chloro-2-(3,5-dimethyl-1H-pyrazol-1-yl)pyridine, and 2.5 mmol of NH_4BF_4. The reaction yielded an orange solid in 70% yield.

Table 4.27: Analytical data for complex [(η^6-*p*-cymene)(3-chloro-6-(3,5-dimethyl-1H-pyrazol-1-yl)pyridazine)Ru(I)]BF_4 (**4c**)

Technique	Data
Yield	70%, orange solid
MS (ESI^+)	m/z = 571 (100%), $[C_{19}H_{24}ClN_4RuI+H]^+$
^{1}H NMR (500 MHz, DMSO-d_6)	δ (ppm): 1.05 (dd, J = 16.9, 6.9 Hz, 6H, CH_3 isopropyl, *p-cym*), 2.17 (s, 3H, CH_3, *p-cym*), 2.64 (m, 1H, CH isopropyl, *p-cym*), 2.72 (s, 3H, CH_3 pzn), 2.78 (s, 3H, CH_3 pzn), 5.97 (m, 2H, Ar–*p-cym*), 6.11 (dd, J = 6.4, 1.2 Hz, 1H, Ar–*p-cym*), 6.29 (dd, J = 6.4, 1.2 Hz, 1H, Ar–*p-cym*), 6.74 (s, 1H, Ar–*p-cym*), 7.20 (s, 1H, pdzn), 8.40 (d, J = 2.8 Hz, 1H, pdzn)
^{13}C NMR (100 MHz, DMSO-d_6)	δ (ppm): 14.3, 16.7 (CH_3, pzn), 20.5 (CH_3, *p-cym*), 21.5, 23.0 (CH_3 isopropyl, *p-cym*), 31.7 (CH isopropyl, *p-cym*), 84.3, 85.2, 85.3, 86.0, 88.7, 103.7, 107.8 (Ar–*p-cym*), 114.7, 122.3, 133.3 (C=C, pzn), 146.7, 151.5 (C=C, pdzn), 153.0 (N=C–Cl, pdzn), 159.0 (N–C–N, pdzn)
FTIR (KBr, cm^{-1})	3099 (w, ν(C–H_arom)), 2976 (w, br, ν(C–H_aliph)), 2092 (ν(N=N, pdzn)), 1578 (w, sharp, ν(C=N, pdzn/pzn)), 1432 (s, sharp, ν(C=C, cym/pzn/pdzn)), 1287 (m, sharp, Ar–β–CH, cym), 1030 (vs, sharp, ν(BF_4^-)), 820–850, 780, 650 (m, sharp, ν(Ru–N, Ru–C_centroid, Ru–Cl))
Elemental Analysis	Calculated (%): C 39.98; H 4.06; N 6.21 Found (%): C 39.85; H 3.96; N 9.84
Figures	Figures 4.64-67

w/m/$s_{shrp/br}$ (= weak/medium/strong/sharp/broad $\nu_{(funct.\ gr)}$)

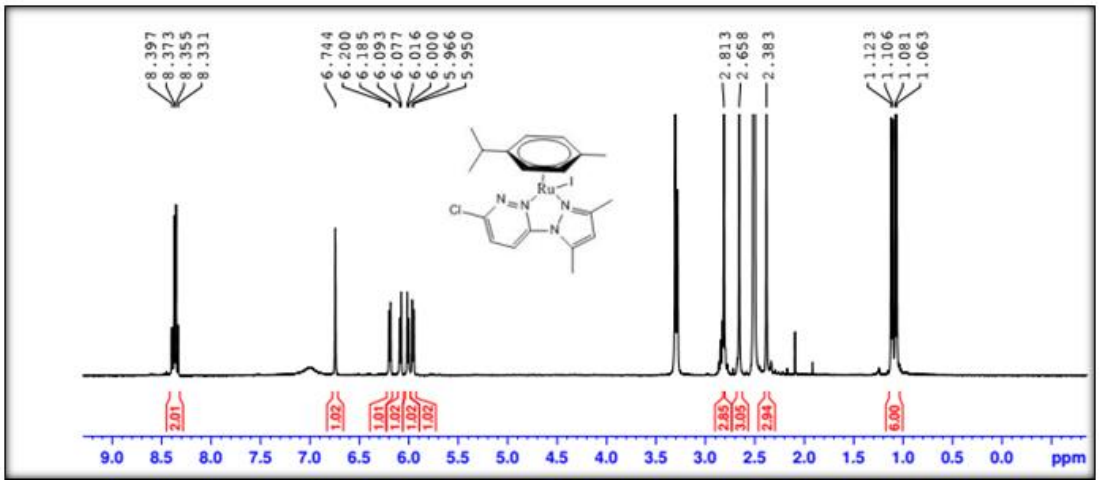

Figure 4.64: ^{1}H NMR spectrum (500 MHz, DMSO-d_6) of complex **4c**

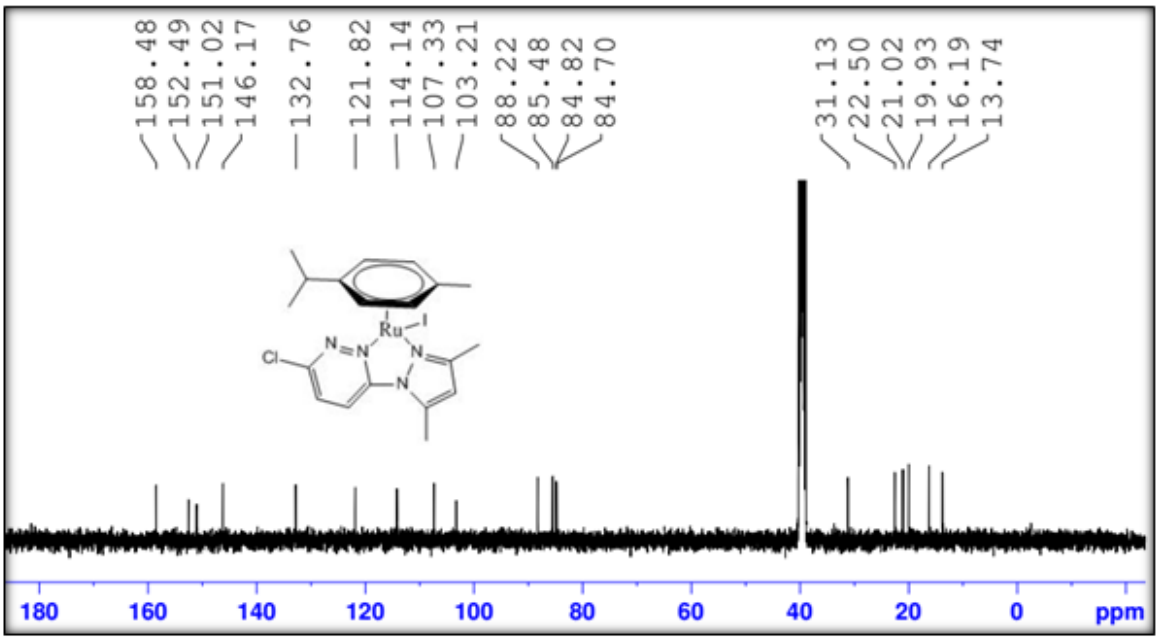

Figure 4.65: ^{13}C NMR spectrum (100 MHz, DMSO-d_6) of complex **4c**

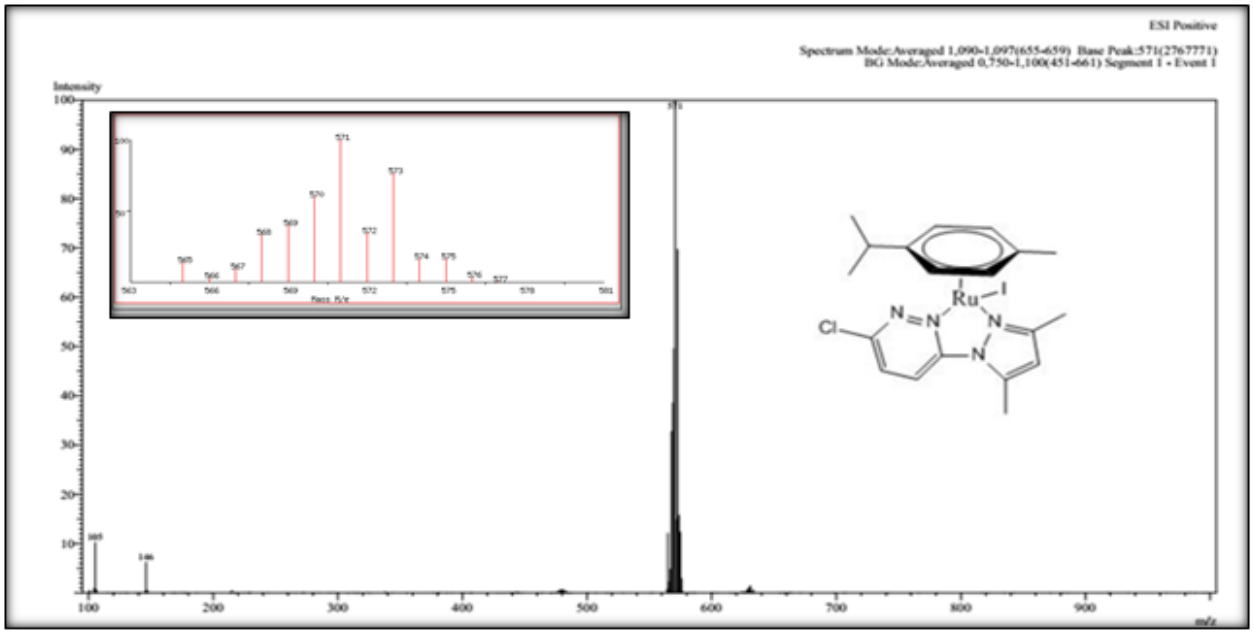

Figure 4.66: Low-resolution mass spectrum of complex **4c**, showing a base peak at m/z 571 (100%) corresponding to the pseudo-molecular ion $[C_{19}H_{24}ClN_4RuI+H]^+$. Inset: Predicted isotopic distribution generated using the SIS Isotope Pattern Calculator (https://www.sisweb.com/mstools/isotope.htm, accessed December 13, 2024).

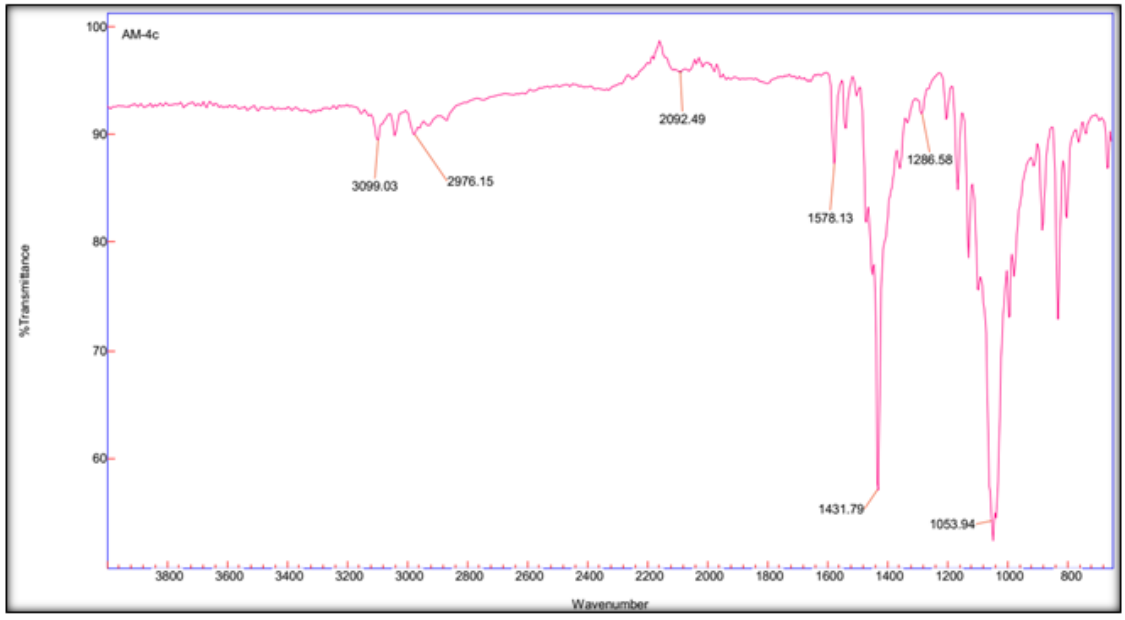

Figure 4.67: FTIR spectrum (dispersed in KBr) of complex **4c**

[(η^6-toluene)(3-chloro-6-(1H-pyrazol-1-yl)pyridazine)Ru(Cl)]BF_4 (9):

The complex was synthesised by reacting 581 mg of [(η^6-toluene)Ru(μ-Cl)(Cl)]$_2$, 399.4 mg of 3-chloro-6-(1H-pyrazol-1-yl)pyridazine, and 2.5 mmol of NH_4BF_4. The reaction afforded orange crystalline solids in 55.6% yield.

Table 4.28: Analytical data for [(η^6-Toluene)(3-chloro-6-(1H-pyrazol-1-yl)pyridazine)Ru(Cl)]BF_4 **(9)**

Technique	Data
Yield	55.6%, orange crystalline solid
MS (ESI^+)	m/z = 409 (100%), $[C_{14}H_{13}ClN_4RuCl+H]^+$
^{1}H NMR (500 MHz, DMSO-d_6)	δ (ppm): 2.23 (s, 3H, CH_3, toluene), 5.94 (dd, J = 6.0, 15.3 Hz, Ar_toluene), 6.20 (t, J = 5.9 Hz, 1H, Ar_toluene), 6.29 (t, J = 5.9 Hz, 1H, Ar_toluene), 7.15 (t, J = 2.6 Hz, 1H, pzn), 8.58 (d, J = 9.3 Hz, 1H, pdzn), 8.81 (d, J = 9.3 Hz, 1H, pdzn), 9.04 (d, J = 2.1 Hz, 1H, pzn), 9.18 (d, J = 3.2 Hz, 1H, pzn)
^{13}C NMR (100 MHz, DMSO-d_6)	δ (ppm): 18.9 (CH_3, toluene), 81.8, 83.9, 84.4, 90.2, 90.3, 105.3 (Ar_toluene), 113.3, 133.4 (C=C, pzn), 122.4, 134.6 (C=C, pdzn), 149.6 (N=C–Cl, pdzn), 151.5 (C=N, pzn), 154.0 (N–C–N, pdzn)
FTIR (KBr, cm^{-1})	3100 (w, ν(C–H_arom)), 2976 (w, br, ν(C–H_aliph)), 2086 (ν(N=N, pdzn)), 1580 (w, sharp, ν(C=N, pdzn/pzn)), 1407 (s, sharp, ν(C=C, cym/pzn/pdzn)), 1170 (m, sharp, Ar–β–CH, toluene), 1038 (vs, sharp, ν(BF_4^-)), 820–850, 780, 650 (m, sharp, ν(Ru–N, Ru–C_centroid, Ru–Cl))
Elemental Analysis	Calculated (%): C 43.80; H 4.97; N 12.02 Found (%): C 40.97; H 3.12; N 13.72
Figures	Figures 4.68-71

w/m/$s_{shrp/br}$ (= weak/medium/strong/sharp/broad $\nu_{(funct.\ gr)}$)

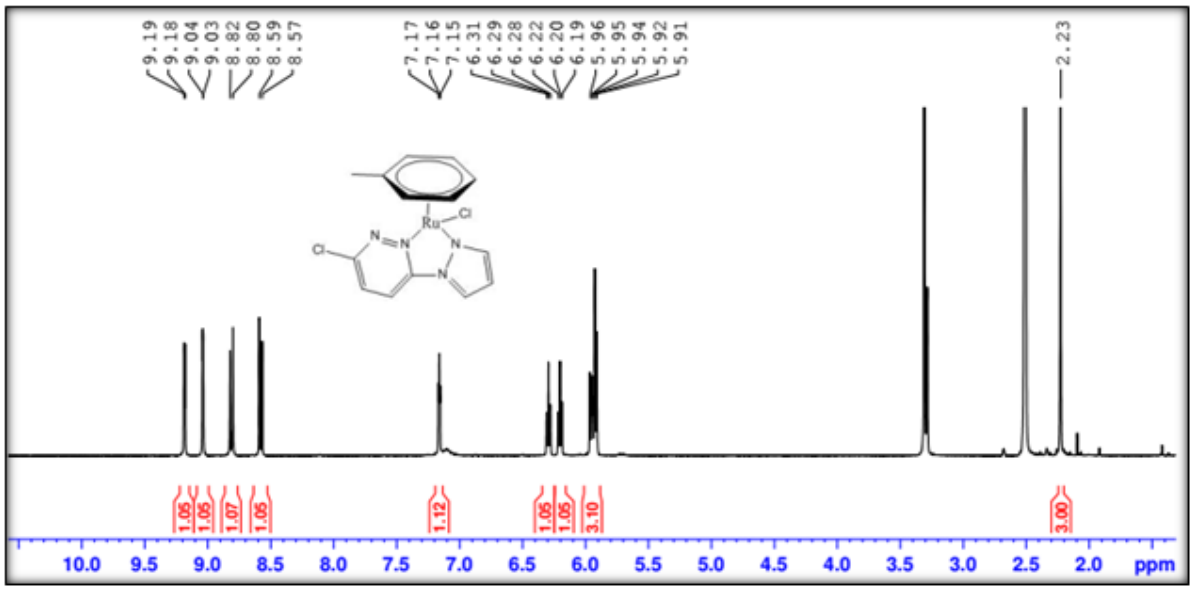

Figure 4.68: ^{1}H NMR spectrum (500 MHz, DMSO-d_6) of complex **9**

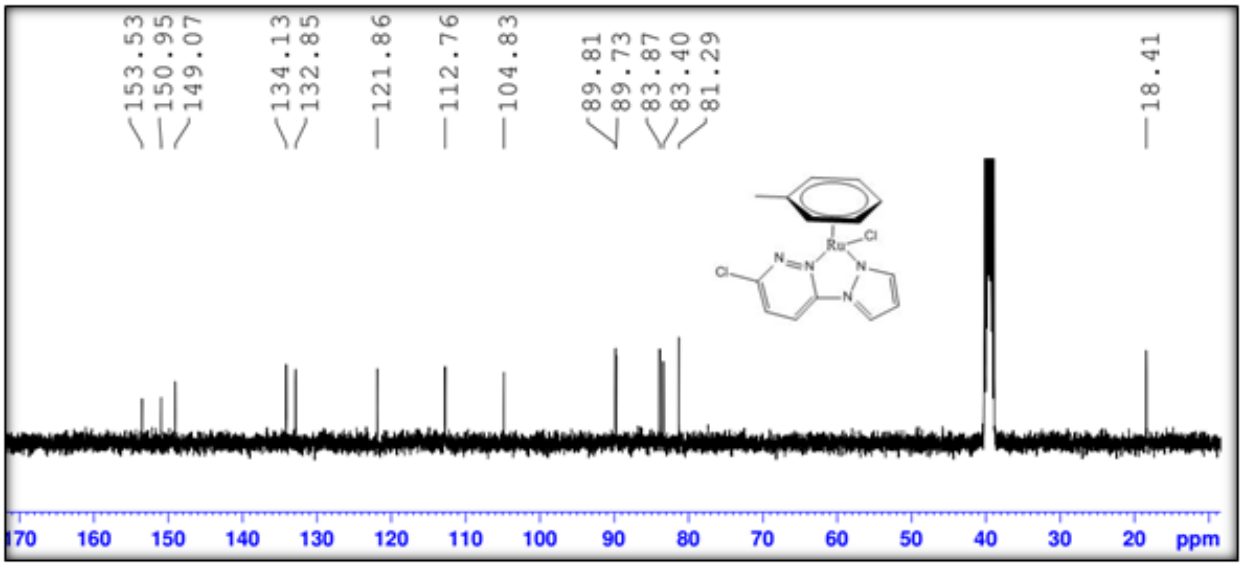

Figure 4.69: ^{13}C NMR spectrum (100 MHz, DMSO-d_6) of complex **9**

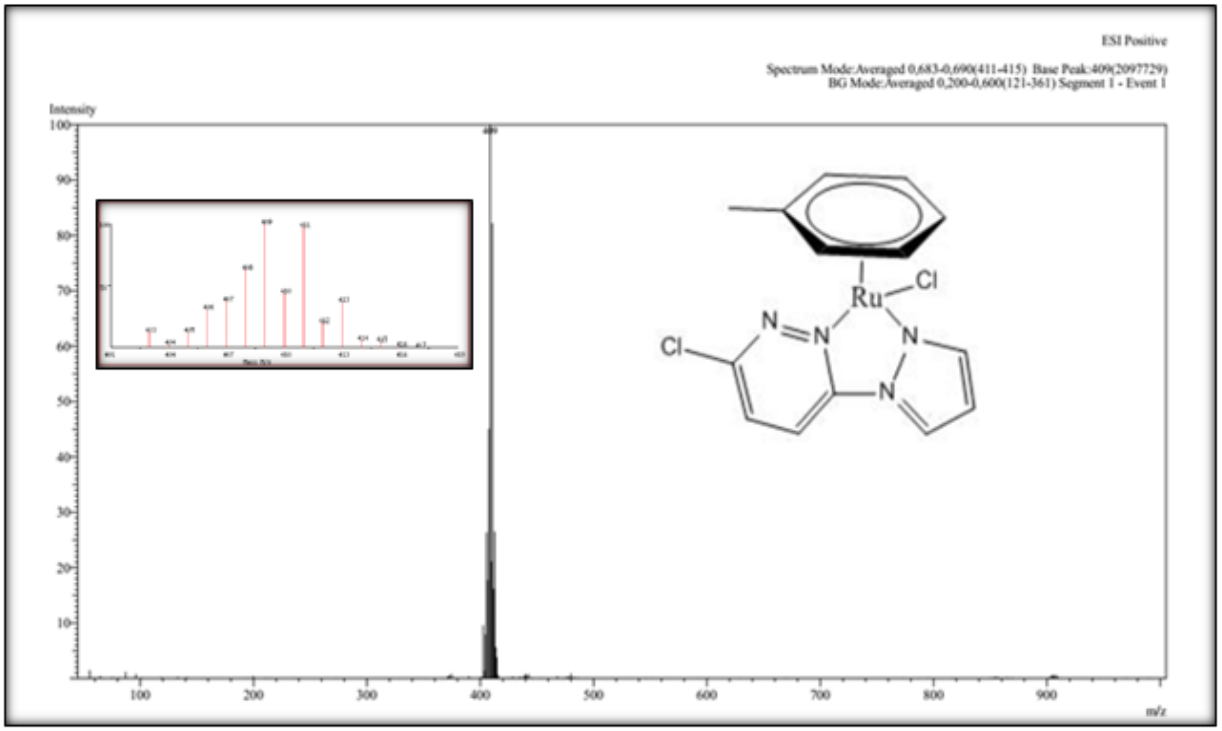

Figure 4.70: Low-resolution mass spectrum of complex **9**, showing a base peak at m/z 409 (100%) corresponding to the pseudomolecular ion $[C_{14}H_{13}ClN_4RuCl+H]^+$. Inset: Predicted isotopic distribution generated using SIS Isotope Pattern Calculator (https://www.sisweb.com/mstools/isotope.htm; accessed December 13, 2024).

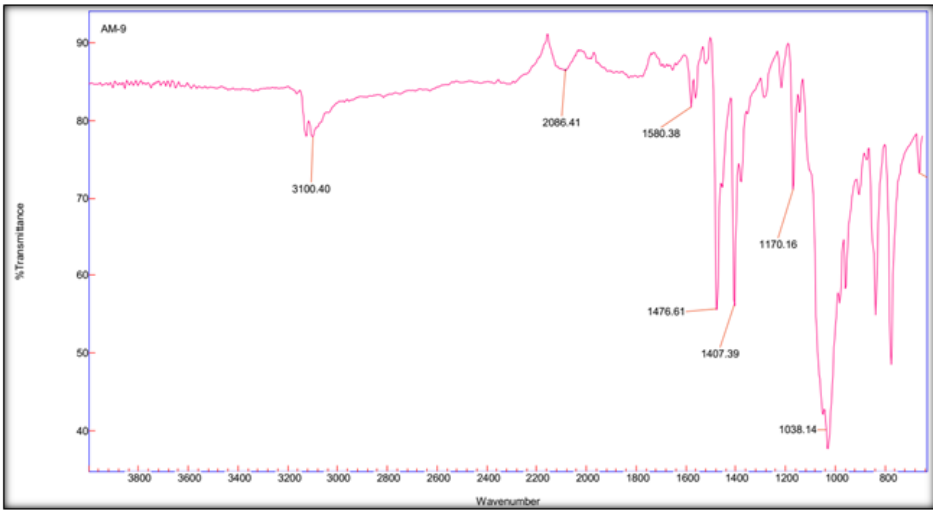

Figure 4.71: FTIR spectrum (dispersed in KBr) of complex **9**

4.3.2 Crystal Structures of 3a-c

Suitable single crystals of **3a-c** for X-ray diffraction measurements were afforded by slow evaporations of concentrated methanol/diethyl ether ($MeOH/Et_2O$) solutions, and their molecular structures were solved by crystallographic analysis. The thermal ellipsoids (at 50% probability) depicting the molecular structures of the three complexes are shown in Figure 4.72. Data on the cell dimensions and other details on the data collection, refinement, and key structural parameters are presented in Tables 4.29 and d-i in the appendix D. Selected bond lengths and angles are presented in Table 4.30.

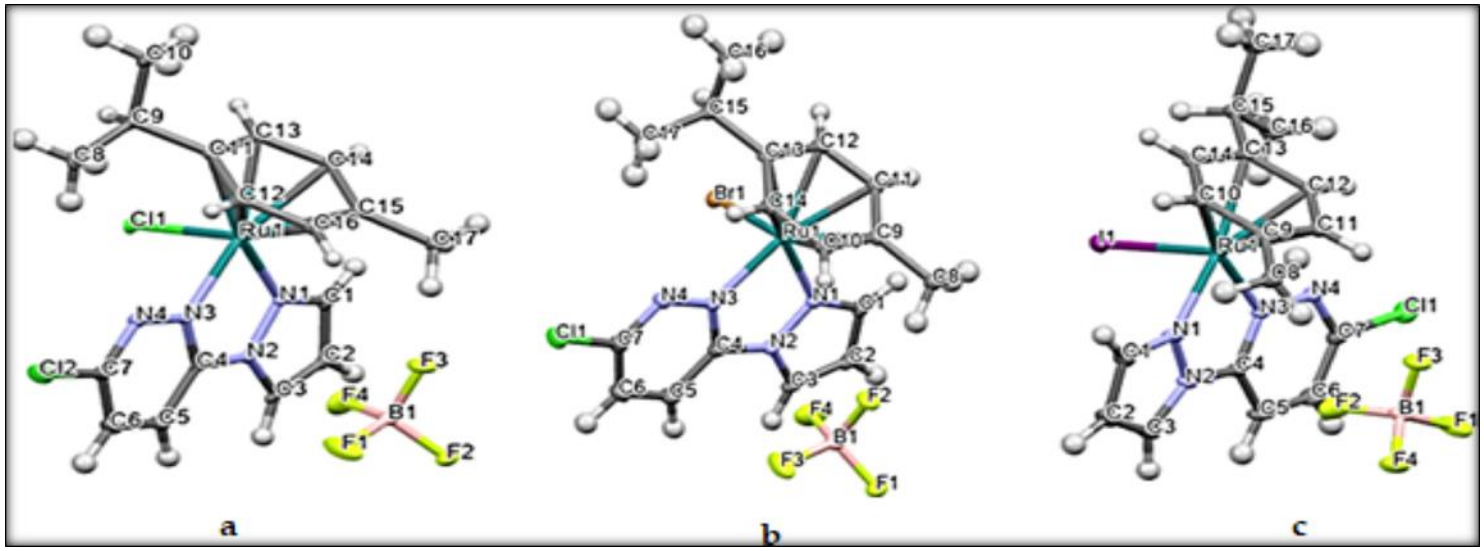

Figure 4.72: ORTEP diagrams of the Ru(II) complexes, [(η^6-*p*-cymene)(3-chloro-6-(1H-pyrazol-1-yl)pyridazine)Ru(X)]BF_4: (a) **3a** (X = Cl); (b) **3b** (X = Br); (c) **3c** (X = I), showing the asymmetric units. Atomic displacement ellipsoids are drawn at the 50% probability level.

Table 4.29: Summary of crystallographic data for complexes **3a–3c.**

Chemical Formula	$C_{17}H_{19}BCl_2F_4N_4Ru$	$C_{17}H_{19}BBrClF_4N_4Ru$	$C_{17}H_{19}BClF_4IN_4Ru$
M	538.14	582.60	629.59
T (K)	104	100	102.6
Crystal system	Monoclinic	Monoclinic	Monoclinic
Space group	$P2_1/c$	$P2_1/c$	$P2_1/n$
Unit cell dimensions			
a/Å	14.0177(5)	14.2238(3)	14.5324(3)
b/Å	10.6465(4)	10.6770(2)	10.7441(2)
c/Å	14.9362(5)	15.1270(3)	15.1862(3)
α/°	90	90	90
β/°	115.6560(10)	117.1390(10)	117.1050(10)
γ/°	90	90	90
Volume ($Å^3$)	2009.30(12)	2044.37(7)	2110.72(7)
Z	4	4	4
d_{cal} g/cm^3	1.779	1.893	1.981
Absorption coefficient (mm^{-1})	9.206	10.136	19.085
F(000)	1072	1144	1216
Crystal size (mm^3)	0.656 × 0.395 × 0.295	0.285 × 0.130 × 0.125	0.240 × 0.130 × 0.125
2θ range for data collection (°)	6.996 to 142.948	6.984 to 135.992	6.98 to 136.082
Index ranges	$-16 \le h \le 16, -12 \le k \le 12, -18 \le l \le 17$	$-17 \le h \le 16, -11 \le k \le 10, -18 \le l \le 15$	$-17 \le h \le 17, -12 \le k \le 12, -18 \le l \le 18$
$N_{(hkl)}$, $N_{(hkl)unique}$, R_{int}	34776, 3815, 0.0419	25766, 3638, 0.0266	24963, 3808, 0.0318
Data/restraints/ Parameters	3815/0/265	3638/0/265	3808/0/265

Goodness-of-fit on F^2	1.17	1.132	1.11
Final R indices	R_1 = 0.0313,	R_1 = 0.0188,	R_1 = 0.0183,
[$I \geq 2\sigma$ (I)]	wR_2 = 0.0794	wR_2 = 0.0469	wR_2 = 0.0424
Final R indices	R_1 = 0.0313,	R_1 = 0.0190,	R_1 = 0.0186,
[all data]	wR_2 = 0.0794	wR_2 = 0.0470	wR_2 = 0.0425
Largest diff. peak/hole/e Å^{-3}	0.79/−1.58	0.55/−0.64	0.53/−0.72

‡X = Cl (**3a**); Br (**3b**); I (**3c**).

Table 4.30: Selected bond length/Å and angles (°) from the crystal data for **3a-c**.

Complex	**$C_{17}H_{19}BCl_2F_4N_4Ru$**	**$C_{17}H_{19}BBrClF_4N_4Ru$**	**$C_{17}H_{19}BClF_4IN_4Ru$**
	Length (Å)		
Ru1-‡X1	2.3920(6)	2.5228(2)	2.6996(2)
Ru1-$N1_{pzn}$	2.080(2)	2.0718(17)	2.073(2)
Ru1-$N3_{pdzn}$	2.079(2)	2.0712(17)	2.0743(19)
Ru-$Cym_{centroid}$	1.676	1.676	1.679
	Angle (°)		
N1-Ru1-X1	84.03(7)	86.02(5)	82.85(6)
N3-Ru1-X1	84.61(7)	83.50(5)	88.44(6)
N3-Ru1-N1	76.18(9)	76.33(7)	76.19(8)

‡X = Cl (**3a**); Br (**3b**); I (**3c**).

4.3.3. DFT-Calculated Optimised Structures

The computed geometry-optimised structures for **3a-c** were in methanol as a solvent. The structures (Table 4.32, first column) and the energies of the frontier molecular orbitals are presented in Table 4.32. Some of these DFT-calculated data are included together with the crystal structure (solid-state) for comparison purposes in Tables 4.31 and 4.33.

Table 4.31: DFT-calculated data for complexes **3a-c**.

Parameter	**3a**	**3b**	**3c**
HOMO-LUMO energy/eV			
−(LUMO), eV	3.164	3.162	3.150
−(HOMO), eV	6.513	6.417	6.254
Band gap, ΔE, eV	3.349	3.255	3.104
Global electrochemical parameter			
Chemical hardness (η)	1.675	1.627	1.552
Chemical potential (μ)	−4.838	−4.790	−4.702
Chemical softness (σ)	0.597	0.614	0.644
Electronegativity (χ)	4.838	4.790	4.702
Electrophilicity index (ω)	6.988	7.048	7.122
Nucleophilicity (ε)	0.143	0.142	0.140
Dipole moments	7.8607	8.5126	9.1474
(NBO) charge			
Ru	+0.090	−0.057	−0.130
X	−0.295	−0.213	−0.110
N1	−0.184	−0.186	−0.188
N3	−0.211	−0.213	−0.215

Table 4.32: Overlays of the geometry-optimised structures on their crystal structures, and HOMO and LUMO electron density mappings for **3a-c.**

DFT-Optimized (Blue); Crystal Structure (Red)	HOMO	LUMO
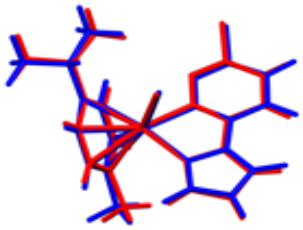 3a	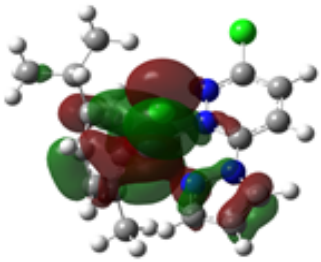	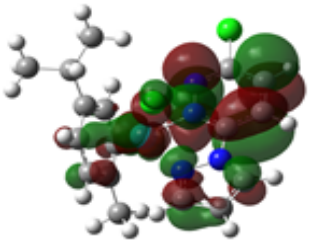
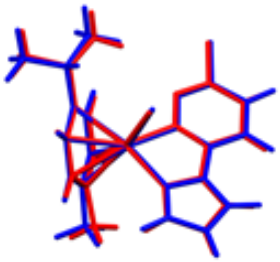 3b	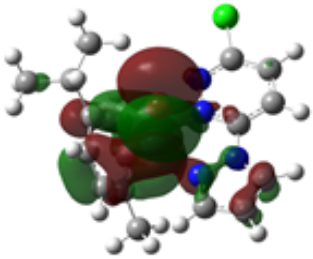	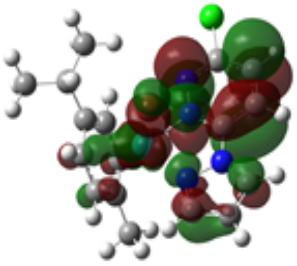
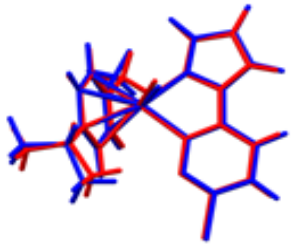 3c	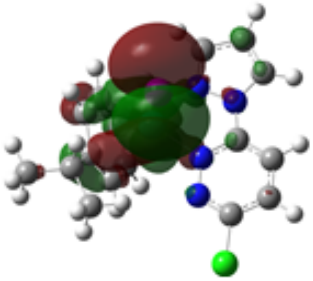	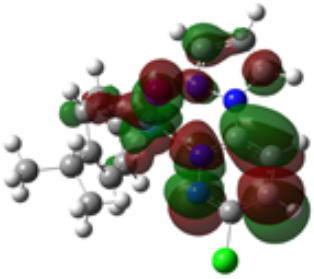

Table 4.33: Comparison of selected DFT-calculated parameters with experimental crystallographic data for complexes **3a–3c.**

Bond lengths	Cryst.	Theoret.	%RE	Cryst	Theoret.	%RE	Cryst.	Theoret.	%RE
	3a				3b			3c	
Ru-‡X	2.3921	2.4529	2.5	2.5228	2.5982	3.0	2.6997	2.7644	2.4
Ru-$C_{Cym(centroid)}$	1.6760	1.8530	10.6	1.6760	1.8610	11.0	1.6790	1.8730	11.5
Ru-N1	2.0789	2.0458	1.6	2.0719	2.0452	1.3	2.0711	2.0439	1.3
Ru-N3	2.0802	2.0587	1.0	2.0743	2.0587	0.8	2.0731	2.0577	0.7

‡X = Cl (**3a**); Br (3b); I (**3c**). Theoret. = DFT-calculated data; Cryst = crystal data taken as the accurate data; % % relative error (RE) = {(DFT Theoret. − Cryst)/Cryst} × 100.

4.3.4. Discussion

NMR, UV-Vis, and FTIR spectroscopic techniques, X-ray crystallography, and elemental analysis were used to characterise and confirm the structures of the complexes. Their analytical data are consistent with the formulations.

The molecular structures of the *N,N'*-bidentate ligand and its complexes **3/4a-c** and **9** in solution were probed by $^{1}H/^{13}C$ NMR spectra and 2D-NMR techniques (correlation spectroscopy (COSY) and heteronuclear single quantum coherence (HSQC)). The $^{1}H/^{13}C$ NMR data for the ligand and the complexes appear in the experimental section, and their respective spectra are in Figures 4.50-53, 4.58-61, 4.64-65, and 4.68-69, respectively. The ^{1}H-NMR resonances for the free ligand (Figures 4.48-49) appear upfield relative to those of **3a-c**. The $^{1}H/^{13}C$ NMR spectra of **3a-c** show common chemical shifts in the resonances of the ^{1}H and ^{13}C nuclei. This is an indication that the variation in the halide co-ligand has little or no influence on the electronic environment of the spins of the nuclei of the two coordinated non-leaving ligands. The ^{3}J-constants of non-singlet peaks/(hyperfine-split resonances) in the ^{1}H-NMR spectra of **3a-c** (Figures. 4.50, 4.52 and 4.74) were used to confirm correlated protons in distinctive chemical environments of the complexes. The ^{1}H spectrum of **3a** features four common resonance (absorption) peaks, while **3a** and **3b** have three peaks in the range of δ = 5.90–6.30 ppm. The chemical equivalence of four protons due to the C_2-symmetry of the facially coordinated η^6-cymene is broken by spin coupling with the diastereotopic protons of the methyl groups of the isopropyl moiety. Additionally, the pseudo-octahedral (piano stool) arrangement of four different

ligands around the Ru(II) ion makes the latter a chiral centre. Thus, the complexes will exhibit stereoisomerism that breaks the C_2-symmetry of the cymene and its spin resonance absorption (Morris *et al.*, 2001). The resonance peaks of the three protons of pzn and two of pdzn appear as five resonance peaks downfield (δ = 7.16–9.18 ppm), attributed to the ^{1}H nuclei on the C=N, C-N, and C=C groups and those of the η^6-cymene, respectively. As expected, these peaks were slightly deshielded compared to those of the free ligand (Figure 4.48), which range between δ = 6.69 and 8.80. The aliphatic protons of the cym appear at 2.79 ppm (*m*, $1H_{CH(CH3)2}$), 2.12 ppm (*s*, $3H_{methyl}$), and 1.15 ppm (*dd*, $2 \times 3H_{methyl\ isopropyl}$). The total number of carbon atoms and the range of their chemical shifts (ppm) agree with the different possible bonding environments of the C nuclei of the ligand framework for the proposed structures. Curiously, the aromatic resonances for the η^6-cym protons do not feature as two doublets as in the spectrum of the respective dimer precursors.

The 1D NMR data (Figures 4.50, 4.52, and 4.74) were corroborated by those of the COSY, HSQC, and other related correlated techniques, and these data are presented only for **3c** (refer to Figure 4.76 and Table 4.34). The absence of the ^{1}H/^{13}C cross peaks for C4, C7 (*N,N'*-bidentate) and C8, C11 (cym) in the HSQC of **3c** (Figure 4.75 hydrogen, and for the carbon numbering, Figure 4.72) confirms the quaternary nature of these carbons. The correlation assignments of the rest of the ^{1}H/^{13}C chemical shifts (Figures 4.73 and 4.74) are consistent with the proposed structure of **3c** and its two analogues. These assignments were further corroborated by the COSY data (Figure 4.76b and Table 4.34). In the COSY map of **3c**, common ^{1}H/^{1}H cross-peaks are observed between the absorption resonances of protons on the C1/C2, C2/C3 (pzn), C5/C6 (pdzn), and C9/C10, C12/C13, C15/C16, C15/C17 (cymene), showing that their carbons are bonded together (Figure 4.73).

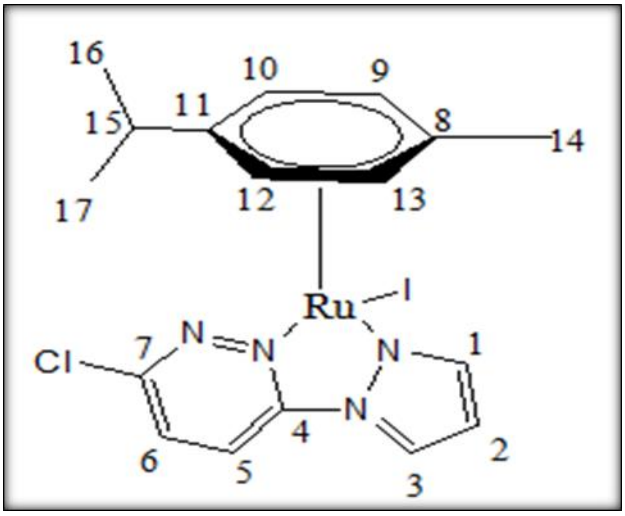

Figure 4.73: Carbon numbering for the ligand on **3c**

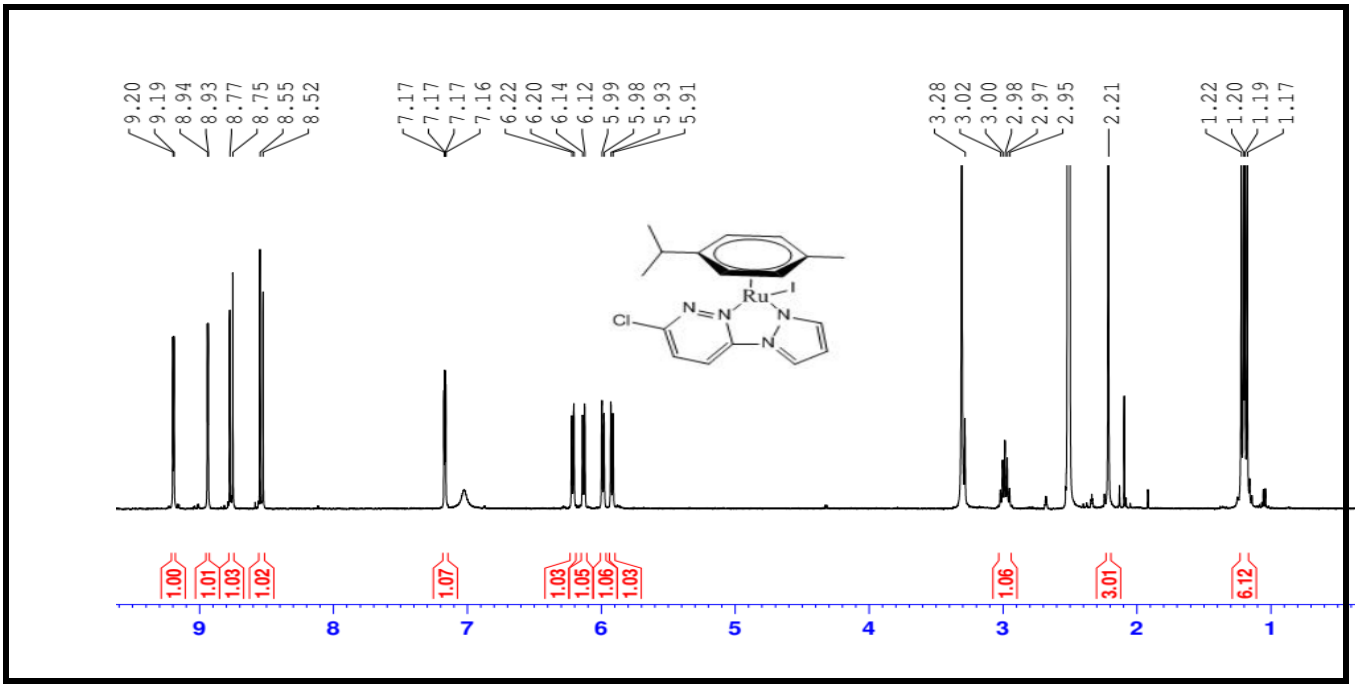

Figure 4.74: ^{1}H NMR spectrum (500 MHz, DMSO-d_6) of complex **3c.**

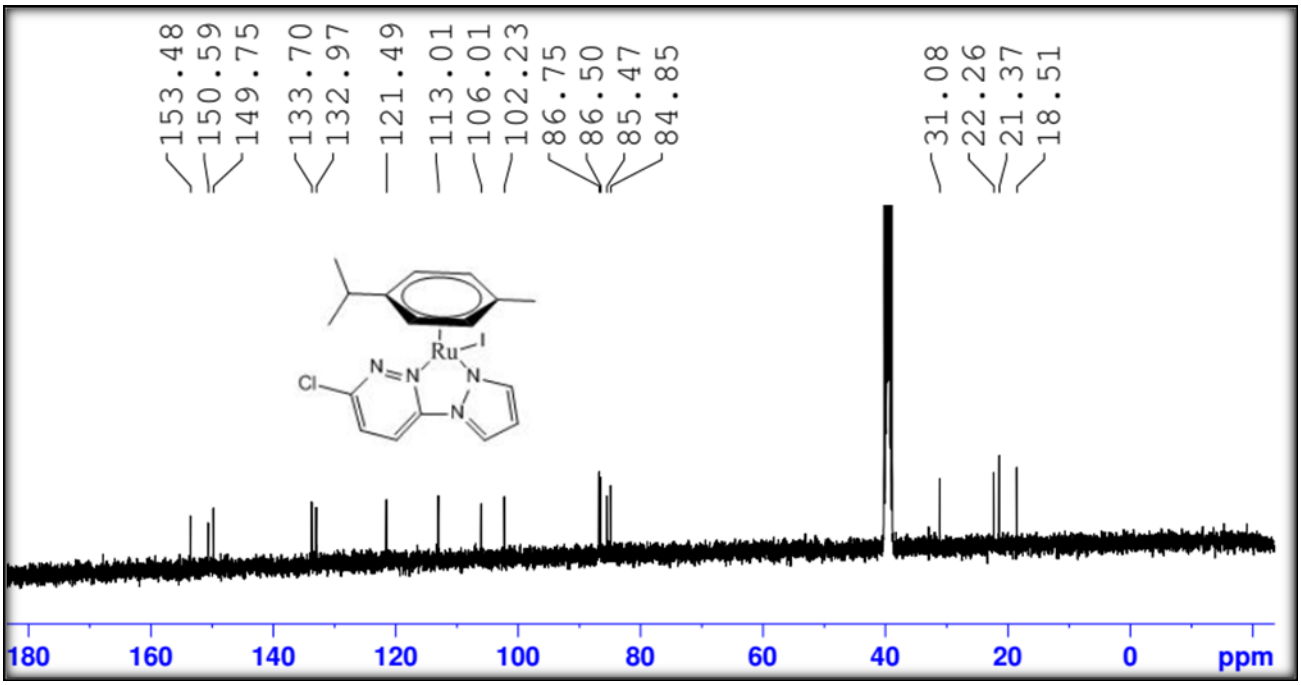

Figure 4.75: ^{13}C NMR spectrum (100 MHz, DMSO-d_6) of complex **3c**.

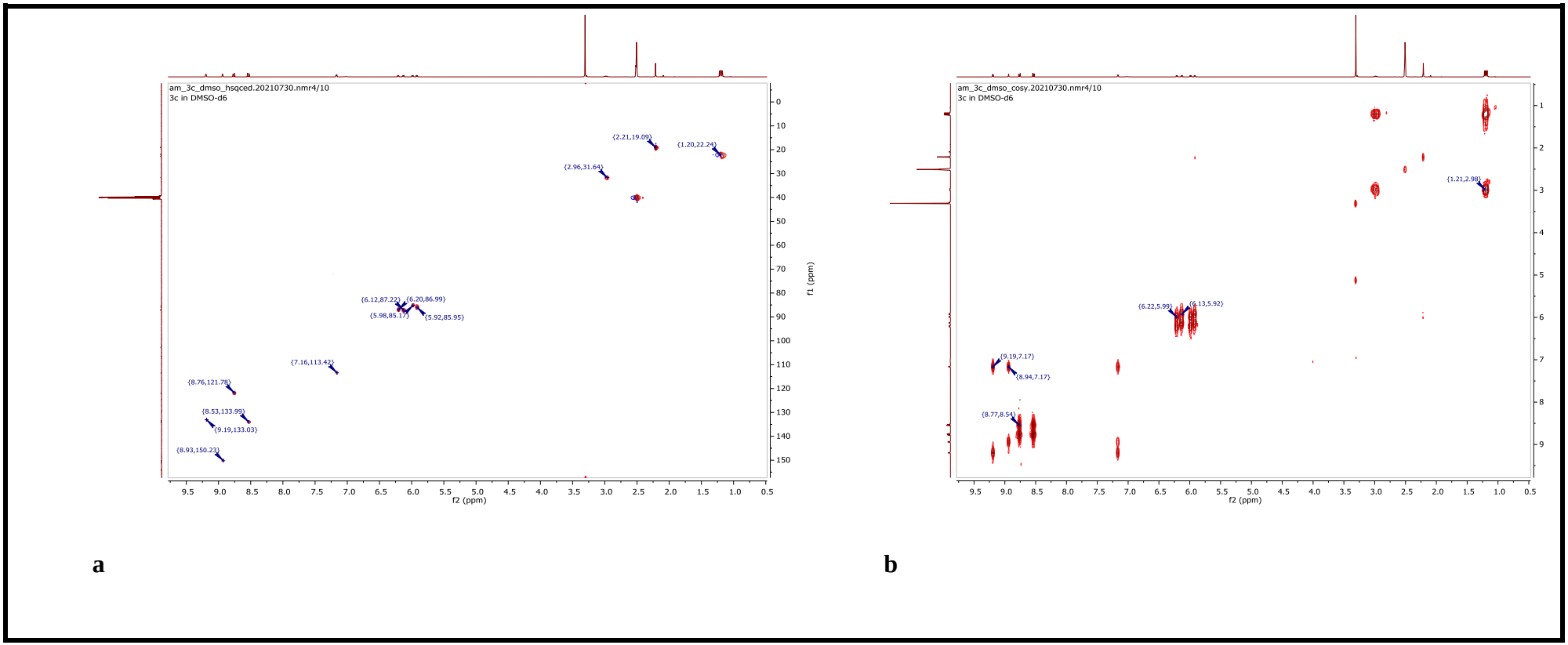

Figure 4.76: **(**a) HSQC and (b) COSY spectra for complex **3c**

Table 4.34: Summary of 2D NMR data (HSQC and COSY) for complex **3c.**

HSQC (see Figure 4.76)			**COSY** (see Figure 4.76)	
Carbon Number	Chemical shifts of correlated nuclei		Chemical shifts (splitting pattern, and ^{3}J coupling constants, Hz) of the correlated nuclei	
	^{13}C (ppm)	^{1}H (ppm)	F1 ^{1}H (ppm)	F2 ^{1}H (ppm)
14	19.1	2.21		
16	21.9	1.20	1.21 (d, 6.9)	2.98 (spt; 6.9)
17	22.8	1.19	1.19 (d; 6.9)	2.98 (spt; 6.9)
15	31.1	2.97	2.98 (spt; 6.9)	1.21 (d, 6.9)
12	84.9	5.99	5.99 (dd; 6,4, 1.4)	6.22 (dd; 6.4, 1.3)
10	85.5	5.94	5.92 (dd; 6.2, 1.2)	6.13 (dd; 6.2, 1.2)
13	86.5	6.21	6.22 (dd; 6.4, 1.3)	5.99 (dd; 6,4, 1.4)
9	86.8	6.14	6.13 (dd; 6.2, 1.2)	5.92 (dd; 6.2, 1.2)
11	102.2			
8	106.0			
2	113.5	7.17	7.17 (dd, 3.2, 2.2)	9.19 (d; 3.2)
5	121.5	8.78	8.77 (d; 9.3)	8.54 (d; 9.3)
1	133.0	9.19	9.19 (d; 3.2)	7.17 (dd, 3.2, 2.2)
6	133.7	8.55	8.54 (d; 9.3)	8.77 (d; 9.3)
3	149.8	8.94	8.94 (dd; 6.2, 1.2)	7.17 (dd, 3.2, 2.2)
7	150.3			
4	153.5			

The molecular structure of complex **9** is isometric to that of **3a** and **3c** due to common donor core rings (pyrazole and pyridazine) of their coordinated *N*,*N*-bidentate ligands. Complex **9** features five resonance peaks in the range of 7.17 - 9.12 ppm, which are very close to those of **3a** and **3c** (7.17 - 9.17 ppm). The inequivalence of the pyridazine ring protons shows up as five well-resolved peaks, possibly due to low coherence between the pyridazine protons and those of the tolyl ring. However, **4a** - **4c** (Figures 4.58, 4.60, and 4.64) feature three resonance peaks within the range of 6.74 - 8.40 ppm due to aromatic protons on the pyrazole and pyridazine. A

common multiplet (resembling two doublets of doublets) was observed at δ = 5.92-6.29 ppm, and this corresponds to the resonance of the four aromatic protons of the *p*-cymene ring. Due to the stereogenicity of the Ru(II) ion, caused by the four different coordinated atoms, an unusual splitting pattern of the *p*-cymene protons is induced by the correlation of the spin of the diastereotopic methyl proton of the isopropyl group (Prasad *et al.*, 2008). In comparing the chemical shifts of **4a** and **3a** or to those of **4c** and **3c**, the protons of the former are more shielded against the magnetic field due to the positive inductive effect of the methyl group at the 5-position of the pyrazole rings of the *N,N'* ligand of the former complexes. Besides the aromatic resonance, both **4a** and **4c** show a singlet within the chemical shift range, δ = 2.72 - 2.78 ppm, which corresponds to the methyl protons of the coordinated pyrazolyl ring. In addition, **4a** and **4c** exhibit two doublets in the range δ = 1.05 – 1.19, as well as a multiplet in the range δ = 2.60–2.97 for the single proton on the secondary carbon of the isopropyl group and a singlet at 2.17 ppm for the methyl protons of the *p*-cymene. Complex **9** exhibits a singlet at δ = 2.17 for the methyl on the benzene ring, a doublet of doublets with partial overlap between them, and a triplet in the range δ = 5.97 - 6.29. These chemical shifts are due to the protons of the tolyl, pyrazolyl, and pyridazine rings.

The ^{1}H-NMR data was corroborated by 2D-NMR data. For example, in the HSQC spectrum of **4c** (Figure. 4.78), the absence of hetero-correlated (^{1}H/^{13}C) cross-peaks for C1, C3, C4, C7 (3-chloro-6-(3, 5-dimethyl-1H-pyrazol-1-yl)pyridazine ligand), and C8, and C11 (cymene) confirmed the quaternary nature of these carbons, and for the carbon numbering, see the inset in Figure. 4.77. The remaining ^{1}H/^{13}C hetero-correlation assignments of the chemical shifts are consistent with the proposed structure of **4c** and its analogues. Figure 4.77 presents the COSY spectrum of **4c** from which the ^{1}H/^{1}H correlated assignments could be made. In the COSY spectrum, the 1H/1H cross peaks are observed between H15/H16, H15/H17, H12/H13, and H9/H10.

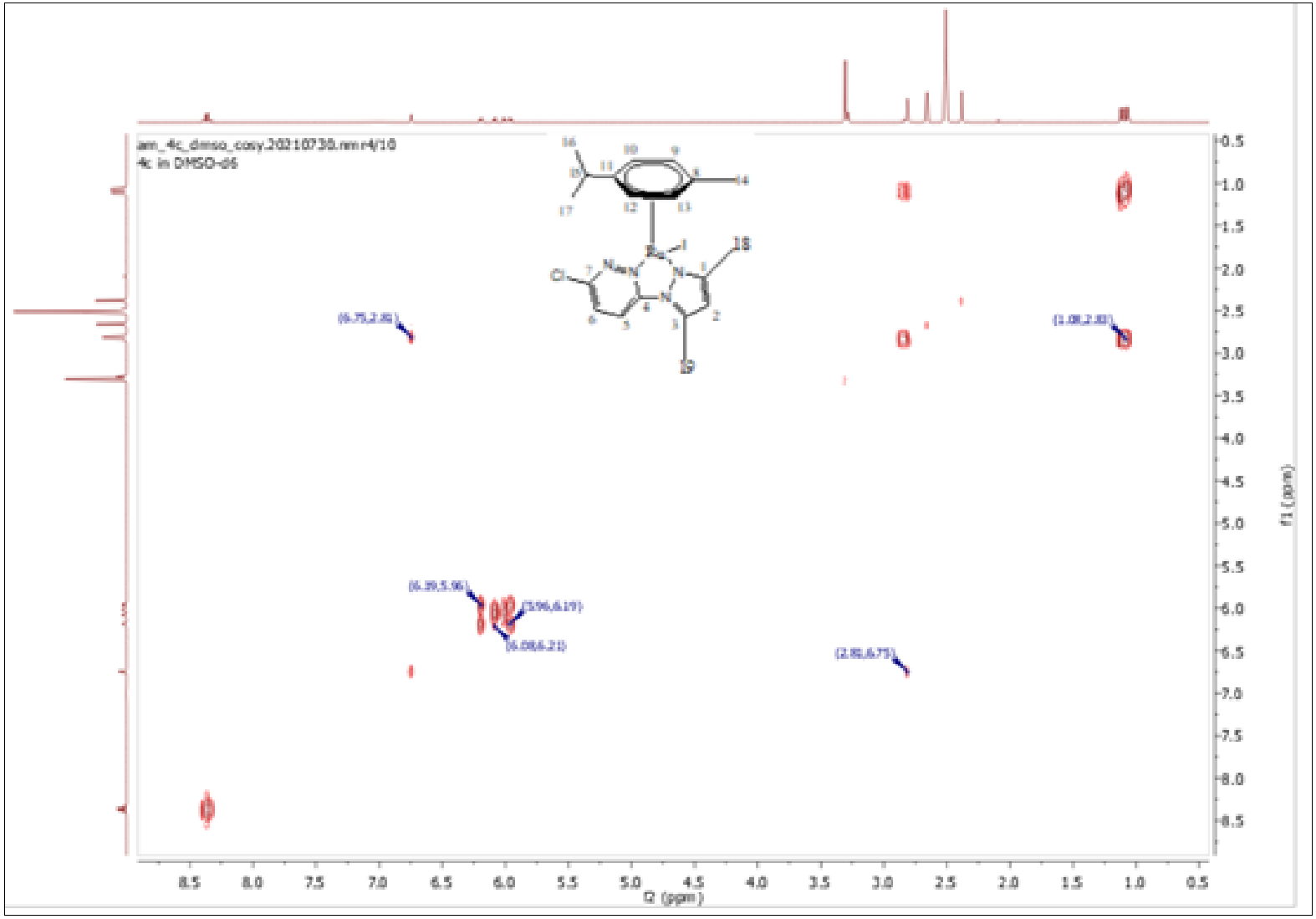

Figure 4.77: COSY spectrum of complex **4c**

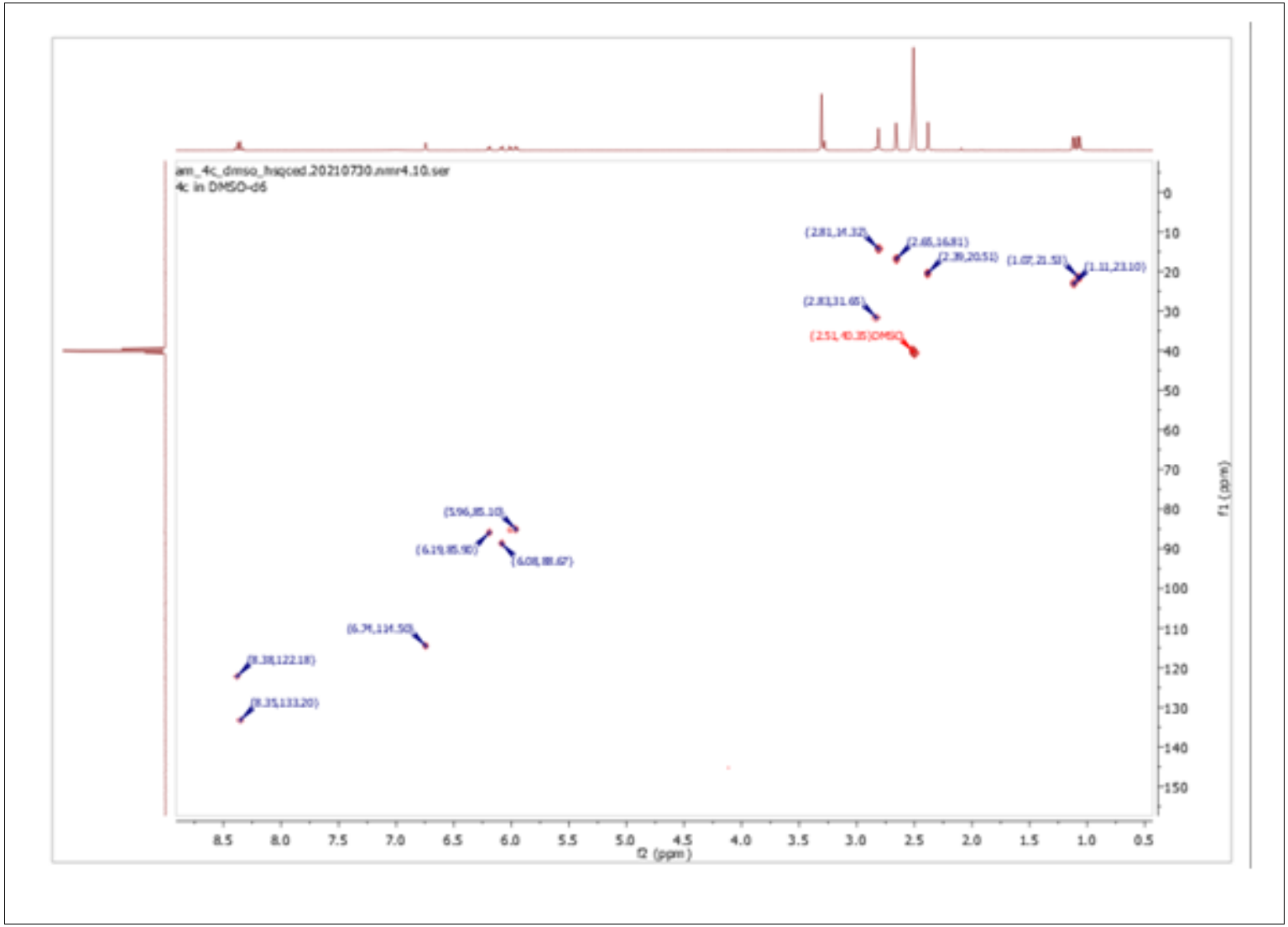

Figure 4.78: HSQC spectrum of complex **4c**

The chemical purity of **3a - c, 4a - c,** and **9** was checked by elemental (CHNS) analysis, while their structural elucidation in the solution was accomplished by various spectroscopic techniques. The elemental compositions of these complexes were within 5% of their theoretically calculated data (see the elemental data listed in the result section). This confirmed the high purity of the crystalline salts of **3a - c, 4a - c**, and **9**.

The respective ion peaks (in their low-resolution mass spectra) were recorded at *m/z* values of 451 amu (100%), 543 amu (100%), 480 (100), 571 (100), and 409 (100) (figures 4.54, 4.56, 4.63, 4.66, 4.70, and 4.79). The observed nominal *m/z* peaks correspond to the respective pseudo-protonated molecular ions $[C_{17}H_{19}ClN_4RuCl+H]^+$ (for **3a**), $[C_{17}H_{19}ClN_4RuBr+H]^+$ (for **3b**), $[C_{17}H_{19}ClN_4RuI+H]^+$ (for **3c**), $[C_{19}H_{24}ClN_4RuCI+H]^+$ (for **4a**), $[C_{19}H_{24}ClN_4RuBr+H]^+$ (for **4b**), $[C_{19}H_{24}ClN_4RuI+H]^+$ (for **4c**), and $[C_{14}H_{13}ClN_4RuCl+H]^+$ (for **9**). The zoomed-out peaks show isotopic distribution patterns that are congruent to the theoretical patterns for the corresponding calculated formulas (insets in Figures 4.54, 4.56, 4.63, 4.66, 4.70, and 4.79). The match between the experimental (isotopic patterns) and the theoretically calculated pattern fingerprints the identity of the complexes and hence the successful synthesis of the complexes.

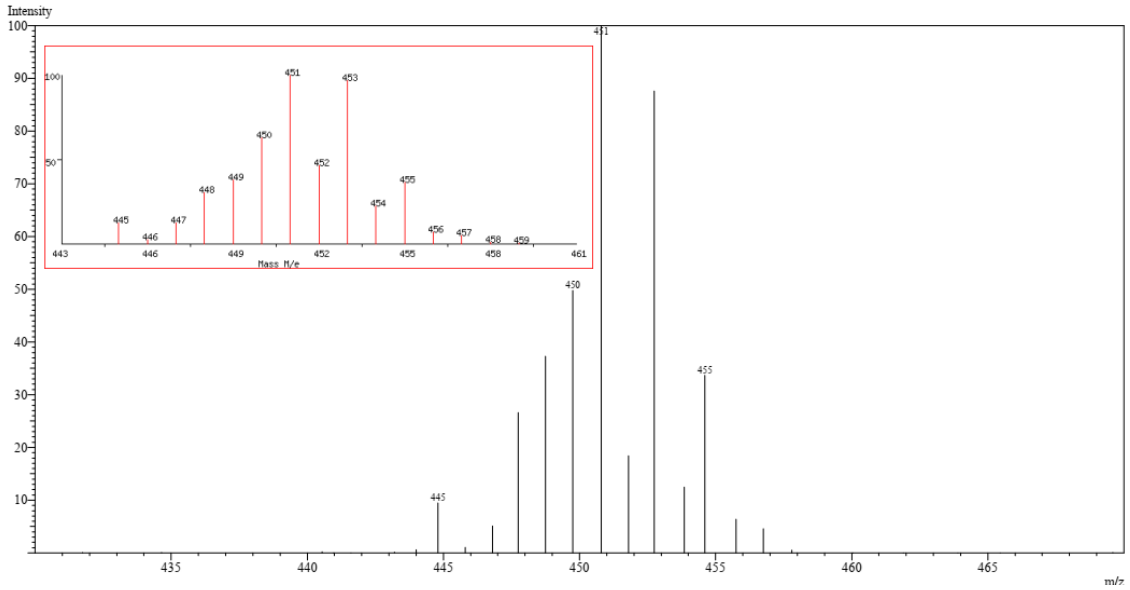

Figure 4.79: Low-resolution mass spectrum of complex 3a, showing a base peak at *m/z* 451 (100%) corresponding to the pseudomolecular ion $[C_{17}H_{19}ClN_4RuCl+H]^+$. Inset: Predicted isotopic distribution generated using SIS Isotope Pattern Calculator (https://www.sisweb.com/mstools/isotope.htm; accessed December 13, 2024).

UV-visible electronic absorption spectra of the complexes **3a - c** in solution are depicted in Figure 4.80. All the electronic spectra of the complexes show similar spectral bands to those reported for other pseudo-octahedral complexes (Gupta *et al.*, 2010). Characteristic absorption peaks include the medium-intensity bands in the region 250–260 nm, which are assigned to π–π* electronic transitions. An intense band also features in the 280–320 nm region, and it is assigned to the inter-/intra-ligand π–π*/n–π* transition within the pyrazolyl-pyridazine bidentate ligand (Gichumbi *et al.*, 2016a). The absorption band (low intensity) in the region 450–470 nm is assigned to the Ru(II)-to-ligand charge transfer (MLCT). However, the intensities of the absorption bands for **3c** are weaker compared to those of **3a** or **3b**. In general, these observed spectral data are comparable to those of other η^6-arenes Ru(II) complexes bearing an *N,N'* donor chelate (Gupta *et al.*, 2010). As already stated, solutions of **3a - c** precipitate as orange crystalline solids. This shows that the halide ligand has little influence on the crystal field strength of the complexes. The presence of the 3-chloro-6-(1H-pyrazol-1-yl)pyridazine as a common spectator ligand and the LUMO fragment ensures an overriding metal-to-ligand charge transfer (MLCT) limited to a narrow range band gap (3.3–3.1 eV, see data in Table 4.31) between the three complexes. This leads to homologous halo-Ru(II) complexes with the same colour.

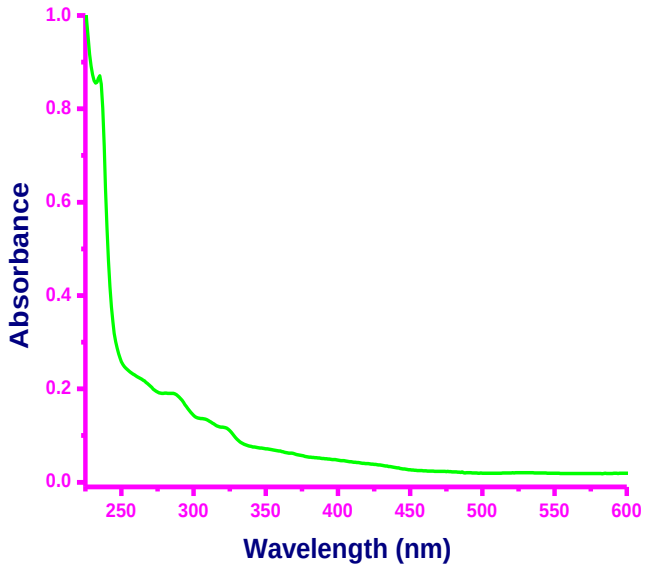

a) 3a

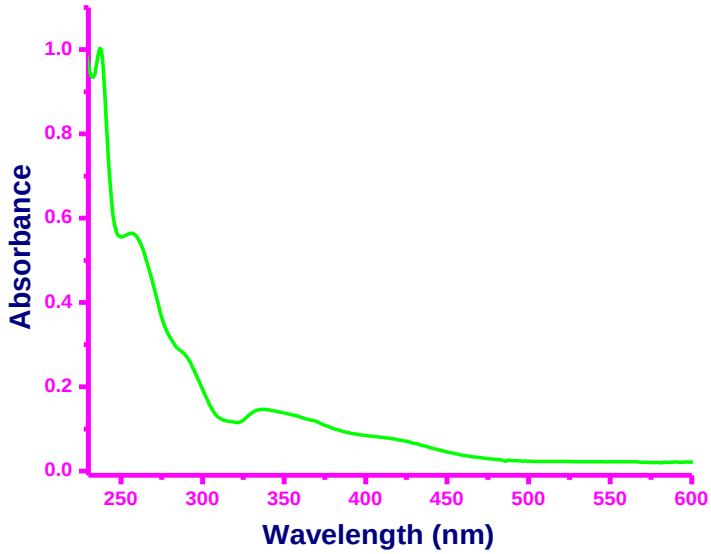

b) 3b

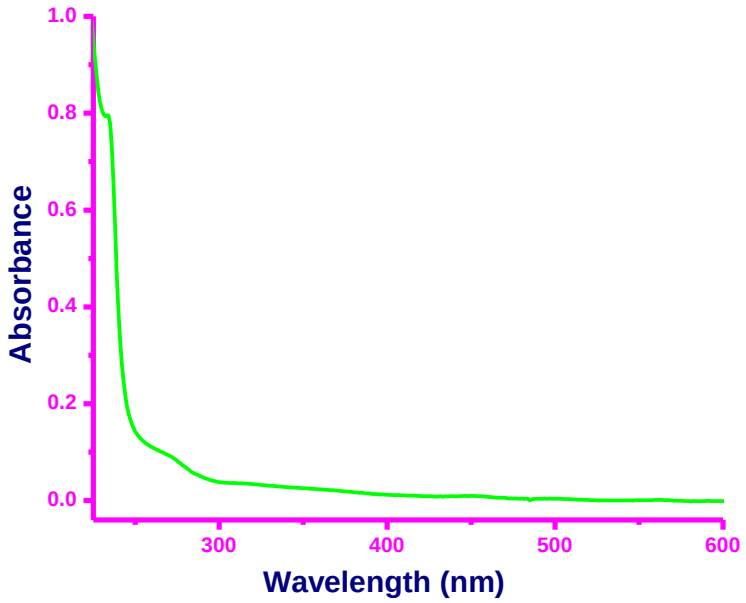

c) 3c

Figure 4.80: UV-Visible absorption spectra of **3a-3c** (1.0 x 10^{-5} M) in methanol

The FTIR spectra for **3a - c, 4a - c,** and **9** were recorded and are presented in Figures 4.55, 4.57, 4.63, 4.67, 4.71, and 4.81. Key vibrational stretching bands for the coordinated *N,N'*-pyrazolyl pyridazine (pzn-pdzn, Figure 4.82) ligands are shifted to longer wavelengths compared to their corresponding metal-free forms. This is in line with these bidentate ligands being coordinated with the Ru(II) ions. The C-C/N bonds of the *p*-cymene/toluene and pzn-pdzn bidentate ligands exhibit common vibrational bands in the FTIR spectra for **3a - c, 4a - c,** and **9**. This means that the leaving halide group does not affect the vibrational frequencies of the functional groups of the carrier ligands. The functional groups of the coordinated pzn-pdzn-*N,N'* bidentate ligands, the *p*-cym/toluene ligands, and the borate counter ion are the main contributors to the observed absorption bands. As an illustration, in Figure 4.81 (the spectrum of the **3a**), two absorption bands are observed at 3085 and 2873 cm^{-1}; these low-intensity bands are for the ν_{C-H} stretching frequencies for the aromatic and aliphatic stretches, respectively. Another common featuring band is the 1582 cm^{-1} (medium, $\nu_{C=N\ (pzn/pdzn)}$ and $\nu_{N=N\ (pdzn)}$ stretch). The absorption bands of the cym occur as an intense duet at 1479 and 1404 cm^{-1} (intense $\nu_{C=C(cym)}$ stretching). The bands that appear within the range of 1200 and 1400 cm^{-1} (sharp, medium) are due to the $\nu_{C=C}$ vibration asymmetric stretches of the pzn/pdzn ring carbons. A low-intensity absorption

band is seen at 3100 cm^{-1} in figure 4.71 (the spectrum of the **9**); this band corresponds to the ν_{CH} stretching frequency for the aromatic and aliphatic stretches. The 1580 cm^{-1} (medium, C=N (pzn/pdzn) and N=N (pdzn) stretch) is another common featuring band. At 1477 and 1407 cm^{-1}, the toluene absorption bands form an intense duet (intense, $C=C_{(tol)}$ stretching). The asymmetric stretches of the carbons in the pzn/pdzn ring that result from the C=C vibration are what caused the bands to appear between 1200 and 1400 cm^{-1} (sharp, medium). Due to the asymmetric stretching of the B-F bond of the BF_4^- counter ion of these complexes, a strong absorption band is seen in the 1020–1053 cm^{-1} range. The sharp bands below 800 cm^{-1} (medium intensities) are due to the vibrational stretches of the Ru-C, Ru-$N_{pzn/pdzn}$, and Ru-Cl bonds. These frequency bands occur in the range reported in the literature (Albertin *et al.*, 2011; Matveevskaya *et al.*, 2021; Morris *et al.*, 2001; Romero-Canelón *et al.*, 2013).

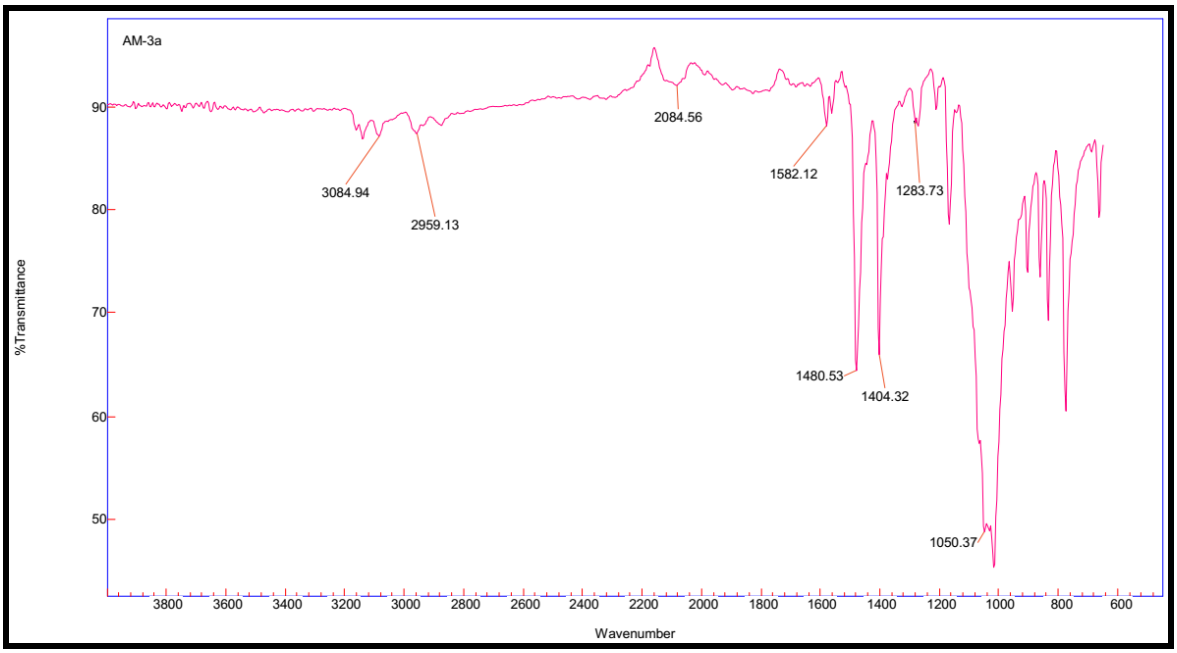

Figure 4.81: FTIR spectrum (dispersed in KBr) of **3a.**

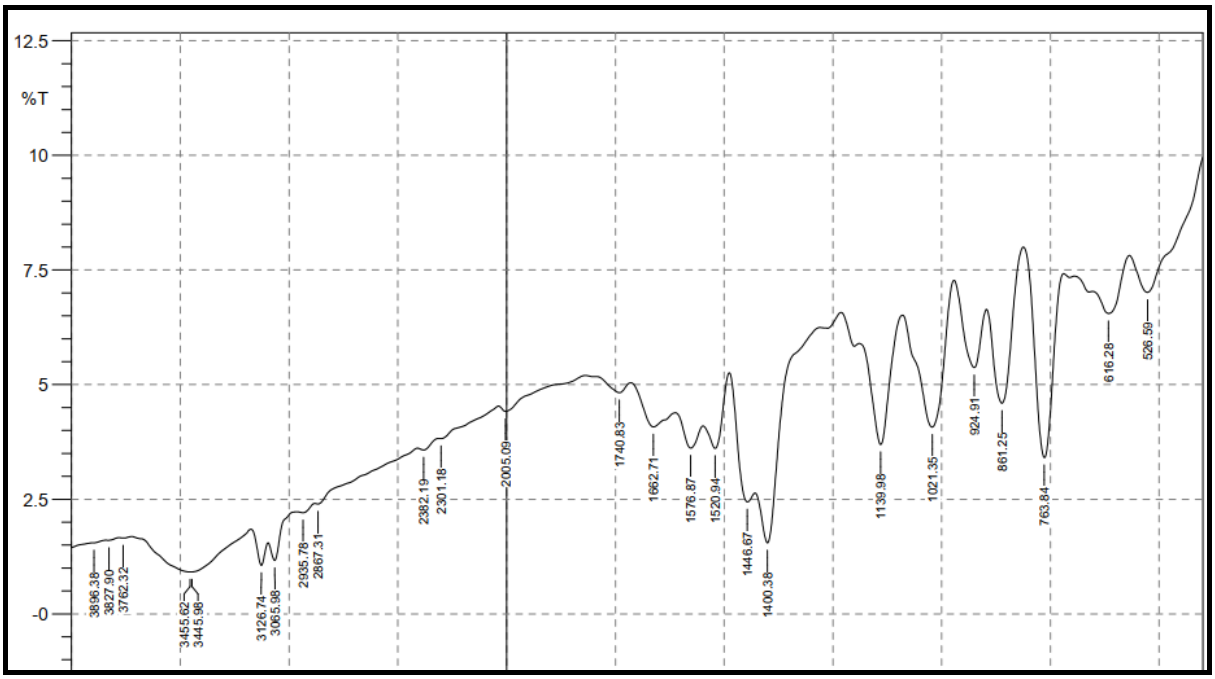

Figure 4.82: FTIR spectrum of 3-chloro-6-(1H-pyrazol-1-yl)pyridazine (dispersed in KBr).

Complexes **3a** - **c** were crystallised from their respective MeOH/Et_2O solutions as non-solvated salts comprising the respective cations of the general formula $[(\eta^6\text{-}p\text{-cymene})(3\text{-chloro-6-}(1H\text{-pyrazol-1-yl})\text{pyridazine})Ru(X)]^+$ (X = Cl, Br, I), and BF_4^- as the counter anion. The structures are as depicted in Figure 4.72. All three complexes assume a pseudo-octahedral geometry, which is widely reported for η^6-arene Ru(II) half-sandwich-shaped complexes (Morris *et al.*, 2001; Romero-Canelón *et al.*, 2013; Zeng *et al.*, 2017). The characteristic of these complexes is the facial π-coordination of the η^6-arene, leaving three (for octahedral) and, in some cases, two (for trigonal- or square-pyramidal) coordination vacancies on the d^6 Ru(II) metal ion. The arene for these Ru(II) complexes is η^6-cymene (η^6-cym) and forms three nearly equivalent Ru-C π-bonds. The Ru to η^6-cym $_{centroid}$ bond distances are 1.676 Å (**3a, 3b**) and 1.679 Å (**3c**), respectively, and are within the range reported for similar structured Ru(II) complexes (Gupta *et al.*, 2009). These short centroid bond distances and the strong Ru-C π-bonds render them robust complexes with remarkable thermodynamic stability against hydrolysis or nucleophilic attack under ambient or aqueous conditions. These attributes make η^6-arenes appealing ligands for stabilising d^6 organometallic complexes for various applications, including in the biomedical field (Morris *et al.*, 2001; Romero-Canelón *et al.*, 2013; Zeng *et al.*, 2017). The remaining coordination vacancies are occupied by the halide as the labile co-ligand, and the 3-chloro-6-

(1*H*-pyrazol-1-yl)pyridazine bidentate *via* its $N3_{pdzn}$, $N1_{pzn}$ donor atoms. The latter forms a five-membered chelate ring with the Ru(II) ion.

Coordination Inorganic chemists are enchanted by the geometric distortions (conformational arrangements) of the octahedral η^6-arene-bearing complexes of Ru(II) such as **3a - c**. They liken the distortion of the geometry to a 'piano stool'. The facially coordinated η^6-cymene is akin to the illusory 'seat' of the stool. The halide (X = Cl, Br, or I for **3a - c**), the $N3_{pdzn}$, $N1_{pzn}$ donor arms/atoms of the bidentate, are conformationally pronged onto the feet of the pseudo legs of the stool (Albertin *et al.*, 2011; Gichumbi *et al.*, 2017a; Gichumbi *et al.*, 2016b; Gichumbi *et al.*, 2018; Gupta *et al.*, 2009; Matveevskaya *et al.*, 2021; Morris *et al.*, 2001; Romero-Canelón *et al.*, 2013). Despite this dramatic distortion from the perfect octahedral geometry, these η^6-arene complexes have sufficient chemical and thermal stability.

The pzn and the pdzn rings of the *N,N'*-bidentate ligand remain coplanar upon their chelation to the Ru(II) ion. The N_1-N_2-C_4-N_3 torsion angles are near zero and equal to −0.1(9)°, −0.8(3)°, and −5.4(3)° for **3a - c,** respectively. The Ru-N bond lengths of the compounds lie between 2.0712(17) and 2.080(2) Å, which are similar to those reported for other η^6-arene Ru(II) complexes with *N,N'*- donor ligands (Albertin *et al.*, 2011; Gichumbi *et al.*, 2016b; Gichumbi *et al.*, 2018; Gupta *et al.*, 2009; Matveevskaya *et al.*, 2021; Morris *et al.*, 2001; Romero-Canelón *et al.*, 2013). The N-Ru-N bond angles range from 76.18(9)° to 76.33(9)°, while the N-Ru-X bond angles range from 83.50(5)° to 88.44(6)°. These ranges are similar to those reported for related η^6-arene Ru(II) complexes with *N,N'*-bidentate ligands. The Ru-X bond lengths increase as expected in the order Ru-Cl (2.3920(6) Å) (Albertin *et al.*, 2011; Gichumbi *et al.*, 2016c; Gupta *et al.*, 2009; Morris *et al.*, 2001), Ru–Br (2.5228(2) Å (Neels *et al.*, 1999), and Ru–I (2.6996(2) Å) (Bacchi *et al.*, 2013; Romero-Canelón *et al.*, 2013) for **3a - c** in line with the size of the labile ligand and the increase in the polarizability of the Ru-X bond. The bond lengths are comparable to those reported for related compounds: Ru–Cl (Wang *et al.*, 2017), Ru–Br (Neels *et al.*, 1999), and Ru–I (Bacchi *et al.*, 2013; Romero-Canelón *et al.*, 2013). The lengths and angles of all C—C, C—N, and B—F bonds are within the expected ranges for (N,N/O-bidentate)(η^6-cym)Ru(II) complexes (Mendoza-Ferri *et al.*, 2008). There are many inter and intramolecular interactions in the solid state of these Ru(II) borate salts (refer to Table i in appendix D) for a list of selected stabilising short contacts or non-conventional hydrogen bonds). Some of these interactions occur between the fluorine and hydrogen atoms of *p*-cymene. Examples are the F…H–C short contact

bonds (*e.g.*, C17–H17···F3, *d* = 2.868(4) for **3a**, while for **3b** and **3c**, similar non-conventional hydrogen bonds occur between the leaving group (X) and the hydrogen atom of the neighbouring cation in the lattice, as exemplified by the C–H17…Br1 = 3.024 Å and C16-H16…I1 = 3.67 Å. A noteworthy difference in the relative conformational geometry and orientation of the ligands around the Ru(II) metal centre is that the pzn and pdzn rings of **3c** are coordinated in contrastingly distinct orientations (when referenced to the orientations of substituents on the cymene) to that of the same rings in **3b**, as well as the analogue of **3a** reported in (Gupta *et al.*, 2009). It is unclear what drives the difference in the orientations of the two non-leaving ligands, which incidentally put these complexes in two coordinational or configurational sub-domains. In **3c**, the propyl group of the *p*-cymene is oriented closer to the larger ring of the pdzn ligand, , which seems to increase electron-to-electron repulsion between the groups, leading to a longer Ru-$C_{Cym(centroid)}$ distance for **3c** relative to that of either **3a** or **3b**. Contrastingly, the methanolic solutions afforded orange crystalline salts of **3a - c**, an indication that the coordinated halide ligand has little or no influence on the strength of the crystal field. The trend in the DFT-calculated data (Table 4.16) shows that there is no significant difference in the magnitude of the HOMO-LUMO energy band gaps of the three complexes. Which supports the commonality in the colour of the salts of homologous halo-Ru(II) complexes reported for the series of [(η^6-arene)Ru(II)]N-N')X]$^+$, X = Cl, Br, and I complexes. Only when the counter ion in the analogous salts of **3a** was changed from BF_4^- to PF_6^- was there a distinct colour change from orange to yellow (Gupta *et al.*, 2009).

The HOMO mappings of **3a - c** (Table 4.30) have a common distribution. They show significant electron density, which is delocalized over the η^6-cym ring, the Ru(II)-X (X = Cl, Br, I) bond, and the pzn donor arm. However, for **3c**, the density over the pzn is restricted only to the N donor atoms and is much smaller than that on the iodo ligand. In summary, the pdzn ring makes little contribution to the HOMO for **3a** and **3b**. This is as expected, since there is π- and σ-donation of electron density from their η^6-cym and pzn rings, respectively. These donations reduce the effective positive charge on the Ru(II) ion, making it less electrophilic towards substitutions by nucleophiles. The LUMOs of **3a - c** are more localised on the pdzn rings. Conversely, there is no significant contribution to the LUMOs from the pzn rings. Thus, the electron density on the metal can easily be back-donated into the π* orbitals of the pdzn ring rather than into the pzn donor arm. This means that the pdzn arm of the *N,N'*-bidentate is a π-

acceptor comparable to pyridine or pyrazine. Overall, the *N,N'* bidentate of these complexes can be an effective electron density modulator through a pull-and-push mechanism towards the Ru(II) metal centre since pdzn is a better π-acceptor than pzn. This is important in producing complexes that have moderate reactivity and are therefore less prone to deactivation on transit to the cellular targets. Furthermore, the energy for 3′s LUMO is the highest, and hence this complex is the poorest π-acceptor, and least electrophilic. However, it is likely to be the most reactive towards incoming nucleophiles because its iodo ligand is the best leaving group due to the high polarisability of its metal bond.

To probe and predict the substitutional reactivity of **3a** - **c**, their HOMO-LUMO band gaps and global electrochemical descriptors (chemical hardness (η) (Desoize & Madoulet, 2002), chemical potential (μ), electrophilicity (ω) (Wekesa & Jaganyi, 2014), and charge density) were compared. As the halide, X is changed from Cl (**3a**) to I (**3c**), and the band gap, electronegativity, and η decrease; thus, **3a** is predicted to be the most stable and least reactive. The chemical potential, softness, and electrophilicity also increase from **3a** to **3c**, which is a clear indication of the greater ability of **3c** to accept electron density from the incoming nucleophile, thus enhancing the π-back bonding of electrons from the Ru into the π* orbital and stabilizing the transition state. Chemical species' biological activity increases with higher HOMO and forbidden energy (HOMO–LUMO), softness, electronegativity, and nucleophilicity index (Erkan *et al.*, 2020). From this, 3a is likely to be more reactive because of its high nucleophilicity index value.

Looking at the calculated NBO charges in Table 4.14, the effective charge on the Ru(II) centre decreases in the order **3a** > **3b** > **3c**. Thus, the charges on the complexes are affected by the nature of the leaving group. The Ru(II) ion in **3a** has the highest positive charge, indicating that it is the most electrophilic. Complex **3c** is soft and has a high ability for accepting electrons from the soft Ru(II) ion, and hence is expected to be slightly more reactive than **3a** or **3b**. The large size of the atomic orbitals of the iodo ligand and hence its ease of polarisability result in an instantaneously large dipole that decreases the positive charge on the Ru(II). On one hand, the chloro ligand withdraws electron density from the metal centre by resonance, which increases the positive charge on Ru(II). As a result, it is not the charge on the metal that determines reactivity, but rather the general increase in the negative charge on the ligand moiety, as indicated by electrophilicity indices (Wekesa & Jaganyi, 2014).

Overlays of the DFT-optimised structures (in methanol) of **3a - c** and their respective X-ray crystal structures show a good fit (root mean square deviation, *rmsd*) of < 2%) of the DFT-optimised structures. The superimposed structures are in the first column of Table 4.15. The computed bond lengths, distances, and angles are all within a 10% difference from the solid-state data from X-ray crystallographic analysis (Tables d - k in the appendices), thereby validating the accuracy of the theoretically calculated metric data of the complexes.

For sections 4.4 - 4.7, since most of the results appear in graphical form, the results and discussions are together.

4.4 Solution Behaviour in DMSO and Aqueous Media

Since metal complexes can readily undergo ligand exchange reactions in DMSO (which is a medium used in the solutions for biological screenings), it can affect the structural integrity of the complexes (Patra *et al.*, 2013). The stability of some derivatives in water and DMSO depends on the choice of ligands and the overall structure of the complexes. Hence, before commencing biological testing/evaluation (cell survival remaining 100%) the stability of the complexes was investigated. The stability of the complexes in DMSO and in the PBS buffer media, using UV-visible absorption spectroscopy at 37 °C to simulate the chemical environment, and by conductivity at 25 ^{o}C; showed that **9** (see the overlay spectra presented in Figures 4.83) as well as its analogues were stable against ligand substitution by the nucleophilic DMSO (Moon *et al.*, 2015). The peaks' positions and absorbance remained invariant over a 72-hour period, an indication that solvent species did not exchange or substitute with the chloro ligand. An aqueous test was also performed to determine the stability of the complexes in the PBS buffer medium (which was used in DNA titration experiments) as the binding of an aqueous species on a metal centre influences electron transfer rate constants (Tan *et al.*, 2008). Figure 4.83b is an exemplary spectral evolution of **9** in an aqueous buffer, which shows that complex **9** as well as its analogues are stable in the PBS buffer solution. As was the case in the DMSO, no significant changes in the electronic absorption spectral data were observed within 48 h, indicating excellent stability of **9** (and its analogues) in aqueous media. The molar conductance (Λ_M) values of these 1:1 cationic salts in DMSO ranged from 20.22 to 24.77 S cm^2 mol^{-1}, in line with their non-electrolytic behaviour in this aprotic solution (Mondal & Paira, 2020). Moreover, the Λ_M values for all the complexes were invariant over a 48-h period, underscoring the kinetic stability of the complexes

in the DMSO medium (Table 4.35). Therefore, **3a, 3c, 4a, 4c,** and **9** exhibited appreciable stability, sufficient to be investigated for cytotoxicity. Similar stability in DMSO was demonstrated using ^{1}H-NMR spectroscopy for Ru(II) η^{6}-*p*-cymene complexes with pyrazole-benzimidazole as a bidentate ligand (Bhattacharyya *et al.*, 2017; Chakraborty *et al.*, 2021).

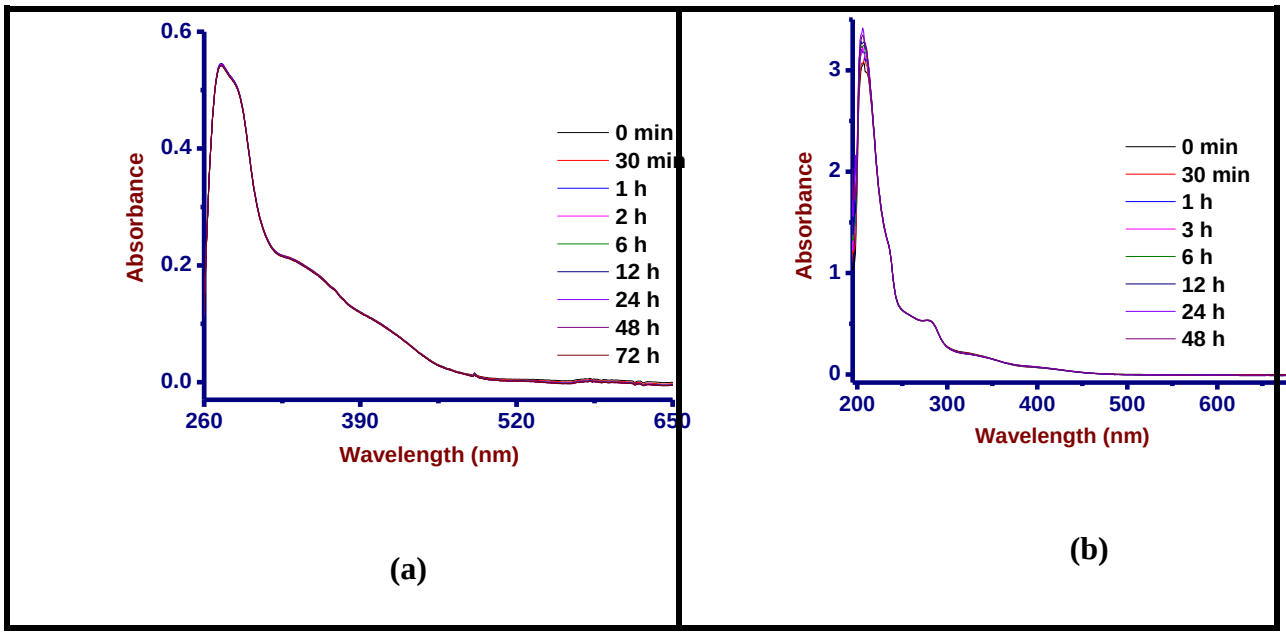

Figure 4.83: (a) UV–Visible absorption spectra showing the stability of complex **9** in DMSO over a 72-hour period at 25 °C. (b) Spectral monitoring of complex **9** in PBS buffer to evaluate its aqueous stability over 48 hours at 25 °C.

Table 4.35: Time dependent molar conductivity (Λ_M) of complexes in DMSO over 48 h at 25 °C

Compound	**Λ_M (S cm^2 mol^{-1})**				
	0 h	0.5 h	6 h	12 h	48 h
3a	23.87	23.89	23.89	23.92	23.98
3c	21.66	21.66	21.70	21.72	21.74
4a	24.67	24.69	24.69	24.75	24.77
4c	20.22	20.29	20.29	20.32	20.35
9	22.44	22.44	20. 48	20.48	20.50

4.5 DNA Interaction Studies

The study of the interaction of the complexes with DNA can provide simulative information, which is essential in understanding the mode of tumour inhibition and relating it to the variation in their chemotherapeutic potential. The major tools employed to study the binding of the drug molecules with DNA include UV-visible, fluorescence spectroscopies, circular dichroism, mass spectrometry, electrophoresis, thermal denaturation, viscosity measurements, and voltammetry studies. In this work, the binding of the complexes (**3a**, **3c**, **4a**, **4c**, and **9**) with calf-thymus DNA (CT-DNA), deactivation of these complexes by glutathione (GSH) was by observed by electronic spectra and a competitive binding assay using Hoechst 33258 as the quencher by fluorescence spectroscopy. To explore the redox behaviour of the five Ru(II) compounds, cyclic voltammograms were obtained using a glassy carbon electrode in Ar-saturated 0.10 M $TBABF_4$ (in DMSO) solution.

4.5.1 Calf Thymus-DNA Studies

Although the mechanism of action of metal-based drugs is not fully known, it is generally believed that DNA is the most likely biological target (Khanvilkar *et al.*, 2021). The binding of a drug to DNA is likely to interfere with the DNA replication mechanisms and thus facilitate cell death (Galindo-Murillo *et al.*, 2015). Metal complexes have illustrated diverse non-covalent interactions with cellular DNA. These interactions can be, intercalative, partially intercalative, or groove-binding, wherein the encounter complexes are stabilised by hydrophobic, dipolar hydrogen bonding, or electrostatic (ion-ion, ion-dipole) interactions (Pages *et al.*, 2015; Snyder & Hendry, 2005). These preassociative interactions are primordial to the mechanism of action of most metallodrugs that have found widespread use as anticancer medicines. Electronic absorption titration is one of the most commonly used methods for determining the type of interactions between metal complexes and their bio-targets, such as DNA (Bhadra & Kumar, 2011; Jaumot & Gargallo, 2012).

Upon the addition of CT-DNA in increasing concentration to a fixed concentration of the complexes in PBS buffer (pH 7.2); there was a hyperchromic shift in absorbance at 300 nm (Figures. 4.84 - 4.88). However, there were no significant changes in the absorbance of the complexes in the MLCT region with the gradual addition of DNA. These observations suggest that the complexes interacted with CT-DNA mainly *via* groove binding mode of binding. The

intrinsic binding constant (K_b) and Gibbs free energy (ΔG) of the complexes were calculated from the spectral data using equations 3.4 and 3.5, respectively, gave a qualitative comparison of their DNA binding affinities. The intrinsic binding constants indicate the stability of the binder-DNA adducts, whereas the magnitude of the free energy represents the spontaneity or non-spontaneity of the interactions of the binder with DNA (Mukherjee *et al.*, 2017). The DNA-binding constants (K_b) of the complexes were between 3.41-1.29×10^4 (Table 4.21), showing a good binding efficacies with CT-DNA. These values of K_b are in close agreement with previously reported values (6.50-1.80×10^4) for non-covalent interactions of similar η^6-arene Ru(II) complexes bearing *N,N'*-bidentate ligands (Alsaeedi *et al.*, 2020; Čanović *et al.*, 2017; Paitandi *et al.*, 2018; Paitandi *et al.*, 2017). Interestingly, the K_b of the tolyl-bearing complex, **9,** is higher than that of the *p*-cymene-bearing complex, **3a**; while the K_b values for the chloro complexes **3a**/**4a** are slightly larger than those of their iodo analogues, **3c/4c**. What is apparent is that the less sterically demanding the carrier groups are, or the smaller the atomic size of the halide is, the stronger the binding to DNA (Purkait *et al.*, 2015). Compared to a similar study done for Ru(II) η^6-*p*-cymene complexes with pyrazole-benzimidazole as a bidentate ligand (Bhattacharyya *et al.*, 2017; Chakraborty *et al.*, 2021), a similar mode of interaction with CT-DNA is observed as in the studied complexes **(3a, 3c, 4a, 4c, 9),** though the latter exhibit stronger binding affinities. In both cases, structural variations are observed, *viz*., tolyl (**9**) *vs*. cymene (**3a**); and chloro (**3a**/**4a**) *vs.* iodo (**4a/4c**). What is apparent is that the less sterically demanding the carrier groups are, or the smaller the atomic size of the halide is, the stronger the binding to DNA (Purkait *et al.*, 2015). The dimethyl substituents on the pyrazole (**4a** *vs.* **3a** or **4c** *vs.* **3c)** have little or no significant effect on the strength of the binding of the complexes, which could have been associated with strain on the minor groove. The negative values of ΔG for all complexes (Table 4.36) imply the spontaneous interactions among the η^6-arene Ru(II) complexes and the CT-DNA that ensued *via* non-covalent attractive forces which stabilised the encounter (Mukherjee *et al.*, 2017).

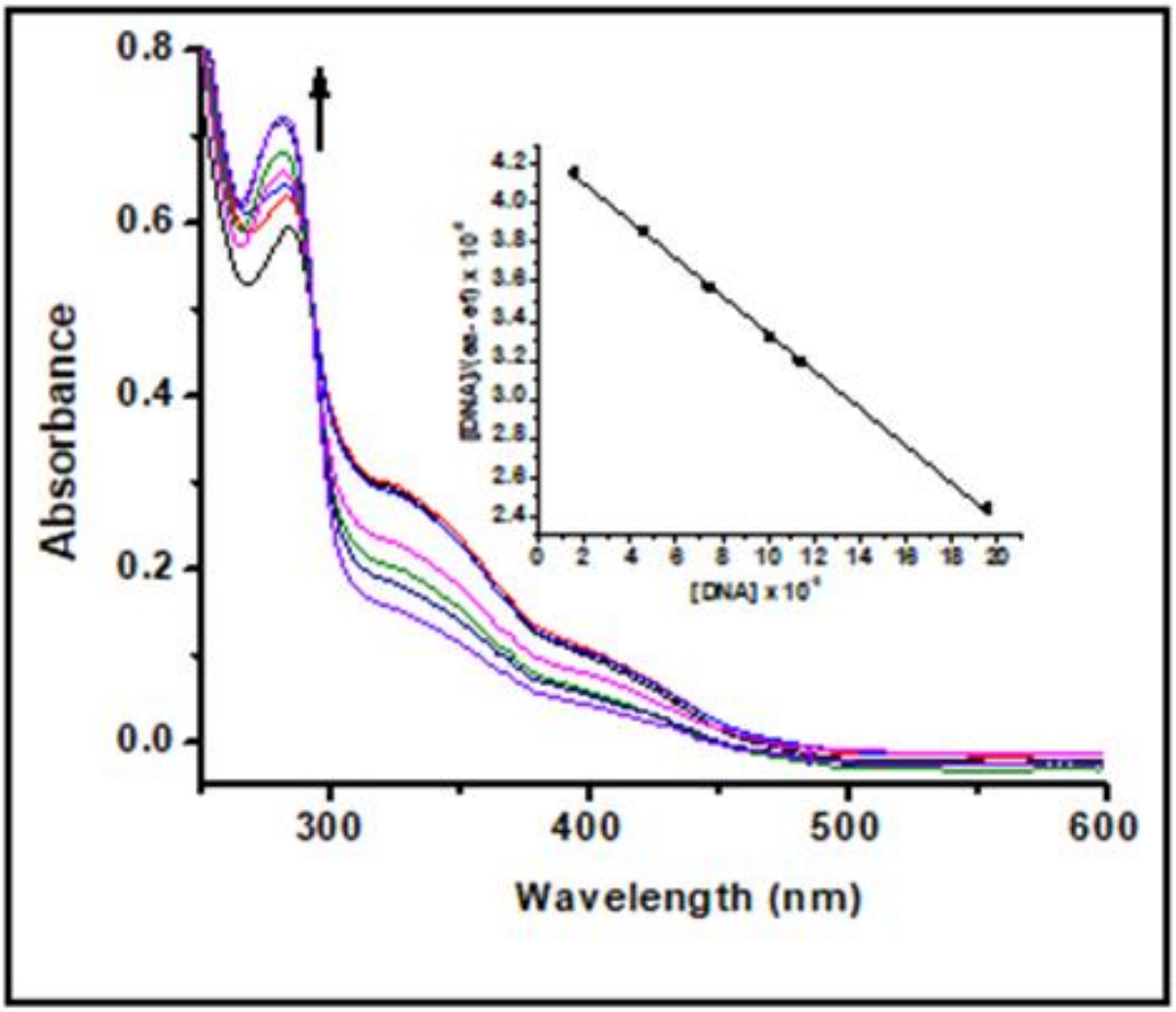

Figure 4.84: UV–Visible absorption spectra of complex **3a** in PBS buffer (pH 7.2) upon incremental addition of CT-DNA at room temperature. Inset: Plot of [DNA]/(εa- εf) vs [CT-DNA]. The arrow indicates absorbance changes with the increasing CT-DNA concentration.

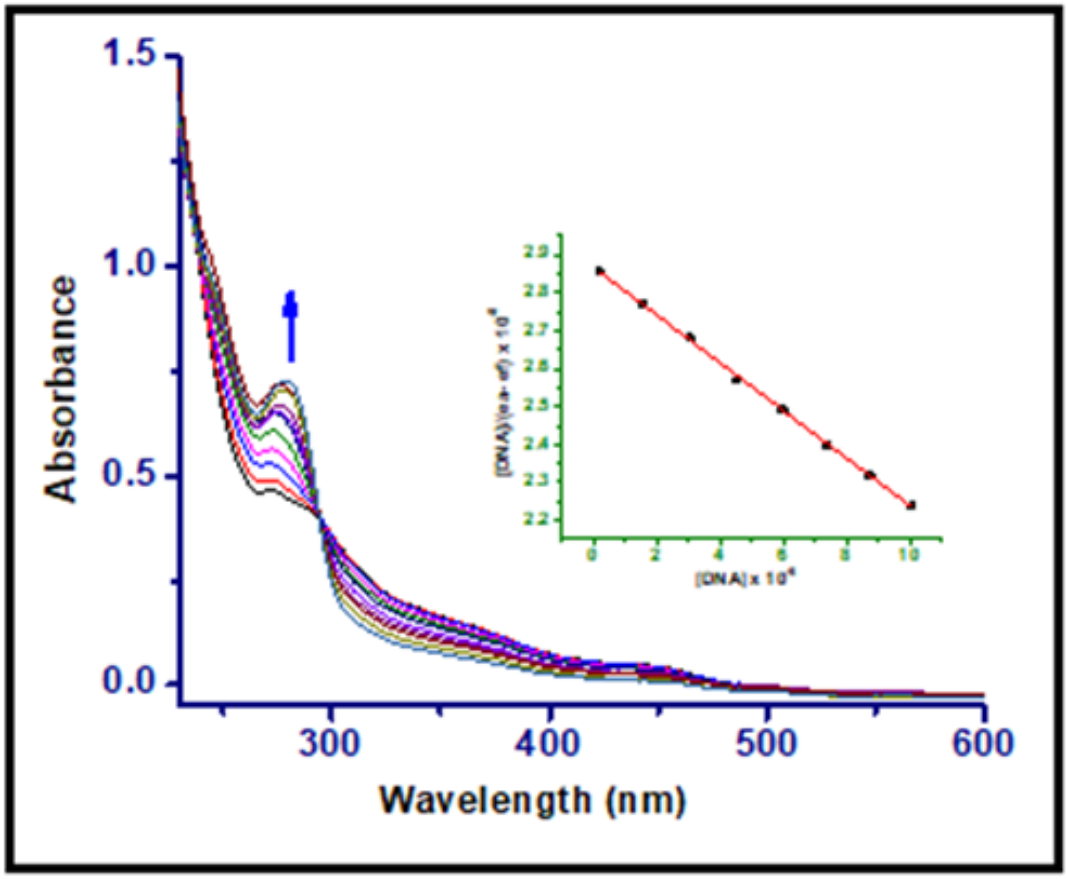

Figure 4.85: UV–Visible absorption spectra of complex **3c** in PBS buffer (pH 7.2) upon incremental addition of CT-DNA at room temperature. *Inset:* Plot of [DNA]/(ε_a- ε_f) *vs* [CT-DNA]. The arrow indicates absorbance changes with the increasing CT-DNA concentration. The changes in the electronic spectra were followed at 270 nm.

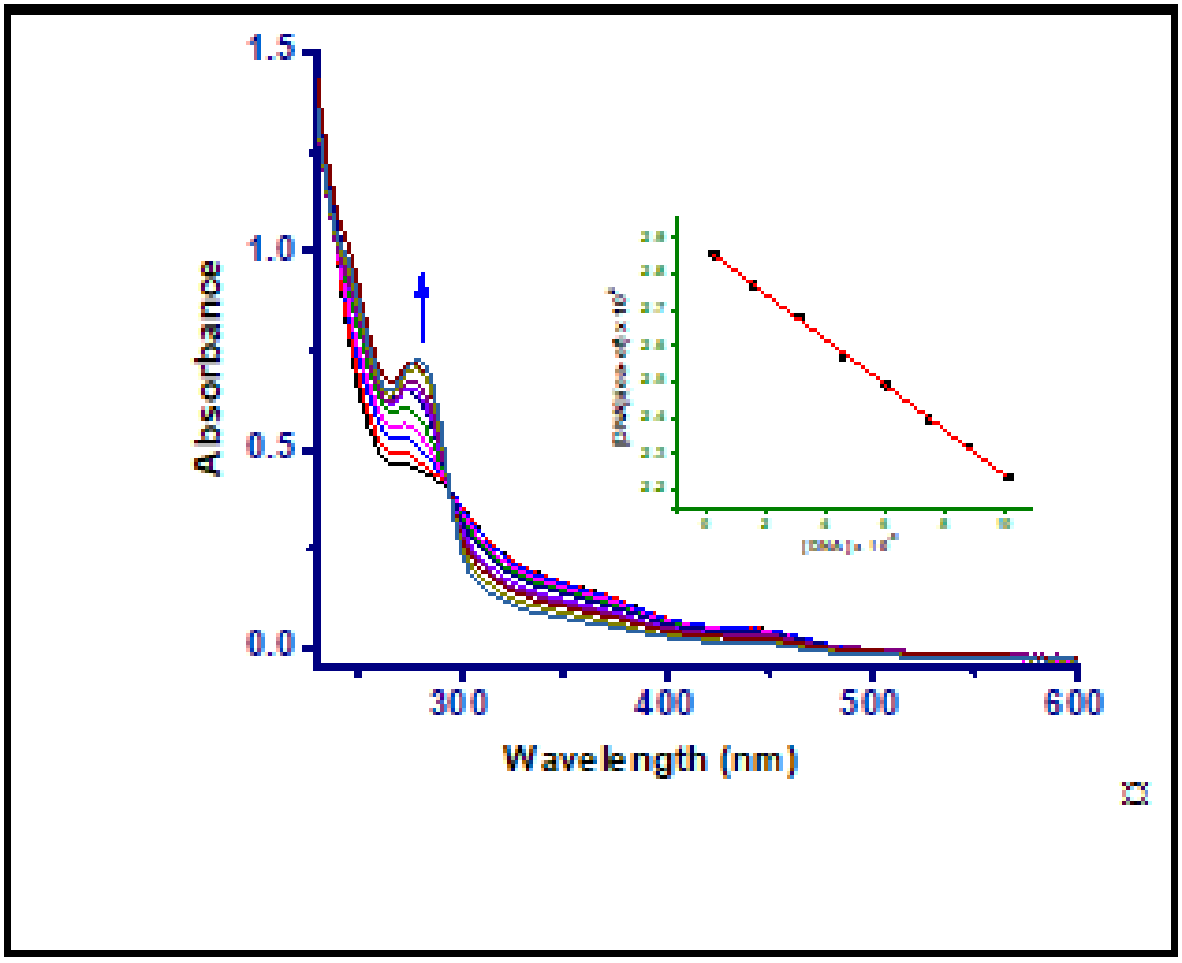

Figure 4.86: UV–Visible absorption spectra of complex **4a** in PBS buffer (pH 7.2) upon incremental addition of CT-DNA at room temperature. *Inset:* Plot of [CT-DNA] *vs* [DNA]/(ε_a-ε_f). The arrow depicts hyperchromic shift on the addition of increasing amounts of DNA.

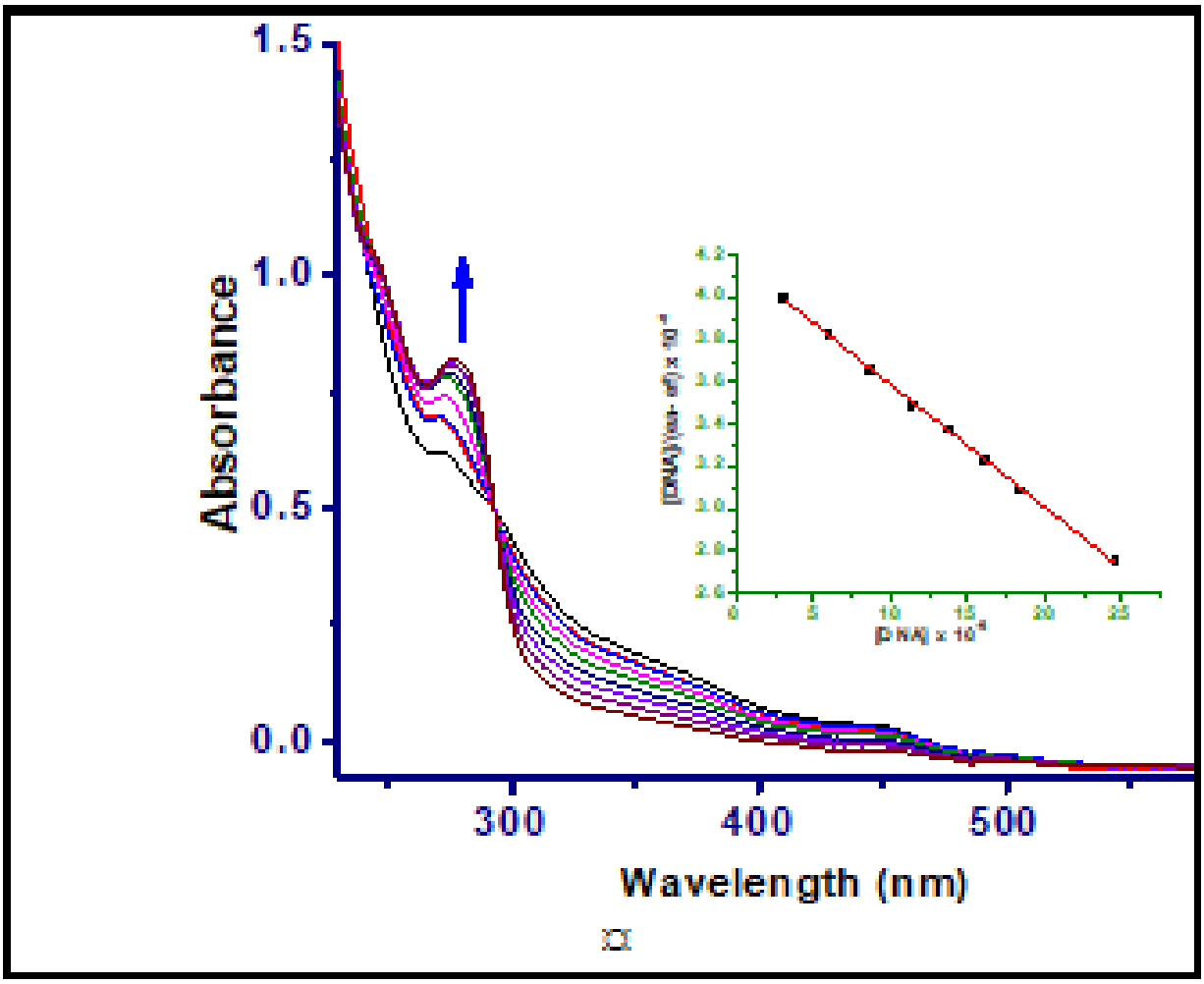

Figure 4.87: UV–Visible absorption spectra of complex **4c** in PBS buffer (pH 7.2) upon incremental addition of CT-DNA at room temperature. *Inset:* Plot of [CT-DNA] *vs* [DNA]/(ε_a-ε_f). The arrow depicts hyperchromic shift on the addition of increasing amounts of DNA.

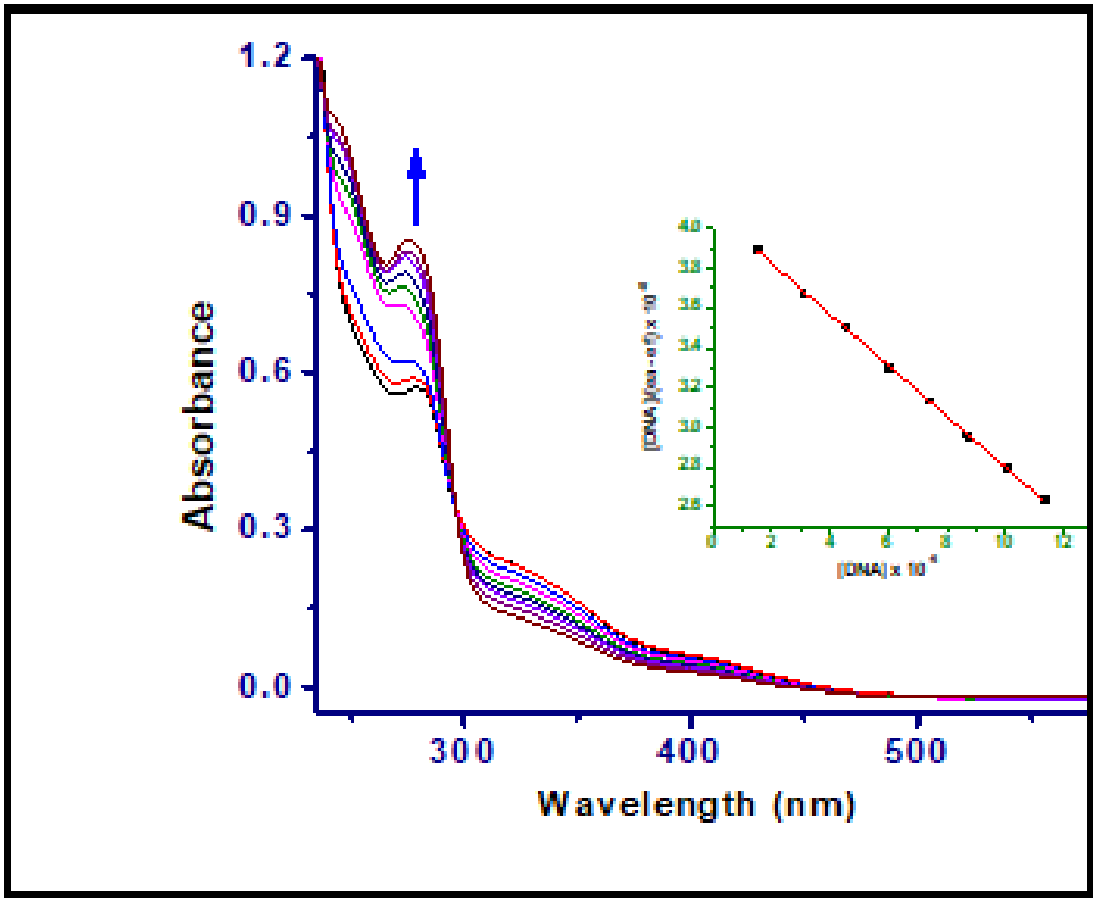

Figure 4.88: UV–Visible absorption spectra of complex **9** in PBS buffer (pH 7.2) upon incremental addition of CT-DNA at room temperature. *Inset:* Plot of [DNA]/(ε_a- ε_f) *vs* [CT-DNA]. The arrow shows the change in absorbance upon increasing the CT-DNA concentration.

Table 4.36: DNA-binding constants for η^6-arene Ru(II) complexes calculated from UV-Visible absorption and Hoechst fluorescence titrations.

Complex	UV-Visible absorption titration		Fluorescence emission titration			
	K_b (10^4 M^{-1})	$\Delta G^{\neq}_{25°C}$ (kJ mol^{-1})	K_{SV} (10^5 M^{-1})	k_q (10^{12} M^{-1} s^{-1})	K_F (10^5 M^{-1})	*n*
3a	1.98 ± 0.11	-24.5	1.91 ± 0.20	8.22 ± 0.60	1.61 ± 0.10	0.98
3c	1.64 ± 0.23	-24.0	1.88 ± 0.30	8.18 ± 0.30	1.45 ± 0.10	0.99
4a	2.22 ± 0.18	-24.8	1.98 ± 0.30	8.34 ± 0.40	3.81 ± 0.30	1.10
4c	1.42 ± 0.13	-23.7	1.67 ± 0.10	0.72 ± 0.01	1.08 ± 0.20	0.95
9	3.14 ± 0.27	-25.7	2.42 ± 0.20	8.65 ± 0.50	4.19 ± 0.40	1.21

4.5.2 Competitive Quenching Studies between Hoechst and Complexes for CT-DNA

Hoechst 33258 was used as a fluorescence probe to further investigate the mode of interactions of the η^6-arene Ru(II) complexes with CT-DNA. Changes in the emission spectrum of Hoechst with increasing amounts of the Ru(II) complexes are shown in Figures 4.89-4.93 for **3a**, **3c**, **4a**, **4c**, and **9**, respectively. A significant decrease in the fluorescence intensity of the emission occurred at 450 nm, depicting the competitive displacement of Hoechst from DNA's minor grooves. This decrease in fluorescence intensity clearly showed the capability of these complexes to displace Hoechst molecules bound to CT-DNA. The Stern-Volmer constant (K_{SV}) and bimolecular quenching rate constant (k_q) were determined from Stern-Volmer plots (Figure 4.88b) using equation 3.6. The K_{SV} values (1.71-2.62 × 10^5 M^{-1}) in Table 4.36 confirmed groove binding and are close to those of other Ru complexes (Medjedović *et al.*, 2020). The observed low-order K_{sv} values in substituted methyl substituted complexes reveal that the complexes are not able to strongly groove-bind with DNA so as to replace the stronger groove binder Hoechst 33258. The calculated values of the bimolecular quenching rate constant (k_q) ranged from 0.72 to 9.15 × 10^{12} M^{-1} s^{-1}. These values are a hundred times higher than the maximum rate known for quenching rate constants (2.0 × 10^{10} L mol^{-1} s^{-1}) for dynamic interactions (Maikoo *et al.*, 2021), suggesting the quenching interactions of the Ru(II) complexes are static. The high values of the quenching rate constants, k_q (*ca.* 10^{12} M^{-1} s^{-1}), indicate ultra-fast bimolecular quenching kinetics as a result of facile binding of the η^6-arenes Ru(II) complexes to the target sites (Sankareswari *et al.*, 2014). Further, the interactions between these complexes and CT-DNA were affirmed to occur by groove binding *via* favourable non-covalent interactions between the Ru(II) complexes' ligand moieties and the hydrophobic groups within the DNA groove. Such interactions include cooperative van der Waals attractions, hydrogen bonding, and electrostatic interactions which collectively cause a change in the structure of the double helix of DNA hosting the Hoechst 33258 groove binder (Pages *et al.*, 2015). From the Scatchard plots of the data (Figures 4.89-4.93), the association binding constant, K_F, and the number of Ru(II) complexes binding sites per nucleotide, *n*, were computed, and the data is presented in Table 4.36. These compounds gave almost similar "n = 0.95-1.21" values for DNA, indicating that there was only one binding site in the DNA for each compound during their interactions.

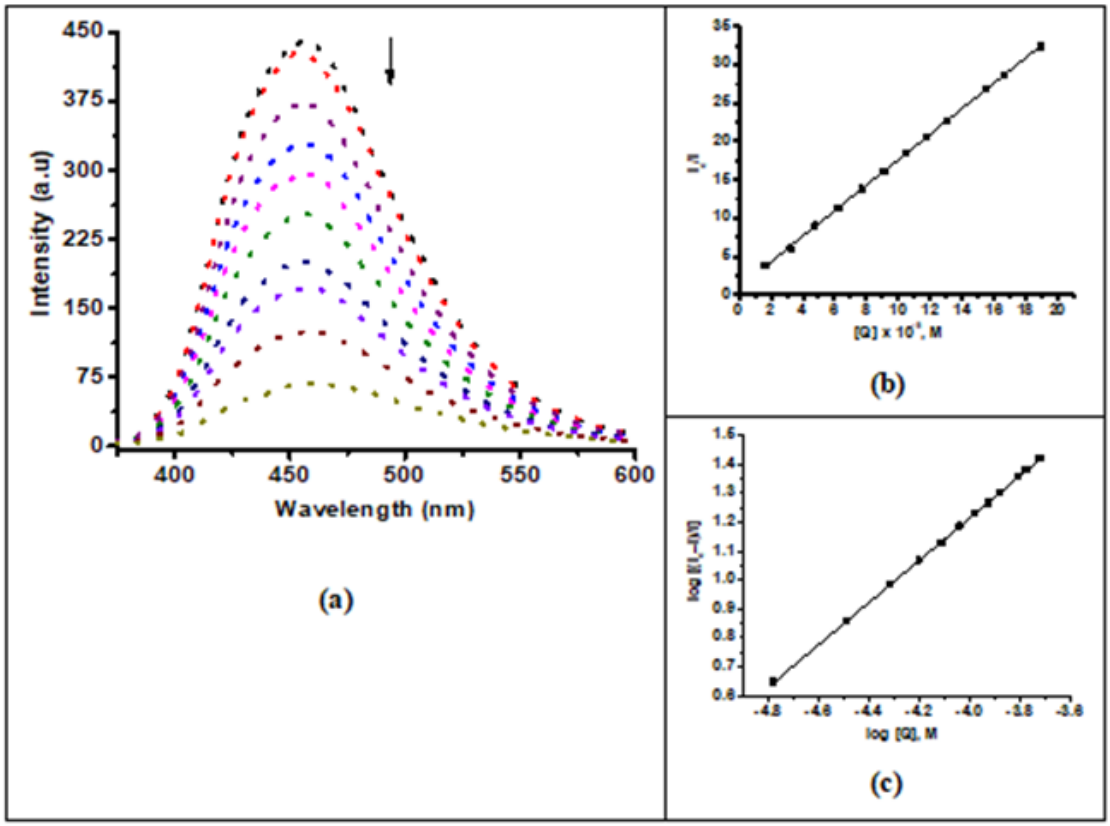

Figure 4.89: (a) Emission spectra of the Hoechst 33258–CT-DNA complex (λ_{ex} = 343 nm) in PBS buffer (pH 7.2, 25 °C) in the presence of increasing concentrations of complex **3a**. The arrow denotes the change in fluorescence intensity upon addition of the metal complex. (b) Stern-Volmer plot of I_o/I as function of [Q]. (c) Scatchard plot of log $[(I_o–I)/I]$ *versus* log [Q].

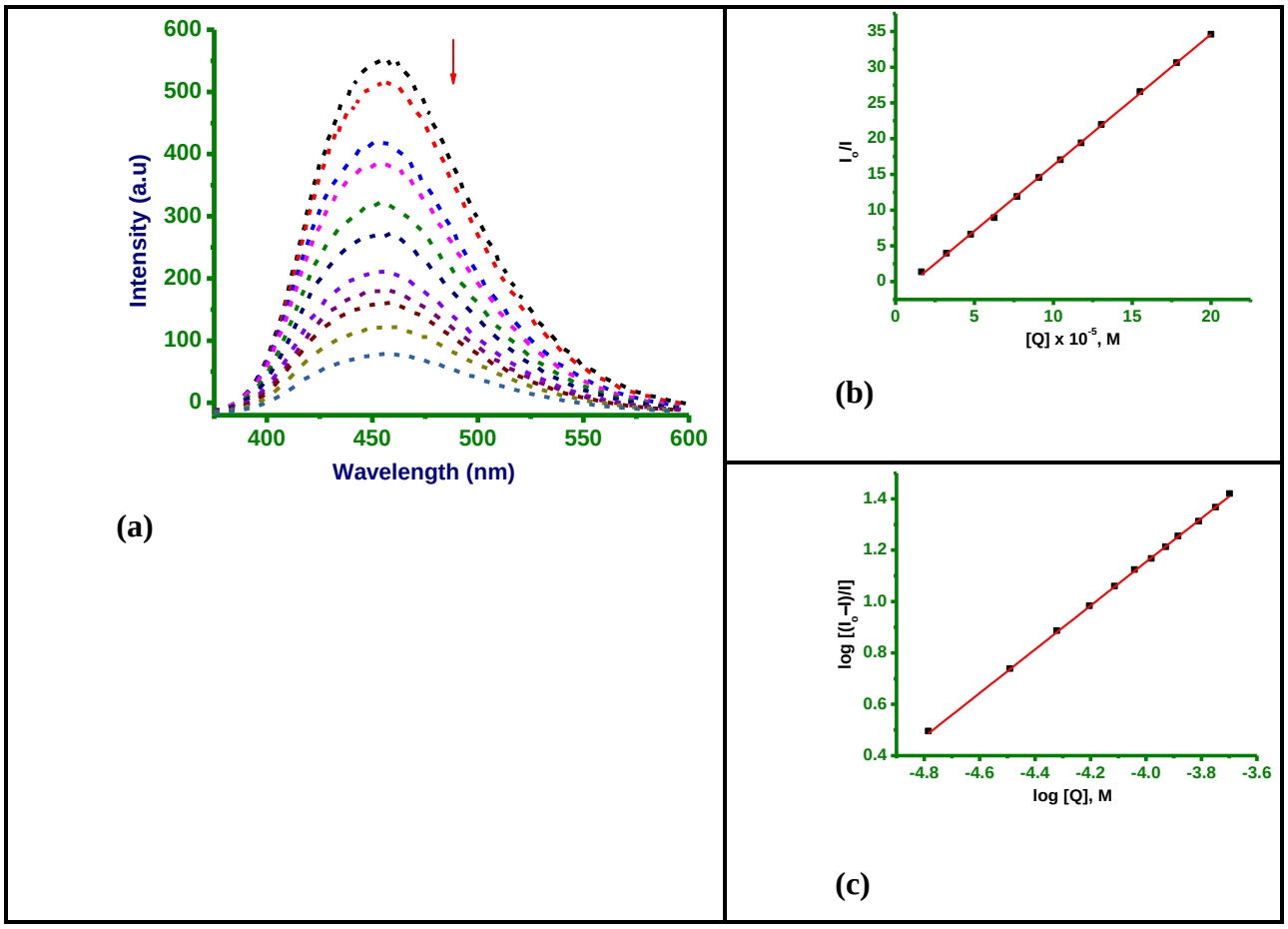

Figure 4.90: (a) (a) Emission spectra of the Hoechst 33258–CT-DNA complex (λex = 343 nm) in PBS buffer (pH 7.2, 25 °C) in the presence of increasing concentrations of complex **3c**. The arrow denotes the change in fluorescence intensity upon addition of the metal complex. (b) Stern-Volmer plot of Io/I as function of [Q]. (c) Scatchard plot of log [(Io–I)/I] *versus* log [Q].

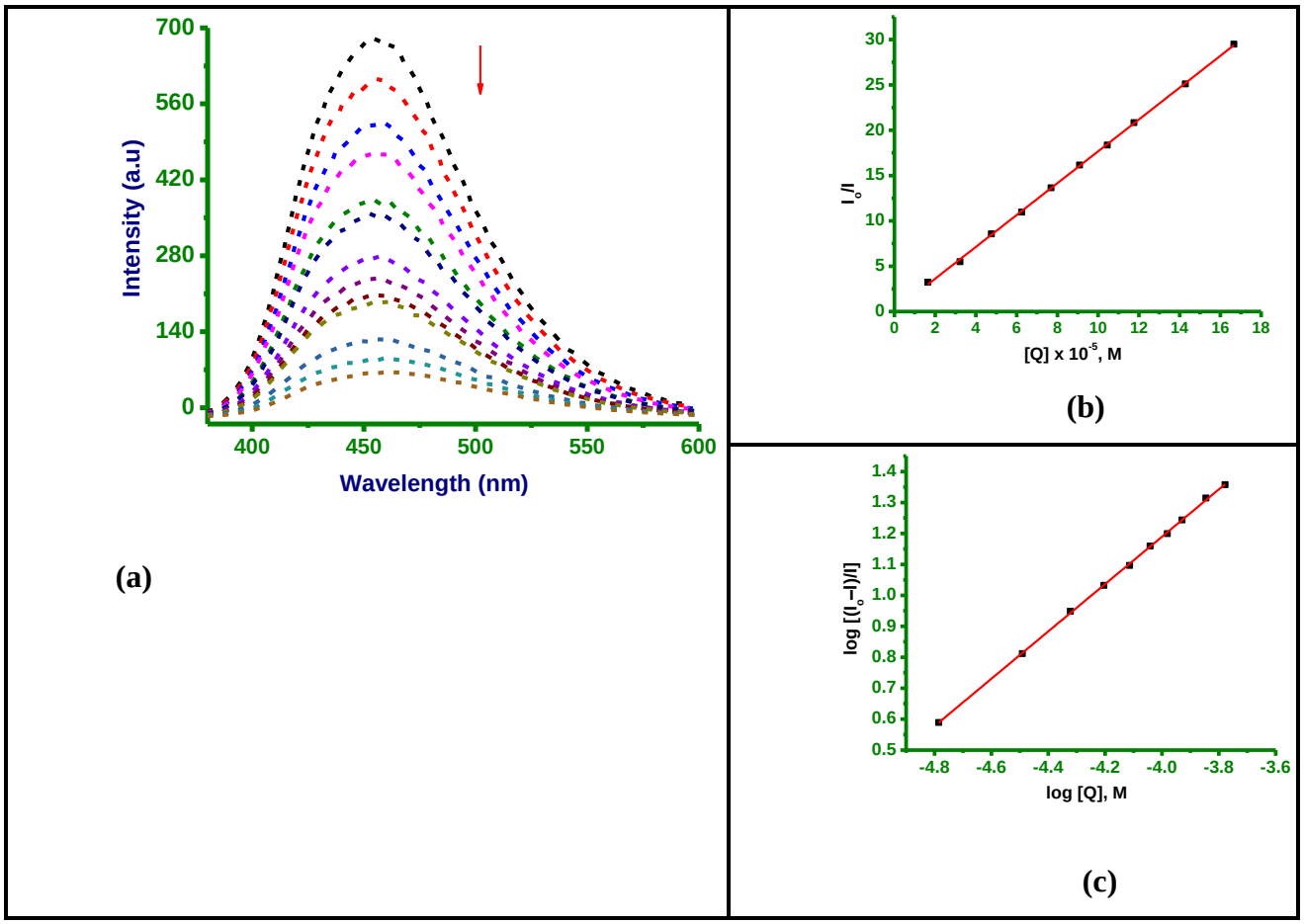

Figure 4.91: (a) Emission spectra of the Hoechst 33258–CT-DNA complex (λex = 343 nm) in PBS buffer (pH 7.2, 25 °C) in the presence of increasing concentrations of complex 4a. The arrow denotes the change in fluorescence intensity upon addition of the metal complex. (b) Stern-Volmer plot of I_o/I as function of [Q]. (c) Scatchard plot of log [(Io–I)/I] *versus* log [Q].

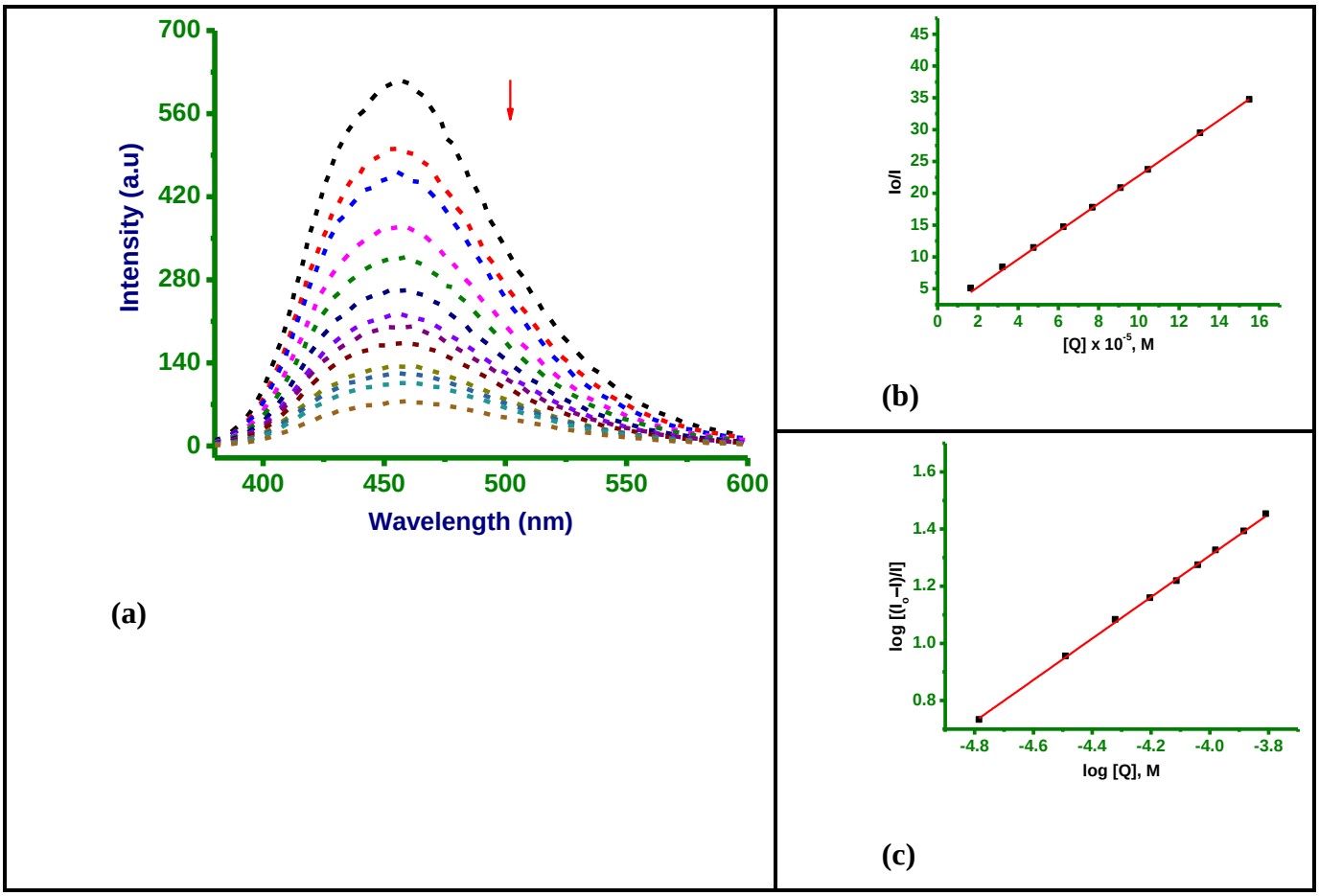

Figure 4.92: (a) Emission spectra of the Hoechst 33258–CT-DNA complex (λex = 343 nm) in PBS buffer (pH 7.2, 25 °C) in the presence of increasing concentrations of complex **4c**. The arrow denotes the change in fluorescence intensity upon addition of the metal complex. (b) Stern-Volmer plot of I_o/I as function of [Q]. (c) Scatchard plot of log $[(I_o–I)/I]$ versus log [Q].

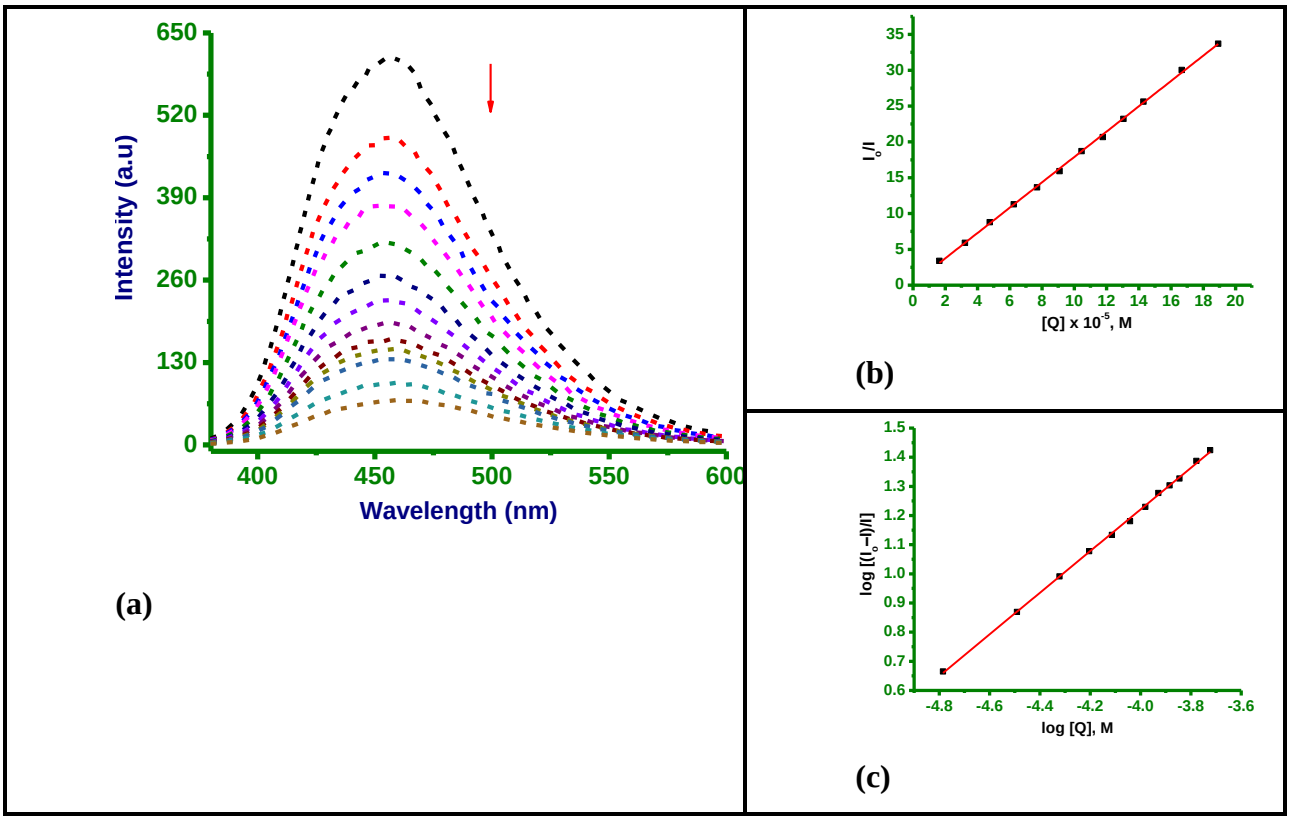

Figure 4.93: (a) The effect of adding **9** on the emission intensity of Hoechst 33258 bound to CT-DNA (λex = 343 nm) at varying concentrations of **9** in PBS (at pH = 7.2, 25°C). The arrow shows the change in absorbance with the addition of the metal complex. (b) Stern-Volmer plot of Io/I *vs* [Q]. (c) Scatchard plot of log [(I_o–I)/I] *vs* log [Q].

4.5.3 Reactions with Glutathione

GSH is a crucial antioxidant, thio-enzyme cofactor, and detoxifier that is normally overexpressed in hypoxic cancer cells. It deactivates the antitumour capabilities of most metal-based drugs, such as cisplatin, by substituting the labile group(s) to form stable GS-conjugated products (Balendiran *et al.*, 2004; Wang *et al.*, 2002). The formation of the GS-metal adduct reduces the concentration of the drug, eventually reaching the cancer cells. The substitution reaction between these η^6-arene Ru(II) complexes with GSH caused hypochromism at 350 nm (Figures 4.94-4.98). From the K_b values summarised in Table 4.37, the iodo substitution by GSH occurs seven times slower than the chloro substitution, *i.e.*, **3a** *vs.* **3c**, **4a** *vs.* **4c**, while the

complex with cymene (**3a**) is three times slower than that of the tolyl group (**9**) in the chloro substitution. Advertently, the chloro complexes exhibit better capabilities for scavenging reactive oxygen species (ROS), which may chemo-protect the indiscriminate apoptosis of healthy cells. Also, the introduction of a methyl group in the *N,N'*-bidentate ligand decreases the deactivation of the complex by two times (**3a** *vs.* **4a** and **3c** *vs.* **4c**). The most bulky group appears to exhibit higher resistance to GSH (Purkait *et al.*, 2016). The greater resistance of the Ru-I bond to deactivation may further enhance their potency compared with chlorido complexes (Dougan *et al.*, 2008). The GSH-substituted complexes are relatively inactive towards further substitution by bio-nucleophiles. Hence, the trends observed in the rate of ligand exchange from **3a**, **3c**, **4a**, and **4c** by GSH, demonstrates that if such inactivation were to happen *in vivo*, it would be controlled by the polarisability of the halide leaving group and the electronic properties of the substituents on the *N,N'*-bidentate (Bhattacharyya *et al.*, 2017; Chakraborty *et al.*, 2021). The number of binding sites per Ru(II) complex, n, is approximately 2 (Table 4.37), implying two binding sites are available in the GSH for these Ru(II) complexes.

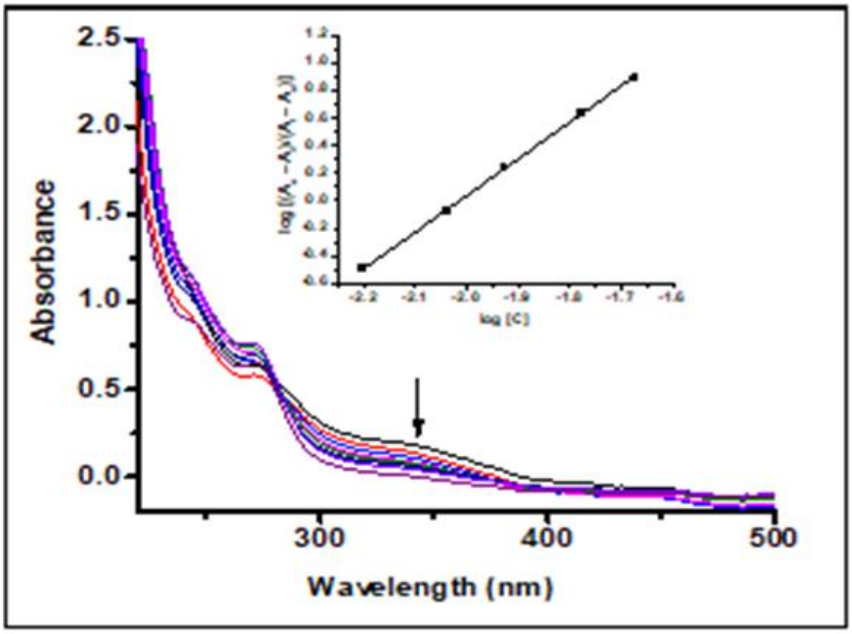

Figure 4.94: UV-Visible spectral variations of complex **3a** upon stepwise addition of glutathione (GSH) in PBS buffer (pH 7.2) at ambient temperature.

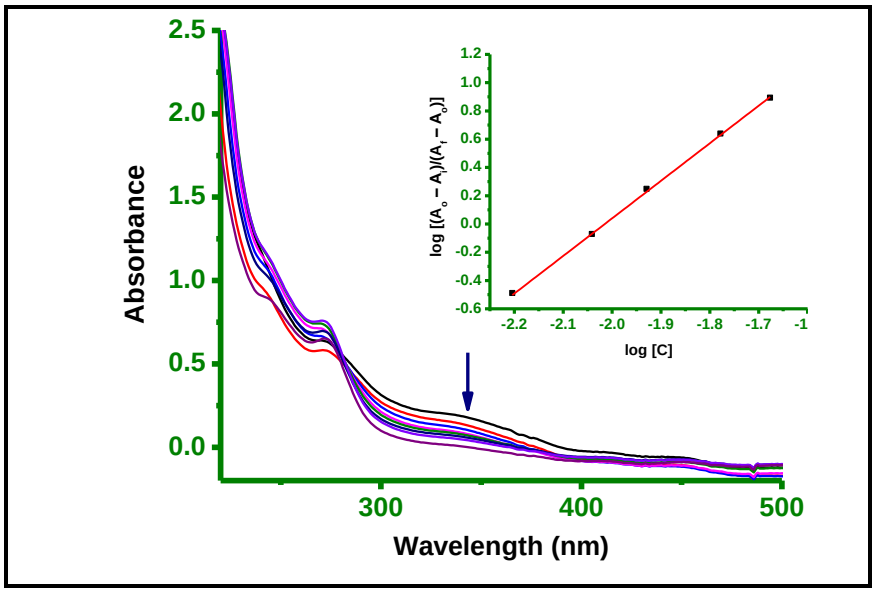

Figure 4.95: UV-Visible spectral changes of complex **3c** upon titration with glutathione (GSH) in PBS buffer (pH 7.2) at ambient temperature.

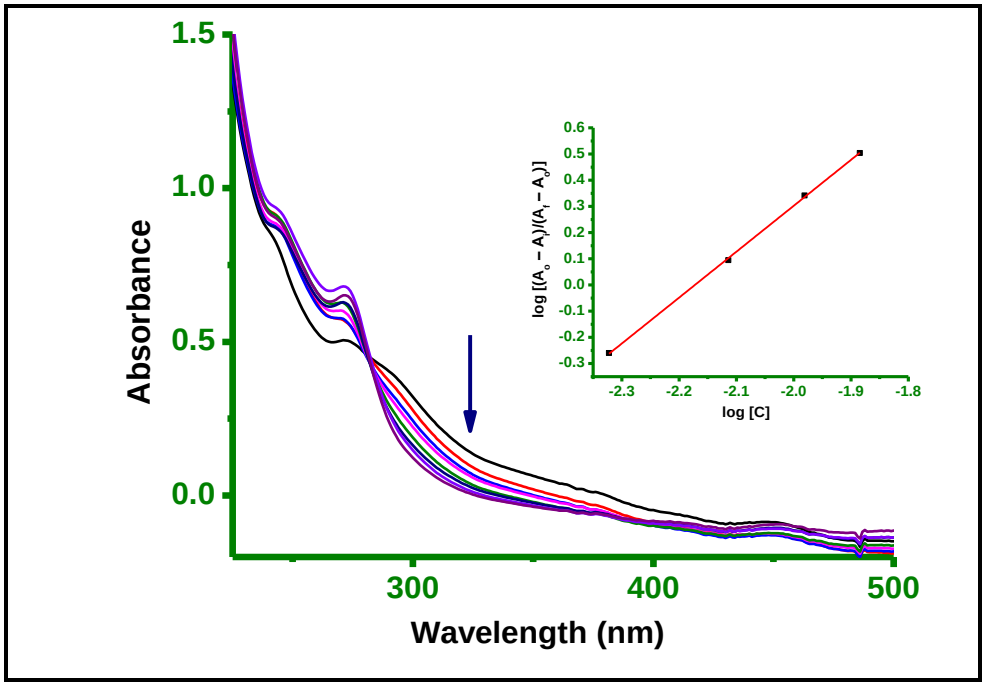

Figure 4.96: UV-Visible spectral changes of complex **4a** upon titration with glutathione (GSH) in PBS buffer (pH 7.2) at ambient temperature.

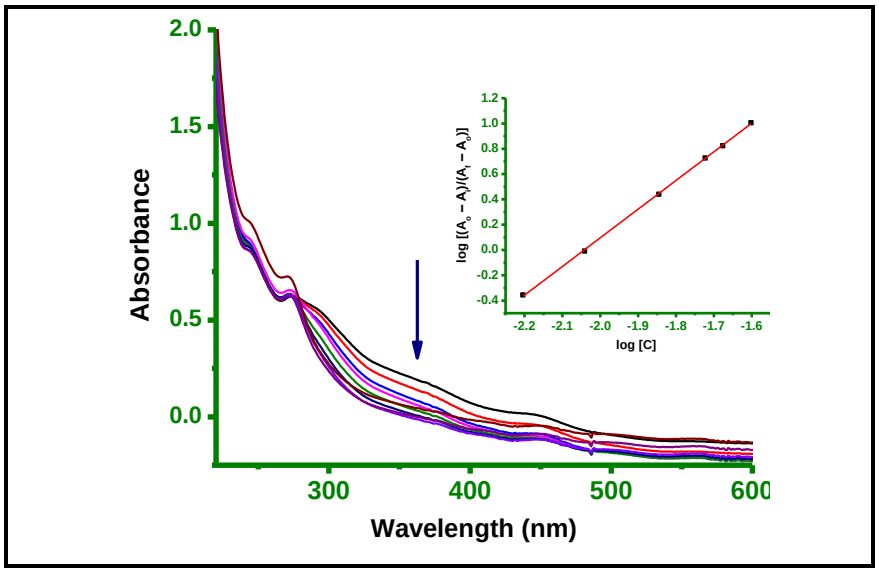

Figure 4.97: UV-Visible spectral changes of complex **4c** upon titration with glutathione (GSH) in PBS buffer (pH 7.2) at ambient temperature.

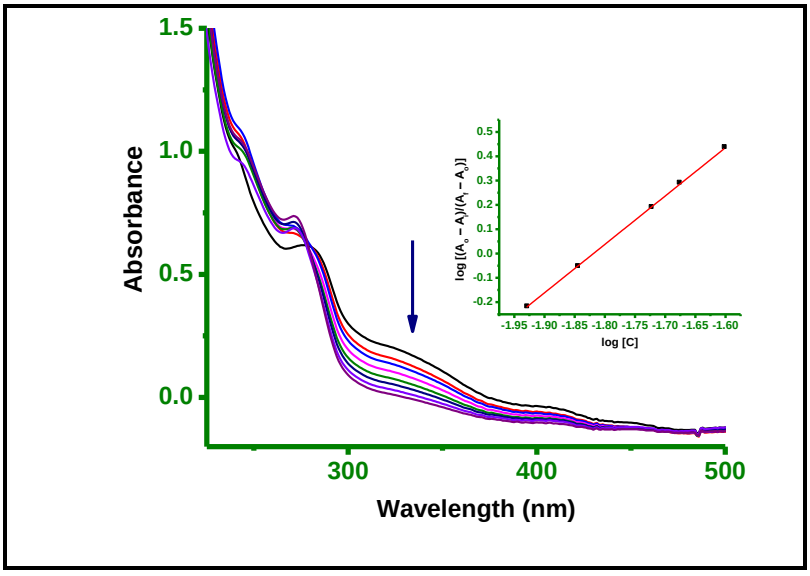

Figure 4.98: UV-Visible spectral changes of complex **9** upon titration with glutathione (GSH) in PBS buffer (pH 7.2) at ambient temperature.

Table 4.37: Binding constants and number of binding sites for the interactions of η6-arene Ru(II) complexes with GSH

Complexes	K_b (10^3 M^{-1})	n
3a	13.33	1.9
3b	94.45	1.8
4a	6.44	2.1
4c	42.51	1.8
9	4.18	2.0

4.5.4 Redox Properties

The electronic behaviour of the complexes was explored through cyclic voltammetry, which provided insight into their redox characteristics. The measured oxidation potentials reflect how the electronic nature of the ligands—particularly their ability to donate electron density (σ-donation) or accept electron density (π-acceptance)—influences the ruthenium(II) metal centres. These redox data are crucial for understanding the electronic structure and reactivity of the complexes, offering a basis for predicting their chemical behaviour in subsequent transformations (Matsinha *et al.*, 2013). Figures 4.99-4.103 for the complexes show a common Ru^{II}/Ru^{III} oxidation peak on the forward scan initiated at the negative potential values. The coupled reduction was recorded in the return scan. The introduction of electron-donating methyl groups to the pyrazolyl-pyridazine ligand or changing the labile ligand to I^- (ligands display high basicity) shifts the potential of the redox couple to more negative values. Thus, Ru^{II} centre in **4a** is more easily oxidised than the rest of the complexes, indicating that the coordinated ligands have better σ- electron donor or weak π- accepting properties. Methyl groups readily add electron density to the ruthenium centre *via* the pyrazolyl-pyridazine ring, rendering the Ru^{II}/Ru^{III} oxidation easier. Complexes **3a** and **9** have considerably higher values of Ru^{II}/Ru^{III} oxidation potential attributed to the least σ- donating abilities/stronger π- acceptor character of coordinated Cl^-/unsubstituted pyrazolyl-pyridazine. All peaks correspond to a quasi-reversible one-electron transfer process (Wang *et al.*, 2020). The relative magnitudes of the redox potential of the $Ru^{II/III}$ couple are **3a** > **3c** ≈ **4a** > **4c** (for Cl and I, respectively), and **3a** > **4a** ≈ **4c** > **3c** (for –H and $–CH_3$, respectively) in Table 4.38. Therefore, the changes in oxidation and reduction

potentials are attributed to the relative stabilisation of Ru(II) over Ru(III) as a result of the combined effects of σ- donor and π- acceptor that arise from ligands (Wu *et al.*, 2013). The $E_{1/2}$ values were close to those of other Ru(II) complexes (Pastuszko *et al.*, 2013).

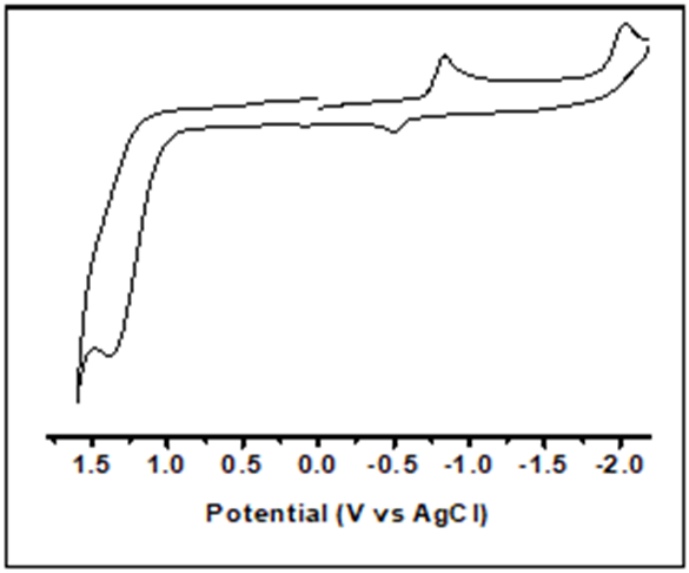

Figure 4.99: Cyclic voltammetric profile of complex **3a** recorded in DMSO with 0.10 M NH_4BF_4 as the supporting electrolyte, using a glassy carbon working electrode (WE), Ag/Ag^+ reference electrode (RE), and platinum wire as the counter electrode (CE) at a scan rate of 0.10 V/s.

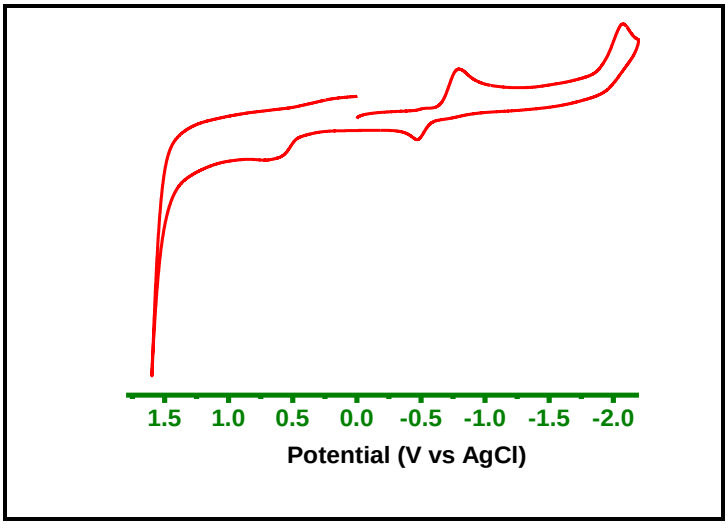

Figure 4.100: Cyclic voltammogram of complex **3c** in DMSO (0.10 M NH_4BF_4, WE: GC, RE: Ag/Ag^+, CE: Pt, scan rate: 0.10 V/s).

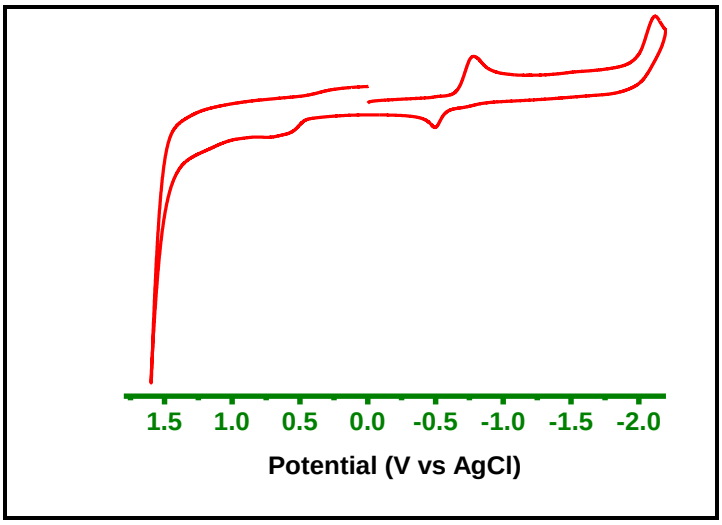

Figure 4.101: Cyclic voltammogram of complex **4a** in DMSO (0.10 M NH_4BF_4, WE: GC, RE: Ag/Ag^+, CE: Pt, scan rate: 0.10 V/s).

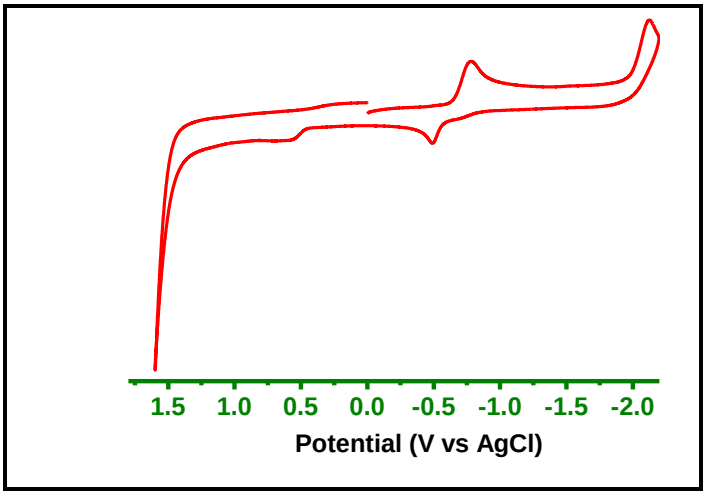

Figure 4.102: Cyclic voltammogram of complex **4c** in DMSO (0.10 M NH_4BF_4, WE: GC, RE: Ag/Ag^+, CE: Pt, scan rate: 0.10 V/s).

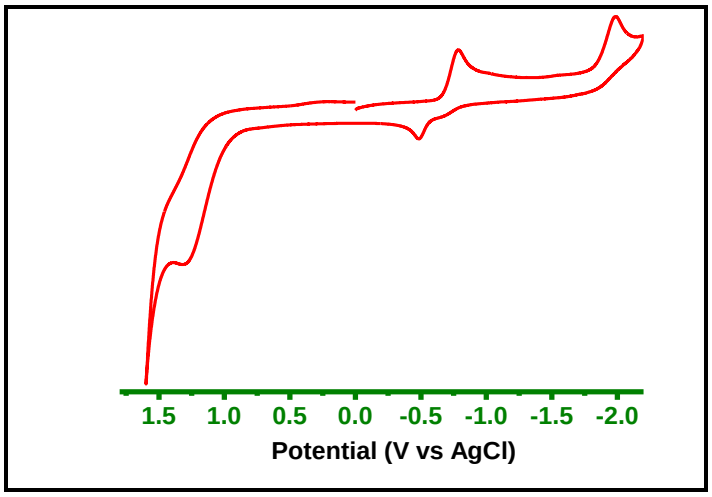

Figure 4.103: Cyclic voltammogram of complex **9** in DMSO (0.10 M NH_4BF_4, WE: GC, RE: Ag/Ag^+, CE: Pt, scan rate: 0.10 V/s).

Table 4.38: Half-wave potentials ($E_{1/2}$, V) of complexes **3a, 3c, 4a, 4c,** and **9**, measured relative to the Ag/Ag^+ reference electrode.

Complexes	E_{pa} (V)	E_{pc} (V)	$E_{1/2}$ (V)
3a	-0.80	-0.50	-0.65
3c	-0.81	-0.49	-0.65
4a	-0.83	-0.51	-0.67
4c	-0.80	-0.54	-0.67
9	-0.75	-0.50	-0.63

The half-wave potential ($E_{1/2}$) was calculated as the average of the anodic (E_{pa}) and cathodic (E_pc) peak potentials, using the relation: $E_{1/2} = (E_{pa} + E_{pc})/2$.

4.5.5 In Silico Docking Simulation

Molecular docking offers valuable insights into the interaction dynamics between potential drug candidates and biomolecular targets. Based on prior experimental evidence of DNA-binding activity, docking simulations were carried out for the Ru(II) complexes **3a, 3c, 4a, 4c,** and **9** to predict their preferred binding modes within the DNA structure, assuming both the ligand and DNA remain conformationally rigid. The docking results (see Table 4.39) revealed that all the η^6-arene Ru(II) complexes preferentially associate with the minor groove of the DNA double helix. Their binding stability varied according to the structural features of each complex.

The calculated binding affinities were -5.6 kcal/mol for **3a**, -5.4 kcal/mol for **3c**, -5.7 kcal/mol for 4a, -5.3 kcal/mol for **4c**, and -5.8 kcal/mol for **9**, whereas cisplatin showed a comparatively weaker binding affinity of -3.6 kcal/mol. These values suggest that the Ru(II) complexes exhibit stronger interactions with DNA than cisplatin, with more negative scores reflecting greater binding strength.

The relative stabilities of the poses of the DNA-η^6-arene Ru complexes correlated positively with binding constants calculated from the DNA titrations (Table 4.36). From the visual inspection of the molecular docking results, it is evident that the changing of the halide (**3a** *vs.* **3c** and **4a** *vs.* **4c**) and the steric factors of the spectator chelating ligands (**3a** *vs.* **4a** and **3c** *vs.* **4c**) inhibit DNA interactions. Complex **3a** forms π-π T-shaped interactions with the nucleotide, DC11 (C = cytosine) with a mutual distance of 4.77 Å, and π-alkyl interactions with DG10, and DG16 (G = guanine) with distances of 5.00 and 5.15 Å, respectively. Complex **3c** exhibits π-π T-shaped interactions (DG22, 4.63 Å), carbon-hydrogen bonding (DC23, 2.41 Å), and π-alkyl interactions (DG4, 5.37 Å; DA5, 4.84 Å), A = adenine. In addition, **3c** interacts with DG4 (3.54 Å), DG22 (4.87 Å), and DC3, 5.31 Å *via* π-alkyl interactions. Furthermore, nucleotides DG22 (4.64 Å), DC3 (4.64 Å), and DG4 (3.64 Å) participate in π-alkyl interaction with **4c**. The complex **9** exerted π-alkyl interactions with DC9 (5.19 Å), DG12 (3.55 Å) and DG16 (4.88 Å), and DA17 (4.67 Å).

In all cases, the complexes depicted non-conventional H-bond interactions (Figure 4.104). The docked conformations of the DNA-η^6-arene Ru complexes adducts are thermodynamically stable and occur in the minor groove of the former.

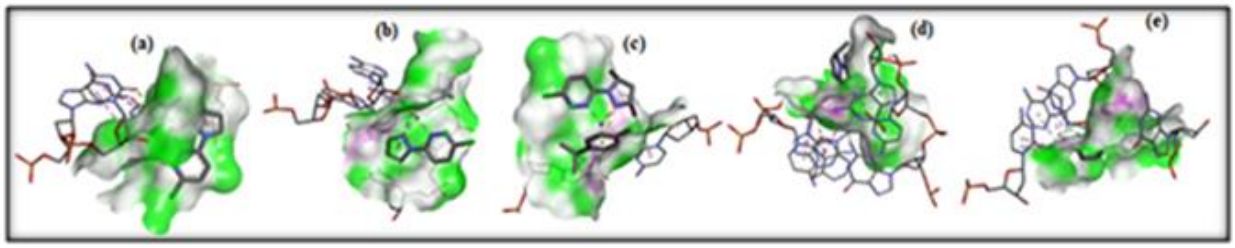

Figure 4.104: Visualization of non-classical hydrogen bonding interactions observed in the docked conformations of complexes **3a** (a), **3c** (b), **4a** (c), **4c** (d), and **9** (e), represented using stick models.

Table 4.39: Predicted binding interactions and potential nucleotide targets of Ru(II) complexes with DNA receptors

Complex	Best Docked diagram	Nucleotide interactions	Docking score (kcal/mol)
3a		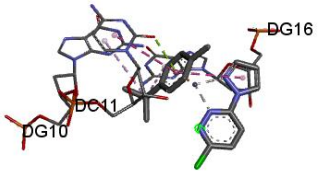	-5.6
3c	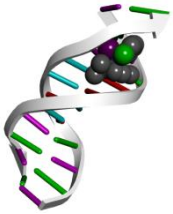	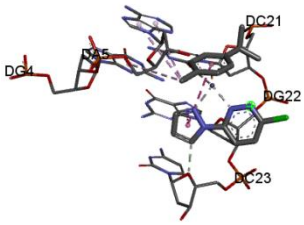	-5.4
4a		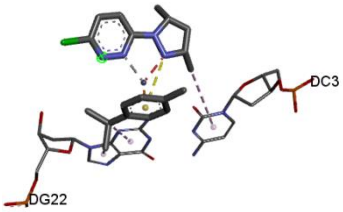	-5.7
4c	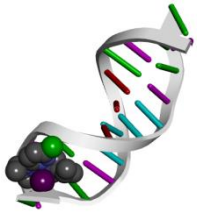	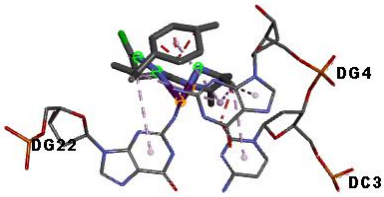	-5.3
9	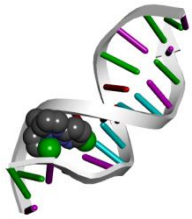	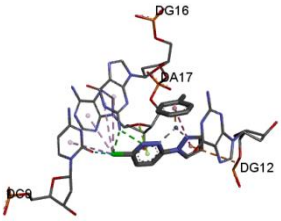	-5.8
Cisplatin	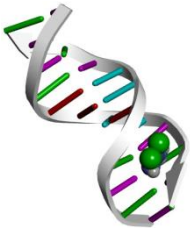	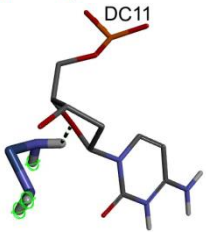	-3.6

4.6 *In Vitro* Anticancer Evaluation

Given the observed DNA-binding capacity of the complexes, their potential antitumour activity warranted further biological evaluation. The cytotoxic potential of the synthesised compounds was evaluated using the MTT assay, wherein cultured cells were treated with a range of compound concentrations to determine their dose-dependent viability responses. The η^6-arene Ru(II) complexes (**3a, 3c, 4a, 4c,** and **9**) were tested against MCF-7 breast cancer cells using 10 µM and 20 µM doses, with DMSO concentrations maintained below 0.1% to avoid solvent-induced toxicity. An initial concentration of 10 µM was employed for cytotoxicity screening, consistent with the threshold recommended by the National Cancer Institute (NCI) for the preliminary assessment of novel anticancer agents (Welsh *et al.*, 2020). At this lower concentration, the compounds exhibited only mild cytotoxic effects, with cell viability ranging between 68% and 92%. Exposure to a 20 µM concentration led to a more significant decline in cell viability, exhibiting a clear dose-responsive trend, with cell survival rates dropping by roughly 29–45%. For reference, cisplatin was used as a comparative standard.

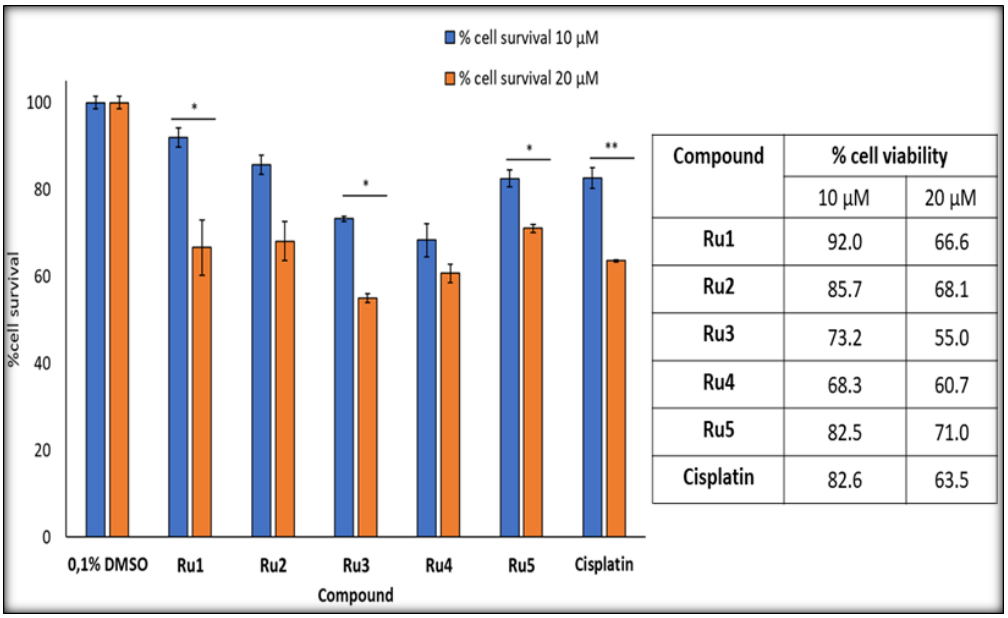

Compound	% cell viability	
	10 µM	20 µM
Ru1	92.0	66.6
Ru2	85.7	68.1
Ru3	73.2	55.0
Ru4	68.3	60.7
Ru5	82.5	71.0
Cisplatin	82.6	63.5

Figure 4.105: MCF-7 breast cancer cell viability percentages obtained from the MTT assay following treatment with test compounds.

The MCF-7 breast cancer cells were exposed to either 0.1% DMSO (used as the solvent control), varying concentrations (10 µM or 20 µM) of the investigated Ru(II) complexes (**3a-Ru1, 3c-Ru2, 4a-Ru3, 4c-Ru4,** and **9-Ru5**), or cisplatin as a standard reference compound.

The initial cytotoxic screening of the η⁶-arene Ru(II) complexes was expanded to include the triple-negative MDA-MB-231 breast cancer cell line, a model known for its aggressive behaviour, high invasiveness, and metastatic potential (Mizumura *et al.*, 2001). The complexes were evaluated at two concentrations, 10 µM and 20 µM, with a 48-hours incubation period. According to the data presented in Figure 4.106, the compounds exhibited negligible impact on cell survival, with survival rates remaining close to 100% across both doses. In contrast, cisplatin, used as a standard reference, led to approximately a 40% reduction in cell viability at 20 µM under identical experimental conditions.

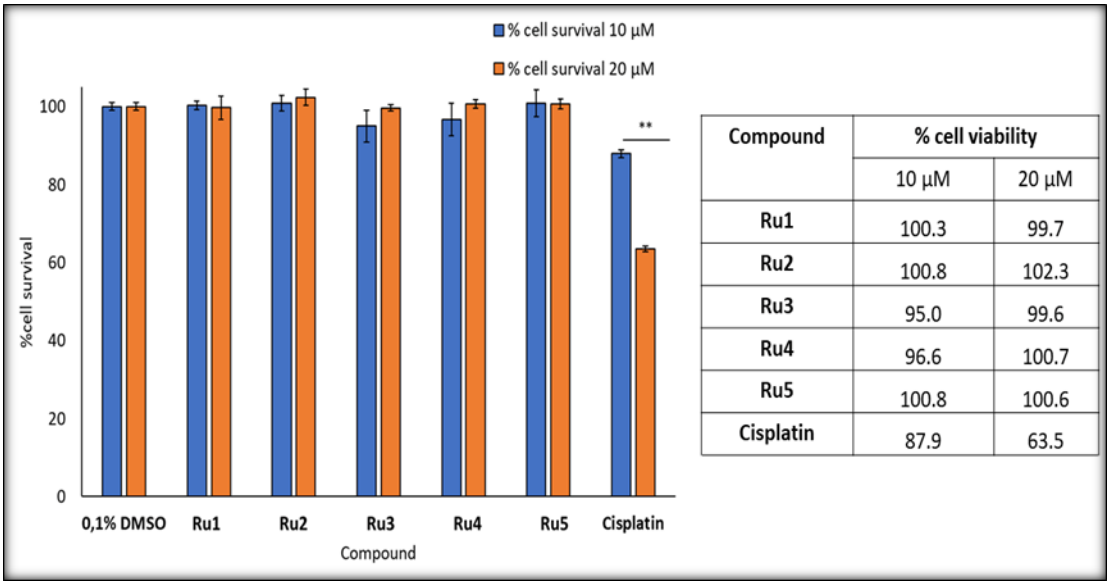

Compound	% cell viability	
	10 µM	20 µM
Ru1	100.3	99.7
Ru2	100.8	102.3
Ru3	95.0	99.6
Ru4	96.6	100.7
Ru5	100.8	100.6
Cisplatin	87.9	63.5

Figure 4.106: The MTT assay-derived cell survival percentages in MDA-MB-231 triple-negative breast cancer cells.

The experimental setup involved exposing the cancer cells to 0.1% DMSO (serving as the vehicle control), selected η⁶-arene ruthenium(II) complexes (**3a-Ru1, 3c-Ru2, 4a-Ru3, 4c-Ru4,** and **9-Ru5**), or the standard chemotherapeutic agent cisplatin at concentrations of 10 µM and 20 µM.

The cytotoxic profiles of complexes **3a, 4a,** and **9** were determined through 48-hour exposure assays across a concentration range of 5–35 µM in MCF-7 and MDA-MB-231 breast carcinoma cell lines, and their effects on cellular viability were assessed using the MTT assay. The corresponding IC_{50} values, derived from non-linear regression analysis using GraphPad Prism v5.01, are presented in Figure 4.107 and Table 4.40. The relative cytotoxic potency followed the order **9 > 4a > 3a**, with complex **9** exhibiting the most pronounced inhibitory effect

on MCF-7 cells, yielding an IC_{50} of 41.94 ± 2.05 μM. Although all three compounds demonstrated modest activity, their potency was approximately half that of cisplatin under the same experimental conditions. Interestingly, the IC_{50} values recorded for these complexes were comparable to those previously reported for structurally related arene–ruthenium(II) compounds of the general formula $[(\eta^6\text{-}p\text{-cymene})Ru(C_5H_4N_2\text{–}CH{=}N\text{–}Ar)X]PF_6$, where X = Br or I and Ar represents various substituted phenyl groups (Gichumbi *et al.*, 2017b). Furthermore, at lower concentrations (*e.g.*, 10 μM), higher cytotoxic effects were observed for complexes that displayed greater resistance to glutathione-mediated degradation (see Table 4.37), suggesting a potential correlation between glutathione stability and anticancer activity.

Upon doubling the concentration, the chlorido-containing complexes (**3a** and **4a**) demonstrated slightly greater cytotoxicity against MCF-7 breast cancer cells than their iodo counterparts (**3c** and **4c**). This observation may be attributed to the smaller atomic radius of chlorine compared to iodine, which potentially facilitates stronger interactions with DNA strands, as previously discussed by (Purkait *et al.*, 2016). Interestingly, this finding appears to contradict earlier reports by (Romero-Canelón *et al.*, 2013), who suggested that substituting chloride with iodide in η^6-arene Ru(II) complexes tends to enhance cytotoxic activity.

A notable deviation from this trend was observed in complex **9**, which incorporates a toluene-based arene instead of *p*-cymene, along with 3-chloro-6-(1H-pyrazol-1-yl)pyridazine as the non-labile ligand and a chlorido leaving group. This compound showed a marked improvement in anticancer activity over its structural analogue **3a**, registering an IC_{50} of 41.94 ± 2.05 μM against the MCF-7 cell line, making it the most potent complex among those tested. Complex **9** exhibited enhanced biological activity, potentially due to its Ru(II) centre possessing greater electrophilicity, which could intensify its electrostatic affinity for DNA's anionic backbone. This highlights the significant role of electronic effects—particularly the electron-withdrawing capacity of the coordinated ligands—over steric factors such as the bulkier isopropyl substituents present on the *p*-cymene moiety in reducing biological efficacy. Because the ruthenium complexes undergo associative ligand substitution reactions *via* a pseudo-seven-coordinated transition state (Wang *et al.*, 2013), the substitution of the labile ligands like chloride ions in complex **9** and other related compounds, is favoured by facile transport of the Ru(II)-arene complex through ligand exchange kinetics (Bashir *et al.*, 2023). However, η^6-arene Ru(II) bearing arenes with sterically demanding alkyl complexes, due to the increased lipophilicity of

the complexes, are usually more potent towards various cancer cells lines (Adhikari *et al.*, 2024; Elguero, 1996).

The cytotoxic profiles of the complexes across the tested cell lines were only marginally affected by changes in the halide-leaving group, suggesting that this structural feature plays a limited role in modulating their anticancer activity (Bhattacharyya *et al.*, 2017; Chakraborty *et al.*, 2021). The incorporation of methyl groups at the 3- and 5-positions of the pyrazole rings within the N,N′-bidentate ligands led to a notable enhancement in cytotoxic effects against cancer cells, following the trend **3a < 4a** and **3c < 4c**. This pattern supports earlier findings by (Pastuszko *et al.*, 2013), which indicated that replacing hydrogen atoms with methyl substituents on the bidentate ligand resulted in more pronounced Inhibition of cell proliferation in MCF-7 breast cancer cells. Moreover, this modification appeared to have a greater influence on cytotoxicity than altering either the halide leaving group or the nature of the coordinated η^6-arene moiety.

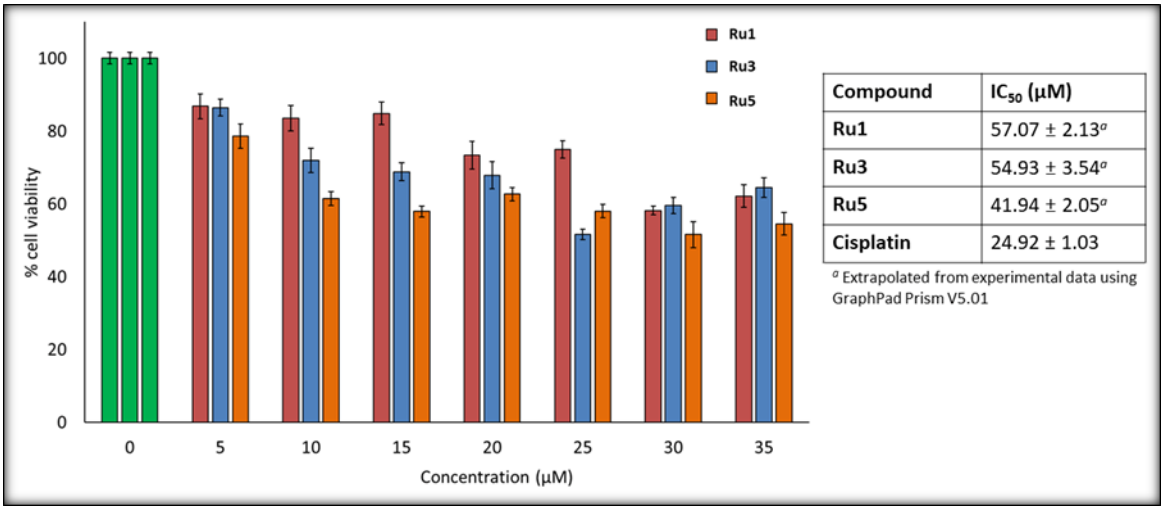

Compound	IC_{50} (µM)
Ru1	57.07 ± 2.13[a]
Ru3	54.93 ± 3.54[a]
Ru5	41.94 ± 2.05[a]
Cisplatin	24.92 ± 1.03

[a] Extrapolated from experimental data using GraphPad Prism V5.01

Figure 4.107: MTT assay results showing the viability of MCF-7 breast cancer cells following treatment with escalating doses of complexes **3a-Ru1, 4a-Ru3,** and **9-Ru5.**
The inserted table summarises the IC_{50} values obtained for each tested complex, along with cisplatin, which was used as the standard reference drug.

Based on the preliminary screening results, a multi-concentration assessment of complexes **3a, 4a,** and **9** was carried out on the triple-negative MDA-MB-231 breast cancer cell line. However, none of these compounds demonstrated a substantial inhibitory effect on cell viability across the tested concentration range. Consequently, unlike the observations made with

the MCF-7 cell line (Figure 4.108), it was not feasible to derive IC_{50} values from the dose–response plots for this particular cell line.

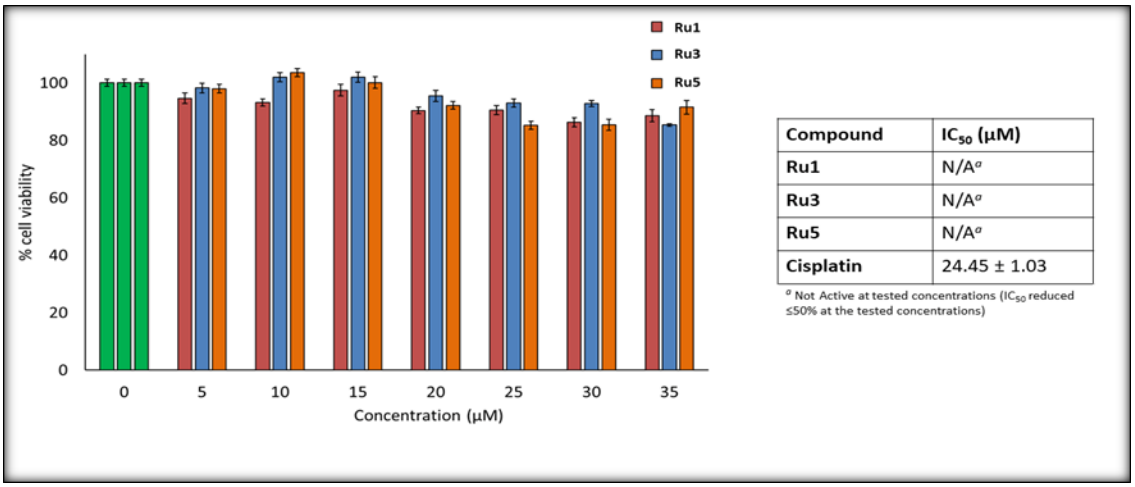

Compound	IC_{50} (µM)
Ru1	N/A[a]
Ru3	N/A[a]
Ru5	N/A[a]
Cisplatin	24.45 ± 1.03

[a] Not Active at tested concentrations (IC_{50} reduced ≤50% at the tested concentrations)

Figure 4.108: MTT assay-based evaluation of cell viability in MDA-MB-231 triple-negative breast cancer cells following treatment with increasing concentrations of complexes **3a-Ru1, 4a-Ru3,** and **9-Ru5.**

The inserted table presents the IC_{50} values for complexes **3a, 4a,** and **9**, alongside cisplatin, which served as a reference compound for comparison.

Table 4.40: Half-maximal inhibitory concentration (IC_{50}, µM) of complexes **3a, 4a,** and **9.**

Complex	MCF-7	MDA-MB-231
3a	57.07 ± 2.13	N/A
4a	54.93 ± 3.54	N/A
9	41.94 ± 2.05	N/A
Cisplatin	24.92 ± 1.03	24.45 ± 1.03

N/A = not active

The half-sandwich arene–ruthenium(II) complexes **3a, 3c, 4a, 4c,** and **9** exhibited only modest antiproliferative effects against the MCF-7 and MDA-MB-231 breast cancer cell lines. This limited cytotoxic response was evidenced by their relatively high IC_{50} values, suggesting suboptimal interaction with intracellular targets or reduced cellular uptake under the tested conditions. When benchmarked against structurally analogous compounds reported in previous studies, their potency appears notably lower. For instance, Bhattacharyya *et al.* (2017) reported IC_{50} values in the range of 6.4–6.9 µM for related complexes tested against MCF-7 and LNCaP

prostate cancer cells, while (Chakraborty *et al.*, 2021) documented values between 9 and 12 µM for similar systems evaluated against MDA-MB-231 cells. Comparable findings of low cytotoxicity have also been observed in the literature for analogous η^6-arene ruthenium(II) species against HeLa cells. In those cases, biological activity improved significantly only upon exposure to light, as demonstrated in the photoactivation studies by (Paitandi *et al.*, 2018), highlighting the potential of light-responsive mechanisms to enhance therapeutic effects.

CHAPTER FIVE

CONCLUSIONS AND RECOMMENDATIONS

5.1 Conclusions

i. A total of fifteen air-stable half-sandwich η^6-arene complexes of osmium(II) and ruthenium(II) were successfully synthesised. These compounds were derived from their respective dimeric precursors and featured either bis(pyrazol-1-yl)methane or pyrazolyl-pyridazine ligands.

ii. Structural confirmation and purity assessment of the synthesised complexes were achieved using a range of spectroscopic techniques. Their molecular geometry was elucidated *via* single-crystal X-ray diffraction and further validated through density functional theory (DFT) calculations. Both experimental and computational data affirmed a characteristic pseudo-octahedral 'piano-stool' configuration around the central metal atom, comprising coordination from an η^6-arene ring, two nitrogen donor atoms from the bidentate ligand, and a halide (Cl, Br, or I). DFT-derived bond parameters were within 10% of those obtained from X-ray analysis, confirming the reliability of theoretical models used.

iii. The solution stability of the complexes was examined in both DMSO and PBS buffer using UV-Visible spectroscopy and molar conductivity measurements. Results showed minimal or slow ligand exchange in the presence of solvent, especially for complexes containing BF_4^- counter-ions. Conductivity values (Λ_M = 20.22–24.77 $S \cdot cm^2 \cdot mol^{-1}$) were indicative of non-electrolytic behaviour in DMSO, supporting the integrity of the complexes in solution. Electrochemical studies revealed that redox properties are influenced by ligand characteristics, particularly σ- and π-acceptor abilities. Ligands bearing methyl substituents increased electron density at the metal centre, facilitating Ru(II) to Ru(III) oxidation, as evidenced by the trend: **3a** > **3c** ≈ **4a** > **4c** for halides, and **3a** > **4a** ≈ **4c** for ligand substituents.

iv. DNA-interaction experiments revealed strong binding affinity of the complexes toward calf thymus DNA, predominantly *via* the minor groove with an average binding stoichiometry of two sites per molecule. Competitive binding studies using Hoechst 33258 confirmed that the ruthenium(II) η^6-arene complexes can displace the dye,

affirming minor groove interaction. Among the series, complex **9** exhibited the highest binding constant (K_b), likely due to its reduced steric hindrance, which facilitates more favourable interactions with the DNA. These experimental findings were supported by In Silico molecular docking simulations, which showed a positive correlation between binding free energies and experimentally determined K_b values.

v. The cytotoxic potential of the complexes was evaluated *in vitro* against MCF-7 breast cancer cells. The data indicated that structural factors such as steric hindrance and electron density at the metal centre played a key role in modulating biological activity. Complex **9**, characterised by lower steric bulk, emerged as the most effective, suggesting that cytotoxicity in this series is not solely dependent on the polarizability of the halide ligand. Conversely, complexes based on the bis(pyrazol-1-yl)methane scaffold showed limited activity across a panel of cancer cell lines including cervical (Caski, HeLa), breast (MCF-7, T-47D, MDA-MB-231), pancreatic (CFPAC-1, PANC-1), and rhabdomyosarcoma (RH-30, RD). Overall, the results underscore that although these compounds exhibit favourable DNA-binding characteristics, such interactions alone are insufficient to ensure potent anticancer activity.

5.2 Recommendations

i. The synthesised η^6-arene metal complexes may serve as potential homogeneous catalysts or catalyst precursors in various chemical transformations, including hydrogenation, esterification, olefin metathesis, and Diels–Alder cycloadditions. It is recommended that their catalytic capabilities be explored in these reactions.

ii. The current study indicates that η^6-arene ruthenium(II) complexes incorporating bis(pyrazol-1-yl)methane and pyrazolyl-pyridazine ligands exhibit limited cytotoxic potential. However, since complex **9** demonstrated notable activity against breast cancer cells, future work should focus on designing new η^6-arene ruthenium(II) derivatives structurally related to this compound.

iii. Structural analysis through DFT and X-ray crystallography revealed high similarity between the synthesised η^6-arene Ru(II) and Os(II) complexes. Nonetheless, there is a need for further biological evaluation, particularly cytotoxicity and DNA-binding studies, of the osmium-based compounds to substantiate their potential.

iv. η^6-Arene complexes of Ru(II) and Os(II) continue to attract interest as promising non-platinum chemotherapeutic candidates. Further investigation into their kinetic profiles, interactions with biomolecules (DNA and proteins), transport mechanisms, and toxicity in biological systems is essential. Expanding this research to a broader spectrum of cancer types is also advisable, given the diverse biological characteristics of different tumour.

v. The η^6-arene ruthenium(II) complexes synthesised in this study exhibited selective antiproliferative activity against MCF-7 breast cancer cells. Notably, complex **9** demonstrated cytotoxicity comparable to cisplatin, yet showed minimal toxicity towards healthy cells at the tested concentrations. This highlights its potential as a lead compound for further development.

REFERENCES

Aakeröy, C. B., Evans, T. A., Seddon, K. R., & Pálinkó, I. (1999). The C–H⋯ Cl hydrogen bond: does it exist? *New Journal of Chemistry*, *23*(2), 145-152. doi.org/10.1039/A809309A

Adhikari, S., Nath, P., Das, A., Datta, A., Baildya, N., Duttaroy, A. K., & Pathak, S. (2024). A review on metal complexes and its anti-cancer activities: Recent updates from *in vivo* studies. *Biomedicine & Pharmacotherapy*, *171*, 116211. doi.org/10.1016/j.biopha.2024.116211

Albertin, G., Antoniutti, S., Castro, J., & García-Fontán, S. (2011). Preparation of pyrazole–pyrazolate half-sandwich complexes of ruthenium and osmium. *European Journal of Inorganic Chemistry, 2011*(4), 510-520. doi:10.1002/ejic.201000799

Alberto, M. E., Butera, V., & Russo, N. (2011). Which one among the Pt-containing anticancer drugs more easily forms monoadducts with G and A DNA bases? A comparative study among oxaliplatin, nedaplatin, and carboplatin. *Inorganic Chemistry*, *50*(15), 6965-6971. doi.org/10.1021/ic200148n

Allardyce, Claire S. D, & Paul. (2001). Ruthenium in medicine: current clinical uses and future prospects. *Platinum Metals Reviews, 45*(2), 62-69. doi.org/10.1595/003214001X4526269

Alsaeedi, M. S., Babgi, B. A., Abdellattif, M. H., Jedidi, A., Humphrey, M. G., & Hussien, M. A. (2020). DNA-binding capabilities and anticancer activities of ruthenium(II) cymene complexes with (Poly) cyclic aromatic diamine ligands. *Molecules*, *26*(1), 76. doi:10.3390/molecules26010076

Amptoulach, S., & Tsavaris, N. (2011). Neurotoxicity caused by the treatment with platinum analogues. *Chemotherapy Research and Practice*, *2011*(1), 843019. doi.org/10.1155/2011/843019

Anand, P., Kunnumakara, A. B., Sundaram, C., Harikumar, K. B., Tharakan, S. T., Lai, O. S.,…Aggarwal, B. B. (2008). Cancer is a preventable disease that requires major lifestyle changes. *Pharmaceutical Research, 25,* 2097-2116. doi.org/10.1007/s11095-008-9661-9

Anthony, E. J., Bolitho, E. M., Bridgewater, H. E., Carter, O. W., Donnelly, J. M., Imberti, C.,…Palau, M. (2020). Metallodrugs are unique: Opportunities and challenges of discovery and development. *Chemical Science*, *11*(48), 12888-12917. doi:10.1039/D0SC04082G

Antonarakis, E. S., & Emadi, A. (2010). Ruthenium-based chemotherapeutics: are they ready for prime time? *Cancer Chemotherapy and Pharmacology*, *66*(1), 1-9. doi.org/10.1007/s00280-010-1293-1

Arjmand, F., & Jamsheera, A. (2011). DNA binding studies of new valine derived chiral complexes of tin(IV) and zirconium(IV). *Spectrochimica Acta Part A: Molecular and Biomolecular Spectroscopy*, *78*(1), 45-51. doi.org/10.1016/j.saa.2010.06.009

Bacchi, A., Cantoni, G., & Pelagatti, P. (2013). Polymorphs and co-crystal with half-sandwich Ru(II) dimers $[(\eta^6\text{-arene})RuX_2]_2$. *Crystal Engineering Communication*, *15*(34), 6722-6728. doi:10.1039/C3CE40618K

Balendiran, G. K., Dabur, R., & Fraser, D. (2004). The role of glutathione in cancer. *Cell Biochemistry and Function: Cellular biochemistry and its modulation by active agents or disease*, *22*(6), 343-352. doi:10.1002/cbf.1149

Barone, V., & Cossi, M. (1998). Quantum calculation of molecular energies and energy gradients in solution by a conductor solvent model. *The Journal of Physical Chemistry A*, *102*(11), 1995-2001. doi:10.1021/jp9716997

Barry, N. P., & Sadler, P. J. (2013). Exploration of the medical periodic table: towards new targets. *Chemical Communications*, *49*(45), 5106-5131. Doi: 10.1039/C3CC41143E

Bashir, M., Mantoo, I. A., Arjmand, F., Tabassum, S., & Yousuf, I. (2023). An overview of advancement of organoruthenium(II) complexes as prospective anticancer agents. *Coordination Chemistry Reviews*, *487*, 215169. doi.org/10.1016/j.ccr.2023.215169

Becke, A. D. (1993). Becke's three parameter hybrid method using the LYP correlation functional. *Journal of Chemical Physics*, *98*(492), 5648-5652. doi.org/10.1063/1.464913

Berridge, M. V., & Tan, A. S. (1993). Characterization of the cellular reduction of 3-(4,5-dimethylthiazol-2-yl)-2,5-diphenyltetrazolium bromide (MTT): subcellular localization, substrate dependence, and involvement of mitochondrial electron transport in MTT reduction. *Archives of Biochemistry and Biophysics*, *303*(2), 474-482. doi:10.1006/abbi.1993.1311

Bhadra, K., & Kumar, G. S. (2011). Interaction of berberine, palmatine, coralyne, and sanguinarine to quadruplex DNA: a comparative spectroscopic and calorimetric study. *Biochimica et Biophysica Acta (BBA)-General Subjects*, *1810*(4), 485-496. doi:10.1016/j.bbagen.2011.01.011

Bhattacharyya, S., Purkait, K., & Mukherjee, A. (2017). Ruthenium(II) *p-cymene* complexes of a benzimidazole-based ligand capable of VEGFR2 inhibition: hydrolysis, reactivity and cytotoxicity studies. *Dalton Transactions*, *46*(26), 8539-8554. doi: 10.1039/C7DT00938K

Biancalana, L., Zanda, E., Hadiji, M., Zacchini, S., Pratesi, A., Pampaloni, G.,…Marchetti, F. (2021). Role of the (pseudo) halido ligand in ruthenium(II)-*p*-cymene α-amino acid complexes in speciation, protein reactivity and cytotoxicity. *Dalton Transactions*, *50*(43), 15760-15777. doi:10.1039/D1DT03274G

Bloemink, M. J., & Reedijk, J. (1996). Cisplatin and derived anticancer drugs: mechanism and current status of DNA binding. *Metal Ions in Biological Systems*, *32*, 641. PMID: 8640534.

Boulikas, T., Pantos, A., Bellis, E., & Christofis, P. (2007). Designing platinum compounds in cancer: structures and mechanisms. *Cancer Therapy*, *5*, 537-583.

Brindell, M., Stawoska, I., Supel, J., Skoczowski, A., Stochel, G., & van Eldik, R. (2008). The reduction of (ImH)[trans-Ru(III)Cl_4(dmso)(Im)] under physiological conditions: preferential reaction of the reduced complex with human serum albumin. *Journal of Biological Inorganic Chemistry*, *13*(6), 909-918. doi:10.1007/s00775-008-0378-3

Bruijnincx, P. C., & Sadler, P. J. (2009). Controlling platinum, ruthenium, and osmium reactivity for anticancer drug design. *Advances in Inorganic Chemistry*, *61*, 1-62. doi.org/10.1016/S0898-8838(09)00201-3

Bruker, A. (2009). *Saint and SADABS*. Bruker AXS Inc., Madison, Wisconsin, USA.

Büchel, G. E., Stepanenko, I. N., Hejl, M., Jakupec, M. A., Keppler, B. K., & Arion, V. B. (2011). En route to osmium analogues of KP1019: Synthesis, structure, spectroscopic properties and antiproliferative activity of trans-[$Os^{IV}Cl_4$(Hazole)$_2$]. *Inorganic Chemistry*, *50*(16), 7690. doi: 10.1021/ic200728b

Čanović, P., Simović, A. R., Radisavljević, S., Bratsos, I., Demitri, N., Mitrović, M.,…Bugarčić, Ž. D. (2017). Impact of aromaticity on anticancer activity of polypyridyl ruthenium(II) complexes: synthesis, structure, DNA/protein binding, lipophilicity and anticancer activity. *Journal of Biological Inorganic Chemistry*, *22*(7), 1007-1028. doi:10.1007/s00775-017-1479-7

Carter, M. T., & Bard, A. J. (1987). Voltammetric studies of the interaction of tris(1, 10-phenanthroline)cobalt(III) with DNA. *Journal of the American Chemical Society*, *109*(24), 7528-7530. doi.org/10.1021/ja00258a046

Casini, A., Temperini, C., Gabbiani, C., Supuran, C. T., & Messori, L. (2010). The X-ray structure of the adduct between NAMI-A and carbonic anhydrase provides insights into the reactivity of this metallodrug with proteins. *ChemMedChem*, *5*(12), 1989-1994. doi.org/10.1002/cmdc.201000331

Catalano, M., Lapucci, A., Nobili, S., De Gennaro Aquino, I., Vascotto, I. A., Antonuzzo, L.,…Roviello, G. (2024). Platinum-based chemotherapy in metastatic prostate cancer: what possibilities? *Cancer Chemotherapy and Pharmacology*, *93*(1), 1-9. doi.org/10.1007/s00280-023-04604-w

Cebrián-Losantos, B., Krokhin, A. A., Stepanenko, I. N., Eichinger, R., Jakupec, M. A., Arion, V. B., & Keppler, B. K. (2007). Osmium NAMI-A analogues: Synthesis, structural and spectroscopic characterization, and antiproliferative properties. *Inorganic Chemistry*, *46*(12), 5023-5033. doi.org/10.1021/ic700405y

Cepeda, V., Fuertes, M. A., Castilla, J., Alonso, C., Quevedo, C., & Perez, J. M. (2007). Biochemical mechanisms of cisplatin cytotoxicity. *Anti-Cancer Agents in Medicinal Chemistry (Formerly Current Medicinal Chemistry-Anti-Cancer Agents)*, *7*(1), 3-18. doi.org/10.2174/187152007779314044

Chakraborty, A., Roy, S., Chakraborty, M. P., Roy, S. S., Purkait, K., Koley, T. S.,…Mukherjee, A. (2021). Cytotoxic ruthenium(II) complexes of pyrazolylbenzimidazole ligands that inhibit VEGFR2 phosphorylation. *Inorganic Chemistry*, *60*(23), 18379-18394. doi.org/10.1021/acs.inorgchem.1c02979

Chattaraj, P. K., & Maiti, B. (2003). HSAB principle applied to the time evolution of chemical reactions. *Journal of the American Chemical Society*, *125*(9), 2705-2710. doi.org/10.1021/ja0276063

Chen, H., Parkinson, J. A., Morris, R. E., & Sadler, P. J. (2003). Highly selective binding of organometallic ruthenium ethylenediamine complexes to nucleic acids: novel recognition mechanisms. *Journal of the American Chemical Society*, *125*(1), 173-186. doi.org/10.1021/ja027719m

Chrzanowska, M., Katafias, A., Kozakiewicz, A., Puchta, R., & Van Eldik, R. (2018). Systematic tuning of the reactivity of [RuII(terpy)(N^N)Cl]Cl complexes. *Journal of Coordination Chemistry*, *71*(11-13), 1761-1777. doi.org/10.1080/00958972.2018.1498972

Clarke, M., Bailey, V., Doan, P. E., Hiller, C., LaChance-Galang, K., Daghlian, H.,…Lang, D. (1996). ^{1}H NMR, EPR, UV− Vis, and Electrochemical studies of imidazole complexes of Ru(III). Crystal structures of *cis*-$[(Im)_2(NH_3)_4Ru^{III}]Br_3$ and $[(1MeIm)_6Ru^{II}]Cl_2.2H_2O$. *Inorganic Chemistry, 35*(17), 4896-4903. doi.org/10.1021/ic960355c

Clarke, M. J. (1980). Oncological implications of the chemistry of ruthenium. *Metal Ions in Biological Systems, 11,* 231-283.

Coffetti, G., Moraschi, M., Facchetti, G., & Rimoldi, I. (2023). The challenging treatment of cisplatin-resistant tumour: State of the art and future perspectives. *Molecules*, *28*(8), 3407. doi.org/10.3390/molecules28083407

Cohen, S. M., Goel, A., Phillips, J., Ennis, R. D., & Grossbard, M. L. (2006). The role of perioperative chemotherapy in the treatment of urothelial cancer. *The Oncologist*, *11*(6), 630-640. doi.org/10.1634/theoncologist.11-6-630

Cossi, M., Rega, N., Scalmani, G., & Barone, V. (2003). Energies, structures, and electronic properties of molecules in solution with the C-PCM solvation model. *Journal of Computational Chemistry*, *24*(6), 669-681. doi:10.1002/jcc.10189

CrysAlis, C. (2008). *CrysAlis Red.* (Xcalibur PX Software), Oxford Diffraction Ltd.

Cseh, K., Geisler, H., Stanojkovska, K., Westermayr, J., Brunmayr, P., Wenisch, D.,…Koellensperger, G. (2022). Arene variation of highly cytotoxic tridentate naphthoquinone-based ruthenium(II) complexes and in-depth in vitro studies. *Pharmaceutics*, *14*(11), 2466. doi.org/10.3390/pharmaceutics14112466

Cvitkovic, E. (1998). Cumulative toxicities from cisplatin therapy and current cytoprotective measures. *Cancer Treatment Reviews*, *24*(4), 265-281. doi.org/10.1016/S0305-7372(98)90061-5

Desoize, B., & Madoulet, C. (2002). Particular aspects of platinum compounds used at present in cancer treatment. *Critical Reviews in Oncology/Hematology*, *42*(3), 317-325. doi:10.1016/S1040-8428(01)00219-0

Dhariyal, K., Parveen, S., Kumar, S., Banerjee, M., Sharma, P., Singh, S. K., & Singh, A. K. (2023). Half-sandwich ruthenium–arene thiosemicarbazones complexes: Synthesis, characterization, biological evaluation and DFT calculations. *Inorganic Chemistry Communications*, *152*, 110678. doi.org/10.1016/j.inoche.2023.110678

Dogné, J.-M., Supuran, C. T., & Pratico, D. (2005). Adverse cardiovascular effects of the coxibs. *Journal of Medicinal Chemistry*, *48*(7), 2251-2257. doi.org/10.1021/jm0402059

Dolomanov, O., Bourhis, L., Gildea, R., Howard, J., & Puschmann, H. (2009). OLEX2: A complete structure solution, refinement and analysis program. *Journal of Applied Crystallography 42*, 339-341. doi:10.1107/S0021889808042726

Domínguez-Jurado, E., Ripoll, C., Lara-Sánchez, A., Ocaña, A., Vitórica-Yrezábal, I. J., Bravo, I., & Alonso-Moreno, C. (2024). Evaluation of heteroscorpionate ligands as scaffolds for the generation of Ruthenium(II) metallodrugs in breast cancer therapy. *Journal of Inorganic Biochemistry*, *253*, 112486. doi: 10.1016/j.jinorgbio.2024.112486]

Dougan, S. J., Habtemariam, A., McHale, S. E., Parsons, S., & Sadler, P. J. (2008). Catalytic organometallic anticancer complexes. *Proceedings of the National Academy of Sciences, 105*(33), 11628-11633. doi:10.1073/pnas.0800076105

Dougan, S. J., & Sadler, P. J. (2007). The design of organometallic ruthenium arene anticancer agents. *CHIMIA International Journal for Chemistry*, *61*(11), 704-715. doi.org/10.2533/chimia.2007.704

Dyson, P. J. (2007). Systematic design of a targeted organometallic antitumour drug in pre-clinical development. *CHIMIA International Journal for Chemistry*, *61*(11), 698-703. doi.org/10.2533/chimia.2007.698

Elguero, J. (1996). Comprehensive Heterocyclic Chemistry II. *Journal: Comprehensive Heterocyclic Chemistry II*, 1-75. doi: 10.1016/b978-008096518-5.00059-9

Erkan, S., Kaya, S., Sayin, K., & Karakaş, D. (2020). Structural, spectral characterization and molecular docking analyses of *mer*-ruthenium(II) complexes containing the bidentate chelating ligands. *Spectrochimica Acta Part A: Molecular and Biomolecular Spectroscopy*, *224*, 117399. doi.org/10.1016/j.saa.2019.117399

Eswaran, J., Mariappan, A., Arumugham, N., Murugan, T., sp Bhuvanesh, N., Anathakrishnan, N. M.,…Kanthapazham, R. (2022). Ruthenium(III) and (II) complexes containing

pyridine moiety: Synthesis, crystal structure and *in vitro* biological evaluation. *Journal of Molecular Structure*, *1270*, 133929. doi.org/10.1016/j.molstruc.2022.133929

Farrugia, L. J. (2012). WinGX and ORTEP for Windows: an update. *Journal of Applied Crystallography*, *45*(4), 849-854. doi.org/10.1107/S00218898120291

Feng, Q., Li, N.-Q., & Jiang, Y.-Y. (1997). Electrochemical studies of porphyrin interacting with DNA and determination of DNA. *Analytica Chimica Acta*, *344*(1-2), 97-104. doi.org/10.1016/S0003-2670(97)00008-1

Ferlay, J., Colombet, M., Soerjomataram, I., Parkin, D. M., Piñeros, M., Znaor, A., & Bray, F. (2021). Cancer statistics for the year 2020: An overview. *International Journal of Cancer*, *149*(4), 778-789. doi.org/10.1002/ijc.33588

Ferlay, J., Ervik, M., Lam, F., Colombet, M., Mery, L., Piñeros, M., ... & Bray, F. (2020). Global cancer observatory: cancer today. *Lyon: International Agency for Research on Cancer*, *20182020*. doi:10.1002/ijc.33588

Fernández, R., Melchart, M., Habtemariam, A., Parsons, S., & Sadler, P. J. (2004). Use of chelating ligands to tune the reactive site of half-sandwich ruthenium(II)–arene anticancer complexes. *Chemistry – A European Journal*, *10*(20), 5173-5179. doi.org/10.1002/chem.200400640

Field, L. D., Messerle, B. A., Soler, L., Buys, I. E., & Hambley, T. W. (2001). Polypyrazolylmethane complexes of ruthenium. *Journal of the Chemical Society, Dalton Transactions*, *2001*(13), 1959-1965. doi.org/10.1039/B103939N

Frey, U., Ranford, J. D., & Sadler, P. J. (1993). Ring-opening reactions of the anticancer drug carboplatin: NMR characterization of cis-[Pt(NH_3)$_2$(CBDCA-O)(5'-GMP-N7)] in solution. *Inorganic Chemistry*, *32*(8), 1333-1340. doi.org/10.1021/ic00060a005

Frezza, M., Hindo, S., Chen, D., Davenport, A., Schmitt, S., Tomco, D., & Ping Dou, Q. (2010). Novel metals and metal complexes as platforms for cancer therapy. *Current Pharmaceutical Design*, *16*(16), 1813-1825. doi.org/10.2174/138161210791209009

Frisch, M. J., Trucks, G. W., Schlegel, H. B., Scuseria, G. E., Robb, M. A., Cheeseman, J. R., Montgomery, J. A., Jr., Vreven, T., Kudin, K. N., Burant, J. C., Millam, J. M., Iyengar, S. S., Tomasi, J., Barone, V., Mennucci, B., Cossi, M., Scalmani, G., Rega, N., Petersson, G. A., ... Fox, D. J. (2009). *Gaussian 09* (Revision D.01). Gaussian, Inc.

Fu, R., Zhao, B., Chen, M., Fu, X., Zhang, Q., Cui, Y.,…Zhou, W. (2023). Moving beyond cisplatin resistance: Mechanisms, challenges, and prospects for overcoming recurrence in clinical cancer therapy. *Medical Oncology*, *41*(1), 9. doi.org/10.1007/s12032-023-02237-w

Fu, Y., Sadler, P. J., & Habtemariam, A. (2017). *U.S. Patent No. 9,598,448*. U.S. Patent and Trademark Office.

Fuentes, L., Quiroga, A. G., Organero, J. A., & Matesanz, A. I. (2020). Exploring DNA binding ability of two novel α-N-heterocyclic thiosemicarbazone palladium(II) complexes. *Journal of Inorganic Biochemistry*, *203*, 110875. doi.org/10.1016/j.jinorgbio.2019.110875

Galindo-Murillo, R., García-Ramos, J. C., Ruiz-Azuara, L., Cheatham, T. E., & Cortés-Guzmán, F. (2015). Intercalation processes of copper complexes in DNA. *Nucleic Acids Research*, *43*(11), 5364-5376. doi:10.1093/nar/gkv467

Gandin, V., Hoeschele, J. D., & Margiotta, N. (2023). Special issue "cisplatin in cancer therapy: molecular mechanisms of action 3.0". *International Journal of Molecular Sciences*, *24*(9), 7917. doi.org/10.3390/ijms24097917

Garzon, F., Berger, M., Keppler, B., & Schmähl, D. (1987). Comparative antitumour activity of ruthenium derivatives with 5′-deoxy-5-fluorouridine in chemically induced colorectal tumour in SD rats. *Cancer Chemotherapy and Pharmacology*, *19*(4), 347-349. doi.org/10.1007/BF00261487

Gichumbi, J., Friedrich, H., B, & Omondi, B. (2017a). Crystal structure of chlorido-(η^6–1-isopropyl-4-methylbenzene)-(1-(pyridin-2-yl)-N-(*p*-tolyl)methanimine-κ^2N,N′)ruthenium(II) hexafluorophosphate(V), $C_{23}H_{26}ClF_6N_2PRu$. *Zeitschrift für Kristallographie-New Crystal Structures*, *232*(2), 285-287. doi:10.1515/ncrs-2016-0241

Gichumbi, J., Omondi, B., Lazarus, G., Singh, M., Shaikh, N., Chenia, H. Y., & Friedrich, H. B. (2017b). Influence of halogen substitution in the ligand sphere on the antitumour and antibacterial activity of half-sandwich ruthenium(II) complexes [RuX(η^6-arene)(C_5H_4N-2-CH=N-Ar)]$^+$. *Zeitschrift für Anorganische und Allgemeine Chemie*, *643*(11), 699-711. doi.org/10.1002/zaac.201600427

Gichumbi, J. M., & Friedrich, H. B. (2018). Half-sandwich complexes of platinum group metals (Ir, Rh, Ru and Os) and some recent biological and catalytic applications. *Journal of Organometallic Chemistry*, *866*, 123-143. doi:10.1016/j.jorganchem.2018.04.021

Gichumbi, J. M., Friedrich, H. B., & Omondi, B. (2016a). Solvato-polymorph of [(η^6-C_6H_6)RuCl (L)]PF_6 (L = (2,6-dimethyl-phenyl-pyridin-2-yl methylene amine). *Journal of Molecular Structure*, *1113*, 55-59. doi:10.1016/j.molstruc.2016.02.040

Gichumbi, J. M., Friedrich, H. B., & Omondi, B. (2016b). Synthesis and characterization of half-sandwich ruthenium(II) complexes with N-alkyl pyridyl-imine ligands and their application in transfer hydrogenation of ketones. *Transition Metal Chemistry*, *41*(8), 867-877. doi:10.1007/s11243-016-0089-5

Gichumbi, J. M., Friedrich, H. B., & Omondi, B. (2016c). Synthesis and characterization of piano-stool ruthenium complexes with N,N′-pyridine imine bidentate ligands and their application in styrene oxidation. *Journal of Organometallic Chemistry*, *808*, 87-96. doi.org/10.1016/j.jorganchem.2016.02.015

Gichumbi, J. M., Friedrich, H. B., Omondi, B., Naicker, K., Singh, M., & Chenia, H. Y. (2018). Synthesis, characterization, antiproliferative, and antimicrobial activity of osmium(II) half-sandwich complexes. *Journal of Coordination Chemistry*, *71*(2), 342-354. doi:10.1080/00958972.2018.1434164

Gichumbi, J. M., Omondi, B., & Friedrich, H. B. (2017c). Half-sandwich osmium(II) complexes with bidentate N,N-chelating ligands and their use in the transfer hydrogenation of ketones. *European Journal of Inorganic Chemistry*, *2017*(5), 915-924. doi.org/10.1002/ejic.201601249

Gichumbi, J. M., Omondi, B., & Friedrich, H. B. (2020). Crystal structure of η^6-*p-cymene*-iodido-(N-isopropyl-1-(pyridin-2-yl)methanimine-κ^2N,N′)ruthenium(II) hexafluorophosphate(V), $C_{19}H_{26}IN_2F_6Ru$. *Zeitschrift für Kristallographie-New Crystal Structures*, *235*(2), 485-487. doi:10.1515/ncrs-2019-0786

González-Ruiz, V., Olives, A. I., Martín, M. A., Ribelles, P., Ramos, M. T., & Menéndez, J. C. (2011). An overview of analytical techniques employed to evidence drug-DNA interactions. Applications to the design of genosensors. *Biomedical Engineering, Trends, Research and Technologies*, *32*, 215-219.

Govender, P., Antonels, N. C., Mattsson, J., Renfrew, A. K., Dyson, P. J., Moss, J. R.,…Smith, G. S. (2009). Anticancer activity of multinuclear arene ruthenium complexes coordinated to dendritic polypyridyl scaffolds. *Journal of Organometallic Chemistry*, *694*(21), 3470-3476. doi.org/10.1016/j.jorganchem.2009.06.028

Gupta, G., Prasad, K. T., Das, B., Yap, G. P., & Rao, K. M. (2009). Ruthenium half-sandwich complexes with tautomerized pyrazolyl-pyridazine ligands: Synthesis, spectroscopic and molecular structural studies. *Journal of Organometallic Chemistry*, *694*(16), 2618-2627. doi:10.1016/j.jorganchem.2009.03.043

Gupta, G., Prasad, K. T., Rao, A. V., Geib, S. J., Das, B., & Rao, K. M. (2010). Novel mononuclear η^5-pentamethylcyclopentadienyl complexes of platinum group metals bearing pyrazolylpyridazine ligands: Syntheses and spectral studies. *Inorganica Chimica Acta*, *363*(10), 2287-2295. doi:10.1016/j.ica.2010.03.052

Habtemariam, A., Melchart, M., Fernández, R., Parsons, S., Oswald, I. D., Parkin, A.,…Aird, R. E. (2006). Structure-activity relationships for cytotoxic ruthenium(II) arene complexes containing N,N-, N,O-, and O,O-chelating ligands. *Journal of Medicinal Chemistry*, *49*(23), 6858-6868. doi:10.1021/jm060596m

Hadjiliadis, N., & Sletten, E. (2009). *Metal complex-DNA interactions*. John Wiley & Sons.

Han Ang, W., & Dyson, P. J. (2006). Classical and non-classical ruthenium-based anticancer drugs: Towards targeted chemotherapy. *European Journal of Inorganic Chemistry*, *2006*(20), 4003-4018. doi.org/10.1002/ejic.200600723

Hanif, M., Babak, M. V., & Hartinger, C. G. (2014). Development of anticancer agents: wizardry with osmium. *Drug Discovery Today*, *19*(10), 1640-1648. doi:10.1016/j.drudis.2014.06.016

Haq, I., Lincoln, P., Suh, D., Norden, B., Chowdhry, B. Z., & Chaires, J. B. (1995). Interaction of. delta- and lambda-$[Ru(phen)_2DPPZ]^{2+}$ with DNA: a calorimetric and equilibrium binding study. *Journal of the American Chemical Society*, *117*(17), 4788-4796. doi.org/10.1021/ja00122a008

Hartinger, C. G., & Dyson, P. J. (2009). Bioorganometallic chemistry—from teaching paradigms to medicinal applications. *Chemical Society Reviews*, *38*(2), 391-401. doi.org/10.1039/B707077M

Hartinger, C. G., Jakupec, M. A., Zorbas-Seifried, S., Groessl, M., Egger, A., Berger, W.,…Keppler, B. K. (2008). KP1019, a new redox-active anticancer agent–Preclinical development and results of a clinical phase I study in tumour patients. *Chemistry & Biodiversity*, *5*(10), 2140-2155. doi.org/10.1002/cbdv.200890195

Hartinger, C. G., Phillips, A. D., & Nazarov, A. A. (2011). Polynuclear ruthenium, osmium and gold complexes. The quest for innovative anticancer chemotherapeutics. *Current Topics in Medicinal Chemistry*, *11*(21), 2688-2702. doi.org/10.2174/156802611798040769

Hartinger, C. G., Zorbas-Seifried, S., Jakupec, M. A., Kynast, B., Zorbas, H., & Keppler, B. K. (2006). From bench to bedside–preclinical and early clinical development of the anticancer agent indazolium*trans*-[tetrachlorobis(1H-indazole)ruthenate(III)] (KP1019 or FFC14A). *Journal of Inorganic Biochemistry*, *100*(5-6), 891-904. doi.org/10.1016/j.jinorgbio.2006.02.013

Hernández-García, A., Marková, L., Santana, M. D., Prachařová, J., Bautista, D., Kostrhunová, H.,…Kašpárková, J. (2023). Cyclometalated benzimidazole osmium(II) complexes with antiproliferative activity in cancer cells disrupt calcium homeostasis. *Inorganic Chemistry*, *62*(16), 6474-6487. doi.org/10.1021/acs.inorgchem.3c00501

Hildebrandt, J., Häfner, N., Kritsch, D., Görls, H., Dürst, M., Runnebaum, I. B., & Weigand, W. (2022). Highly cytotoxic osmium(II) compounds and their ruthenium(II) analogues targeting ovarian carcinoma cell lines and evading cisplatin resistance mechanisms. *International Journal of Molecular Sciences*, *23*(9), 4976. doi.org/10.3390/ijms23094976

Hosoya, N., & Miyagawa, K. (2014). Targeting DNA damage response in cancer therapy. *Cancer Science*, *105*(4), 370-388. doi.org/10.1111/cas.12366

Hu, H., Zhang, H., Zhong, R., Yang, Y., Huang, C., Chen, J.,…Liu, Y. (2023). Synthesis, RNA-sequence and evaluation of anticancer efficacy of ruthenium(II) polypyridyl complexes toward HepG2 cells. *Journal of Inorganic Biochemistry*, *244*, 112230. doi.org/10.1016/j.jinorgbio.2023.112230

Huang, C., Zhang, H., Yang, Y., Liu, H., Chen, J., Wang, Y.,…Liu, Y. (2023). Synthesis, characterization, molecular docking, RNA-sequence and anticancer efficacy evaluation *in vitro* of ruthenium(II) complexes on B16 cells. *Journal of Inorganic Biochemistry*, *247*, 112329. doi.org/10.1016/j.jinorgbio.2023.112329

Jakupec, M. A., Galanski, M., Arion, V. B., Hartinger, C. G., & Keppler, B. K. (2008). Antitumour metal compounds: more than theme and variations. *Dalton Transactions 2008*(2), 183-194. doi.org/10.1039/B712656P

Jaumot, J., & Gargallo, R. (2012). Experimental methods for studying the interactions between G-quadruplex structures and ligands. *Current Pharmaceutical Design*, *18*(14), 1900-1916. doi:10.2174/138161212799958486

Kanaoujiya, R., Srivastava, S., Singh, R., & Mustafa, G. (2023). Recent advances and application of ruthenium complexes in tumour malignancy. *Materials Today: Proceedings, 72,* 2822-2827. doi.org/10.1016/j.matpr.2022.07.098

Kanyora, A. K., Omondi, R. O., Ongoma, P., Omolo, J. O., Welsh, A., Prince, S.,…Smith, G. S. (2024). Mononuclear η^6-arene ruthenium(II) complexes with pyrazolyl–pyridazine ligands: synthesis, CT-DNA binding, reactivity towards glutathione, and cytotoxicity. *Journal of Biological Inorganic Chemistry*, *29*(2), 251-264. doi.org/10.1007/s00775-024-02043-3

Kapoor, R., Kataria, A., Kapoor, P., & Venugopalan, P. (2004). Coordination chemistry of N,N,N′,N′-tetraethylpyridine-2,6-dithiocarboxamide: crystal and molecular structure of chloro (N,N,N′,N′-tetraethylpyridine-2,6-dithiocarboxamide)cobalt(II) monocations and di-μ-chlorobis[dichlorocobaltate(II)]dianions, $[\{Co(DETP)Cl\}^{+}]_2[Co_2Cl_4(\mu_2\text{-}Cl_2)]^{2-}$. *Transition Metal Chemistry*, *29*(4), 425-429. doi.org/10.1023/B:TMCH.0000027459.47135.ee

Keck, M. V., & Lippard, S. J. (1992). Unwinding of supercoiled DNA by platinum-ethidium and related complexes. *Journal of the American Chemical Society*, *114*(9), 3386-3390. doi.org/10.1021/ja00035a033

Kelly, J. M., Tossi, A. B., McConnell, D. J., & OhUigin, C. (1985). A study of the interactions of some polypyridylruthenium(II) complexes with DNA using fluorescence spectroscopy, topoisomerisation and thermal denaturation. *Nucleic Acids Research*, *13*(17), 6017-6034. doi.org/10.1093/nar/13.17.6017

Kennard, O. (1993). DNA-drug interactions. *Pure and Applied Chemistry, 65*(6), 1213-1222. doi.org/10.1351/pac199365061213

Keppler, B., & Rupp, W. (1986). Antitumour activity of imidazolium-bisimidazole-tetrachlororuthenate(III). A representative of a new class of inorganic antitumour agents.

Journal of Cancer Research and Clinical Oncology, *111*(2), 166-168. doi.org/10.1007/bf00400758

Khan, T. A., Bhar, K., Thirumoorthi, R., Roy, T. K., & Sharma, A. K. (2020). Design, synthesis, characterization and evaluation of the anticancer activity of water-soluble half-sandwich ruthenium(II) arene halido complexes. *New Journal of Chemistry*, *44*(1), 239-257. doi: 10.1039/C9NJ03663F

Khanvilkar, P., Dash, S. R., Banerjee, D., Vohra, A., Devkar, R., & Chakraborty, D. (2021). Organoruthenium(II) complexes featuring pyrazole-linked thiosemicarbazone ligands: Synthesis, DNA/BSA interactions, molecular docking, and cytotoxicity studies. *Applied Organometallic Chemistry*, *35*(10), e6343. doi:10.1002/aoc.6343

Khater, M., Brazier, J. A., Greco, F., & Osborn, H. M. (2023). Anticancer evaluation of new organometallic ruthenium(II) flavone complexes. *RSC Medicinal Chemistry*, *14*(2), 253-267. doi: 10.1039/D2MD00304J

Khusi, B. B. (2015). *An investigation into the influence of substituents and extended π-conjugation on the substitution reactions of bifunctional platinum (II) complexes* (Doctoral dissertation). [University of Kwa Zulu-Natal, Pietermaritzburg].

Kimani, F., Sharif, S. K., & Bashir, I. (2012). *National Cervical Cancer Prevention Program in Kenya: Strategic plan 2012–2015*. Ministry of Public Health and Sanitation and Ministry of Medical Services. https://www.example.go.ke/cc-strategic-plan-2012-2015.pdf

Kinunda, G. (2013). *A kinetic and mechanistic study on the substitution behaviour of mononuclear and dinuclear Platinum(II) complex* (Doctoral dissertation). [University of Kwa Zulu-Natal, Pietermaritzburg].

Kokkosi, A., Garofallidou, E., Zacharopoulos, N., Tsoureas, N., Diamanti, K., Thomaidis, N. S.,…Philippopoulos, A. I. (2024). Ruthenium *p*-cymene complexes incorporating substituted pyridine–quinoline-based ligands: synthesis, characterization, and cytotoxic properties. *Molecules, 29*(13), 3215. doi.org/10.3390/molecules29133215

Komeda, S., Kalayda, G. V., Lutz, M., Spek, A. L., Yamanaka, Y., Sato, T.,…Reedijk, J. (2003). New isomeric azine-bridged dinuclear platinum(II) complexes circumvent cross-resistance to cisplatin. *Journal of Medicinal Chemistry*, *46*(7), 1210-1219. 10.1021/jm020004+

Kopel, P., Wawrzak, D., Langer, V., Cihalova, K., Chudobova, D., Vesely, R.,…Kizek, R. (2015). Biological activity and molecular structures of bis(benzimidazole) and trithiocyanurate complexes. *Molecules*, *20*(6), 10360-10376. doi.org/10.3390/molecules200610360

Kostova, I. (2006). Platinum complexes as anticancer agents. *Recent patents on anti-cancer drug discovery*, *1*(1), 1-22. doi.org/10.2174/157489206775246458

Lakowicz, J. R. (2006). *Principles of fluorescence spectroscopy* (3rd ed.).Springer doi.org/10.1007/978-0-387-46312-4_2

Lee, C., Yang, W., & Parr, R. G. (1988). Development of the Colle-Salvetti correlation-energy formula into a functional of the electron density. *Physical Review B*, *37*(2), 785-789. doi:10.1103/PhysRevB.37.785

Lee, H. Z. S., Leong, W. K., Top, S., & Vessières, A. (2014). Cytotoxic triosmium carbonyl clusters: a structure–activity relationship study. *ChemMedChem*, *9*(7), 1453-1457. doi.org/10.1002/cmdc.201300394

Lee, R. F., Escrig, S., Maclachlan, C., Knott, G. W., Meibom, A., Sava, G., & Dyson, P. J. (2017). The differential distribution of RAPTA-T in non-invasive and invasive breast cancer cells correlates with its anti-invasive and anti-metastatic effects. *International Journal of Molecular Sciences*, *18*(9), 1869. doi.org/10.3390/ijms18091869

Lei, Z. N., Tian, Q., Teng, Q. X., Wurpel, J. N., Zeng, L., Pan, Y., & Chen, Z. S. (2023). Understanding and targeting resistance mechanisms in cancer. *Medical Communication*, *4*(3), e265. doi.org/10.1002/mco2.265

Lerman, L. (1961). Structural considerations in the interaction of DNA and acridines. *Journal of Molecular Biology*, *3*(1), 18-30. doi.org/10.1016/S0022-2836(61)80004-1

Li, J., Tian, M., Tian, Z., Zhang, S., Yan, C., Shao, C., & Liu, Z. (2018). Half-sandwich iridium(III) and ruthenium(II) complexes containing P^P-chelating ligands: A new class of potent anticancer agents with unusual redox features. *Inorganic Chemistry*, *57*(4), 1705-1716. doi.org/10.1021/acs.inorgchem.7b01959

Li, W.-Y., Xu, J.-G., Guo, X.-Q., Zhu, Q.-Z., & Zhao, Y.-B. (1997). Study on the interaction between rivanol and DNA and its application to DNA assay. *Spectrochimica Acta Part A: Molecular and Biomolecular Spectroscopy*, *53*(5), 781-787. doi.org/10.1016/S1386-1425(97)00015-2

Li, X.-B., Wang, H.-Y., Lv, R., Wu, W.-D., Luo, J.-S., & Tang, Y.-J. (2009). Correlations of the stability, static dipole polarizabilities, and electronic properties of yttrium clusters. *The Journal of Physical Chemistry A, 113*(38), 10335-10342. doi.org/10.1021/jp904420z

Lippert, B. (1999). *Cisplatin: chemistry and biochemistry of a leading anticancer drug*. John Wiley & Sons.

Liu, H.-K., & Sadler, P. J. (2011). Metal complexes as DNA intercalators. *Accounts of Chemical Research, 44*(5), 349-359. doi.org/10.1021/ar100140e

Liu, J.-X., Zhou, G.-B., Chen, S.-J., & Chen, Z. (2012). Arsenic compounds: revived ancient remedies in the fight against human malignancies. *Current Opinion in Chemical Biology, 16*(1-2), 92-98. doi.org/10.1016/j.cbpa.2012.01.015

Liu, J., Zhang, T., Lu, T., Qu, L., Zhou, H., Zhang, Q., & Ji, L. (2002). DNA-binding and cleavage studies of macrocyclic copper(II) complexes. *Journal of Inorganic Biochemistry, 91*(1), 269-276. doi.org/10.1016/S0162-0134(02)00441-5

Lopez-Valbuena, M., J., Escudero-Adan, C., E., Benet-Buchholz, Jordi Freixa,…M., P. W. N. (2010). An approach to bimetallic catalysts by ligand design. *Dalton Transactions, 39*(36), 8560-8574. doi.org/10.1039/C0DT00011F

Lu, Y., Zhu, D., Le, Q., Wang, Y., & Wang, W. (2022). Ruthenium-based antitumour drugs and delivery systems from monotherapy to combination therapy. *Nanoscale, 14*(44), 16339-16375. doi: 10.1039/D2NR02994D

Macrae, C. F., Bruno, I. J., Chisholm, J. A., Edgington, P. R., McCabe, P., Pidcock, E.,…Wood, P. A. (2008). Mercury CSD 2.0–new features for the visualization and investigation of crystal structures. *Journal of Applied Crystallography, 41*(2), 466-470. doi.org/10.1107/S0021889807067908

Maikoo, S., Chakraborty, A., Vukea, N., Dingle, L. M. K., Samson, W. J., de la Mare, J.-A.,…Booysen, I. N. (2021). Ruthenium complexes with mono-or bis-heterocyclic chelates: DNA/BSA binding, antioxidant and anticancer studies. *Journal of Biomolecular Structure and Dynamics, 39*(11), 4077-4088. doi:10.1080/07391102.2020.1775126

Mambanda, A., Kanyora, A. K., Ongoma, P., Gichumbi, J., & Omondi, R. O. (2022a). Chlorido-(η^6-*p*-cymene)-(bis(pyrazol-1-yl)methane-κ^2N,N′)osmium(II) tetrafluoroborate, $C_{17}H_{22}BClF_4N_4Os$. *Molbank, 2022*(3), M1429. doi.org/10.3390/M1429

Mambanda, A., Ongoma, P., Gichumbi, J., Omondi, R. O., Hunter, L. A., & Kanyora, A. K. (2022b). Crystal structures of half-sandwich Ru(II) complexes, [(η^6-*p*-cymene)(3-chloro-6-(1H-pyrazol-1-yl)pyridazine)Ru(X)]BF_4, (X= Cl, Br, I). *Molbank*, *2022*(4), M1477. doi.org/10.3390/M1477

Marchetti, F., Pettinari, C., Pettinari, R., Cerquetella, A., Di Nicola, C., Macchioni, A.,…Piccinelli, F. (2008). Synthesis and intramolecular and interionic structural characterization of half-sandwich (arene) ruthenium(II) derivatives of bis(pyrazolyl) alkanes. *Inorganic Chemistry, 47*(24), 11593-11603. doi:10.1021/ic801150c

Martinez, R., & Chacon-Garcia, L. (2005). The search of DNA-intercalators as antitumoural drugs: what it worked and what did not work. *Current Medicinal Chemistry*, *12*(2), 127-151. doi.org/10.2174/0929867053363414

Matsinha, L. C., Malatji, P., Hutton, A. T., Venter, G. A., Mapolie, S. F., & Smith, G. S. (2013). Water-soluble half-sandwich Ru^{II}–arene complexes: synthesis, structure, electrochemistry, DFT studies, and aqueous phase hydroformylation of 1-octene. *European Journal of Inorganic Chemistry*, *2013*(24), 4318-4328. doi:10.1002/ejic.201300503

Matveevskaya, V. V., Pavlov, D. I., Samsonenko, D. G., Ermakova, E. A., Klyushova, L. S., Baykov, S. V.,…Potapov, A. S. (2021). Synthesis and structural characterization of half-sandwich arene–ruthenium(II) complexes with bis(imidazol-1-yl)methane, Imidazole and Benzimidazole. *Inorganics*, *9*(5), 34. doi:10.3390/inorganics9050034

Maximiano, I., Henriques, C., Teixeira, R. G., Marques, F., Valente, A., & Antunes, A. M. (2024). Lead to hit ruthenium-cyclopentadienyl anticancer compounds: Cytotoxicity against breast cancer cells, metabolic stability and metabolite profiling. *Journal of Inorganic Biochemistry*, *251*, 112436. doi.org/10.1016/j.jinorgbio.2023.112436

Medjedović, M., Simović, A. R., Ćoćić, D., Milutinović, M., Senft, L., Blagojević, S.,…Petrović, B. (2020). Dinuclear ruthenium(II) polypyridyl complexes: Mechanistic study with biomolecules, DNA/BSA interactions and cytotoxic activity. *Polyhedron, 178,* 114334. doi:10.1016/j.poly.2019.114334

Meggers, E., Atilla-Gokcumen, G. E., Gründler, K., Frias, C., & Prokop, A. (2009). Inert ruthenium half-sandwich complexes with anticancer activity. *Dalton Transactions 2009*(48), 10882-10888. doi.org/10.1039/B917792B

Mendoza-Ferri, M.-G., Hartinger, C. G., Eichinger, R. E., Stolyarova, N., Severin, K., Jakupec, M. A.,…Keppler, B. K. (2008). Influence of the spacer length on the *in vitro* anticancer activity of dinuclear ruthenium-arene compounds. *Organometallics, 27*(11), 2405-2407. doi:10.1021/om800207t

Mendoza-Ferri, M. G., Hartinger, C. G., Nazarov, A. A., Eichinger, R. E., Jakupec, M. A., Severin, K., & Keppler, B. K. (2009). Influence of the arene ligand, the number and type of metal centres, and the leaving group on the *in vitro* antitumour activity of polynuclear organometallic compounds. *Organometallics*, *28*(21), 6260-6265. doi:10.1021/om900715j

Mishra, H., & Mukherjee, R. (2006). Half-sandwich η^6-benzene Ru(II) complexes of pyridylpyrazole and pyridylimidazole ligands: synthesis, spectra, and structure. *Journal of Organometallic Chemistry*, *691*(16), 3545-3555. doi.org/10.1016/j.jorganchem.2006.04.037

Mizuhara, T., Kato, T., Hirai, A., Kurihara, H., Shimada, Y., Taniguchi, M.,…Matsuoka, M. (2013). Structure–activity relationship study of phenylpyrazole derivatives as a novel class of anti-HIV agents. *Bioorganic & Medicinal Chemistry Letters*, *23*(16), 4557-4561. doi.org/10.1016/j.bmcl.2013.06.026

Mizumura, Y., Matsumura, Y., Hamaguchi, T., Nishiyama, N., Kataoka, K., Kawaguchi, T.,…Kakizoe, T. (2001). Cisplatin-incorporated polymeric micelles eliminate nephrotoxicity, while maintaining antitumour activity. *Japanese Journal of Cancer Research*, *92*(3), 328-336. doi:10.1111/j.1349-7006.2001.tb01099.x

Mondal, A., & Paira, P. (2020). Hypoxia efficient and glutathione-resistant cytoselective Ruthenium(II)-*p*-cymene-arylimidazophenanthroline complexes: biomolecular interaction and live cell imaging. *Dalton Transactions*, *49*(36), 12865-12878. doi.org/10.1039/D0DT02069A

Moon, S., Hanif, M., Kubanik, M., Holtkamp, H., Söhnel, T., Jamieson, S. M., & Hartinger, C. G. (2015). Organoruthenium and osmium anticancer complexes bearing a maleimide functional group: Reactivity to cysteine, stability, and cytotoxicity. *ChemPlusChem*, *80*(1), 231-236. doi:10.1002/cplu.201402390

Morris, R. E., Aird, R. E., del Socorro Murdoch, P., Chen, H., Cummings, J., Hughes, N. D.,…Jodrell, D. I. (2001). Inhibition of cancer cell growth by ruthenium(II) arene complexes. *Journal of Medicinal Chemistry*, *44*(22), 3616-3621. doi:10.1021/jm010051m

Mosmann, T. (1983). Rapid colorimetric assay for cellular growth and survival: application to proliferation and cytotoxicity assays. *Journal of Immunological Methods*, *65*(1-2), 55-63. doi:10.1016/0022-1759(83)90303-4

Moucheron, C., & Kirsch-De Mesmaeker, A. (1998). New DNA-binding ruthenium(II) complexes as photo-reagents for mononucleotides and DNA. *Journal of Physical Organic Chemistry*, *11*(8-9), 577-583. doi.org/10.1002/(SICI)1099-1395(199808/09)11:8/9<577::AID-POC53>3.0.CO;2-X

Mukherjee, S., Mitra, I., Fouzder, C., Mukherjee, S., Ghosh, S., Chatterji, U., & Moi, S. C. (2017). Effect of Pt(II) complexes on cancer and normal cells compared to clinically used anticancer drugs: Cell cycle analysis, apoptosis and DNA/BSA binding study. *Journal of Molecular Liquids*, *247*, 126-140. doi:10.1016/j.molliq.2017.09.104

Muley, A., Karumban, K. S., Gupta, P., Kumbhakar, S., Giri, B., Raut, R.,…Maji, S. (2021). Synthesis, structure, spectral, redox properties and anti-cancer activity of Ruthenium (II) Arene complexes with substituted Triazole Ligands. *Journal of Organometallic Chemistry*, *954*, 122074. doi.org/10.1016/j.jorganchem.2021.122074

Nabiyeva, T., Marschner, C., & Blom, B. (2020). Synthesis, structure and anti-cancer activity of osmium complexes bearing π-bound arene substituents and phosphane Co-Ligands: A review. *European Journal of Medicinal Chemistry*, *201*, 112483-112498. doi:10.1016/j.ejmech.2020.112483

Nahari, G., & Tshuva, E. Y. (2021). Synthesis of asymmetrical diaminobis(alkoxo)-bisphenol compounds and their C1-symmetrical mono-ligated titanium(IV) complexes as highly stable highly active antitumour compounds. *Dalton Transactions*, *50*(19), 6423-6426. doi:10.1039/D1DT00219H

Neels, A., Stoeckli-Evans, H., Plasseraud, L., Fidalgo, E. G., & Süss-Fink, G. (1999). Di-μ-bromo-bis[bromo(η^6-*para*-cymene)ruthenium(II)] benzene solvate and di-μ-iodo-bis[(η^6-para-cymene)iodoruthenium(II)] toluene solvate. *Acta Crystallographica Section C: Crystal Structure Communications*, *55*(12), 2030-2032. doi:10.1107/S0108270199010410

Ni, Y., Lin, D., & Kokot, S. (2006). Synchronous fluorescence, UV–visible spectrophotometric, and voltammetric studies of the competitive interaction of bis(1, 10-phenanthroline) copper(II) complex and neutral red with DNA. *Analytical Biochemistry*, *352*(2), 231-242. doi.org/10.1016/j.ab.2006.02.031

Nongpiur, C. G. L., Verma, A. K., Singh, R. K., Ghate, M. M., Poluri, K. M., Kaminsky, W., & Kollipara, M. R. (2023). Half-sandwich ruthenium(II), rhodium(III) and iridium(III) fluorescent metal complexes containing pyrazoline based ligands: DNA binding, cytotoxicity and antibacterial activities. *Journal of Inorganic Biochemistry, 238,* 112059. doi.org/10.1016/j.jinorgbio.2022.112059

Nováková, O., Nazarov, A. A., Hartinger, C. G., Keppler, B. K., & Brabec, V. (2009). DNA interactions of dinuclear Ru^{II} arene antitumour complexes in cell-free media. *Biochemical Pharmacology*, *77*(3), 364-374. doi.org/10.1016/j.bcp.2008.10.021

O'Riley, H. A., Levina, A., Aitken, J. B., & Lay, P. A. (2017). Synthesis, reactivities and anti-cancer properties of ruthenium(II) complexes with a thiaether macrocyclic ligand. *Inorganica Chimica Acta*, *454,* 128-138. doi.org/10.1016/j.ica.2016.07.050

Obuah, C., Ainooson, M. K., & Darkwa, J. (2018). Effects of electrochemical properties of ferrocenylpyrazolylnickel(II) and palladium(II) compounds on their catalytic activities in ethylene oligomerisation reactions. *Royal Society of Chemistry Advances*, *8*(10), 5362-5371. doi: 10.1039/C7RA13588B

Ojwach, S. O., Guzei, I. A., Darkwa, J., & Mapolie, S. F. (2007). Palladium complexes of multidentate pyrazolylmethyl pyridine ligands: Synthesis, structures and phenylacetylene polymerization. *Polyhedron*, *26*(4), 851-861. doi.org/10.1016/j.poly.2006.09.007

Oliver, T. G., Mercer, K. L., Sayles, L. C., Burke, J. R., Mendus, D., Lovejoy, K. S.,…Powers, S. (2010). Chronic cisplatin treatment promotes enhanced damage repair and tumour progression in a mouse model of lung cancer. *Genes & Development*, *24*(8), 837-852. doi: 10.1101/gad.1897010

Omondi, R. O., Bellam, R., Ojwach, S. O., Jaganyi, D., & Fatokun, A. A. (2020). Palladium(II) complexes of tridentate bis(benzazole) ligands: Structural, substitution kinetics, DNA interactions and cytotoxicity studies. *Journal of Inorganic Biochemistry*, *210*, 111156. doi:10.1016/j.jinorgbio.2020.111156

Omondi, R. O., Fadaka, A. O., Fatokun, A. A., Jaganyi, D., & Ojwach, S. O. (2022). Synthesis, substitution kinetics, DNA/BSA binding and cytotoxicity of tridentate N^ E^ N (E = NH, O, S) pyrazolyl palladium(II) complexes. *Journal of Biological Inorganic Chemistry*, *27*(7), 653-664. doi:10.1007/s00775-022-01959-y

Omondi, R. O., Jaganyi, D., Ojwach, S. O., & Fatokun, A. A. (2018). (Pyridyl) benzoazole ruthenium(III) complexes: Kinetics of ligand substitution reaction and potential cytotoxic properties. *Inorganica Chimica Acta*, *482*, 213-220. doi.org/10.1016/j.ica.2018.06.020

Omondi, R. O., Sibuyi, N. R., Fadaka, A. O., Meyer, M., Jaganyi, D., & Ojwach, S. O. (2021). Role of π-conjugation on the coordination behaviour, substitution kinetics, DNA/BSA interactions, and in vitro cytotoxicity of carboxamide Palladium(II) complexes. *Dalton Transactions*, *50*(23), 8127-8143. doi:10.1039/D1DT00412C

Ongoma, P., & Jaganyi, D. (2012). The π-acceptor effect in the substitution reactions of tridentate N-donor ligand complexes of Platinum(II): a detailed kinetic and mechanistic study. *Dalton Transactions*, *41*(35), 10724-10730. doi.org/10.1039/C2DT31041D

Ongoma, P. O. (2012). *Turning reactivity of Platinum(II) complexes: a kinetic and mechanistic investigation into substitution behaviour of mono-and Dinuclear Platinum(II) complexes* (Doctoral dissertation). [University of Kwa Zulu-Natal, Pietermaritzburg].

Ott, I., & Gust, R. (2007). Non platinum metal complexes as anti-cancer drugs. *Archiv der Pharmazie: An International Journal Pharmaceutical and Medicinal Chemistry*, *340*(3), 117-126. doi.org/10.1002/ardp.200600151

Padma-Nathan, H. (2006). Sildenafil citrate (Viagra) treatment for erectile dysfunction: an updated profile of response and effectiveness. *International Journal of Impotence Research*, *18*(5), 423-431. doi.org/10.1038/sj.ijir.3901492

Pages, B. J., Ang, D. L., Wright, E. P., & Aldrich-Wright, J. R. (2015). Metal complex interactions with DNA. *Dalton Transactions*, *44*(8), 3505-3526. doi:10.1039/C4DT02700K

Paitandi, R. P., Sharma, V., Singh, V. D., Dwivedi, B. K., Mobin, S. M., & Pandey, D. S. (2018). Pyrazole appended quinoline-BODIPY based arene ruthenium complexes: their anticancer activity and potential applications in cellular imaging. *Dalton Transactions*, *47*(48), 17500-17514. doi.org/10.1039/C8DT02947D

Paitandi, R. P., Singh, R. S., Mukhopadhyay, S., Sharma, G., Koch, B., Vishnoi, P., & Pandey, D. S. (2017). Synthesis, characterization, DNA binding and cytotoxicity of fluoro-dipyrrin based arene ruthenium(II) complexes. *Inorganica Chimica Acta, 454,* 117-127. doi:10.1016/j.ica.2016.03.003

Pal, D., Saha, S., & Singh, S. (2012). Importance of pyrazole moiety in the field of cancer. *International Journal of Pharmacy and Pharmaceutical Sciences, 4*(2), 98-104.

Parker, C., & Rees, W. (1962). Fluorescence spectrometry. A Review. *Analyst*, **8***7*(1031), 83-111. doi:10.1039/AN9628700083

Parkin, D. M. (2011). 14. Cancers attributable to occupational exposures in the UK in 2010. *British Journal of Cancer*, *105*, S70-S72. doi.org/10.1038/bjc.2011.487

Parr, R. G., Szentpály, L. V., & Liu, S. (1999). Electrophilicity index. *Journal of the American Chemical Society, 121*(9), 1922-1924. doi.org/10.1021/ja983494x

Pastuszko, A., Niewinna, K., Czyz, M., Jóźwiak, A., Małecka, M., & Budzisz, E. (2013). Synthesis, X-ray structure, electrochemical properties and cytotoxic effects of new arene ruthenium(II) complexes. *Journal of Organometallic Chemistry, 745,* 64-70. doi:10.1016/j.jorganchem.2013.07.020

Patra, M., Joshi, T., Pierroz, V., Ingram, K., Kaiser, M., Ferrari, S.,…Gasser, G. (2013). DMSO-mediated ligand dissociation: renaissance for biological activity of N-heterocyclic-[Ru(η^6-arene)Cl_2] drug candidates. *Chemistry–A European Journal*, *19*(44), 14768-14772. doi:10.1002/chem.201303341

Păunescu, E., Nowak-Sliwinska, P., Clavel, C. M., Scopelliti, R., Griffioen, A. W., & Dyson, P. J. (2015). Anticancer organometallic osmium(II)-*p*-cymene complexes. *ChemMedChem*, *10*(9), 1539-1547. doi:10.1002/cmdc.201500221

Peacock, A. F., Habtemariam, A., Fernández, R., Walland, V., Fabbiani, F. P., Parsons, S.,…Sadler, P. J. (2006). Tuning the reactivity of osmium(II) and ruthenium(II) arene complexes under physiological conditions. *Journal of the American Chemical Society*, *128*(5), 1739-1748. doi.org/10.1021/ja055886r

Peacock, A. F., Habtemariam, A., Moggach, S. A., Prescimone, A., Parsons, S., & Sadler, P. J. (2007). Chloro half-sandwich Osmium(II) complexes: influence of chelated N,N-ligands on hydrolysis, guanine binding, and cytotoxicity. *Inorganic Chemistry*, *46*(10), 4049-4059. doi:10.1021/ja068335p

Peacock, A. F., & Sadler, P. J. (2008). Medicinal organometallic chemistry: designing metal arene complexes as anticancer agents. *Chemistry–An Asian Journal*, *3*(11), 1890-1899. doi:10.1002/asia.200800149

Potapov, A. S., & Khlebnikov, A. I. (2006). Synthesis of mixed-ligand copper(II) complexes containing bis(pyrazol-1-yl) methane ligands. *Polyhedron*, *25*(14), 2683-2690. doi.org/10.1016/j.poly.2006.03.016

Prasad, K. T., Therrien, B., & Rao, K. M. (2008). Cationic half-sandwich complexes (Rh, Ir, Ru) containing 2-substituted-1, 8-naphthyridine chelating ligands: Syntheses, X-ray structure analyses and spectroscopic studies. *Journal of Organometallic Chemistry*, *693*(18), 3049-3056. doi:10.1016/j.jorganchem.2008.06.026

Puckett, C. A., Ernst, R. J., & Barton, J. K. (2010). Exploring the cellular accumulation of metal complexes. *Dalton Transactions*, *39*(5), 1159-1170. doi.org/10.1039/B922209J

Purkait, K., Chatterjee, S., Karmakar, S., & Mukherjee, A. (2016). Alteration of steric hindrance modulates glutathione resistance and cytotoxicity of three structurally related Ru^{II}-*p-cymene* complexes. *Dalton Transactions*, *45*(20), 8541-8555. doi: 10.1039/C5DT04781A

Purkait, K., Karmakar, S., Bhattacharyya, S., Chatterjee, S., Dey, S. K., & Mukherjee, A. (2015). A hypoxia efficient imidazole-based Ru(II) arene anticancer agent resistant to deactivation by glutathione. *Dalton Transactions*, *44*(13), 5969-5973. doi:10.1039/C4DT03983A

Reedijk, J. (1996). Improved understanding in platinium antitumour chemistry. *Chemical Communications 1996*(7), 801-806. doi.org/10.1039/CC9960000801

Romero-Canelon, I., Salassa, L., & Sadler, P. J. (2013). The contrasting activity of iodido versus chlorido ruthenium and osmium arene azo-and imino-pyridine anticancer complexes: control of cell selectivity, cross-resistance, p53 dependence, and apoptosis pathway. *Journal of Medicinal Chemistry*, *56*(3), 1291-1300. doi:10.1021/jm3017442

Romerosa, A., Campos-Malpartida, T., Lidrissi, C., Saoud, M., Serrano-Ruiz, M., Peruzzini, M.,…García-Maroto, F. (2006). Synthesis, characterization, and DNA binding of new water-soluble cyclopentadienyl ruthenium(II) complexes incorporating phosphines. *Inorganic Chemistry*, *45*(3), 1289-1298. doi.org/10.1021/ic051053q

Rosenberg, B., & Vancamp, L. (1969). Platinum compounds: a new class of potent antitumour agents. *Nature*, *222*, 385-386. doi.org/10.1038/222385a0

Sankareswari, V. G., Vinod, D., Mahalakshmi, A., Alamelu, M., Kumaresan, G., Ramaraj, R., & Rajagopal, S. (2014). Interaction of oxovanadium(IV)–salphen complexes with bovine serum albumin and their cytotoxicity against cancer. *Dalton Transactions*, *43*(8), 3260-3272. doi:10.1039/C3DT52505H

Sava, G., Bergamo, A., Zorzet, S., Gava, B., Casarsa, C., Cocchietto, M.,…Iengo, E. (2002). Influence of chemical stability on the activity of the antimetastasis ruthenium compound NAMI-A. *European Journal of Cancer*, *38*(3), 427-435. doi.org/10.1016/S0959-8049(01)00389-6

Schäfer, S., Ott, I., Gust, R., & Sheldrick, W. S. (2007). Influence of the polypyridyl (pp) ligand size on the DNA binding properties, cytotoxicity and cellular uptake of organoruthenium(II) complexes of the type $[(\eta^6\text{-}C_6Me_6)RuL)(pp)]^{n+}$ [L = Cl, n= 1; L= $(NH_2)_2CS$, n = 2]. *European Journal of Inorganic Chemistry*, *2007*(19), 3034-3046. doi.org/10.1002/ejic.200700206

Schmid, W. F., John, R. O., Arion, V. B., Jakupec, M. A., & Keppler, B. K. (2007). Highly antiproliferative ruthenium(II) and osmium(II) arene complexes with paullone-derived ligands. *Organometallics*, *26*(26), 6643-6652. doi.org/10.1021/om700813c

Schreiber, D. F., O'Connor, C., Grave, C., Müller-Bunz, H., Scopelliti, R., Dyson, P. J., & Phillips, A. D. (2013). Synthesis, characterization, and reactivity of the first osmium β-diketiminato complexes and application in catalysis. *Organometallics*, *32*(24), 7345-7356. doi:10.1021/om400875r

Sharma, A., Jasrotia, S., & Kumar, A. (2024). Effects of chemotherapy on the immune system: implications for cancer treatment and patient outcomes. *Naunyn-Schmiedeberg's Archives of Pharmacology*, *397*(5), 2551-2566. doi.org/10.1007/s00210-023-02781-2

Sheldrick, G. M. (2008). A short history of SHELX. *Acta Crystallographica Section A: Foundations of Crystallography*, *64*(1), 112-122. doi:10.1107/S0108767307043930

Sheldrick, G. M. (2015). SHELXT–Integrated space-group and crystal-structure determination. *Acta Crystallographica Section A: Foundations and Advances*, *71*(1), 3-8. doi:10.1107/S2053273314026370

Shoeib, T., & Sharp, B. L. (2012). Interactions of oxaliplatin with the cytoplasmic thiol containing ligand glutathione. *Metallomics*, *4*(12), 1308-1320. 10.1039/c2mt20127e

Silvestri, C., & Brodbelt, J. S. (2013). Tandem mass spectrometry for characterization of covalent adducts of DNA with anticancer therapeutics. *Mass Mpectrometry Reviews*, *32*(4), 247-266. doi.org/10.1002/mas.21363

Singh, S. K., Chandra, M., Pandey, D., Puerta, M., & Valerga, P. (2004). Helices of ruthenium complexes involving pyridyl–azine ligands: synthesis, spectral and structural aspects. *Journal of Organometallic Chemistry*, *689*(22), 3612-3620. doi.org/10.1002/mas.21363

Sirajuddin, M., Ali, S., & Badshah, A. (2013). Drug–DNA interactions and their study by UV–Visible, fluorescence spectroscopies and cyclic voltammetry. *Journal of Photochemistry and Photobiology B: Biology*, *124*, 1-19. doi.org/10.1016/j.jphotobiol.2013.03.013

Sirajuddin, M., Ali, S., Haider, A., Shah, N. A., Shah, A., & Khan, M. R. (2012). Synthesis, characterization, biological screenings and interaction with calf thymus DNA as well as electrochemical studies of adducts formed by azomethine [2-((3,5-dimethylphenylimino) methyl)phenol] and organotin(IV) chlorides. *Polyhedron*, *40*(1), 19-31. doi.org/10.1016/j.poly.2012.03.048

Snyder, R. D., & Hendry, L. B. (2005). Toward a greater appreciation of noncovalent chemical/ DNA interactions: application of biological and computational approaches. *Environmental and Molecular Mutagenesis*, *45*(2-3), 100-105. doi:10.1002/em.20096

Sodhi, R. K., & Paul, S. (2019). Metal complexes in medicine an overview and update from drug design perspective. *Cancer Therapy & Oncology International Journal*, *14*(1), 25-32. doi: 10.19080/CTOIJ.2019.14.555883

Stewart, B., & Wild, C. P. (2017). World Cancer Report 2014. *Health*.

Sze, J. H., Raninga, P. V., Nakamura, K., Casey, M., Khanna, K. K., Berners-Price, S. J.,…Tonissen, K. F. (2020). Anticancer activity of a Gold(I) phosphine thioredoxin reductase inhibitor in multiple myeloma. *Redox Biology*, *28***,** 101310-110321. doi:10.1016/j.redox.2019.101310

Tan, C., Liu, J., Li, H., Zheng, W., Shi, S., Chen, L., & Ji, L. (2008). Differences in structure, physiological stability, electrochemistry, cytotoxicity, DNA and protein binding properties between two Ru(III) complexes. *Journal of Inorganic Biochemistry*, *102*(2), 347-358. doi:10.1016/j.jinorgbio.2007.09.008

Taylor, R., & Kennard, O. (1982). Crystallographic evidence for the existence of CH. cntdot.. cntdot.. cntdot. O, CH. cntdot.. cntdot.. cntdot. N and CH. cntdot.. cntdot.. cntdot. Cl

hydrogen bonds. *Journal of the American Chemical Society*, *104*(19), 5063-5070. doi.org/10.1021/ja00383a012

Thangavel, S., Rajamanikandan, R., Friedrich, H. B., Ilanchelian, M., & Omondi, B. (2016). Binding interaction, conformational change, and molecular docking study of N-(pyridin-2-ylmethylene) aniline derivatives and carbazole Ru(II) complexes with human serum albumins. *Polyhedron*, *107*, 124-135. doi:10.1016/j.poly.2016.01.017

Thompson, L. K., Woon, T., Murphy, D. B., Gabe, E. J., Lee, F. L., & Le Page, Y. (1985). Binuclear copper(II) complexes of a series of tetradentate pyrazolyldiazines. Crystal and molecular structures of [μ-3,6-bis(3,5-dimethyl-1-pyrazolyl)pyridazine-N,μ-N^3,μ-N^3,N](μ-hydroxo)dichlorodicopper(II)aquotrichlorocuprate hydrate, $Cu_3C_{14}H_{21}Cl_5N_6O_3$, and [μ-3,6-bis(3,5-dimethyl-1-pyrazolyl)pyridazine-N,μ-N^6,μ-N^7,N](μ-hydroxo)tris(nitrato)diaquodicopper(II) hydrate, $Cu_2C_{14}H_{23}N_9O_{13}$. *Inorganic Chemistry*, *24*(26), 4719-4725. doi:10.1021/ic00220a057

Ting-WaiáCheung, M., & Wai-YináSun, R. (2011). Osmium(VI) complexes as a new class of potential anti-cancer agents. *Chemical Communications*, *47*(7), 2140-2142. doi.org/10.1039/C0CC04515B

Tomaz, A. I., Jakusch, T., Morais, T. S., Marques, F., De Almeida, R. F., Mendes, F.,…Kiss, T. (2012). $[Ru^{II}(\eta^5\text{-}C_5H_5)(bipy)(PPh_3)]^+$, a promising large spectrum antitumour agent: Cytotoxic activity and interaction with human serum albumin. *Journal of Inorganic Biochemistry*, *117*, 261-269. doi.org/10.1016/j.jinorgbio.2012.06.016

Tripathy, S. K., Taviti, A. C., Dehury, N., Sahoo, A., Pal, S., Beuria, T. K., & Patra, S. (2015). Synthesis, characterisation and antibacterial activity of $[(p\text{-}cym)RuX\ (L)]^{+}/^{2+}$(X = Cl, H_2O; L= bpmo, bpms) complexes. *Dalton Transactions*, *44*(11), 5114-5124. doi.org/10.1039/C4DT03647F

Trott, O., & Olson, A. J. (2010). AutoDock Vina: improving the speed and accuracy of docking with a new scoring function, efficient optimization, and multithreading. *Journal of Computational Chemistry*, *31*(2), 455-461. doi:10.1002/jcc.21334

Vajpayee, V., Song, Y. H., Lee, M. H., Kim, H., Wang, M., Stang, P. J., & Chi, K. W. (2011). Self-assembled arene–ruthenium-based rectangles for the selective sensing of multi-carboxylate anions. *Chemistry–A European Journal*, *17*(28), 7837-7844. doi.org/10.1002/chem.201100242

van Rijt, S. H., Peacock, A. F., Johnstone, R. D., Parsons, S., & Sadler, P. J. (2009). Organometallic Osmium(II) arene anticancer complexes containing picolinate derivatives. *Inorganic Chemistry*, *48*(4), 1753-1762. doi:10.1021/ic8020222

Versantvoort, C., Broxterman, H., Bagrij, T., Scheper, R., & Twentyman, P. (1995). Regulation by glutathione of drug transport in multidrug-resistant human lung tumour cell lines overexpressing multidrug resistance-associated protein. *British Journal of Cancer*, *72*(1), 82-89. doi.org/10.1038/bjc.1995.281

Wang, F., Chen, H., Parkinson, J. A., Murdoch, P. d. S., & Sadler, P. J. (2002). Reactions of a Ruthenium(II) arene antitumour complex with cysteine and methionine. *Inorganic Chemistry*, *41*(17), 4509-4523. doi:10.1021/ic025538f

Wang, H., Sayed, S. Y., Luber, E. J., Olsen, B. C., Shirurkar, S. M., Venkatakrishnan, S.,…McCreery, R. L. (2020). Redox flow batteries: how to determine electrochemical kinetic parameters. *American Chemical Society Nano*, *14*(3), 2575-2584. doi.org/10.1021/acsnano.0c01281

Wang, H., Zeng, X., Zhou, R., & Zhao, C. (2013). A comparative DFT study on aquation and nucleobase binding of ruthenium(II) and osmium(II) arene complexes. *Journal of molecular modeling*, *19*(11), 4849-4856. doi.org/10.1007/s00894-013-1987-5

Wang, H., Sayed, S. Y., Luber, E. J., Olsen, B. C., Shirurkar, S. M., Venkatakrishnan, S.,…McCreery, R. L. (2020). Redox flow batteries: how to determine electrochemical kinetic parameters. *American Chemical Society Nano*, *14*(3), 2575-2584. doi.org/10.1021/acsnano.0c01281

Wang, H. Y., Qian, Y., Wang, F. X., Habtemariam, A., Mao, Z. W., Sadler, P. J., & Liu, H. K. (2017). Ruthenium(II)–arene metallacycles: crystal structures, interaction with DNA, and cytotoxicity. *European Journal of Inorganic Chemistry*, *2017*(12), 1792-1799. doi:10.1002/ejic.201601226

Wani, W. A., Baig, U., Shreaz, S., Shiekh, R. A., Iqbal, P. F., Jameel, E.,…Hun, L. T. (2016). Recent advances in iron complexes as potential anticancer agents. *New Journal of Chemistry*, *40*(2), 1063-1090. doi:10.1039/C5NJ01449B

Wekesa, I. M., & Jaganyi, D. (2014). Kinetic and mechanistic studies of 1,3-bis(2-pyridylimino) isoindolate Pt(II) derivatives. Experimental and new computational approach. *Dalton Transactions*, *43*(6), 2549-2558. doi:10.1039/c3dt52272e

Welsh, A., Rylands, L. I., Arion, V. B., Prince, S., & Smith, G. S. (2020). Synthesis and antiproliferative activity of benzimidazole-based, trinuclear neutral cyclometallated and cationic, N^N-chelated ruthenium(II) complexes. *Dalton Transactions*, *49*(4), 1143-1156. doi:10.1039/C9DT03902C

Wheate, N. J., Taleb, R. I., Krause-Heuer, A. M., Cook, R. L., Wang, S., Higgins, V. J., & Aldrich-Wright, J. R. (2007). Novel platinum(II)-based anticancer complexes and molecular hosts as their drug delivery vehicles. *Dalton Transactions*, *43*, 5055-5064. doi.org/10.1039/B704973K

Wong, D. Y. Q., & Ang, W. H. (2012). Development of platinum(IV) complexes as anticancer prodrugs: the story so far. *COSMOS*, *8*(01), 121-134. doi.org/10.1142/S0219607712300020

Wu, Q., He, J., Mei, W., Zhang, Z., Wu, X., & Sun, F. (2014). Arene ruthenium(II) complex, a potent inhibitor against proliferation, migration and invasion of breast cancer cells, reduces stress fibers, focal adhesions and invadopodia. *Metallomics*, *6*(12), 2204-2212. doi.org/10.1039/c4mt00158c

Wu, X., Ye, R., Jia, A. Q., Chen, Q., & Zhang, Q. F. (2013). Syntheses, crystal structures and electrochemical properties of acetylacetonato-ruthenium complexes containing substituted pyridine ligands. *Zeitschrift für Naturforschung B*, *68*(9), 993-999. doi:10.5560/znb.2013-2344

Yan, Y. K., Melchart, M., Habtemariam, A., & Sadler, P. J. (2005). Organometallic chemistry, biology and medicine: ruthenium arene anticancer complexes. *Chemical Communications 2005*(38), 4764-4776.

Ywaya, D. O., Ibrahim, H., Friedrich, H. B., Bala, M. D., Soobramoney, L., Daniels, A., & Singh, M. (2024). Chemotherapeutic activities of New η^6-*p-cymene* Ruthenium(II) and osmium(II) complexes with chelating SS and tridentate SNS ligands. *Molecules*, *29*(5), 944. doi.org/10.3390/molecules29050944

Zeng, L., Gupta, P., Chen, Y., Wang, E., Ji, L., Chao, H., & Chen, Z.-S. (2017). The development of anticancer ruthenium(II) complexes: from single molecule compounds to nanomaterials. *Chemical Society Reviews*, *46*(19), 5771-5804. doi:10.1039/C7CS00195A

Zhang, P., & Huang, H. (2018). Future potential of osmium complexes as anticancer drug candidates, photosensitizers and organelle-targeted probes. *Dalton Transactions*, *47*(42), 14841-14854. doi:10.1039/C8DT03432J

Zhou, Q., Chen, S., Xu, Z., Liu, G., Zhang, S., Wang, Z.,…Zhu, G. (2023). Multitargeted platinum(IV) anticancer complexes bearing pyridinyl ligands as axial leaving groups. *Angewandte Chemie International Edition*, *62*(18), e202302156. doi.org/10.1002/anie.202302156

Zinman, P. S., Welsh, A., Omondi, R. O., Khan, S., Prince, S., Nordlander, E., & Smith, G. S. (2024). Aminoquinoline-based Re(I) tricarbonyl complexes: Insights into their antiproliferative activity and mechanisms of action. *European Journal of Medicinal chemistry, 266*, 116094. https://doi.org/10.1016/j.ejmech.2023.116094

APPENDICES

Appendix A: Published Papers

molbank

MDPI

Short Note

Chlorido-(η^6-*p*-cymene)-(bis(pyrazol-1-yl)methane-κ^2N,N')Osmium(II) Tetrafluoroborate, $C_{17}H_{22}BClF_4N_4Os$

Allen Mambanda [1,*], Amos K. Kanyora [2,*], Peter Ongoma [2], Joel Gichumbi [3] and Reinner O. Omondi [1,4]

[1] School of Chemistry and Physics, University of KwaZulu-Natal, Private Bag X01, Scottsville, Pietermaritzburg 3209, South Africa
[2] Department of Chemistry, Egerton University, Egerton P.O. Box 536-20115, Kenya
[3] Department of Physical Sciences, Chuka University, Chuka P.O. Box 109-60400, Kenya
[4] Department of Chemistry, University of Cape Town, Rondebosch 7701, South Africa
* Correspondence: mambanda@ukzn.ac.za (A.M.); kimem.aka12@gmail.com (A.K.K.)

Abstract: The powder of the arene osmium(II) complex, [Os(II)(dpzm)(η^6-*p*-cym)Cl]BF_4 (dpzm = di(1*H*-pyrazol-1-yl)methane; η^6-*p*-cym = *para*-cymene), with a formula of $C_{17}H_{22}BClF_4N_4Os$ (referred to herein as **1**) was isolated from the reaction of [(η^6-*p*-cym)Os(μ-Cl)(Cl)]$_2$ with dpzm dissolved in acetonitrile and under a flow of nitrogen gas. It was characterized by spectroscopic techniques (*viz.*, FTIR, ^{1}H NMR, UV-Visible absorption). Yellow crystal blocks of **1** were grown by the slow evaporation from the methanolic solution of its powder. The single-crystal X-ray structure of **1** was solved by diffraction analysis on a Bruker APEX Duo CCD area detector diffractometer using the Cu(K_α), λ = 1.54178 Å as the radiation source, and **1** crystallizes in the monoclinic crystal system and the C2/c (*no.* 15) space group.

Keywords: arene osmium(II) complex; di(1*H*-pyrazol-1-yl)methane; *para*-cymene; piano stool geometry; pseudo-octahedral geometry

Citation: Mambanda, A.; Kanyora, A.K.; Ongoma, P.; Gichumbi, J.; Omondi, R.O. Chlorido-(η^6-*p*-cymene)-(bis(pyrazol-1-yl)methane-κ^2N,N')Osmium(II) Tetrafluoroborate, $C_{17}H_{22}BClF_4N_4Os$. *Molbank* **2022**, *2022*, M1429. https://doi.org/10.3390/M1429

1st publication

1. Introduction

The acute toxicity, side effects, and development of resistance are some of the dis-

molbank

MDPI

Communication

Crystal Structures of Half-Sandwich Ru(II) Complexes, [(η^6-*p*-Cymene)(3-chloro-6-(1*H*-pyrazol-1-yl)pyridazine)Ru(X)]BF_4, (X = Cl, Br, I)

Allen Mambanda [1,*], Peter Ongoma [2], Joel Gichumbi [3], Reinner O. Omondi [1,4], Leigh A. Hunter [1] and Amos K. Kanyora [2,*]

[1] School of Chemistry and Physics, University of KwaZulu-Natal, Private Bag X01, Scottsville, Pietermaritzburg 3209, South Africa
[2] Department of Chemistry, Egerton University, Egerton P.O Box 536-20115, Kenya
[3] Department of Physical Sciences, Chuka University, Chuka P.O. Box 109-60400, Kenya
[4] Department of Chemistry, University of Cape Town, Rondebosch 7701, South Africa
* Correspondence: mambanda@ukzn.ac.za (A.M.); kimem.aka12@gmail.com (A.K.K.)

Abstract: Herein, we report the synthesis and single-crystal X-ray structures of three (η^6-*p*-cymene)Ru(II) tetrafluoroborate salts, viz., [(η^6-*p*-cymene)(3-chloro-6-(1*H*-pyrazol-1-yl)pyridazine)Ru(X)]BF_4, (X = Cl, Br, I), **Ru1-3**. They were prepared by the reactions of [(η^6-*p*-cymene)Ru(μ-X)(X)]$_2$, (X = Cl, Br, I) with two-mole equivalents of 3-chloro-6-(1H-pyrazol-1-yl)pyridazine, under inert conditions at ambient temperatures, and subsequently precipitated by the addition of excess BF_4^- ions. Orange crystalline precipitates were obtained in good yields, from which the respective single crystals for X-ray diffraction analysis were recrystallized by slow evaporation from their methanolic/diethyl ether solutions. The Ru(II) complexes were characterized by various spectroscopic techniques and chemical methods, which included FTIR, $^1H/^{13}C$ NMR, UV-visible absorption, mass spectrometry, and elemental analysis. The molecular structures were solved by single-crystal X-ray crystal diffraction analysis. The complexes crystallized in the monoclinic crystal system in the $P2_1/c$ (**Ru1-2**) and $P2_1/n$ (**Ru3**) space groups. Density Functionals Theoretical (DFT) calculations were performed in methanol to gain an understanding of the electronic and structural properties of the complexes. Trends in the data metrics were established, and selected data were compared with the diffraction data. The electrophilicity indices of **Ru1-3** follow the order **Ru3** > **Ru2** > **Ru1**, and the trend is in line with their anticipated order of reactivity towards nucleophiles.

Keywords: single-crystal X-ray structure; 3-chloro-6-(1H-pyrazol-1-yl)pyridazine; pyridazine; *p*-cymene ruthenium(II) complexes; DFT geometry optimized structure

Citation: Mambanda, A.; Ongoma, P.; Gichumbi, J.; Omondi, R.O.; Hunter, L.A.; Kanyora, A.K. Crystal Structures of Half-Sandwich Ru(II) Complexes, [(η^6-*p*-Cymene)(3-chloro-6-(1*H*-pyrazol-1-yl)pyridazine)Ru(X)]BF_4, (X = Cl, Br, I). *Molbank* **2022**, *2022*, M1477. https://doi.org/10.3390/M1477

Academic Editor: Kristof Van Hecke

Received: 6 August 2022
Accepted: 24 October 2022
Published: 31 October 2022

2nd Publication

JBIC Journal of Biological Inorganic Chemistry
https://doi.org/10.1007/s00775-024-02043-3

ORIGINAL PAPER

Mononuclear η^6-arene ruthenium(II) complexes with pyrazolyl–pyridazine ligands: synthesis, CT-DNA binding, reactivity towards glutathione, and cytotoxicity

Amos K. Kanyora[1] · Reinner O. Omondi[2] · Peter Ongoma[1] · Josiah O. Omolo[1] · Athi Welsh[2] · Sharon Prince[3] · Joel Gichumbi[4] · Allen Mambanda[5] · Gregory S. Smith[2]

Received: 6 July 2023 / Accepted: 8 January 2024

Abstract

Organometallic η^6-arene ruthenium(II) complexes with 3-chloro-6-(1*H*-pyrazol-1-yl)pyridazine (**Ru1**, **Ru2,** and **Ru5**) and 3-chloro-6-(3,5-dimethyl-1H-pyrazol-1-yl)pyridazine (**Ru3**-**4**) N,N' heterocyclic and η^6-arene (cymene (**Ru1**-**4**) or toluene (**Ru 5**)) have been synthesized. The ruthenium(II) complexes have common "three-legged piano-stool" pseudo-octahedral structures known for half-sandwich complexes. Evolution of their UV–Visible absorption spectra in PBS buffer or DMSO over 24 h confirmed their good solvolysis stability. Titrations of the complexes with the calf thymus DNA (CT-DNA) were monitored using UV–Visible absorption and fluorescence spectroscopies. The complexes interact moderately with CT-DNA and their binding constants are in the order of 10^4 M^{-1}. Competitive binding of the complexes to a DNA-Hoechst 33,258 depicted competitive displacement of Hoechst from DNA's minor grooves. These complexes bind to glutathione forming GSH-adducts through S coordination by replacement of a halide, with the iodo-analogues having higher binding constants than the chloro-complexes. Cyclic voltammograms of the complexes exhibited one electron-transfer quasi-reversible process. Trends in the molecular docking data of **Ru1**-**5**/DNA were similar to those for DNA binding constants. Of the five, only **Ru1**, **Ru3** and **Ru5** showed some activity (moderate) against the MCF-7 breast cancer cells with IC_{50} values in the range of 59.2–39.9 for which **Ru5** was the most active. However, the more difficult-to-treat cell line, MDA-MB 231 cell was recalcitrant to the treatment by these complexes.

3rd Publication

Journal of Molecular Structure

Crystal Structures, Computational Analysis, and Preliminary Cytotoxicity Evaluation of Half Sandwich η6-Arene Ruthenium(II) Complexes with Bis(pyrazol-1-yl)methane Ligands

--Manuscript Draft--

Manuscript Number:	MOLSTRUC-D-25-07193
Article Type:	Research Paper
Section/Category:	Medicinal chemistry
Keywords:	crystal structures; Density Functional Theory (DFT); arene-ruthenium(II) complexes; bis(pyrazol-1-yl)methane; anticancer activity.
Corresponding Author:	AMOS KIMEMIA KANYORA, MSc Egerton University - Njoro Campus EGERTON, NAKURU KENYA
First Author:	AMOS KIMEMIA KANYORA, MSc
Order of Authors:	AMOS KIMEMIA KANYORA, MSc
	Athi Welsh
	Peter Ongoma
	Josiah O. Omolo
	Joel Gichumbi
	Allen Mambanda
	Sharon Prince
	Gregory S. Smith
	Reinner O. Omondi
Abstract:	Reactions of bis(pyrazol-1-yl)methane (dpzm) or bis(3,5-dimethylpyrazol-1-yl)methane (bdmpzm) with arene ruthenium precursors, [(h6-arene)Ru(μ-Cl)Cl]2, in acetonitrile yielded four cationic mononuclear half-sandwich ruthenium(II) complexes of the general formula [(h6-cymene)Ru(dpzm/bdmpzm)Cl]+. The isolated complexes include [(η^6-cymene)Ru(dpzm)Cl]$^+$ (C1), [(η^6-cymene)Ru(bdmpzm)Cl]$^+$ (C2), [(η^6-toluene)Ru(bdmpzm)Cl]$^+$ (C6), and [(η^6-toluene)Ru(dpzm)Cl]$^+$ (C7), all obtained as tetrafluoroborate salts. Structural variations in both the arene and heterocyclic ligands were examined to assess their influence on cytotoxicity. The solution structures were characterised by FTIR, NMR, ESI-MS, and elemental analysis. Single-crystal X-ray diffraction confirmed the characteristic "three-legged piano-stool" geometries. Density Functional Theory (DFT) calculations revealed that complexes containing the methyl-substituted bdmpzm ligand exhibit smaller HOMO–LUMO gaps and higher global electrophilicity indices, indicating more electrophilic metal centres. Preliminary cytotoxicity screening against a panel of human cancer cell lines, including breast (MCF-7, T-47D, MDA-MB-231), cervical (Caski, HeLa), pancreatic (CFPAC-1, PANC-1), and rhabdomyosarcoma (RH-30, RD)—showed limited biological activity. These results suggest that further suggest that structural modifications and electronic tuning are necessary to enhance the anticancer potential of such complexes.

Fourth manuscript

Appendix B: Research Permit

REPUBLIC OF KENYA

NATIONAL COMMISSION FOR SCIENCE,TECHNOLOGY & INNOVATION

Ref No: 572892

Date of Issue: 17/July/2023

RESEARCH LICENSE

This is to Certify that Mr.. amos kimemia KANYORA of Egerton University, has been licensed to conduct research as per the provision of the Science, Technology and Innovation Act, 2013 (Rev.2014) in Nakuru on the topic: SYNTHESIS OF N-LIGANDS AND THEIR PLATINUM(II) COMPLEXES: KINETICS AND THERMODYNAMIC STUDIES for the period ending : 17/July/2024.

License No: **NACOSTI/P/23/27586**

572892

Applicant Identification Number

Director General
NATIONAL COMMISSION FOR SCIENCE,TECHNOLOGY & INNOVATION

Verification QR Code

NOTE: This is a computer generated License. To verify the authenticity of this document, Scan the QR Code using QR scanner application.

See overleaf for conditions

Appendix C: Arene Osmium(II) Complex

Table a: Fractional Atomic Coordinates ($\times 10^4$) and Equivalent Isotropic Displacement Parameters ($Å^2 \times 10^3$) for 10. Ueq is defined as 1/3 of the trace of the orthogonalised U_{IJ} tensor for complex **10**.

Atom	x	Y	z	U(eq)
Os1	6000.5(2)	3761.0(2)	5863.3(2)	9.57(8)
Cl1	5432.4(3)	3195.7(9)	4447.7(6)	15.23(18)
F1	7585.8(10)	7704(3)	6246(2)	35.0(6)
F3	7442.7(11)	9186(3)	7333(2)	36.8(7)
F4	6842.2(11)	7739(3)	6704(2)	36.5(7)
F2	7058.4(11)	9369(3)	5792(2)	37.6(7)
N4	6066.2(12)	5544(3)	5176(2)	12.1(6)
N2	6887.4(12)	3978(3)	4847(2)	14.3(6)
N1	6546.3(11)	3144(3)	5095(2)	13.4(6)
N3	6497.9(12)	6000(3)	4966(2)	13.2(6)
C3	7120.6(14)	3411(4)	4208(3)	17.6(8)
C11	5511.4(14)	2742(3)	6660(3)	12.7(7)
C6	5931.9(15)	7449(4)	4420(3)	18.1(8)
C10	5474.6(14)	4118(4)	6806(3)	12.7(7)
C5	6427.2(15)	7152(4)	4512(3)	17.4(8)
C8	5869.0(17)	6317(3)	7242(3)	19.6(9)
C4	6950.7(14)	5269(4)	5268(3)	15.0(7)
C7	5719.7(15)	6415(4)	4836(3)	15.7(8)
C9	5906.0(15)	4866(4)	7133(3)	13.8(7)
C13	6409.3(15)	2880(4)	7134(3)	16.8(8)
C14	6376.0(14)	4238(4)	7311(3)	15.1(7)
C15	5977.0(15)	2093(4)	6828(3)	15.9(8)
C2	6931.2(15)	2182(4)	4036(3)	18.8(8)
C1	6573.9(14)	2054(4)	4601(3)	16.1(8)
C16	6031.2(18)	641(4)	6691(3)	23.3(9)

C17	5604(2)	39(4)	5988(3)	33.8(11)
C18	6078(2)	-37(4)	7659(3)	33.1(11)
B1	7227.4(17)	8498(5)	6524(4)	20.4(9)

Table b: Bond Lengths for **10**

Atom	Atom	Length/Å	Atom	Atom	Length/Å
Os1	Cl1	2.3982(9)	N1	C1	1.336(5)
Os1	N4	2.105(3)	N3	C5	1.347(5)
Os1	N1	2.122(3)	N3	C4	1.448(5)
Os1	C11	2.191(3)	C3	C2	1.369(6)
Os1	C10	2.193(4)	C11	C10	1.433(5)
Os1	C9	2.212(3)	C11	C15	1.421(6)
Os1	C13	2.161(4)	C6	C5	1.376(6)
Os1	C14	2.205(4)	C6	C7	1.399(6)
Os1	C15	2.214(4)	C10	C9	1.416(5)
F1	B1	1.394(6)	C8	C9	1.502(5)
F3	B1	1.397(6)	C9	C14	1.422(6)
F4	B1	1.377(5)	C13	C14	1.422(6)
F2	B1	1.396(6)	C13	C15	1.435(6)
N4	N3	1.361(4)	C15	C16	1.514(5)
N4	C7	1.330(5)	C2	C1	1.395(6)
N2	N1	1.365(5)	C16	C17	1.529(7)
N2	C3	1.350(5)	C16	C18	1.545(6)
N2	C4	1.454(5)			

Table c: Bond Angles for **10**

Atom	Atom	Atom	Angle/˚	Atom	Atom	Atom	Angle/˚
N4	Os1	Cl1	84.71(9)	C1	N1	N2	105.9(3)
N4	Os1	N1	83.17(12)	N4	N3	C4	119.3(3)
N4	Os1	C11	141.02(13)	C5	N3	N4	110.9(3)
N4	Os1	C10	105.81(13)	C5	N3	C4	129.7(3)
N4	Os1	C9	88.80(13)	N2	C3	C2	108.0(4)
N4	Os1	C13	133.37(14)	C10	C11	Os1	71.02(19)
N4	Os1	C14	100.82(13)	C15	C11	Os1	72.1(2)
N4	Os1	C15	169.43(13)	C15	C11	C10	121.4(3)
N1	Os1	Cl1	83.83(9)	C5	C6	C7	105.9(3)
N1	Os1	C11	134.04(13)	C11	C10	Os1	70.8(2)
N1	Os1	C10	170.51(13)	C9	C10	Os1	71.9(2)
N1	Os1	C9	142.23(13)	C9	C10	C11	120.4(3)
N1	Os1	C13	90.80(13)	N3	C5	C6	106.9(3)
N1	Os1	C14	108.13(13)	N3	C4	N2	108.5(3)
N1	Os1	C15	101.85(13)	N4	C7	C6	109.9(4)
C11	Os1	Cl1	88.12(10)	C10	C9	Os1	70.6(2)
C11	Os1	C10	38.17(13)	C10	C9	C8	120.2(4)
C11	Os1	C9	68.33(13)	C10	C9	C14	119.3(3)
C11	Os1	C14	80.34(14)	C8	C9	Os1	128.0(3)
C11	Os1	C15	37.64(15)	C14	C9	Os1	71.0(2)
C10	Os1	Cl1	99.83(10)	C14	C9	C8	120.5(4)
C10	Os1	C9	37.51(14)	C14	C13	Os1	72.7(2)
C10	Os1	C14	67.66(14)	C14	C13	C15	121.9(3)
C10	Os1	C15	68.79(14)	C15	C13	Os1	72.9(2)
C9	Os1	Cl1	132.20(11)	C9	C14	Os1	71.5(2)
C9	Os1	C15	81.54(13)	C13	C14	Os1	69.3(2)
C13	Os1	Cl1	140.70(11)	C13	C14	C9	119.9(3)
C13	Os1	C11	68.09(15)	C11	C15	Os1	70.3(2)

C13	Os1	C10	80.81(14)	C11	C15	C13	117.1(3)
C13	Os1	C9	68.51(14)	C11	C15	C16	123.1(4)
C13	Os1	C14	37.99(15)	C13	C15	Os1	68.9(2)
C13	Os1	C15	38.27(15)	C13	C15	C16	119.9(4)
C14	Os1	Cl1	167.23(10)	C16	C15	Os1	131.5(3)
C14	Os1	C9	37.57(15)	C3	C2	C1	105.4(3)
C14	Os1	C15	68.84(14)	N1	C1	C2	110.5(3)
C15	Os1	Cl1	104.97(11)	C15	C16	C17	113.7(4)
N3	N4	Os1	124.0(2)	C15	C16	C18	108.6(3)
C7	N4	Os1	129.7(3)	C17	C16	C18	110.0(4)
C7	N4	N3	106.3(3)	F1	B1	F3	109.0(4)
N1	N2	C4	119.7(3)	F1	B1	F2	108.0(4)
C3	N2	N1	110.2(3)	F4	B1	F1	109.4(4)
C3	N2	C4	130.1(3)	F4	B1	F3	110.4(4)
N2	N1	Os1	122.5(2)	F4	B1	F2	110.3(4)
C1	N1	Os1	130.2(3)	F2	B1	F3	109.8(4

Appendix D: Half Sandwich Arene Ruthenium(II) Complexes of Bis(pyrazol-1-yl)methane

Table d: Fractional Atomic Coordinates ($\times 10^4$) and Equivalent Isotropic Displacement Parameters ($Å^2 \times 10^3$) for 3a. U_{eq} is defined as 1/3 of the trace of the orthogonalised U_{IJ} tensor for complex **3a**.

Atom	*x*	*y*	*z*	U(eq)
Ru1	1808.6(2)	1633.0(2)	3101.3(2)	6.17(9)
Cl1	580.6(5)	2484.6(6)	3659.3(5)	13.06(15)
Cl2	2216.7(6)	6469.9(7)	1932.6(6)	21.75(17)
F2	6649.9(14)	2151.3(17)	4600.9(13)	19.8(4)
F3	5328.7(16)	1559.8(17)	3103.9(14)	23.8(4)
F1	5772(2)	3625.1(19)	3441.6(15)	37.1(6)
F4	4954.9(17)	2593(2)	4247.7(18)	39.6(6)
N1	2836.4(19)	1600(2)	4606.7(18)	10.9(5)
N2	3319.5(18)	2719(2)	4968.2(17)	11.4(5)

N3	2464.0(19)	3424(2)	3377.5(18)	10.1(5)
N4	2183.6(18)	4277(2)	2644.7(17)	12.0(5)
C4	3117(2)	3701(3)	4305(2)	10.2(5)
C13	650(2)	211(3)	2225(2)	9.6(5)
C5	3564(2)	4896(3)	4589(2)	16.6(6)
C15	2573(2)	10(3)	2771(2)	9.4(5)
C16	2516(2)	1012(3)	2132(2)	10.8(5)
C11	584(2)	1238(3)	1578.5(19)	9.5(5)
C1	3146(2)	828(3)	5365(2)	14.9(6)
C3	3960(2)	2632(3)	5962(2)	14.9(6)
C6	3296(2)	5774(3)	3853(2)	18.1(6)
C9	-473(2)	1861(3)	992(2)	12.8(6)
C12	1532(2)	1618(2)	1542(2)	10.4(6)
C10	-1114(2)	1051(3)	76(2)	18.7(6)
C8	-387(3)	3213(3)	696(2)	16.9(6)
C7	2601(2)	5411(3)	2892(2)	13.7(6)
C17	3610(2)	-579(3)	3422(2)	14.3(6)
C14	1612(2)	-400(3)	2798(2)	10.5(5)
C2	3857(2)	1435(3)	6238(2)	16.8(6)
B1	5668(3)	2482(3)	3840(2)	14.1(6)

Table e: Fractional Atomic Coordinates ($\times 10^4$) and Equivalent Isotropic Displacement Parameters ($Å^2 \times 10^3$) for 3b. *Ueq* is defined as 1/3 of the trace of the orthogonalised U_{IJ} tensor for complex **3b**.

Atom	*x*	*y*	*z*	U(eq)
Ru1	8156.1(2)	1619.0(2)	6898.0(2)	9.94(6)
Br1	9423.0(2)	2428.4(2)	6287.6(2)	16.93(7)
Cl1	7738.2(4)	6412.3(5)	8104.0(4)	24.55(12)
F1	3350.7(10)	2141.7(13)	5355.3(9)	22.8(3)
F2	4679.5(11)	1558.8(12)	6863.4(9)	24.8(3)
F3	4201.8(13)	3609.7(14)	6533.5(10)	36.1(4)
F4	5039.0(12)	2639.5(16)	5753.2(12)	39.8(4)
N2	6642.8(13)	2736.3(17)	5030.3(13)	14.4(3)
N3	7526.8(13)	3410.3(16)	6632.9(12)	13.0(3)
N4	7796.2(13)	4254.5(17)	7370.6(13)	16.3(4)
N1	7098.0(13)	1599.0(16)	5399.9(13)	14.2(4)
C11	8352.6(16)	-402.9(19)	7206.6(15)	14.8(4)
C9	7413.3(16)	8.7(19)	7242.2(15)	14.4(4)
C4	6859.9(15)	3711(2)	5698.6(15)	14.2(4)
C12	9320.0(16)	200(2)	7773.4(15)	15.1(4)
C2	6105.7(17)	1474(2)	3751.1(16)	20.1(5)
C13	9414.8(16)	1227(2)	8417.5(14)	14.1(4)
C10	7496.6(16)	1018(2)	7879.7(15)	14.2(4)
C3	6024.4(16)	2667(2)	4025.9(15)	17.4(4)
C1	6781.7(16)	840(2)	4627.5(15)	17.3(4)
C14	8488.1(16)	1617.3(19)	8461.6(15)	14.1(4)
C15	10480.3(16)	1848(2)	8998.8(15)	16.6(4)
C5	6421.4(17)	4905(2)	5422.2(16)	19.8(4)
C8	6362.2(16)	-578(2)	6596.8(16)	18.1(4)
C17	10413.7(17)	3212(2)	9263.4(16)	20.4(5)
C6	6690.0(18)	5767(2)	6163.1(17)	20.8(5)

C7	7377.3(17)	5379(2)	7131.2(16)	18.1(4)
C16	11126.3(17)	1063(2)	9938.2(16)	21.9(5)
B1	4325.7(19)	2482(2)	6132.1(18)	18.3(5)

Table f: Fractional Atomic Coordinates ($\times 10^4$) and Equivalent Isotropic Displacement Parameters ($Å^2 \times 10^3$) for 3c. U_{eq} is defined as 1/3 of the trace of the orthogonalised U_{IJ} tensor for complex **3c.**

Atom	*x*	*y*	*z*	U(eq)
I1	8208.5(2)	2292.4(2)	3768.1(2)	14.75(5)
Ru1	6219.6(2)	1589.2(2)	3106.7(2)	9.14(5)
Cl1	4531.6(5)	6298.3(6)	1874.8(5)	26.11(14)
F3	2884.0(13)	1580.4(14)	3174.2(11)	25.0(3)
F4	3054.9(13)	2140.8(14)	4692.8(11)	25.2(3)
F1	2688.5(16)	3605.9(16)	3507.8(12)	38.1(5)
F2	4274.8(14)	2702.4(19)	4242.1(15)	41.9(5)
N2	6580.7(16)	2743.0(19)	4973.0(15)	15.2(4)
N1	6617.2(16)	1591.2(19)	4602.5(15)	14.4(4)
N4	5395.8(16)	4201.2(19)	2625.1(15)	15.5(4)
N3	5885.1(15)	3387.1(18)	3369.1(14)	12.9(4)
C13	5996.6(18)	1204(2)	1589.3(16)	13.0(5)
C10	6085.6(19)	-421(2)	2787.3(18)	14.7(5)
C14	6496.9(18)	168(2)	2220.4(17)	13.5(5)
C12	5058.2(18)	1614(2)	1554.8(17)	13.2(5)
C9	5134.9(18)	8(2)	2753.2(17)	14.1(5)
C4	6141.4(19)	3702(2)	4301.8(18)	14.9(5)
C11	4628.4(18)	1023(2)	2127.2(17)	14.6(5)
C15	6488(2)	1802(2)	1001.1(18)	16.3(5)
C2	7317(2)	1511(3)	6255.9(19)	21.0(6)

C7	5201(2)	5318(2)	2856.2(19)	18.5(5)
C3	6999(2)	2704(3)	5980.6(18)	19.1(5)
C1	7071.2(19)	849(2)	5377.6(18)	17.4(5)
C16	6246(2)	3185(2)	798.9(19)	20.3(5)
C8	4717(2)	-574(2)	3389.6(19)	18.8(5)
C5	5979(2)	4896(2)	4568.6(19)	21.2(5)
C6	5496(2)	5727(2)	3825(2)	22.3(6)
C17	6169(2)	1067(3)	35.9(18)	20.5(5)
B1	3231(2)	2500(3)	3894(2)	17.0(6)

Table g: Bond Lengths (Å) for **3a**

Atom	Atom	Length/Å	Atom	Atom	Length/Å
Ru1	Cl1	2.3920(6)	N3	N4	1.344(3)
Ru1	N1	2.080(2)	N3	C4	1.321(4)
Ru1	N3	2.079(2)	N4	C7	1.323(4)
Ru1	C13	2.192(3)	C4	C5	1.400(4)
Ru1	C15	2.200(3)	C13	C11	1.435(4)
Ru1	C16	2.182(3)	C13	C14	1.404(4)
Ru1	C11	2.217(3)	C5	C6	1.366(5)
Ru1	C12	2.189(3)	C15	C16	1.410(4)
Ru1	C14	2.204(3)	C15	C17	1.493(4)
Cl2	C7	1.716(3)	C15	C14	1.434(4)
F2	B1	1.398(4)	C16	C12	1.429(4)
F3	B1	1.395(4)	C11	C9	1.510(4)
F1	B1	1.390(4)	C11	C12	1.412(4)
F4	B1	1.382(4)	C1	C2	1.409(4)
N1	N2	1.361(3)	C3	C2	1.366(5)
N1	C1	1.312(4)	C6	C7	1.395(4)
N2	C4	1.383(4)	C9	C10	1.536(4)
N2	C3	1.365(4)	C9	C8	1.526(4)

Table h: Bond Lengths (Å) for **3b**.

Atom	Atom	Length/Å	Atom	Atom
Ru1	Br1	2.5228(2)	N3	C4
Ru1	N3	2.0718(17)	N4	C7
Ru1	N1	2.0712(17)	N1	C1
Ru1	C11	2.199(2)	C11	C9
Ru1	C9	2.201(2)	C11	C12
Ru1	C12	2.189(2)	C9	C10
Ru1	C13	2.2158(19)	C9	C8
Ru1	C10	2.1835(19)	C4	C5
Ru1	C14	2.190(2)	C12	C13
Cl1	C7	1.719(2)	C2	C3
F1	B1	1.396(3)	C2	C1
F2	B1	1.393(3)	C13	C14
F3	B1	1.396(3)	C13	C15
F4	B1	1.384(3)	C10	C14
N2	N1	1.370(2)	C15	C17
N2	C4	1.384(3)	C15	C16
N2	C3	1.367(3)	C5	C6
N3	N4	1.347(2)	C6	C7

Table i: Bond Lengths (Å) for **3c.**

Atom	Atom	Length/Å	Atom	Atom	Length/Å
I1	Ru1	2.6996(2)	N4	N3	1.347(3)
Ru1	N1	2.073(2)	N4	C7	1.317(3)
Ru1	N3	2.0743(19)	N3	C4	1.334(3)
Ru1	C13	2.215(2)	C13	C14	1.432(3)
Ru1	C10	2.203(2)	C13	C12	1.411(3)
Ru1	C14	2.191(2)	C13	C15	1.517(3)
Ru1	C12	2.186(2)	C10	C14	1.403(3)
Ru1	C9	2.211(2)	C10	C9	1.435(3)
Ru1	C11	2.190(2)	C12	C11	1.430(3)
Cl1	C7	1.719(3)	C9	C11	1.413(3)
F3	B1	1.387(3)	C9	C8	1.493(3)
F4	B1	1.404(3)	C4	C5	1.397(4)
F1	B1	1.399(3)	C15	C16	1.525(4)
F2	B1	1.377(4)	C15	C17	1.539(3)
N2	N1	1.370(3)	C2	C3	1.362(4)
N2	C4	1.384(3)	C2	C1	1.407(4)
N2	C3	1.366(3)	C7	C6	1.403(4)
N1	C1	1.323(3)	C5	C6	1.358(4)

Table j: Bond Angles (˚) for **3a.**

Atom	Atom	Atom	Angle/˚	Atom	Atom	Atom	Angle/˚
N1	Ru1	Cl1	84.03(7)	C7	N4	N3	116.9(2)
N1	Ru1	C13	128.42(10)	N2	C4	C5	122.9(3)
N1	Ru1	C15	93.02(9)	N3	C4	N2	114.6(2)
N1	Ru1	C16	114.27(10)	N3	C4	C5	122.5(3)
N1	Ru1	C11	166.40(10)	C11	C13	Ru1	71.96(15)
N1	Ru1	C12	150.50(10)	C14	C13	Ru1	71.84(15)
N1	Ru1	C14	99.92(10)	C14	C13	C11	121.9(2)
N3	Ru1	Cl1	84.61(7)	C6	C5	C4	116.5(3)
N3	Ru1	N1	76.18(9)	C16	C15	Ru1	70.55(15)
N3	Ru1	C13	154.39(10)	C16	C15	C17	120.8(2)
N3	Ru1	C15	123.29(10)	C16	C15	C14	118.1(2)
N3	Ru1	C16	96.94(10)	C17	C15	Ru1	127.94(19)
N3	Ru1	C11	117.17(10)	C14	C15	Ru1	71.16(15)
N3	Ru1	C12	94.43(10)	C14	C15	C17	121.1(2)
N3	Ru1	C14	161.21(10)	C15	C16	Ru1	71.90(15)
C13	Ru1	Cl1	90.66(7)	C15	C16	C12	121.0(2)
C13	Ru1	C15	68.26(10)	C12	C16	Ru1	71.20(15)
C13	Ru1	C11	37.99(10)	C13	C11	Ru1	70.05(15)
C13	Ru1	C14	37.25(10)	C13	C11	C9	119.1(2)
C15	Ru1	Cl1	150.48(7)	C9	C11	Ru1	129.90(19)
C15	Ru1	C11	81.76(10)	C12	C11	Ru1	70.24(15)
C15	Ru1	C14	38.00(10)	C12	C11	C13	117.1(2)
C16	Ru1	Cl1	161.53(8)	C12	C11	C9	123.8(3)
C16	Ru1	C13	79.97(10)	N1	C1	C2	110.4(3)
C16	Ru1	C15	37.55(10)	N2	C3	C2	106.6(3)
C16	Ru1	C11	68.53(10)	C5	C6	C7	117.7(3)
C16	Ru1	C12	38.16(10)	C11	C9	C10	108.6(2)
C16	Ru1	C14	67.55(10)	C11	C9	C8	113.7(2)

C11	Ru1	Cl1	94.31(7)	C8	C9	C10	111.2(2)
C12	Ru1	Cl1	123.43(8)	C16	C12	Ru1	70.65(15)
C12	Ru1	C13	67.37(10)	C11	C12	Ru1	72.37(15)
C12	Ru1	C15	68.54(10)	C11	C12	C16	121.3(3)
C12	Ru1	C11	37.39(10)	N4	C7	Cl2	115.2(2)
C12	Ru1	C14	79.93(10)	N4	C7	C6	124.6(3)
C14	Ru1	Cl1	113.51(7)	C6	C7	Cl2	120.3(2)
C14	Ru1	C11	68.31(10)	C13	C14	Ru1	70.90(15)
N2	N1	Ru1	114.01(17)	C13	C14	C15	120.5(3)
N1	N2	C4	117.7(2)	F3	B1	F2	110.1(3)
N1	N2	C3	110.6(2)	F1	B1	F2	108.6(3)
C3	N2	C4	131.6(3)	F1	B1	F3	110.0(3)
N4	N3	Ru1	120.68(18)	F4	B1	F2	108.0(3)
C4	N3	Ru1	117.34(19)	F4	B1	F3	110.1(3)
C4	N3	N4	121.9(2)	F4	B1	F1	110.1(3)

Table j: Bond Angles (˚) for **3b**

Atom	Atom	Atom	Angle/˚	Atom	Atom	Atom	Angle/˚
N3	Ru1	Br1	86.02(5)	C1	N1	N2	106.01(17)
N3	Ru1	C11	161.62(7)	C9	C11	Ru1	71.10(12)
N3	Ru1	C9	123.72(7)	C12	C11	Ru1	70.96(12)
N3	Ru1	C12	153.77(7)	C12	C11	C9	120.59(19)
N3	Ru1	C13	116.66(7)	C11	C9	Ru1	70.96(12)
N3	Ru1	C10	96.96(7)	C11	C9	C8	121.18(19)
N3	Ru1	C14	94.08(7)	C10	C9	Ru1	70.50(11)
N1	Ru1	Br1	83.50(5)	C10	C9	C11	118.06(19)
N1	Ru1	N3	76.33(7)	C10	C9	C8	120.72(18)
N1	Ru1	C11	100.41(7)	C8	C9	Ru1	128.02(14)
N1	Ru1	C9	93.62(7)	N2	C4	C5	123.17(19)
N1	Ru1	C12	128.78(7)	N3	C4	N2	114.03(18)
N1	Ru1	C13	166.68(7)	N3	C4	C5	122.8(2)

N1	Ru1	C10	114.70(7)	C11	C12	Ru1	71.78(12)
N1	Ru1	C14	150.76(7)	C11	C12	C13	121.94(18)
C11	Ru1	Br1	111.78(5)	C13	C12	Ru1	72.05(11)
C11	Ru1	C9	37.94(8)	C3	C2	C1	106.22(19)
C11	Ru1	C13	68.28(8)	C12	C13	Ru1	70.01(11)
C9	Ru1	Br1	148.67(6)	C12	C13	C15	119.29(18)
C9	Ru1	C13	81.66(8)	C14	C13	Ru1	70.33(11)
C12	Ru1	Br1	89.38(5)	C14	C13	C12	117.25(18)
C12	Ru1	C11	37.27(8)	C14	C13	C15	123.45(19)
C12	Ru1	C9	68.18(8)	C15	C13	Ru1	129.83(14)
C12	Ru1	C13	37.94(8)	C9	C10	Ru1	71.86(11)
C12	Ru1	C14	67.37(8)	C9	C10	C14	120.89(18)
C13	Ru1	Br1	94.03(5)	C14	C10	Ru1	71.20(11)
C10	Ru1	Br1	161.76(5)	C2	C3	N2	106.77(19)
C10	Ru1	C11	67.65(8)	N1	C1	C2	110.5(2)
C10	Ru1	C9	37.64(8)	C13	C14	Ru1	72.27(11)
C10	Ru1	C12	79.99(8)	C13	C14	C10	121.26(19)
C10	Ru1	C13	68.50(7)	C10	C14	Ru1	70.67(11)
C10	Ru1	C14	38.12(8)	C13	C15	C17	113.90(18)
C14	Ru1	Br1	123.87(6)	C13	C15	C16	108.36(17)
C14	Ru1	C11	79.98(8)	C17	C15	C16	111.09(18)
C14	Ru1	C9	68.55(8)	C6	C5	C4	116.8(2)
C14	Ru1	C13	37.40(8)	C5	C6	C7	117.4(2)
N1	N2	C4	117.51(16)	N4	C7	Cl1	115.41(16)
C3	N2	N1	110.53(17)	N4	C7	C6	124.7(2)
C3	N2	C4	131.95(18)	C6	C7	Cl1	119.89(17)
N4	N3	Ru1	121.52(13)	F2	B1	F1	110.17(19)
C4	N3	Ru1	117.59(14)	F2	B1	F3	109.67(18)
C4	N3	N4	120.87(17)	F3	B1	F1	108.45(19)
C7	N4	N3	117.43(17)	F4	B1	F1	108.50(19)
N2	N1	Ru1	114.19(12)	F4	B1	F2	110.32(19)

C1	N1	Ru1	139.34(15)	F4	B1	F3	109.7(2)

Table k: Bond Angles (˚) for **3c**

Atom	Atom	Atom	Angle/˚	Atom	Atom	Atom	Angle/˚
N1	Ru1	I1	82.85(6)	C4	N3	N4	120.7(2)
N1	Ru1	N3	76.19(8)	C14	C13	Ru1	70.12(12)
N1	Ru1	C13	167.37(8)	C14	C13	C15	119.4(2)
N1	Ru1	C10	101.23(8)	C12	C13	Ru1	70.20(13)
N1	Ru1	C14	129.53(8)	C12	C13	C14	117.0(2)
N1	Ru1	C12	150.94(9)	C12	C13	C15	123.5(2)
N1	Ru1	C9	94.52(8)	C15	C13	Ru1	130.42(16)
N1	Ru1	C11	115.17(8)	C14	C10	Ru1	70.92(13)
N3	Ru1	I1	88.44(6)	C14	C10	C9	120.3(2)
N3	Ru1	C13	115.96(8)	C9	C10	Ru1	71.33(13)
N3	Ru1	C10	161.88(8)	C13	C14	Ru1	71.95(13)
N3	Ru1	C14	153.10(8)	C10	C14	Ru1	71.83(13)
N3	Ru1	C12	93.58(8)	C10	C14	C13	122.2(2)
N3	Ru1	C9	123.96(8)	C13	C12	Ru1	72.41(13)
N3	Ru1	C11	97.00(8)	C13	C12	C11	121.4(2)
C13	Ru1	I1	93.65(6)	C11	C12	Ru1	71.08(13)
C10	Ru1	I1	109.19(6)	C10	C9	Ru1	70.73(13)
C10	Ru1	C13	68.37(9)	C10	C9	C8	120.7(2)
C10	Ru1	C9	37.95(9)	C11	C9	Ru1	70.49(14)
C14	Ru1	I1	87.60(6)	C11	C9	C10	118.1(2)
C14	Ru1	C13	37.93(9)	C11	C9	C8	121.2(2)
C14	Ru1	C10	37.25(9)	C8	C9	Ru1	128.33(16)
C14	Ru1	C9	68.02(9)	N2	C4	C5	123.5(2)
C12	Ru1	I1	124.58(6)	N3	C4	N2	113.9(2)
C12	Ru1	C13	37.39(9)	N3	C4	C5	122.6(2)
C12	Ru1	C10	80.04(9)	C12	C11	Ru1	70.79(13)

C12	Ru1	C14	67.28(9)	C9	C11	Ru1	72.06(13)
C12	Ru1	C9	68.45(9)	C9	C11	C12	120.9(2)
C12	Ru1	C11	38.14(9)	C13	C15	C16	113.8(2)
C9	Ru1	I1	146.05(6)	C13	C15	C17	109.0(2)
C9	Ru1	C13	81.59(9)	C16	C15	C17	111.5(2)
C11	Ru1	I1	161.93(6)	C3	C2	C1	106.3(2)
C11	Ru1	C13	68.45(9)	N4	C7	Cl1	115.64(19)
C11	Ru1	C10	67.54(9)	N4	C7	C6	124.4(2)
C11	Ru1	C14	79.74(9)	C6	C7	Cl1	119.9(2)
C11	Ru1	C9	37.45(9)	C2	C3	N2	106.8(2)
N1	N2	C4	117.47(19)	N1	C1	C2	110.3(2)
C3	N2	N1	110.6(2)	C6	C5	C4	117.0(2)
C3	N2	C4	132.0(2)	C5	C6	C7	117.5(2)
N2	N1	Ru1	114.02(14)	F3	B1	F4	109.9(2)
C1	N1	Ru1	138.72(18)	F3	B1	F1	110.0(2)
C1	N1	N2	106.0(2)	F1	B1	F4	107.8(2)
C7	N4	N3	117.6(2)	F2	B1	F3	110.9(2)
N4	N3	Ru1	121.59(14)	F2	B1	F4	108.3(2)
C4	N3	Ru1	117.63(16)	F2	B1	F1	109.8(2)

Table l: Short contacts or non-conventional hydrogen bonds.

3a			3b			3c		
Atom1	Atom2	Length	Atom1	Atom2	Length	Atom1	Atom2	Length
H5	C3	2.833	C3	H5	2.844	C12	H16A	2.841
C12	H8C	2.839	C14	H17C	2.838	H12	C16	2.695
H12	C8	2.65	H14	C17	2.667	H12	H16A	2.279
H12	H8C	2.278	H14	H17C	2.275	C3	H5	2.853
C13	Cl1	3.343	C12	Br1	3.414	C14	I1	3.545
H13	Cl1	2.902	H12	Br1	2.979	H14	I1	3.104
H16	C3	2.678	Br1	H17C	3.024	C2	C8	3.39
N2	F4	2.927	C3	H10	2.714	H11	C3	2.809
C4	F4	2.868	N2	F4	2.947	H16A	I1	3.167
H17A	F3	2.62	C4	F4	2.867	N2	F2	3.012
H17B	F1	2.596	H8A	F2	2.569	C4	F2	2.88
1 H1	F2	2.337	H8B	F3	2.621	H8C	F3	2.537
H1	B1	3.191	H1	F1	2.319	H1	F4	2.319
H17C	F2	2.578	H1	B1	3.132	H1	B1	3.096
C5	F1	3.103	H8C	F1	2.61	C5	F1	3.118
C5	B1	3.503	C5	F3	3.108	C5	B1	3.486
H5	F1	2.292	C5	B1	3.487	H5	F1	2.306
H5	B1	2.863	H5	F3	2.302	H5	F2	2.66
C6	B1	3.619	H5	B1	2.843	H5	B1	2.826
H6	F2	2.618	C6	B1	3.614	C6	B1	3.635
H6	B1	3.098	H6	F1	2.63	H6	F2	2.662
H10B	F2	2.572	H6	B1	3.1	H6	B1	3.128
C3	F3	3.056	H2	F3	2.417	H2	F1	2.405
H3	F3	2.336	H2	B1	3.11	H2	B1	3.071
H2	F1	2.436	C3	F2	3.055	C3	F3	3.072
H2	B1	3.146	H3	F2	2.347	H3	F3	2.389
			H16B	F1	2.61			